Solution-Processed Transparent Electrodes for Emerging Thin-film Solar Cells

Yaokang Zhang, Sze-Wing Ng, Xi Lu, and Zijian Zheng*

Laboratory for Advanced Interfacial Materials and Devices and Research Centre for Smart Wearable Technology, Institute of Textiles and Clothing, the Hong Kong Polytechnic University, Hong Kong, China

E-mail: tczzheng@polyu.edu.hk

Abstract: Solution-processed solar cells are appealing because of the low manufacturing cost, the good compatibility with flexible substrates, and the ease of large-scale fabrication. Whereas solution-processable active materials have been widely adopted for the fabrication of organic, dye-sensitized and perovskite solar cells, vacuum-deposited transparent conducting oxides (TCOs) such as indium tin oxide, fluorine-doped tin oxide and aluminum-doped tin oxide are still the most frequently used transparent electrodes (TEs) for solar cells. These TCOs not only significantly increase the manufacturing cost of the device, but also are too brittle for future flexible and wearable applications. Therefore, developing solution-processed TEs for solar cells is of great interest. This Review provides a detail discussion on the recent development of solution-processed TEs, including the chemical synthesis of the electrode materials, the solution-based technologies for the electrode fabrication, the optical and electrical properties of the solution-processed TEs, and their applications on solar cells.

Keywords: transparent electrode, solar cell, printing, flexible electronics, thin film

Contents

1. Introduction

1.1 Why Solution-processed Transparent Electrodes?

Emerging thin-film solar cells including dye-sensitized solar cells (DSSCs), organic solar cells (OSCs), and perovskite solar cells (PSCs) are attractive because they are easy to fabricate and the power-per-weight of the materials is high, when compared with Si solar cells.[1-7] Nevertheless, it is believed that Si technology is still more favorable in terms of higher power conversion efficiency and longer device life up to date. The unit price of Si solar module reduces by 20% for each doubling of cumulative production because of the technology development and the investment from governments. In 2014, the module cost of Si solar cells was already as low as 0.7 USD/W, which is less than 1% of the cost of Si solar modules in 1970s.[8-10]

In order to compete with the Si technology, it is of critical importance that these emerging thin-film solar cells can produce cost-effective energy at least similar to the level of Si. Whereas the preparation and processing of active materials such as the absorbers and the transporting layers are cheaper than those of Si, the expense of transparent electrodes (TEs) dominates the manufacturing cost.[11-14] Nowadays, the most reported TEs are vacuum-deposited transparent conducting oxides (TCOs) including indium tin oxide (ITO), fluorine-doped tin oxide (FTO) and aluminum-doped tin oxide (ATO).[15-17] The high cost of vacuum-deposited TEs origins from the low materials utilization efficiency, low throughput, and high consumption of electricity.[18] For example, the fabrication of ITO on polyethylene terephthalate (PET) consumes 87% of the energy in the manufacture of an organic solar module, and accounts for over 30% of the material cost.[19,20] This

issue could be more severe for PSCs, for which the vacuum-deposited TCOs electrodes are estimated to be 75% of the material cost.[6]

In contrast, solution-based coating and printing technologies such as spray coating, doctor-blade coating, slot-die coating, inkjet printing, and screen printing are energy-saving, high-material-utilization, and high-throughput.[21-40] Therefore, scientists have advocated to develop solution-based technologies and materials to replace vacuum-deposited TCOs for more than a decade.[41-44] In addition to the cost issue, vacuum-deposited TCOs are brittle, which are not suitable for applications in future flexible and wearable electronics. Developing new solution-processable materials can, in principle, also address the flexibility challenge of the TEs, and can take full advantage of the better mechanical flexibility of the active layers of these emerging thin-films solar cells, in comparison with the brittle Si.[45-51]

1.2 Overview of Material and Fabrication of Solution-processed TEs

Many organic and inorganic types of conductive materials including conducting polymers, metal, metal oxides, and carbon materials have been developed toward the aim of solution-based fabrication of TEs.[52-57] The majority of conducting polymers are conjugated polymers that can transport electrons through delocalized π bonds.[58-60] The advantage of such conducting polymers for TE application is the ease of bandgap tuning via chemical modification and doping.[61-63] Metals are known for their highest electrical conductivity among all materials. Solution-based metal deposition technologies rely on the dispersions of metal nanoparticles/nanowires or metal precursor solutions.[64-67] Apart from pure metal, some metal oxides that show good balance

between optical transmittance and electrical conductivity are also compatible with solution processes.[68,69] Carbon materials are abundant, low-cost, and chemically stable.[70,71] Among them, graphene has been developed as TEs for a decade because of its excellent optical transparency and decent electrical conductivity.[72,73] The ease of wet-etching and transfer-printing of chemical vapor deposition (CVD) graphene provides extra advantages for the manufacturing of flexible photovoltaic devices, especially when combining with existed laminating process.[74-76] Apart from single component TEs, composite electrodes based on multiple conductive materials have also been developed to overcome the disadvantages of a single material. For instance, printed metal grids are commonly adopted as current collecting grids for poly(3,4-ethylenedioxythiophene) polystyrene sulfonate (PEDOT:PSS) electrodes to overcome the large sheet resistance (R_{sh}) issue caused by PEDOT:PSS.[77,78] Nanoscale metal materials are sometimes doped in transparent conducting polymers for increasing light absorption, enhancing conductivity and enabling plasmonic adsorption.[79-81]

TEs with high electrical conductivity is critical for efficient charge transport from the solar cells to external circuits. The electrical conductivity of the materials can be very different. In general, the electrical conductivity of conducting polymers is the lowest compared to the other two categories. Whereas the conductivity of both conducting polymers and carbon materials origins from the delocalization of electrons across the conjugated *p*-orbitals, most of the conjugated polymers require redox doping to increase the mobility.[82] The doped conjugated polymers can reach an electrical conductivity over 10^5 S/m, which is several orders of magnitude higher than that of undoped polymers.[83-85] Although some conjugated polymers such as polyacetylene can be as conductive as metals (> 10^7 S/m), the poor stability limits their application as TE for solar

cells.[86,87] The conductivity of carbon is largely determined by the form and doping of the materials. The conductive allotropes of carbon are in graphite-like form that contains sp^2 hybridized carbon atoms. Whereas the electrical conductivity of individual carbon nanotube (CNT) and graphene may reach 10^7 to 10^8 S/m, thin films of these exhibit < 10^6 S/m conductivity due to defects and the contact resistance between individual nanotubes/nanosheets.[88-90] The electrical conductivity of metal and conductive metal oxide-based electrodes is usually > 10^6 S/m. Similar to conducting polymers, the conductivity of metal oxides is intimately related to the doping concentration. For example, doping of Sn^{4+} in In_2O_3 produces oxygen vacancies, which convert semiconducting In_2O_3 to metallic conductivity.[91,92] The detailed features of the materials mentioned above are discussed in Section 3 to 5.

Optical transmittance is as important as electrical conductivity for TEs of solar cells. As the strongest output of the sunlight lies within the visible range (380 ~ 780 nm), conventional solar cells have an optimal bandgap of ~ 1.4 eV for the efficient harvesting of solar energy.[93] Hence, one principle for the TEs is high optical transmittance at the visible range. However, normally there is a tradeoff between optical transmittance and electrical conductance of TEs. To study such tradeoff, researchers introduced figure of merit (FoM) to evaluate the performance of TEs, which will be discussed in Section 2. **Figure 1** shows the optical transmittance (at 550 nm) and R_{sh} of some representative solution-processed TEs in literature.[71,94-114] The FoM of the state-of-the-art solution-processed TEs lies between that of vacuum-deposited high performance ITO/glass (blue dashed curve) and commercial ITO/PET (red dashed curve).[115,116] Most of the reported TEs exhibit > 70% optical transmittance for sufficient light absorption of the solar cells. The R_{sh} of the conducting polymer and carbon material based TEs usually lies within the range of 20 ~ 200 **Ω**/□,

depending on the processing and post-treatment methods. Transfer-printed monolayer graphene TEs exhibited > 95% optical transmittance, but the R_{sh} was ~ 100 Ω/□ or even larger.[109] The transparent conducting polymer PEDOT:PSS, on the other hand, showed an R_{sh} of 24 Ω/□ and a moderate optical transmittance of ~ 85% when combined with an ionic additive-conductivity and flexibility enhancer.[96] Transparent conductive metal oxides are well-balanced materials for TEs that solution-processed ITO exhibited > 90% optical transmittance while maintaining a low R_{sh} of 30 Ω/□.[103] Whereas pure metals are the best electrical conductors, bulk metals are opaque due to the high reflectivity in the visible range. Meanwhile, the transparent ultrathin (< 20 nm) metal thin films show poor electrical conductivity due to electron scattering from surface and grain boundaries of the films.[117] Fortunately, patterned metal grids/meshes which can be obtained via solution-based coating/printing techniques show good optical transparency while possessing the excellent electrical conductivity of metals. For example, spray-coated silver nanowire (AgNW) networks with an R_{sh} of 2.48 Ω/□ and 89.5% optical transmittance at 550 nm was reported very recently.[101] In addition, solution-processed composite electrodes employing two or more materials have been widely adopted for the emerging thin-film solar cells to overcome the disadvantages of one single material. One example is the composite electrode of metal oxide and metal nanowire, in which the metal oxide serves as a surface smoother, an adhesive, and a stabilizer.[110]

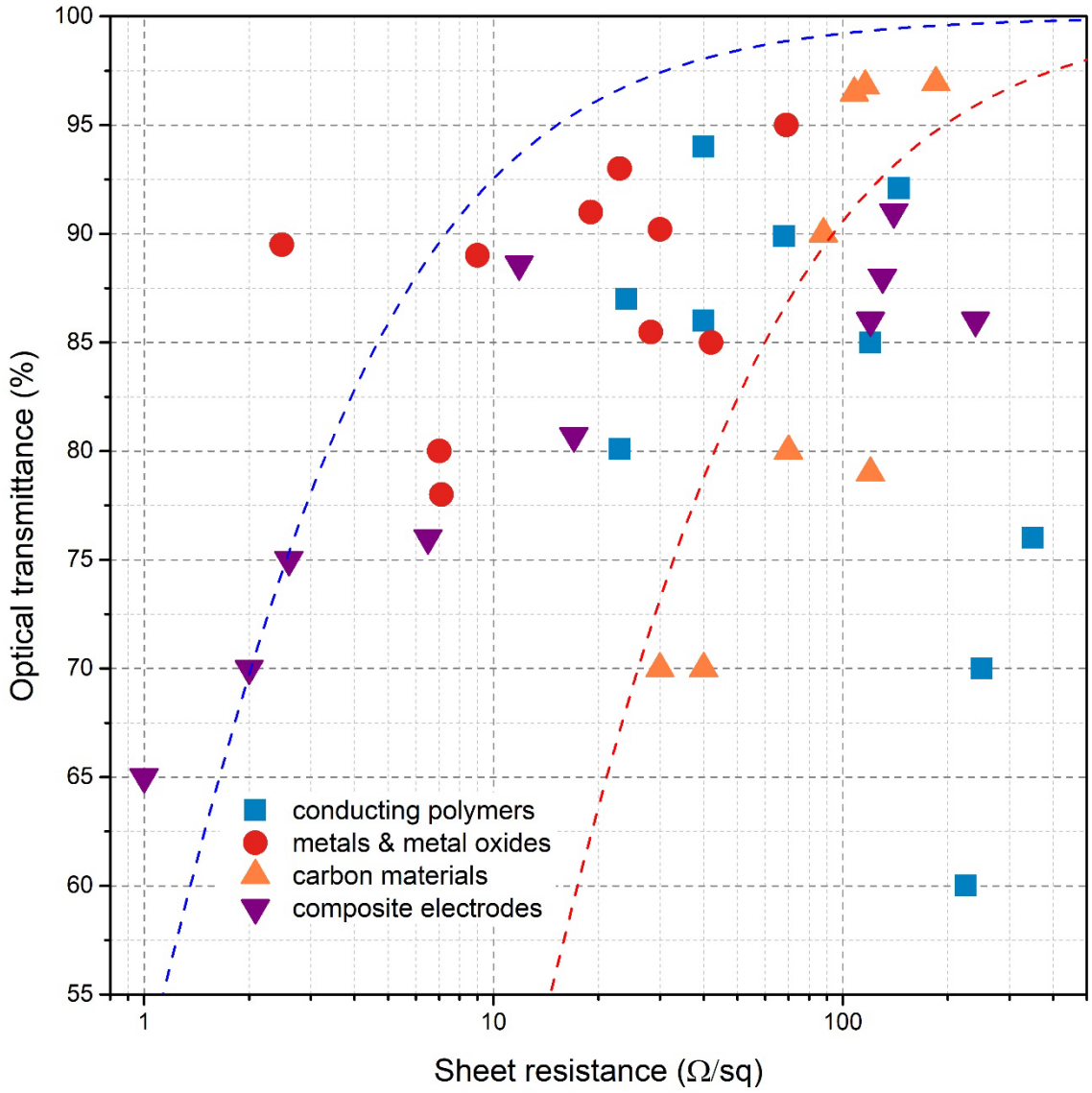

Figure 1. Comparison of the optical transmittance and sheet resistance of solution-processed TEs. The data were obtained from literature.[71,94-114] The blue and red dashed curves are fitted from the data of vacuum-deposited ITO/glass (NREL)[115] and ITO/PET (Sigma)[116].

Figure 2 illustrates the two approaches to achieving high transmittance of conductive electrodes. The first approach is depositing homogeneous thin films of conductive materials, such as PEDOT

and its derivatives, graphene-based materials, and metal oxides, which show low optical absorption. For example, a solution-processed PEDOT:PSS film had an R_{sh} of 46 Ω/□ and an optical transmittance of ~ 90%. Since a smooth an compact TE film is a prerequisite for the successful deposition of other functional layers, intrinsically transparent thin-film electrodes are accepted by most of the reported thin-film solar cells.[72,118] The other approach is structuring the less transparent conductive materials into grid/mesh-like forms. TEs made of Metals normally adapt this approach, because of the high optical absorption of metal over a very broad spectrum. Whereas ultrathin metal films (< 10 nm) show certain degrees of optical transparency, the formation of isolated islands results in very poor electrical conductivity of such ultrathin films.[119-121] Stare-of-the-art metal grid/mesh-based TEs show R_{sh} < 10 Ω/□ and > 90% optical transmittance, which is better than vacuum-deposited ITO thin films.[122-124] However, the high surface roughness induced by the grids/meshes could increase the risk of short circuit of the solar cells.[125] The following sections will discuss the advantages and disadvantages of both approaches with detailed examples.

In either way of making the TEs, the deposition of these conductive materials into TEs generally starts with precursor solution, polymer solution, or a dispersion of building blocks (metal/metal oxide and carbon nanomaterials), as illustrated in **Figure 2**.[114,126,127] One approach to obtaining polymeric TEs is chemical or electrochemical deposition of conducting polymers from precursor solutions. This approach makes use of oxidative polymerization of the monomers to form transparent polymer thin films.[128,129] Whereas the chemical or electrochemical deposition requires specific precursors or substrates, a more versatile approach is the direct coating/printing of solutions of conducting polymer or polymer blends. The solution-based deposition of carbon materials usually starts with the nano-dispersions because bulky carbon materials are not soluble.

In most cases, the carbon nanomaterials are oxidized or functionalized with hydrophilic groups to form stable dispersions in water or common organic solvents.[130-132] For the same reason, metal and metal oxides are firstly synthesized to nanoparticle or nanowire forms before solution-based deposition.[133,134] The widely used solution-based coating and printing techniques including spin coating, spray coating, slot-die coating, inkjet printing, and screen printing are introduced in Section 6, with their advantages and disadvantages being discussed. In addition, other vacuum-free coating and printing processes such as transfer printing (or lamination) are also commonly adopted for solution-based fabrication of TEs are also introduced and discussed. The deposition is not the last step for the above-mentioned processes in most cases because post-treatments such as thermal annealing, laser welding, and ultraviolet (UV) curing are required to improve the performance of solution-processed TEs.[135-139]

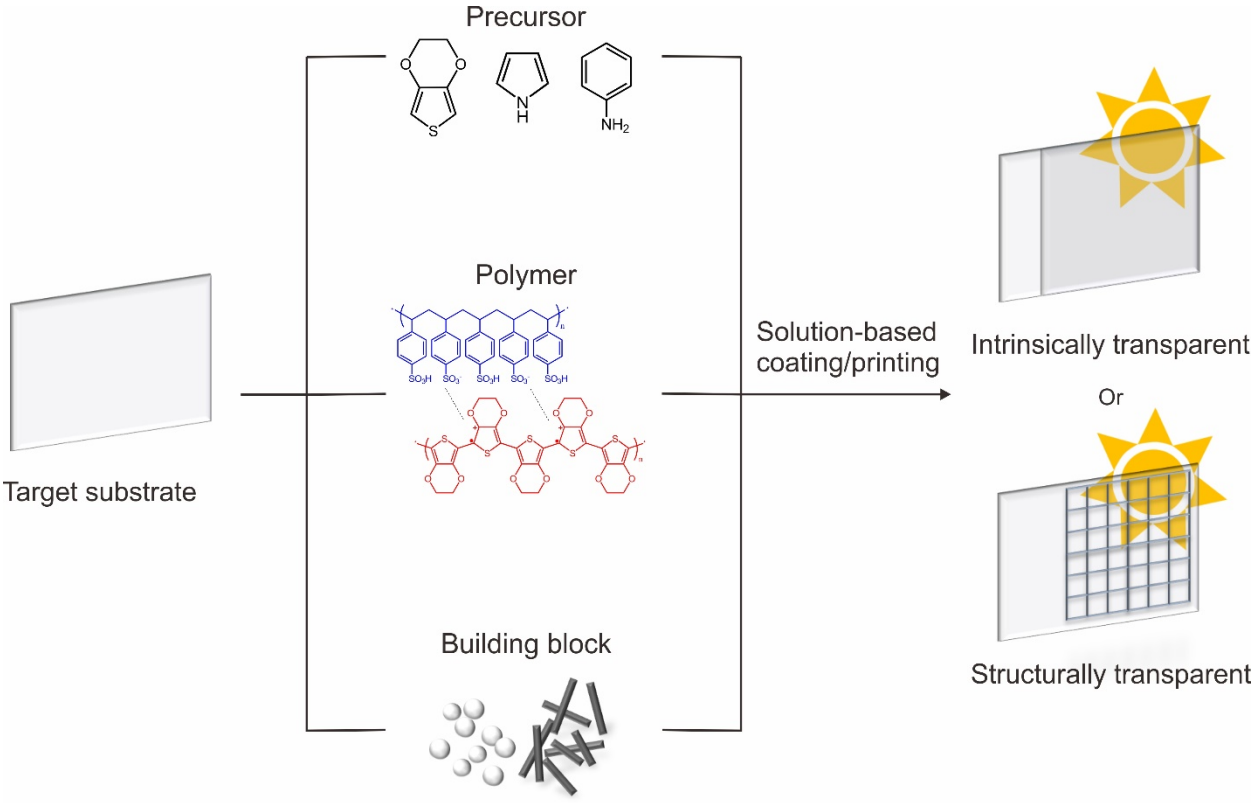

Figure 2. Schematics of solution-processed TEs from soluble or dispersible materials. A solution or dispersion that contains precursors, polymers, or metal/metal oxide/carbon nanomaterials is deposited on the target substrate via solution-based coating/printing techniques. The TE film is either an uniform transparent thin film or a transparent nanomesh/grid.

1.3 Scope of Review

Over the years, there have been some review articles focusing on solution-processed TEs from both materials and application point-of-views. Groenendaal et al. reviewed the synthesis of transparent conducting polymer PEDOT and its derivatives.[140] Hu et al. summarized the structure design, synthesis, properties, and applications of metal nanomaterial-based TEs.[65] Hecht et al. reviewed the emerging carbon and metal-based materials from material synthesis to optical and

electrical properties, and their applications in touch panels, displays, solar cells and LEDs.[70] However, few review articles focus on the solution-processed TEs for the emerging thin-film solar cells, or discuss the coating and printing technologies of fabricating the TEs. In this review, we provide a comprehensive summary of the solution-processed TEs for emerging thin-film solar cells. The Review starts with the synthesis methods and materials properties of transparent conducting polymers, metals and metal oxides, and carbon materials (Section 3, 4 and 5). We then introduce the solution-based coating or printing techniques that are commonly adopted for the fabrication of TEs, with detail discussion of the advantages and disadvantages of each technique in Section 6. Finally, we review the recent progress on the applications of these solution-processed TEs for OSCs, DSSCs, and PSCs in Section 7, and discuss the remaining challenges of this field in Section 8. We hope that this review can enlighten future design and fabrication of low-cost and high-efficiency photovoltaic devices. It is worth noting that TE is only a part of a thin-film solar cell, the optimization of other components such as HTL/ETL,[141,142] active layer,[143-145] and rear electrode[146,147] is equally important for highly efficient devices. In this review, we mainly focus on the influence of TEs when discussing the efficiency of solar cells.

2. Important Properties of TEs for Solar Cells

2.1 Optical Transmittance and Electrical Conductivity

There have been plenty of discussions on the criteria of transparent conductors in the past decades.[17,148-150] Ideally, TEs should acquire both high electrical conductivity and high optical transmittance, which are somewhat contradictory from the physical point of view. This is because a necessary condition for the high electrical conductivity of a material is the high carrier density,

which is limited by the light absorption of the free carriers.[151] The relationship among wavelength λ_p, frequency ω_p, and carrier density n is illustrated by the following equations:

$$\lambda_p = \frac{\omega_p}{2\pi\hbar} \quad (1)$$

$$\omega_p = \sqrt{\frac{ne^2}{m^*\varepsilon_0}} \quad (2)$$

where e is the elementary charge, m^* is the effective mass of the carrier, and ε_0 is the permittivity of free space.[152] To evaluate the optical transmittance and the electrical conductivity of TEs, figure-of-merit (FoM) is often used. There are three ways of defining the FoM. In 1976, Haccke defined the FoM (Φ_{TE}) as:

$$\phi_{TE} = \frac{T^x}{R_{sh}} \quad (3)$$

where T^x is a specific optical transmittance determined by the exponent x.[153] According to the relationship among R_s, T, and film thickness t:

$$R_{sh} = \frac{1}{\sigma t} \quad (4)$$

$$T = e^{-\alpha t} \quad (5)$$

where σ is the electrical conductivity, and α is the optical absorption coefficient. The maximum Φ_{TE} occurs when $T = 0.37$ (i.e., $t_{max} = 1/\alpha$), the transmission of which is too low for TE applications. For common TE applications, x is fixed to 10 (i.e., 90% transmittance at t_{max}) because 90% optical transmittance is a minimum requirement of many industrial applications.[70,153,154] FoM is often adopted for the evaluation of conventional TCOs and metal films, and the optical transmittance at 550 nm is selected because it is close to the most sensitive wavelength of human eyes.[155] Another method for the evaluation of TE is the function between optical transmittance and sheet resistance:

$$T = (1 + \frac{188.5}{R_{sh}} \frac{\sigma_{Op}}{\sigma_{DC}})^{-2} \quad (6)$$

where σ_{Op} is the optical conductivity, and σ_{DC} is the electrical conductivity of the TE film.[156] In this method, the FoM is defined by the ratio σ_{DC}/σ_{Op}. A larger σ_{DC}/σ_{Op} value reveals a higher optical transmittance at certain sheet resistance.

What are the threshold requirements of TEs for solar cells? The answer to this question is related to the expected parasitic losses of the TEs, the design of the solar modules, the active area of the solar cells, and etc. Rowell and McGehee suggested that an optical transmittance ≥ 90% and an $R_{sh} \leq 10$ **Ω**/□ is necessary for monolithically integrated thin-film solar modules in **Figure 3A** by calculation.[148] In such a configuration, the active area of the device is determined by the device width *w* (as the length of each cell is fixed), while the area between dead space width *s* provides zero power output. Figure 3B depicts the relationship between the fraction of nominal efficiency η/η_0 and the *w*. The optimal η/η_0 values for ITO (20 **Ω**/□), a hypothetical 10 times better electrode, and a hypothetical 10 times worse electrode based devices are 0.84, 0.91, and 0.71, respectively. However, the result is very different for a standard solar module using metal current collecting grids (Figure 3C and D). As shown in Figure 3D, the optimal η/η_0 of the 3 electrodes become very close, indicating a less dependence on TE performance for standard cells than that for monolithically integrated solar modules. To evaluate the performance of TEs with their model, the authors employed the value of σ/α as FoM, where σ is the conductivity and α is the absorption coefficient. Here, we convert the σ and α to sheet resistance R_{sh} and optical transmittance T into,

$$\frac{\sigma}{\alpha} = \frac{\frac{1}{R_{sh}t}}{\frac{-\ln T}{t}} = -\frac{1}{R_{sh} \ln T} \quad (7)$$

where *t* is the thickness of the TEs.

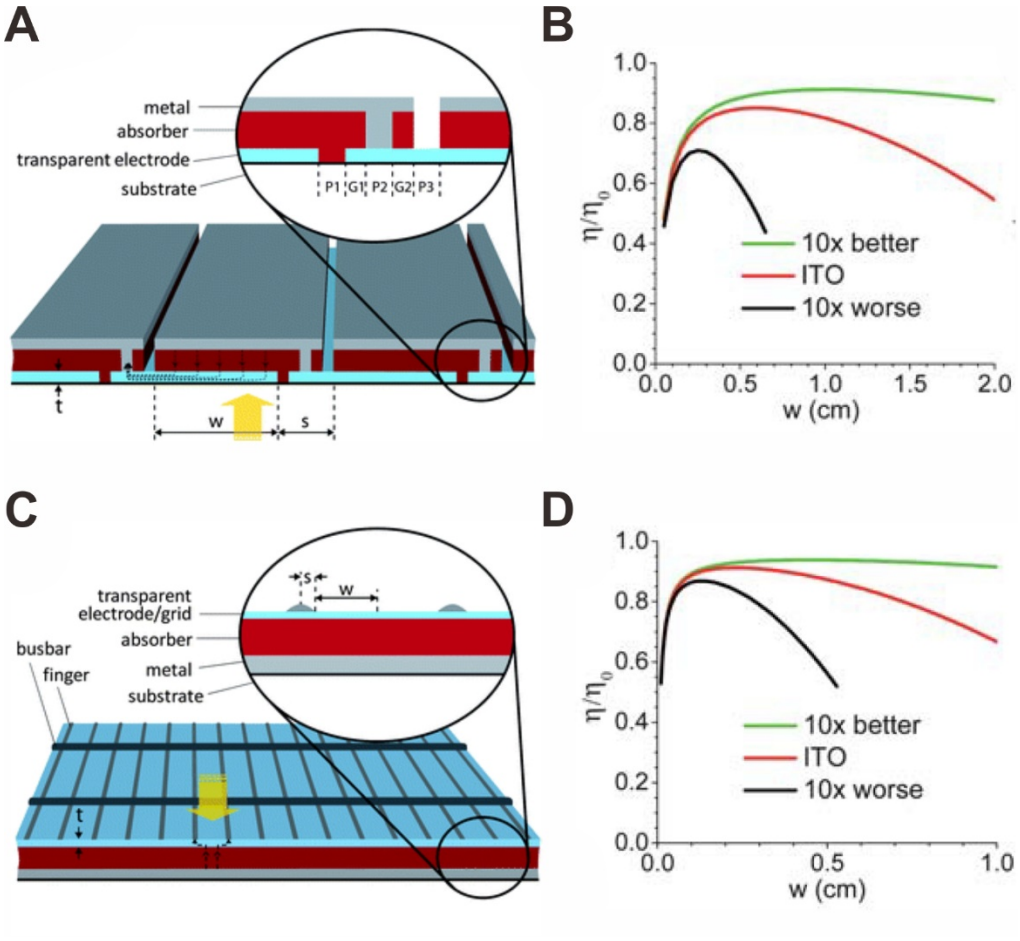

Figure 3. (A) Illustration of a monolithically integrated solar module. (B) The fraction of nominal efficiency as a function of device width *w* for monolithically integrated solar modules. (C) Illustration of a standard solar module. (D) The fraction of nominal efficiency as a function of device width for standard solar modules. Reproduced with permission from Ref[148]. Copyright 2011 The Royal Society of Chemistry.

We further calculate FoMs of different TEs reported in the literature according to the R_{sh} and T values, and list the results in **Table 1**. According to the model by Rowell and McGehee, the fraction

of nominal efficiency η/η_0 dropped dramatically once the σ/α value was reduced below 1 Ω^{-1}, which is equivalent to a TE with an R_{sh} of 10 Ω/□ and a T of 90%.[148] Such a high FoM is very difficult to reach for those polymer-based TEs, although PEDOT:PSS-based TEs with conductivity larger than 4,000 S/cm were reported in recent years via multiple doping and post-treatment processes.[96,157] Carbon material based TEs have the potential to break through the aforementioned FoM limits because of the very high theoretical conductivity. A very thin graphene TE (< 10 nm) could have a low R_{sh} of 10 Ω/□ in theory, as suggested by Wu et al.[158] However, there is a significant gap between the theoretical value and the experimental performance of the carbon material based TEs (Table 1) due to the defects of the materials and the contact resistance.[159,160] On the other hand, metals and metal oxides are competitive candidates for high FoM because of their very high electrical conductivity. As shown in Table 1, the best-reported solution-processed metal and metal oxide-based TEs showed very high $\sigma/\alpha > 1$ Ω^{-1}. Hence, we believe that metals and metal oxides-based materials are the best options to realize high FoM of TEs nowadays. Moreover, a $\sigma/\alpha > 2$ can be obtained by composite TEs consisting of metals/metal oxides and conducting polymers (Table 1). The composite TEs may have other advantages compared to single material based TEs, which will be discussed in the rest parts of this Section.

Table 1. Examples of the figure of merit of state-of-the-art solution-processed thin-film TEs compared with vacuum-deposited ITO/glass.

TE/Substrate	Fabrication Method	T	T^{10}	R_s (Ω/□)	Φ_{TE} (10^{-3} Ω^{-1})	σ_{DC}/σ_{Op}	σ/α (Ω^{-1})	Ref.
ITO/glass	Vacuum sputtering	0.83	0.16	3.1	52	622	1.7	[161]
ITO/glass	Spin coating	0.902	0.357	30	11.9	119	0.32	[103]

ITO/Ag grid/ITO/glass	Inkjet printing	0.741	0.050	2.86	17.4	407	1.2	[112]
AZO/AgNW/AZO /ZnO/glass	Spin coating	0.934[a]	0.505	11.3	44.7	481	1.3	[162]
AgNW/PET	Spray coating	0.947[a]	0.580	20.2	28.7	338	0.91	[163]
embedded AgNW/PET	Spray coating	0.855	0.209	2.48	84.3	933	2.6	[101]
PEDOT:PSS/glass	Spin coating	0.97[a]	0.74	240	3.1	51	0.14	[164]
PEDOT:PSS/PET	Spin coating	0.86	0.22	24	9.1	100	0.28	[96]
PEDOT:PSS/PEN	Transfer printing	0.90[a]	0.35	46	7.6	76	0.21	[157]
PEDOT:PSS/Ag gird/PET	Spin coating/Self-assembly	0.73	0.043	0.62	69	~1,800	5.1	[165]
PEDOT:PSS/embedded Ag-mesh/PET	Spin coating/Nano-imprinting	0.86	0.22	~3	~73	~800	2.2	[49]
Graphene/PET	Transfer printing	~0.90	~0.35	~30	~12	~120	0.32	[166]
Graphene+AgNW /PEN	Spray coating	0.89[a]	0.31	13.7	23	230	0.63	[167]
Graphene/AgNW/ EVA/PET	Transfer printing	0.94[*]	0.54	~8	~68	~750	2	[168]
CNT/PET	Transfer printing	0.90[a]	0.35	41	8.8	86	0.23	[169]
CNT/glass	Dip coating	~0.90[a]	~0.35	~100	~3.5	~35	0.1	[170]

[a]The light absorption of the substrate was excluded.

Whereas thick AgNWs result in high electrical conductivity, the optical loss induced by highly reflective Ag material may reduce the optical transmittance. Sorel et al. studied the impact of the diameter of AgNW on the optical transmittance, sheet resistance, and the FoM of AgNW based TEs.[171] **Figure 4A** depicts the optical transmittance as a function of sheet resistance of AgNW films with different wire diameter. Note that σ_{DC} is dependent on the film thickness when the film

is very thin. Hence, a percolative FoM should be introduced instead of the σ_{DC}/σ_{Op} from equation (6) for bulk-like materials.[172] The solid curves and dashed curves in Figure 4A came from fitting of the experimental data with bulk-like theory and percolation theory, respectively. Figure 4B shows the FoM of the AgNW films with different wire diameters. According to their experimental data, the highest FoM was obtained when the average diameter of AgNW was 63 nm. As 90% optical transmittance is one of the requirements of industrial products, the R_{sh} of the AgNW films at 90% transmittance was also studied (Figure 4C). Once again, the results indicate that the FoM of thinner AgNWs is higher than that of thicker ones.[171] The situation is much simpler for metal grids with regular structures. Muzzillo studied the FoM of metal nanogrids of different designs via analytical calculations.[173] Figure 4D shows the aperture transmittance T_{aper} of 50 nm-thick metal grids as a function of the sheet resistance of different designs. The circular design outperformed all other structures when T_{aper} was lower than 85%. However, the grating structure became the best among all these structures once the T_{aper} goes beyond 85%. The authors also compared the performance of grating metal nanogrids with that of the TCOs reported in the literature (Figure 4E). The metal nanogrids outperform ITO and AZO even if the thickness of metal grids was only 50 nm. Increasing the grid thickness does not decrease optical transparency, but significantly reduces the electrical resistivity of the entire film. However, thick metal grid lines may result in high surface roughness, which is not favorable in manufacturing. In addition, the light scattering (or haze) induced by TEs (especially those with micro- or nanostructures) may contribute to the light harvesting of solar cells. This is because the scattering effect increases the optical path in absorbers to enhance the coupling-in of incident light.[174,175] By tailoring the nanostructures, one can obtain very high optical haze (> 90%) without minimal sacrifice of overall optical transmittance.[176] Preston et al. suggested that the AgNWs with larger diameters (~ 150 nm) show

a higher haze factor than that of AgNWs with smaller diameters (~ 60 nm). Whereas AgNWs with ~ 60 nm diameter had a high34 FoM than that of AgNWs with ~ 150 nm diameter, the high haze factor of AgNWs with ~ 150 nm diameter brought uncertainty for the performance of AgNW TEs. Hence, only FoM itself could be insufficient to evaluate the performance of TEs that produce additional optical haze.[177] The influence of optical haze on solar cell performance is also dependent on the active material of the solar cells. For thin-film solar cells such as OSCs and PSCs, the influence of optical haze is usually significant. For example, the AgNW TE with 5.6% haze factor resulted in 4.47% efficiency for P3HT:PCBM-based OSC, which was 25% higher than that of control device with flat ITO TE. However, the improvement was not so obvious on PTB7:PCBM-based OSCs.[178] Our previous research also suggested that a high haze (~ 75%) could improve the efficiency of OSCs and PSCs for > 10% and > 15%, but show minor (6.8%) improvement on bulk crystalline-Si solar cells.[179]

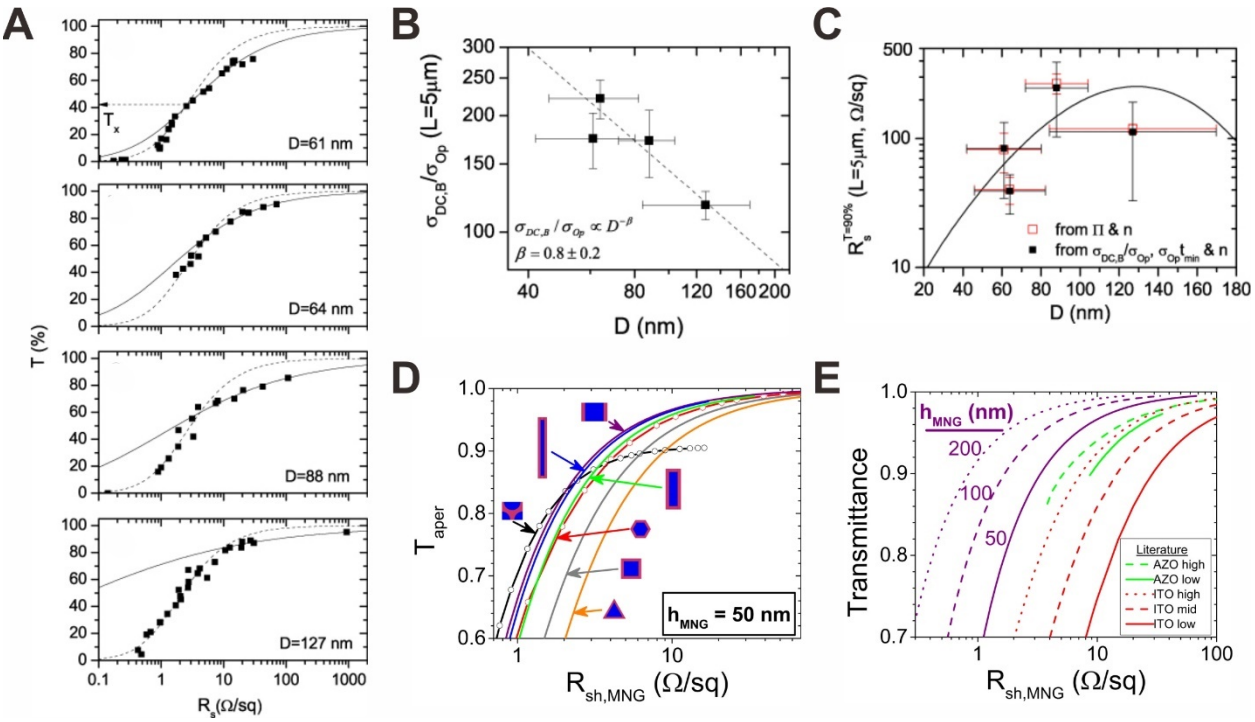

Figure 4. (A) The optical transmittance as a function of sheet resistance of AgNW films with different wire diameter D. (B) The FoM σ_{DC}/σ_{Op} of the AgNW films as a function of wire diameter. (C) The sheet resistance of AgNW films at 90% optical transmittance as a function of wire diameter. Reproduced with permission from Ref[171]. Copyright 2012 IOP Publishing Ltd. (D) Aperture transmittance as a function of sheet resistance of metal nanogrids with different designs. (E) Transmittance of grating metal nanogrids with different grid thickness *h* as a function of sheet resistance. The data of AZO and ITO from other literatures are shown for comparison. Reproduced with permission from Ref[173]. Copyright 2017 Elsevier B.V.

2.2 Work function

Work function is another critical property of TEs. The work function of a material is defined as the difference between the energy of vacuum level and the Fermi level of the surface of the material. For thin-film solar cells, the interface between TEs and other functional layers is critical. The mismatch of work function in solar cells may result in unwanted Schottky contact between the TE and the semiconductor, which generates high contact resistance and reduces the efficiency of the device.[180-182] For OSCs and PSCs, electron transport layers (ETLs) and hole transport layers (HTLs) are often necessary for efficient injection of electrons and holes (**Figure 5**). The conduction band edge or lowest unoccupied molecular orbital (LUMO) of the ETL should be slightly lower than that of the active material. The valance band or highest occupied molecular orbital (HOMO) of the HTL should also be slightly lower than that of the active material to prevent hole injection. As illustrated in Figure 5, the ideal cathode prefers a low work function (i.e., a small difference between vacuum level and Fermi level) for efficient electron transport, while the ideal anode prefers a high work function for efficient hole transport.

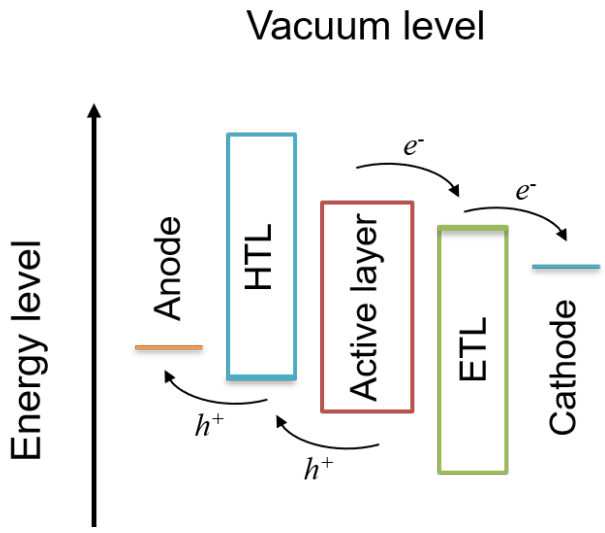

Figure 5. Energy diagram of a typical thin-film solar cell.

Work function is highly relevant to the processing method, doping, surface modification, and post-treatment of TEs. The work function of solution-processed TEs is usually different from that of the vacuum-deposited TEs even if the material is the same. For example, ITOs fabricated via a sol-gel method shows a very low work function ranging from 3.9 to 4.2 eV, which is significantly lower than that of conventional vacuum-deposited ITO TEs (**Table 2**).[183] Chemical doping is an effective approach to tuning the work function. **Figure 6A** shows the shift of surface potential of a graphene film as a function of the doping time in a $AuCl_3$ solution. The Au^{3+} was reduced to Au nanoparticles on graphene surface, and thus induced p-type doping of the graphene film. Measured via a scanning Kelvin probe method (SKPM), a maximum shift of surface potential of ~ 0.5 V (i.e., up-shifting of work function of ~ 0.5 eV) was observed after 20 s doping of $AuCl_3$. Such up-shifting of work function improved the performance of the graphene TE as an anode for Si solar

cells.[184] Surface contamination may affect the work function of a material substantially even if the amount of the contamination is atomic level.[185] Sugiyama et al. studied the dependence of the work function of ITO on different surface cleaning methods. The standard cleaning process of ITO substrates may induce carbon-containing contaminants, which reduced the work function of ITO to 4.5 eV. A UV-ozone treatment can remove most of the contamination, and increase the work function of ITO to 4.75 eV. On the contrary, an Ar^+ sputtering process reduced the work function of ITO to 4.3 eV due to the partially removal of oxygen of ITO.[186] Most PEDOT:PSS-based TEs show a high work function ranging from 4.8 to 5.2 eV, and thus is suitable for anode applications. It can be reduced to less than 4.0 eV or improved to larger than 5.6 eV via multiple doping and post-treatment methods.[187-191] In 2012, Zhou et al. made use of a very thin (1~10 nm) layer of PEI or polyethyleneimine ethoxylated (PEIE), as a universal approach to modifying the work function of cathodes made with different materials. As illustrated in Figure 6B, the work functions of PEDOT:PSS (PH 1000), ITO, and Au reduce significantly from 4.95 eV, 4.40 eV, and 4.70 eV to 3.32 eV, 3.30 eV, and 3.40 eV, respectively, after modifying with 10 nm-thick PEIE. The work function recovered after sonification of the sample in water bath for 50 min, indicating a physical absorption between PEIE/PEI and the electrode (Figure 6C).[192] Others have adopted this facile and solution-processable method to construct novel organic and perovskite solar cells with non-conventional structures.[193-195]

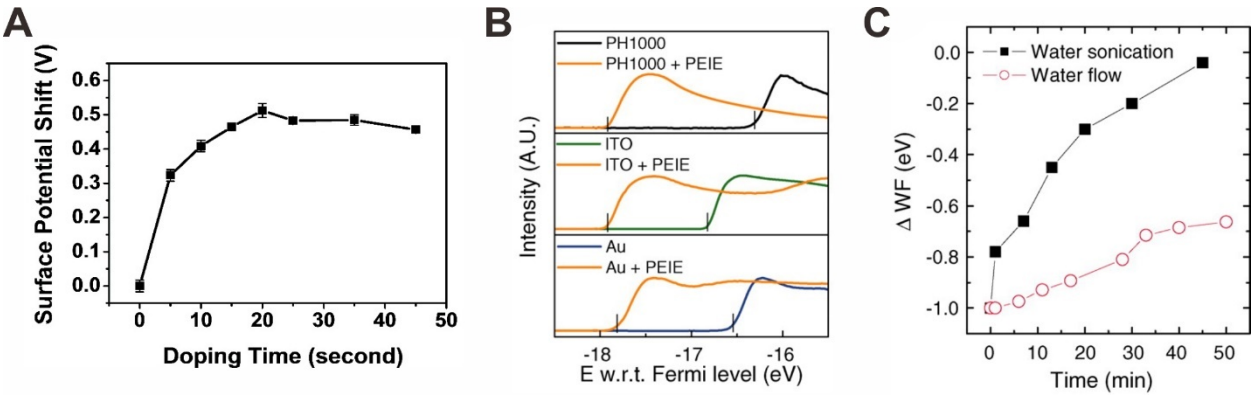

Figure 6. (A) The surface potential shift of graphene films as a function of doping time in $AuCl_3$ solution. Reproduced with permission from Ref[184]. Copyright 2010 American Chemical Society. (B) Ultraviolet photoelectron spectroscopy (UPS) of PEDOT:PSS, ITO and Au electrode with and without the modification of PEIE. (C) The work function variation of PEIE-modified ITO TE after washing with water flow or water sonification bath. Reproduced with permission from Ref[192]. Copyright 2012 American Association for the Advancement of Science.

Table 2. Typical work function values of commonly adopted materials for solution-processed TEs.

Category	Material	Typical Work Function (eV)	Ref.
Conducting Polymers	PEDOT:PSS	4.8 ~ 5.2	196
	PANI	4.5 ~ 4.8	197
	PPy	~ 4.5	198
Carbon Materials	Graphene	~ 4.6	199
	CNT	~ 5.0	200
Metals & Metal Oxides	AgNW	~ 4.5	201
	CuNW	~ 4.7	202
	ITO	~ 4.7	203
	AZO	4.7 ~ 5.2	204

2.3 Other surface properties

Surface energy of TEs are also very important parameters. The surface energy of the underlying layer is critical for the crystallization of the active materials in OSCs and PSCs.[205,206] **Figure 7A** and B show the impact of WO_x doping on the surface free energy of PEDOT:PSS; it increased the surface free energy of PEDOT:PSS film from 59.30 mN/m to 62.09 mN/m, which resulted in a reduction of water contact angle from 51.3° to 45.6°. The change of surface free energy affected the formation of bulk heterojunction (BHJ), which further resulted in improved phase separation and solar cell efficiency.[207]

Surface roughness of TEs are also important because it significantly affects the uniformity and morphology of layers coated/printed on top. It is difficult to determine an exact maximum roughness value as a prerequisite for the successful fabrication of solution-processed thin-film solar cells. But in general, a lower surface roughness of the bottom TEs is preferred to reduce the risk of shunt.[208] The root mean square roughness of a printed/coated dense TE film (e.g., PEDOT:PSS or metal oxide films) is typically less than 10 nm, which is sufficiently smooth for most of the thin-film solar cells.[209-211] In such case, the impacts of the surface roughness could be complicated. For example, Richardson et al. found that the variation of the surface roughness of ZnO ETLs had different impacts on P3HT:PCBM and PTB7:PCBM OSCs. On the one hand, the change of roughness from 2.86 to 4.02 nm caused a dramatic decrease of fill factor from 56% to 44% for P3HT:PCBM based OSCs, which could be attributed to the generation of small voids at ZnO/P3HT:PCBM interface. On the other hand, the performance of PTB7:PCBM based OSCs was barely affected by such small roughness variations.[212] For DSSCs and meso-porous PSCs, rough meso-porous electrodes or scaffolds (roughness > 20 nm) are employed to improve the surface area for efficient charge transport.[213-215] However, the roughness of metal mech/grid-based

TEs can be as high as hundreds of nanometers or even micrometer-scale. For example, a screen-printed Ag grid was > 2,000 nm-thick, which is impossible to spin-coat uniform additional layer on top.[216] Similarly, although AgNW meshes show excellent FoM as mentioned previously, its high roughness led to poor solar cell performance.[217] As a result, researchers have developed multiple approaches to smoothening AgNW films by filling the gaps with additional materials, or compressing the loose meshes to a dense film.[218-220] Figure 7C illustrates a cold isostatic pressing (CIP) method to condense the AgNW films on glass or PET substrates. A solid contact was formed at the junction of AgNWs, as observed from the SEM images (Figure 7D). The roughness of the AgNW films reduced from 42 nm to 26.7 nm, and the R_{sh} dropped from 49.3 Ω/□ to 20.7 Ω/□ at the same time due to the better contact between AgNWs. Both factors led to the higher efficiency of solar cells with CIP-AgNW TEs than untreated AgNW-based solar cells.[221]

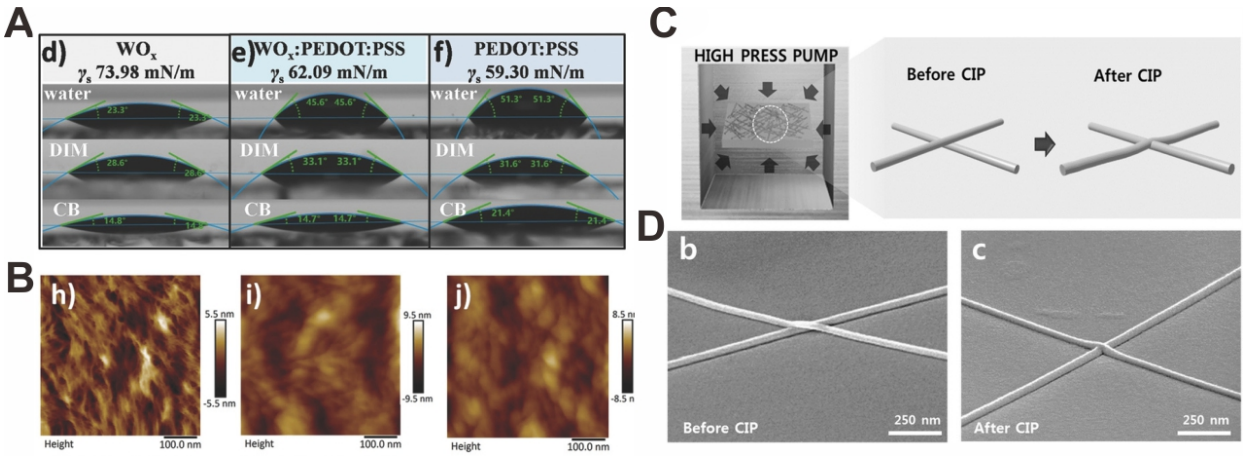

Figure 7. (A) Contact angles of water, diiodomethane (DIM), and chlorobenzene (CB) on WO_x, WO_x:PEDOT:PSS, and PEDOT:PSS films. (B) AFM images of active materials on top of WO_x (left), WO_x:PEDOT:PSS (middle), and PEDOT:PSS films (right), respectively. Adapted with permission from Ref[207]. Copyright 2018 WILEY-VCH Verlag GmbH & Co. KGaA, Weinheim.

(C) Schematics of the CIP process for AgNW. (D) SEM images of AgNWs before and after CIP treatment. Adapted with permission from Ref[221]. Copyright 2017 WILEY-VCH Verlag GmbH & Co. KGaA, Weinheim.

Chemical stability of the TE/semiconductor interface is another parameter. Unstable interface could result in unsatisfactory solar cell performance and rapid degradation of the device. The acidic nature of PEDOT:PSS may induce instability risk to thin-film solar cells. For example, the acidic PEDOT:PSS may erode basic materials such as ITO to induce diffusion of indium at the TE/active layer interface. Such corrosion could lead to unfavorable gap states which further led to the degradation of OSCs.[222] **Figure 8** depicts the structure of a PSC with PEDOT:PSS HTL between the ITO and perovskite active layer. The pH of the PEDOT:PSS was tuned by doping of basic imidazole, and neutral or basic PEDOT:PSS was obtained with 0.5 or 5 wt% doping. The doping process not only increased the work function of PEDOT:PSS, but also improved the chemical stability of PEDOT:PSS at ITO/PEDOT:PSS interface. As a result, the basic PEDOT:PSS based PSC exhibited the highest efficiency as well as stability among all the devices.[223] The possible chemical reaction between halides and metals (especially Ag) should be considered when metal-based TEs are used in PSCs.[224,225] Inserting an interlayer to block the ion diffusion, or embedding the metal TEs in non-reactive metal oxides/conducting polymers is recommended for PSCs using metal thin films as TEs.[110,226,227] To avoid the chemical or electrochemical corrosion of the reactive metal-based TEs, a conventional approach is covering the reactive metal materials with a layer of inert passivation layer.[228] The passivation material can be either a conductive material such as graphene,[168,229] and less-reactive metals or metal oxides,[230,231] or a non-conductive material such as alumina,[232] and poly(methyl methacrylate) (PMMA).[233] The non-conductive passivation layer

should be very thin (less than several nanometers) for efficient charge transport. For example, <5 nm-thick alumina deposited by atomic layer deposition (ALD) is sufficient for effective passivation of nanowire TEs and moisture-sensitive perovskite active materials.[234,235]

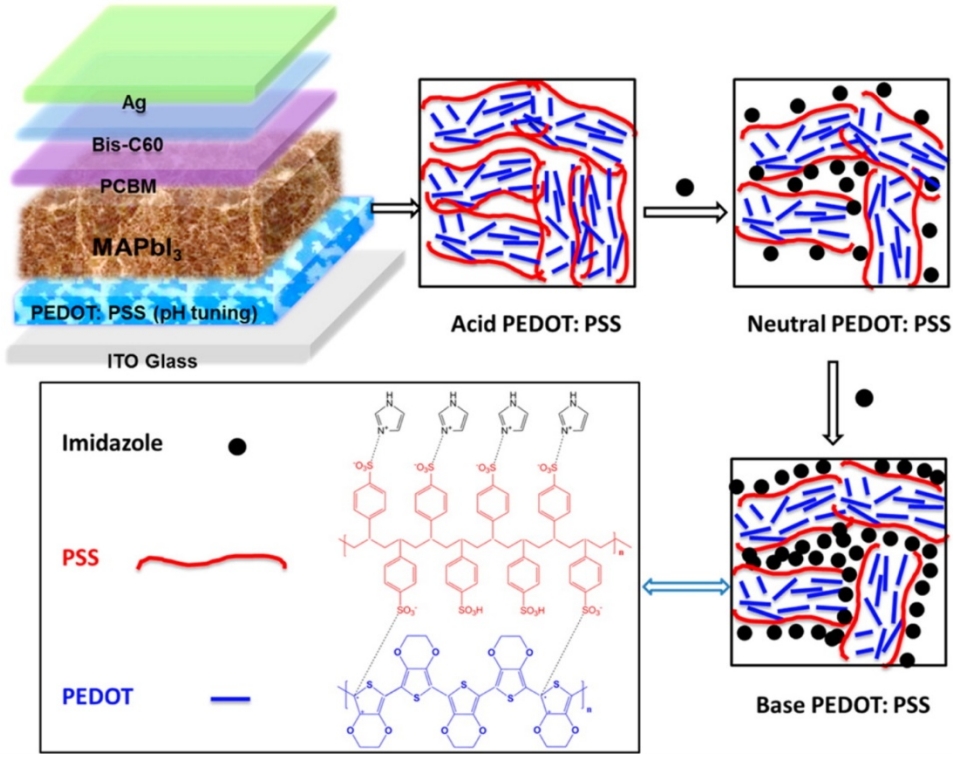

Figure 8. Schematics of a PSC using pH-tuned PEDOT:PSS as HTL between ITO TE and perovskite active layer. Reproduced with permission from Ref[223]. Copyright 2016 American Chemical Society.

In summary, we have discussed the optical, electrical, and interfacial properties of TEs of thin-film solar cells. FoM is introduced to evaluate the tradeoff between optical transparency and electrical conductivity. Since achieving optical transmittance > 90% and sheet resistance < 10 Ω/□

is a requirement of TEs for commercial solar modules, we recommend incorporating high FoM metals/metal oxides with the solution-processed TEs. Sometimes the micro- or nanostructures of the TEs may induce light scattering, which could be beneficial for thin-film solar cells. The surface properties of the TEs are critical for efficiency hole/electron transport. The work function of the TE should be optimized to avoid unwanted barriers. Approaches including doping, surface modification, and post-treatment are employed to tune the work function of TEs for efficiency solar cells. Other surface properties such as surface energy and surface roughness could be important for the successful fabrication of the solution-processed solar cells, as these surface properties affect the film formation of the active layers. These properties should be optimized specifically for different active materials. In addition, the chemical stability of the TE/semiconductor interface could be an issue in some cases, and the chemical reaction between TE and other layers that leads to device degradation should be avoided.

3. Transparent Conducting Polymers

3.1 Poly(3,4-ethylenedioxythiophene)

Oxidized polythiophenes (PThs) have been developed as conducting polymers for many years.[236-238] The bandgap of PTh derivatives can be tuned easily by chemical modification and doping, which result in different colors of the polymers.[239,240] PEDOT is a well-studied PTh derivate that shows outstanding conductivity and good optical transparency in its oxidized state. Unlike some other conducting polymers such as polyacetylene which suffers from the instability problem, PEDOT and its derivatives are stable in highly conductive oxidized form.[241-243] Many recent research suggested that the conductivity of PEDOT can be further improved by multiple doping or

post-treating strategies.[244-246] In the meantime, the insoluble PEDOT can be soluble in water and organic solvents when blended with some negatively charged polymers such as PSS. Thus, PEDOT and its derivatives are regarded as promising transparent conductive materials for solution-processed solar cells, especially for the flexible devices which require low-processing temperature and high-throughput roll-to-roll (R2R) printing.[247,248]

Another key advantage of PEDOT is the low material and manufacturing cost compared with traditional sputtered TCOs. For example, a life cycle analysis of OSC modules indicated that the cost of solution-processed PEDOT:PSS electrodes is less than 1% of that of ITO.[249] On one hand, the manufacturing cost of PEDOT electrodes makes use of solution-based coating/printing technologies, which consume less electricity than traditional vacuum deposition technologies for TCOs. On the other hand, the synthesis of PEDOT starts from low-cost raw materials, and the commonly adopted synthetic routes are simple and high-yield.

3.1.1 Material Synthesis

PEDOT is synthesized by polymerization of the monomer 3,4-ethylenedioxythiophene (EDOT). EDOT and derivatives consist of dioxane and thiophene structures, which are constructed separately in most circumstances.[250-252] As illustrated in **Figure 9**, the traditional synthetic route of EDOT **7** starts from the Hinsberg thiophene synthesis reaction between diethyl thiodiglycolate **1** and diethyl oxalate **2**.[253] The major disadvantage of such classic synthetic route is the low overall yield of EDOT due to too many steps. Besides, the Williamson etherification between dihydroxythiophene derivative **3** and dihalogenated hydrocarbons **4** is highly sensitive to the steric

effect, and thus is very limited when synthesizing EDOT derivatives with long sidechains. To overcome these problems, Caras-Quintero et al. reported a facile approach to obtaining EDOT derivatives by Mitsunobu reaction, which eliminated the steric issue caused by sidechains.[254] Kieseritzky et al. reported a simple one-step synthesis of 3,4-dimethoxythiophene by addition-elimination reaction between 2,3-dimethoxy-1,3-butadiene and sulfur dichloride with 60% yield.[255] Apart from the etherification of thiophene derivatives, Das et al. introduced another synthetic route to obtain EDOT derivatives in one step with a stable diyne precursor.[256]

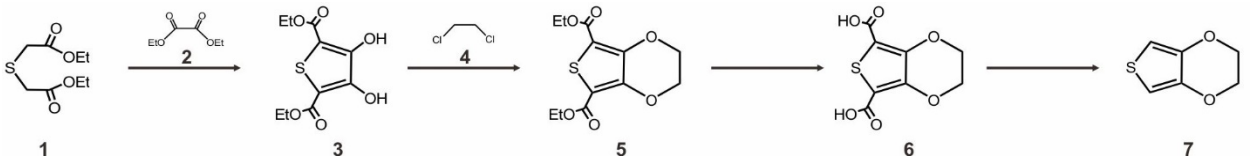

Figure 9. Typical synthetic route for EDOT, starting from diethyl thiodiglycolate.

PEDOT is synthesized with oxidative polymerization of EDOT by either chemical oxidation or electrochemical oxidation, as illustrated in **Figure 10A**. In brief, the EDOT monomers are converted to cation radicals by chemical or electrochemical oxidation, followed by the coupling process between either two cation radicals or, cation radical and neutral molecule. The most frequently used chemical oxidants are iron (III), persulfate-based oxidants, and strong acids.[257-259] For electrochemical synthesis, the EDOT monomer can be polymerized via cyclic potential sweeping, potentiostatic, or galvanostatic approaches.[260-262] Such solution-based polymerization requires negatively charged polyelectrolyte PSS to form a polymer blend with the generated PEDOT because of the insolubility of PEDOT.[187,263] In such a polymer blend, PEDOT exists in an

oxidized state which is more electrically conductive than the neutral PEDOT.[264] However, the non-conductive PSS component always leads to an inferior electrical conductivity of PEDOT:PSS blend compared with pure oxidized PEDOT.[265] As a result, doping of the PEDOT:PSS solution, or post-treatment of the deposited PEDOT:PSS film is always necessary for improving the conductivity of PEDOT:PSS electrode. This will be discussed in more detail later in this section. Meanwhile, anions such as tosylate, trifluoromethanesulfonate, sulfate and dodecylbenzenesulfonate, are adopted as substitutes for PSS^- to improve the conductivity of PEDOT polymer blends.[266-268] Sometimes other anionic substitutes for PSS^- are incorporated with EDOT or PEDOT for simpler synthesis, better wettability, or lower hygroscopicity. For example, McFarlane et al. reported a facile *in-situ* approach to synthesizing highly conductive PEDOT thin-films by mixing EDOT with phosphomolybdic acid hydrate (PMA).[269] Hofmann et al. reported a printable PEDOT dispersion based on PEDOT and poly[4 - styrenesulfonyl (trifluoromethyl sulfonyl) imide potassium salt] (PSTFSIK) to prevent the hygroscopic behavior which is commonly observed from PEDOT:PSS films.[270]

Apart from these wet chemical and electrochemical approaches, vapor phase polymerization (VPP) is also a commonly adopted method for the direct deposition of highly conductive PEDOT on target substrates.[271,272] In a typical fabrication, chemical oxidant (e.g., $FeCl_3$) is firstly deposited on the target substrate by solution-based coating or printing methods such as spin-coating, spray-coating, or electrospinning.[273-275] The oxidative substrate then reacts with EDOT vapor to form a conformable PEDOT film. This synthesis results in highly conductive PEDOT or its derivatives because the *in-situ* polymerization of PEDOT on the target substrate avoids the doping of non-conductive anions for solubility-enhancing purpose. For example, Wang et al. reported highly

conductive PEDOT thin films fabricated via VPP and acid post-treatment with a very high conductivity of 6,259 S/cm, which was close to that of single-crystal PEDOT nanowires.[276] Figure 10B shows the photograph of PEDOT and EDOT-based copolymer poly[anthracene-co-(3,4-ethylenedioxythiophene)] [p(ANTH-*co*-EDOT)] synthesized via VPP. The copolymerization of ANTH improved the optical transmittance of the copolymer at wavelengths of 550 nm and above, and thus is promising for some optoelectronic applications (Figure 10C and D). However, the direct synthesis of PEDOT film on target substrates via VPP requires chamber-based chemical vapor deposition (CVD) equipment, which is not very compatible with large-area R2R fabrication.[247,277] On the contrary, various low-cost PDEOT:PSS inks and pastes are commercially available on the market, which can be printed on target substrate directly via solution-based printing and coating technologies.[278,279]

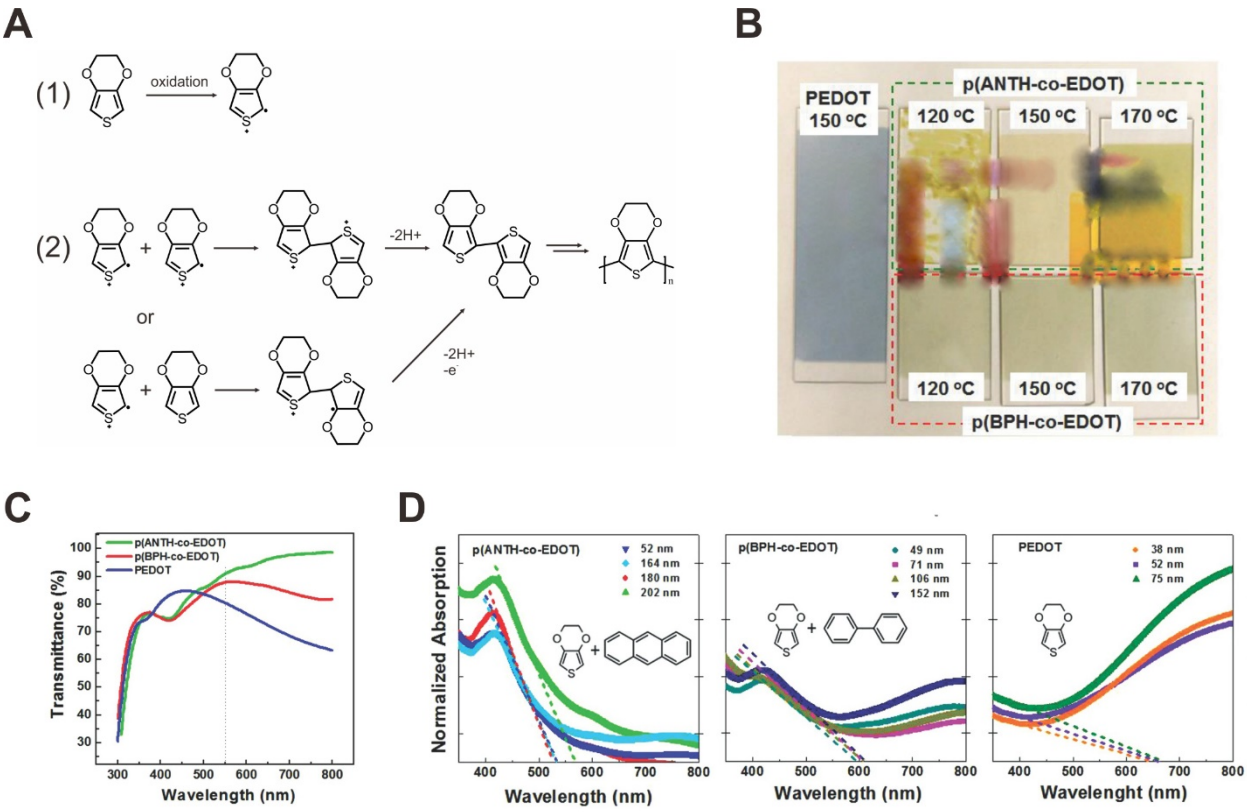

Figure 10. Synthesis of PEDOT and EDOT-based copolymers. (A) Proposed mechanism for PEDOT synthesis via chemical or electrochemical oxidative polymerization.[257-259] (B) Photograph, (C) optical transmittance, and (D) normalized absorption spectra of PEDOT and EDOT-based copolymers synthesized via VPP. Reproduced with permission from Ref[62]. Copyright 2015 WILEY-VCH Verlag GmbH & Co. KGaA, Weinheim.

3.1.2 Optical and Electrical Properties

Commercially available PEDOT:PSS aqueous solution is very compatible with solution-based coating or printing technologies. The solution-processed PEDOT:PSS films possess some other features of TEs suitable for solar cells, such as ideal work function (~ 5.0 eV), continuous and smooth morphology, and good optical transmittance in the visible spectrum.[280-282] However, the

PEDOT:PSS film deposited from pristine PEDOT:PSS solution usually exhibits a poor electrical conductivity of < 1 S/cm, which is too low for TE applications. As a result, improving the electrical conductivity of PEDOT:PSS is of great interest in recent years.[283] In 2000, Granlund et al. firstly demonstrated that the doping of glycerol in PEDOT:PSS water solution would improve the conductivity of micro-contact printed (μCP) PEDOT:PSS.[284] Kim et al. discovered that doping of organic solvents such as N,N-dimethyl formamide (DMF) or dimethyl sulfoxide (DMSO) in the solution also increased the conductivity of the resulted PEDOT:PSS film significantly to ~ 100 S/cm.[285] Later in 2008, Na et al. optimized the doping ratio of DMSO in PEDOT:PSS solution to improve the conductivity of PEDOT:PSS film to > 500 S/cm.[286] The development of doping or post-treatment technologies has further boosted the conductivity of solution-processed PEDOT:PSS film to > 4,000 S/cm in the past decade.[287,288] **Figure 11A** lists the milestones of highly conductive PEDOT film via doping or post-treatment in recent years. Typically, the conductivity-enhancing dopants of a PEDOT:PSS solution include solvents (DMF, DMSO, ethylene glycol (EG), tetrahydrofuran (THF), etc.), surfactants, and ionic liquids. The electrical conductivity of PEDOT:PSS films can be improved to > 2,000 S/cm by such a doping strategy. Post-treatment solution-processed PEDOT:PSS film or VPP PEDOT film with solvents or acids can further boost the conductivity to > 6,000 S/cm.[66,99,164,245,268,276,286,289-296]

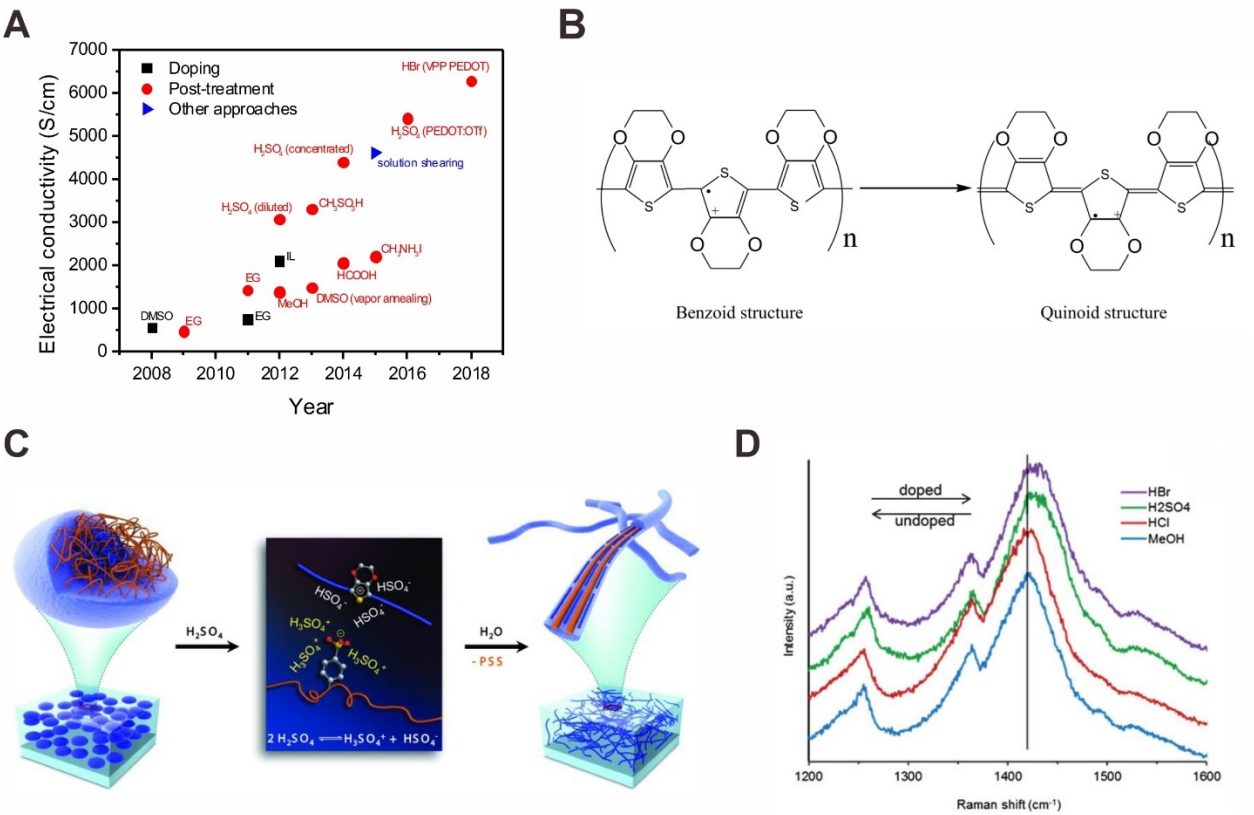

Figure 11. Approaches to improving the conductivity of PEDOT. (A) Summary of highly conductive PEDOT films obtained via doping or post-treatment in recent years. Data are obtained from literature.[66,99,164,245,268,276,286,289-296] (B) Chemical structures of benzoid and quinoid types of PEDOT. (C) Schematics of phase segregation and chain variation of PEDOT:PSS after post-treatment of concentrated sulfuric acid. Reproduced with permission from Ref[294]. Copyright 2014 American Chemical Society. (D) Variation of doping ratio of VPP PEDOT after rinsing of different acid solutions. Reproduced with permission from Ref[297]. Copyright 2013 The Royal Society of Chemistry.

The mechanism of doping and post-treatment of PEDOT may attribute to multiple aspects. Ouyang et al. suggested that such conductivity enhancement is probably resulted from the chain

transformation of PEDOT from a benzoid type to a quinoid type, as illustrated in Figure 11B. Such transformation may lead to the change of PEDOT chains from coil configuration to linear configuration, which results in a strong interaction among PEDOT chains and improved inter-molecular charge transport.[298] Kim et al. proposed the formation of highly crystalline PEDOT nanofibril structure after the post-treatment of concentrated sulfuric acid. The autoprotolysis of concentrated sulfuric acid was believed to stabilize the phase segregation between PEDOT and PSS ions, as illustrated in Figure 11C.[294] Such phase segregation process reduced the effective insulation of PEDOT:PSS caused by non-conductive PSS moieties, and thus improved the electrical conductivity of PEDOT:PSS.[299] The highly crystalline nanofibril structure was then formed because of the π-π stacking between PEDOT chains and the rigid PEDOT networks induced by the orientation of backbones.[294] The post-treatment and additional washing processes also removed part of non-conductive PSS moieties of the PEDOT:PSS film, as suggested by the XPS analysis and the decrease of film thickness after treatment. Another possible reason is the dopant exchange between acids and PEDOT, which the enhances of conductivity and stability of acid treated PEDOT films (Figure 11D). The doping effect may also result in a decrease of work function compared with pristine PEDOT or PEDOT:PSS films.[297,300]

The optical transmittance of PEDOT film is related to the film thickness, chain configuration, doping ratio, and etc.[301-303] For solar cell applications, the optimized PEDOT electrodes usually show an optical transmittance of > 80% at 550 nm.[304-306] **Figure 12A** shows the optical transmittance of methanesulfonic acid-treated PEDOT:PSS on flexible substrates. The acid treatment not only improved the electrical conductivity of PEDOT:PSS, but also increased the optical transmittance of the electrodes because of the removal of residual PSS moieties. Aa a result,

the efficiency of OSCs based on these treated PEDOT:PSS TEs was comparable with the control devices with ITO electrodes.[97] Sometimes the thickness of PEDOT TEs is adjusted not for the trade-off between optical transmittance and electrical conductivity, but for other optoelectronic applications. Figure 12B shows an example of tuning the optical interference by adjusting the thickness of PEDOT:PSS of semi-transparent PSCs. The colorful solar cells were realized by precisely changing the thickness of laminated PEDOT:PSS top electrodes, which exhibited variable optical reflectivity because of optical interference.[307]

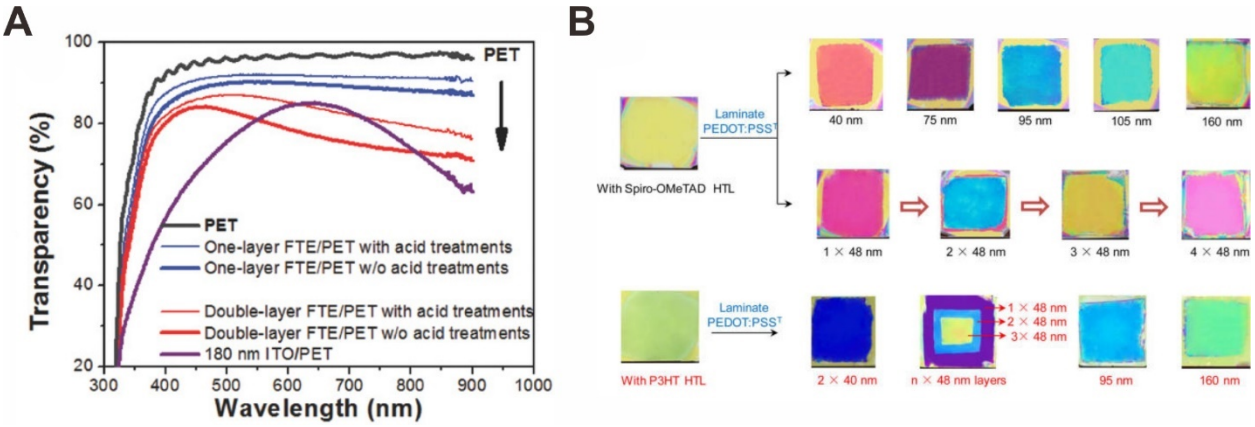

Figure 12. Approaches to tuning the optical transmittance of PEDOT. (A) Optical transmittance of methanesulfonic acid-treated PEDOT:PSS electrodes on PET substrates. Reproduced with permission from Ref[97]. Copyright 2018 WILEY-VCH Verlag GmbH & Co. KGaA, Weinheim. (B) Color-tunable PSCs using transfer-printed PEDOT:PSS top electrodes. Reproduced with permission from Ref[307]. Copyright 2016 American Chemical Society.

3.2 Other Conducting Polymers

Whereas other conducting polymers including polyaniline (PANI), polypyrrole (PPy), poly(p-phenylene-vinylene) (PPV), polyfuran (PF) and other PTh derivatives have been developed for multiple electronic applications, they are less reported as TE materials for solar cells than PEDOT.[308,309] On the other hand, PANI and PPy are employed as TEs for organic light-emitting diodes (OLEDs), OSCs, and DSSCs because of high electrical conductivity, good optical transparency, and high electrochemical activity.[310-314] Similar to PEDOT and its derivatives, the synthesis of PANI and PPy includes chemical and electrochemical oxidative polymerization. The oxidative polymerization of PANI and PPy is significantly influenced by the oxidant and pH value.[315,316] Typical oxidants for aniline and pyrrole polymerization include persulfates,[317,318] Fe^{3+} and other transition metal compounds,[319-322] noble metal compounds,[323-325] peroxides,[326,327] and etc.[328] Stejskal et al. studied the polymerization of aniline with $(NH_4)_2S_2O_8$ oxidant at different pH values. As illustrated in **Figure 13A**, the aniline molecules mainly exist in neutral state when pH value is larger than 4. The oxidation of the neutral aniline molecules stops at non-conductive oligomers or phenazines. The predominant neutral aniline molecules are converted to anilinium cations at pH < 4, but the polymerization takes place only when pH value is less than 2. The pH of the solution becomes lower during the oxidation process because sulfuric acid is a byproduct of this reaction. Figure 13B shows the pH change of mixture solutions of 0.2 M aniline and 0.25 M $(NH_4)_2S_2O_8$ with different initial acidity. The different oxidation mechanisms of aniline at different pH values may explain the self-organized growth of PANI nanoparticles, nanotubes or nanowires.[329-331]

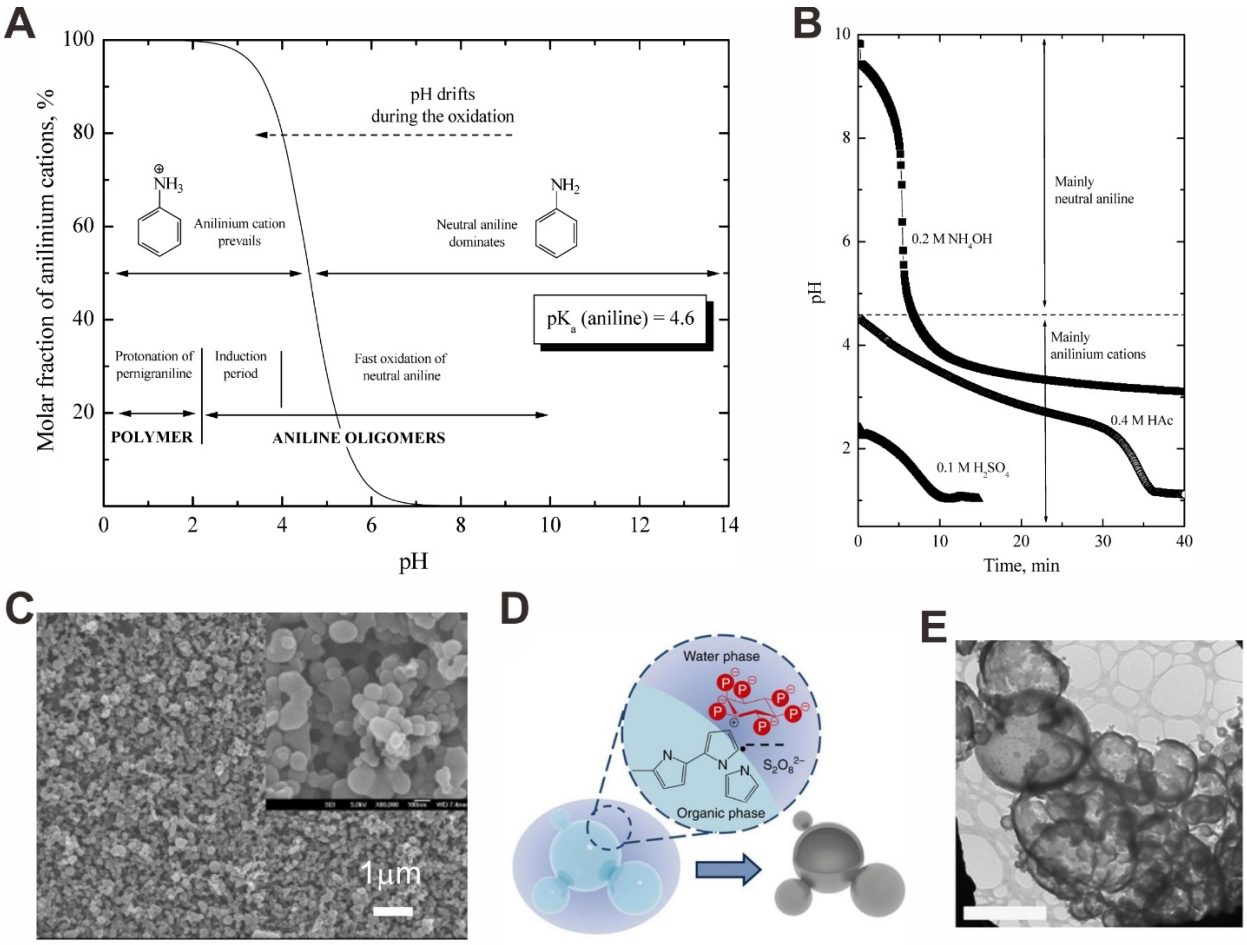

Figure 13. (A) Molar fraction of anilinium cations versus pH value of the solution. The pH of the solution drifts to lower value as the polymerization proceeds. (B) The change of pH value of the solution containing 0.2 M aniline and 0.25 M $(NH_4)_2S_2O_8$ with different initial pH, which was controlled by the addition of ammonia, acetic acid, and sulfuric acid. Reproduced with permission from Ref[329]. Copyright 2008 2008 American Chemical Society. (C) SEM image of PANI nanoparticles synthesized via emulsion polymerization. The magnifications of the images were 10,000 and 80,000 times (inset), respectively. Reproduced with permission from Ref[332]. Copyright 2008 Published by Elsevier B.V. (D) Schematics of hollow PPy microspheres synthesized via emulsion polymerization. (E) TEM image of the synthesized PPy microspheres. Scale bar is 1 μm. Reproduced with permission from Ref[333]. Copyright 2014 Springer Nature.

For DSSCs, the nanostructured PANI and PPy are ideal substitutes for conventional Pt-based counter electrodes because of their high catalytic activity. In 2008, Li et al. firstly applied PANI in DSSCs by using PANI nanoparticles as the counter electrodes. The PANI nanoparticles were synthesized by emulsion polymerization of aniline in a solution containing $(NH_4)_2S_2O_8$ and $HClO_4$. Figure 13C and inset show the SEM images of the ~ 100 nm-scale PANI nanoparticles with 10,000 and 80,000 times magnification, respectively.[332] Emulsion polymerization is also used to synthesize PPy particles. Figure 13D illustrates the structure of hollow-sphere-structured PPy synthesized via emulsion polymerization. The reaction solution contained phytic acid which served as both the negative charge dopant and the crosslinker of PPy. Large-area PPy films can be obtained by simply casting of the synthesized PPy hydrogels. The transmission electron microscope (TEM) image of the particles reveals the hollow structure of the PPy with micro-scale particle size (Figure 13E). Apart from nanoparticles, there are reports using high surface area PANI and PPy nanotubes or nanowires as counter electrodes for DSSCs.[334-336] In recent years, electrochemical polymerization of PANI and PPy on metal and carbon nano-templates has been widely investigated. The obtained nanocomposites show promising electrochemical features for supercapacitors, electrochemical sensors, and DSSCs.[337-339]

Similar to PEDOT and its derivatives, the optical transmittance and electrical conductivity of PANI and PPy are dopant-dependent. The emeraldine base form PANI contains benzenoid type groups which are non-conductive. The doping with H^+ improves the electrical conductivity of PANI significantly from a non-conductive state (~ 10^{-12} S/cm) to a conductive state (1 ~ 10^4 S/cm).[340,341] Chiang and G. Macdiarmid studied the protonation process of emeraldine form PANI, and suggested that the acid doping of PANI resulted in the oxidation of its π system rather than the

p-doping process of other conducting polymers.[342] **Figure 14A** illustrates the protonation process of PANI from an emeraldine base form. The polymer chain is converted to a large delocalized system which is conductive and stable after the protonation process.[343] Among all those acid dopants, camphorsulfonic acid (CSA) is one of the best for solution-processed PANI TEs because it not only improves the electrical conductivity of PANI, but also forms a water-soluble mixture like the aforementioned PEDOT:PSS.[344-346] Figure 14B depicts the relationship among optical transmittance, electrical conductivity, and film thickness of PANI:CSA TE on PET substrate. The 200 nm-thick TE exhibited an R_{sh} of ~ 300 Ω/□ and an optical transmittance of 76% at 550 nm. Whereas such optical and electrical performance was inferior to that of ITO/PET, the mechanical durability of the PANI:CSA TE was significantly higher. In addition, the rigidity of PANI:CSA/PET was found 17% higher than that of the bare PET substrate.[94] Apart from acids, other dopants such as metal salts have been found effective for improving the conductivity of PANI.[347,348] Figure 14C shows the optical transmittance of PPy transparent counter electrodes on fluorine-doped tin oxide (FTO)/glass substrates. The PPy films were deposited on the substrates via *in-situ* chemical polymerization with different pyrrole concentrations. The optimum PPy counter electrode was obtained with 0.3 M pyrrole solution, yielding an optical transmittance of > 60% over the entire visible spectrum. The bifacial DSSC exhibited an efficiency of 3.06% when illuminated from the counter electrode side.[349]

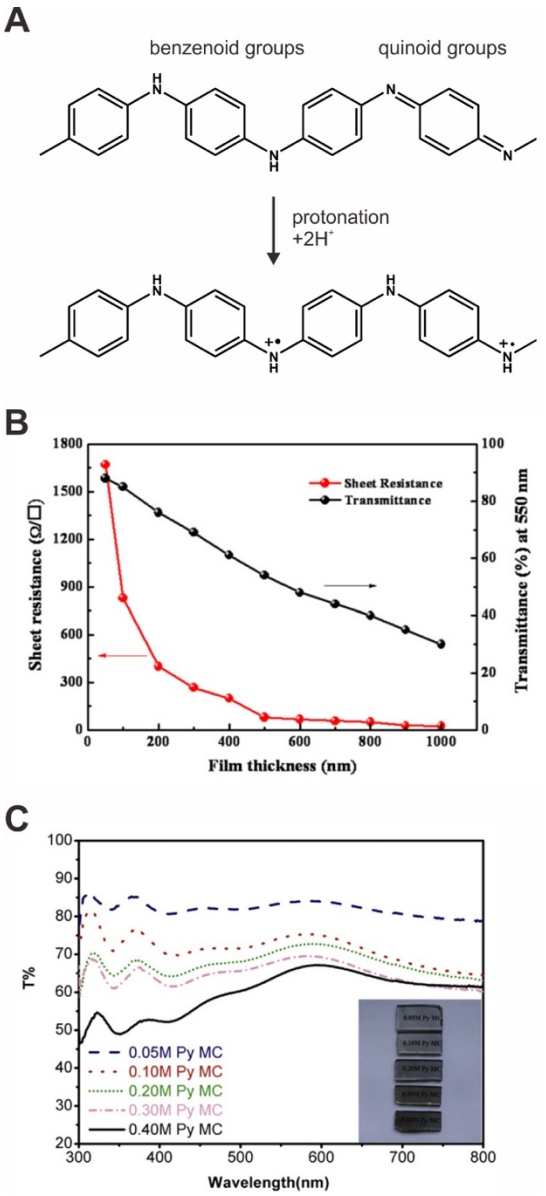

Figure 14. (A) Illustration of the oxidative doping process of PANI by acids. Adapted with permission from Ref[343]. Copyright 2004 American Chemical Society. (B) The relationship between optical transmittance and sheet resistance, and the thickness of PANI films. Reproduced with permission from Ref[94]. Copyright 2012 Elsevier B.V. (C) Optical transmittance of *in-situ*-polymerized PPy films with different pyrrole concentration. Reproduced with permission from Ref[349]. Copyright 2012 Elsevier B.V.

4. Metals and Metal Oxides

4.1 Metal Nanoparticles and Nanowires

Because of the high free-electron density, metal shows the highest electrical conductivity at room temperature among the conducting materials. However, bulk metal material cannot work as TE directly because of its high reflection in the visible range.[350] Therefore, rationally designed architecture is required for metal material to achieve desirable optoelectronic properties. In recent years, metal-based TEs including ultrathin metal films, metal meshes, and metal nanowires, have been widely studied.[70,351] The thickness of the ultrathin metal films is usually limited to 10 nm or thinner to ensure a sufficient optical transparency. Physical vapor deposition (PVD) techniques such as thermal evaporation, sputtering and E-beam PVD are commonly adopted for the thin-film deposition.[352-358] Several reports depicted the solution-based fabrication of ultrathin metal films recently. For example, Mahenderkar et al. introduced an electrodeposition process to fabricate single-crystal gold foils as TEs.[359] However, the high price of Au material limits the large-scale application of Au thin-films as TEs. Meanwhile, many researches focus on solution-based fabrication of metal meshes with metal nanoparticles or metal nanowires. Multiple low-cost metal materials such as Ni, Cu, and Ag have been adopted for TE applications because of their attractive optoelectronic features. For a typical fabrication, metal nanoparticles/nanowires are firstly synthesized as building blocks, followed by printing/coating of the inks that contain the building blocks onto target substrates.[360] In this section, we discuss the material synthesis of these building blocks, and the electrical and optical properties of resulted metal-based TEs.

4.1.1 Material and Synthesis

One typical synthetic route of Ag nanoparticle dispersion reported by Yin et al. in 2002 is evolved from the traditional silver mirror reaction.[361] When aldehyde and silver ammonia complex are mixed together, the former acts as a reductant to produce Ag (0), which nucleates on the surface of the reaction container to form a shiny mirror-like silver layer. This silver mirror reaction is commonly used to examine the aldehyde group in one organic compound (i.e., Tollens test), or to deposit silver thin-film on the target substrate.[362,363] The fundamental reaction in the Tollens test can be simplified as follows:

$$Ag(NH_3)_2^+ + RCHO \rightarrow Ag(s) + RCOOH \quad (8)$$

When high concentration $Ag(NH_3)_2^+$ is reduced in a solution with special stabilizer, the silver mirror reaction can be used to synthesize silver nanoparticles and nanowires with very good stability in solution. The size of silver nanoparticles (AgNPs) can be controlled in the nanoscale dimension, as shown in **Figure 15A**.[361] Apart from aldehydes, a wide variety of reductants have been adopted for the synthesis of AgNPs, such as glucose,[361,364] sodium borohydride ($NaBH_4$),[365] triethanolamine,[366] ascorbic acid,[367] etc. By controlling the concentration of reactants, reaction temperature, and surface stabilizers, the synthesized AgNPs can be controlled under desirable diameter and narrow size distribution.

CuNPs are also promising building blocks for the solution-based fabrication of TEs because Cu is low-cost and highly conductive.[350,368] Similar to the synthesis route of AgNPs, CuNPs are obtained via the reduction of copper salts (such as $CuSO_4$, $CuCl_2$, and etc.). However, the synthesized CuNP dispersions always suffer from poor stability because CuNPs are too reactive to resist oxidation by

air.[362,369] The oxidation of CuNPs will further reduce the conductivity of printed Cu TEs based on these building blocks. To address the instability issue, Park et al. developed a polyol method for the synthesis of highly monodisperse CuNPs in ambient atmosphere. The oxidation of CuNP was inhibited by the nonaqueous solvent. Meanwhile, the presence of poly(vinylpyrrolidone) (PVP) capping agent also protected the CuNPs from oxidation. Figure 15B shows the SEM image of ~ 45 nm-diameter CuNPs synthesized via this method, and the size of the nanoparticles can be tuned by adjusting reactant concentration, reaction temperature, precursor injection rate, and etc.[370]

Metal nanowires are better building blocks for solution-processed TEs than metal nanoparticles because electrically conductive and optically transparent metal nanomeshes can be obtained via a very simple coating process. The synthesis of metal nanowires is similar to that of metal nanoparticles, but the growth of uniform and high-quality nanowires requires appropriate seed and template. Xia's group reported a solution-based synthesis of AgNWs via multiple polyol methods in 2002 for the first time. A typical synthesis employs $AgNO_3$ as the precursor, poly (vinyl pyrrolidone) (PVP) as the stabilizer and capping agent, and EG as reductant.[371-373] The growth mechanism of AgNW synthesized via such method is illustrated in **Figure 16**. The selective growth of AgNW is directed by the capping agent PVP, whose oxygen atoms show a very strong affinity to (100) facet of silver. The capping effect of PVP directs the decahedral seeds to grow into nanowires with a pentagonal cross-section along the fivefold axis, covering the five side faces by (100) planes.[362,371] The good selectivity of PVP ensures a high aspect ratio (length ~ 50 μm, lateral dimension 30 ~ 40 μm) of the synthesized AgNWs (Figure 15C).

Whereas Cu has been a very cost-effective conductor for the electronic industry, employing low-cost CuNWs as TE remains to be challenging. Chang et al. reported a large-scale synthesis of high-quality ultralong (40 ~ 50 μm) copper nanowire for the first time in 2005.[374] In brief, $Cu(NO_3)_2$ was reduced by hydrazine (N_2H_4) in an aqueous solution with ethylenediamine (EDA) as the capping agent. The synthesized CuNWs exhibited a high aspect ratio of >350-450 with a diameter of 90 ~ 120 nm (Figure 15D). In addition to EDA, alkylamines such as octadecylamine,[375] hexadecylamine,[376] and oleylamine[377] have been used as capping agents for successful CuNWs synthesis by corresponding research groups. However, there are few reports on CuNW-based TEs for solar cells due to the limited stability of CuNWs in air.[378,379]

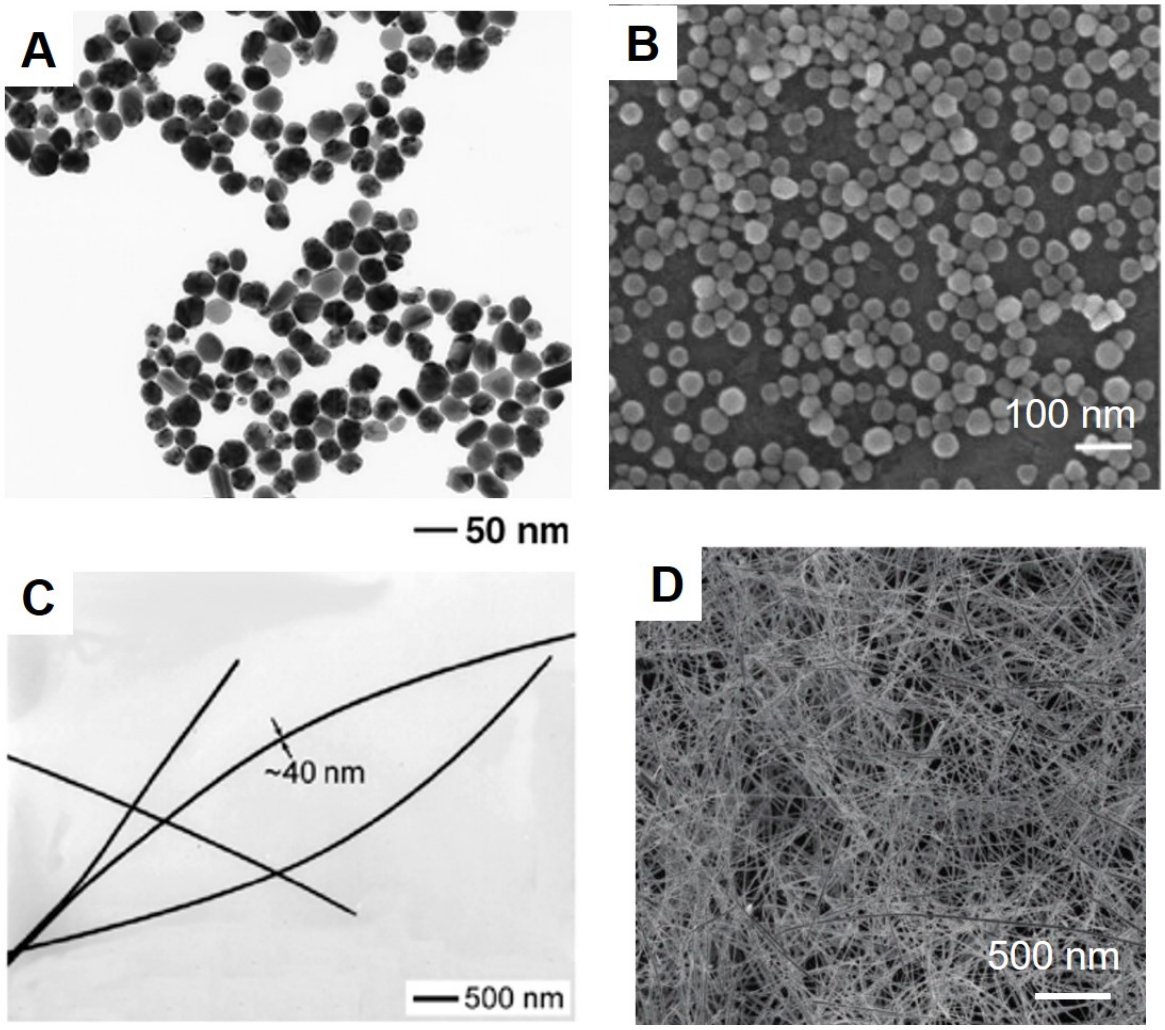

Figure 15. Metallic nanoparticles and nanowires synthesized via a mild solution process. (A) TEM image of AgNPs with a mean size of ~30 nm. Reproduced with permission from Ref[361]. Copyright 2002 The Royal Society of Chemistry. (B) SEM image of CuNPs with a size of ~ 45 nm synthesized by a polyol method. Adapted with permission from Ref[370]. Copyright 2007 Elsevier Inc. (C) TEM images of AgNWs with lateral dimensions of 30 ~40 nm. Reproduced with permission from Ref[371]. Copyright 2002 American Chemical Society. (D) SEM image of CuNWs with a diameter of 90 ~ 120 nm and length of 40 ~ 50 μm. Reproduced with permission from Ref[374]. Copyright 2005 American Chemical Society.

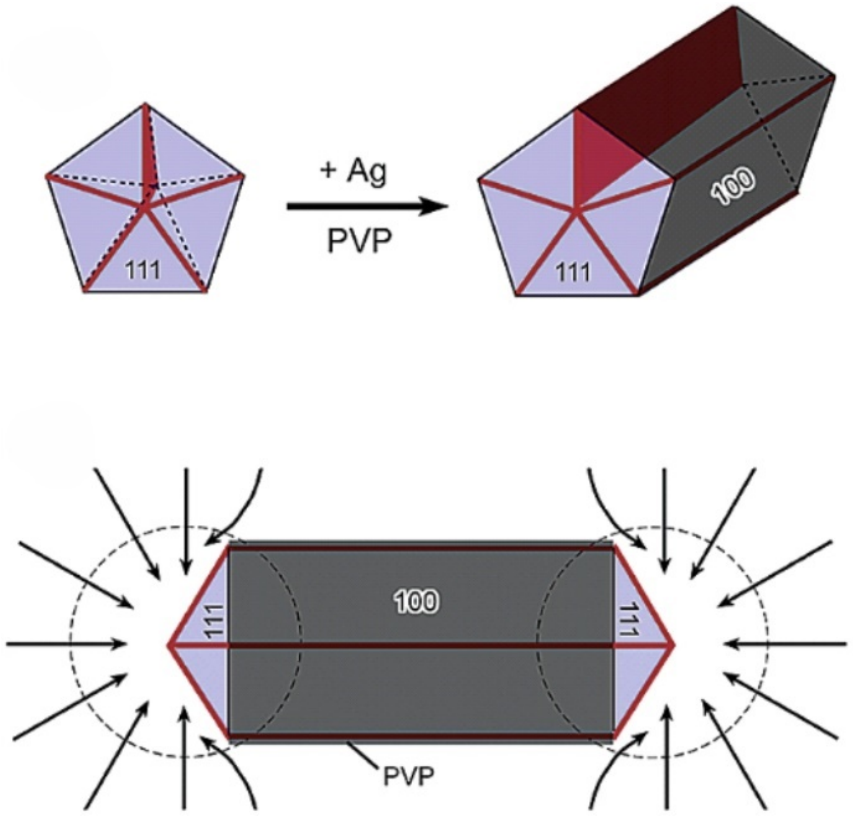

Figure 16. Schematic illustration of the mechanism responsible for the growth of silver nanowires with pentagonal cross-section. Reproduced with permission from Ref[380]. Copyright 2003 American Chemical Society.

4.1.2 Optical and Electrical Properties

The metal nanoparticles or nanowires should be assembled to transparent metal grids, meshes or nanomeshes via multiple solution-based printing or coating techniques to fabricate TEs. In principle, the percolation structures of these metal-based TEs allow light to pass through the gaps between grid lines of meshes. Hence, the optical transmittance and electrical conductivity of these TEs are highly dependent on the grid/mesh structure. In other words, the optical transparency is relative to the area fraction of metal coverage, while the electrical conductivity is also depended on the density of metal materials.

Metal nanoparticles are usually assembled to transparent grids/meshes on target substrates via solution-based printing techniques for TE applications. Apart from the theoretical study mentioned in Section 2.3, researchers have made efforts to optimize the metal TEs in practice. For example, Ahn et al. reported transparent conductive grids by direct writing of concentrated Ag nanoparticle inks on glass and plastic substrates. The relationship between optical transmittance and the pattern pitch of the metal grid was investigated to figure out the optimal condition as TEs. In this work, a high optical transmittance of 94.1% was obtained under 400-μm pitch size for the Ag grids.[381] Apart from square grids, Hong et al. designed triangle and hexagonal shaped Ag grids with different grid sizes, and investigated the optical transmittance and R_{sh} of these grids (**Figure 17A**).

The optimum Ag grids exhibited an R_{sh} of 10 ~20 Ω/□ and an optical transmittance of 85%-90% (Figure 17B). Such a result is comparable to that of commercial vacuum-deposited ITO films (R_{sh} ~ 10 Ω/□, transmittance ~ 90%).[67]

In addition to the pitch size, the linewidth of metal grids/meshes also are very important parameter. Park et al. studied the R_{sh} and optical transmittance of flow-coated AgNP meshes with different grid width (Figure 17C). The R_{sh} decreased from 332 Ω/□ to 132 Ω/□ as the grid width of Ag meshes increased from 7.5 μm to 10.6 μm. However, the increase of grid width also resulted in the loss of optical transmittance (from 88% to 70%), as shown in Figure 17D.[382] A third parameter is the thickness of metal grid lines. Schneider et al. demonstrated thick metal grids fabricated via layer-by-layer electrohydrodynamic (EHD) printing technique. Such method reduced the R_{sh} of printed metal grids with consecutive overprinting, remaining the optical transmittance of the metal grids virtually unaltered.[122] Whereas thicker metal meshes certainly show better electrical conductivity, the protruded metal grids also result in higher surface roughness, which is not desirable for the subsequent deposition of other functional layers of thin-film solar cells. To address the roughness issue, an embedded strategy can be adopted for the thick metal grids to obtain a relatively smooth surface.[383-386] For example, Lu et al. reported imprinted Ag meshes by filling AgNPs into highly ordered concave meshes on PET substrates. These embedded Ag meshes showed a high optical transmittance of > 80% on PET substrates while maintaining a low R_{sh} of < 1.25 Ω/□.[387] In addition, post-treatment of the solution-processed metal nanoparticle grids/meshes is an effective approach to improving the electrical conductivity of metal nanoparticle-based TEs. Kang et al. demonstrated that a post-annealing process of as-deposited Ag nanogrid at 170 °C can reduce the average R_{sh} of the films from 15.2 to 250.3 Ω/□.[388] Such improvement on conductivity

is probably attributed to the vaporization and decomposition of the insulating chemicals adsorbed on the surface of AgNPs, which block the charge transfer between individual AgNPs. [388-390] Since the thermal annealing is an effective and facile process to improve the R_{sh} without sacrificing optical transmittance, it has become a widely adopted post-treatment process for solution-processed metal nanoparticle-based TEs.[122,381-384,386-388,391]

In principle, CuNPs can follow the aforementioned fabrication rules of AgNPs to obtain CuNP-based grids/meshes with desirable optical and electrical properties. However, Cu nanoparticles are easily oxidized in the ambient condition and further loss the electrical conductivity, as mentioned previously in this section. Park et al. reported a method namely transversally extended laser plasmonic (TLP) welding to improve the electrical conductivity and stability of CuNP-based conductors. The CuNPs fabricated via TLP welding showed a reduced amount of oxide fractions and organic residues after the laser sintering process. As a result, the Cu meshes fabricated via this method exhibited excellent an optical transmittance of 95% and a low R_{sh} of 30 Ω/□.[392] Apart from the laser sintering process, acid treatment is an effective solution process to improve the quality of CuNP-based TEs. Kwon et al. combined these two post-processing methods together on the CuNP-based TEs, and demonstrated the application of these TEs on touch screen panels. Such acid-an assisted laser sintering process (ALSP) provided superior oxidation suppression, electrical and mechanical stability over other reported post-treatment methods.[393]

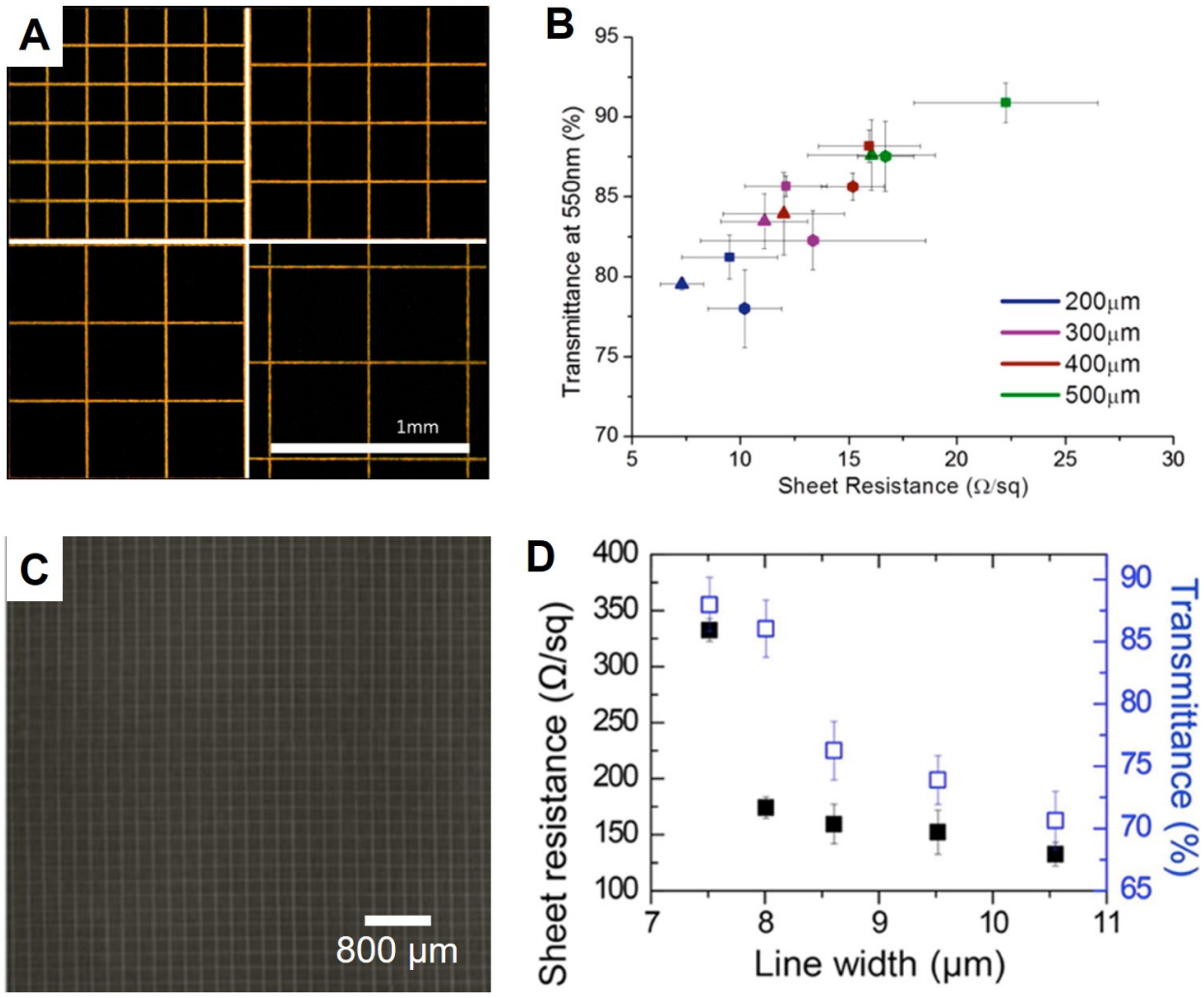

Figure 17. (A) optical images and (B) transmittance versus sheet resistance of AgNP meshes with different pattern pitches (200, 300, 400, and 500 μm). Reproduced with permission form Ref[67]. Copyright 2013 American Chemical Society. (C) Optical image of AgNP meshes, and (D) sheet resistance and optical transmittance of AgNP meshes as a function of the width. Reproduced with permission from Ref[382]. Copyright 2015 American Chemical Society.

Similar to those of metal nanoparticles, suspensions of metal nanowires are also adopted as inks for printed metal mesh-based TEs.[394,395] Direct coating of metal nanowire dispersions can also

result in transparent metal nanowire networks that are eligible for solar cell applications.[201,396,397] Hu et al. studied the optical transparency and electrical conductivity of CNT networks with percolation theory. In brief, the increase of nanowire length l will result in lower percolation threshold N_c (expressed as $(\pi N_c)^{1/2}=4.236/l$). A lower N_c will further improve the probability of having a continuous pathway, resulting in lower R_{sh}.[398,399] As a result, metal nanowires with a high aspect ratio (nanowire length to diameter, l/D) are more desirable for TE applications.[104,400-402] In 2012, Lee et al. reported a successive multistep growth (SMG) method to synthesize > 500 μm-long AgNWs. Such length was at least one order of magnitude higher than that of other reported AgNWs obtained by the traditional method. As a result, the AgNW TEs exhibited superior optical transmittance (89%-95%) and very low R_{sh} (9 Ω/□ ~ 69 Ω/□) (**Figure 18A**).[104] Later in 2014, Ye et al. reported a facile route for the rapid synthesis of high aspect ratio CuNWs with EDA capping agent. An l/D ratio as high as 5,700 was obtained on the longest CuNWs synthesized via this method. As shown in Figure 18B, the optimum CuNWs reached an average length of ~65 μm and a diameter of ~35 nm, leading to a very high l/D ratio of 1,860. The TEs made from these high-aspect-ratio CuNWs exhibited excellent optical and electrical features. For example, the R_{sh} of the long CuNW-based TEs was as low as 100 Ω/□ at 95% high optical transmittance, which were notably higher than that of short CuNW-based TEs with an aspect ratio of 330.[403]

Theoretical study is important for predicting the optimal metal nanowire networks with a low R_{sh}. Ferreira and Boland's research groups performed theoretical and experimental studies in the conductivity of disordered metal nanowire networks.[404,405] The authors extracted a digital model of the AgNW network from the SEM image, and then converted it to a mathematical graph with voltage nodes connected by resistors. The complicated disordered network was then simplified to

a regular homogenous network. The equivalent resistance of the simulated AgNW network as a function of wire density (n_w) matched well with the experimental data. The R_{sh} decreased dramatically as the n_w increased at low-density range ($n_w \lessapprox 0.25$ μm^{-2}), but became less dependent on the n_w at high-density range ($n_w \gtrapprox 0.25$ μm^{-2}).[404] Because the R_{sh} of conventional nanowire network is also relevant to the wire-wire contact resistance (i.e., the junction resistance between nanowires),[406] the key to improving the electrical conductivity is reducing overall contact resistance of the nanowire network.[217] A study in the resistance of single AgNW junctions showed that whereas most of the junctions exhibited a junction resistance of 11 Ω, some junctions exhibited a junction resistance > 200 Ω. Although such "outlier" junctions were a minority of all junctions, the presence of high-resistance junctions could limit the ultimate R_{sh} of AgNW films.[405] There are two strategies to reduce the negative impact of junction resistance on the conductivity of nanowire networks. Employing high-aspect-ratio nanowires is an effective approach to this goal because it reduces the number of junctions. Reducing each junction resistance by specific post-treatment is another approach to realizing the same target. For example, Garnett et al. introduced a light-induced plasmonic nanowelding technique to fabricate large-area interconnected AgNW networks. The welding process was induced by the heat generated at nanowire junctions, where the light was concentrated by the small gaps at each junction. Figure 18C shows the change of AgNW film resistance under continuous light illumination. A short illumination time of 60 s was enough for the complete welding of AgNW networks, leading to a dramatic decrease of film resistance.[407] Similarly, Park et al. reported a flash-induced self-limited plasmonic welding (FPW) post-treatment to weld AgNWs by localized heat energy. The treated AgNW networks exhibited a very low R_{sh} of ~ 5 Ω/□, and a high optical transmittance of 90%.[408] The same strategy was also applied on CuNW networks, followed by a rapid photochemical process to reduce the oxidized CuNWs in

ambient conditions. Figure 18D shows the optical transmittance and R_{sh} of the CuNW networks before and after the welding process. The R_{sh} of the networks dropped dramatically from mega-Ohm scale to ~ 17 Ω/□, while the optical transmittance of the film remained unchanged.[409] Apart from the aforementioned techniques, other post-treatments have been exploited to decrease the wire-wire contact resistance, such as supersonic spaying,[410] mechanical pressing,[411] cold isostatic pressing,[221] electron beam irradiation,[412] electroless welding,[413] thermal annealing,[414] and electroplating welding.[415]

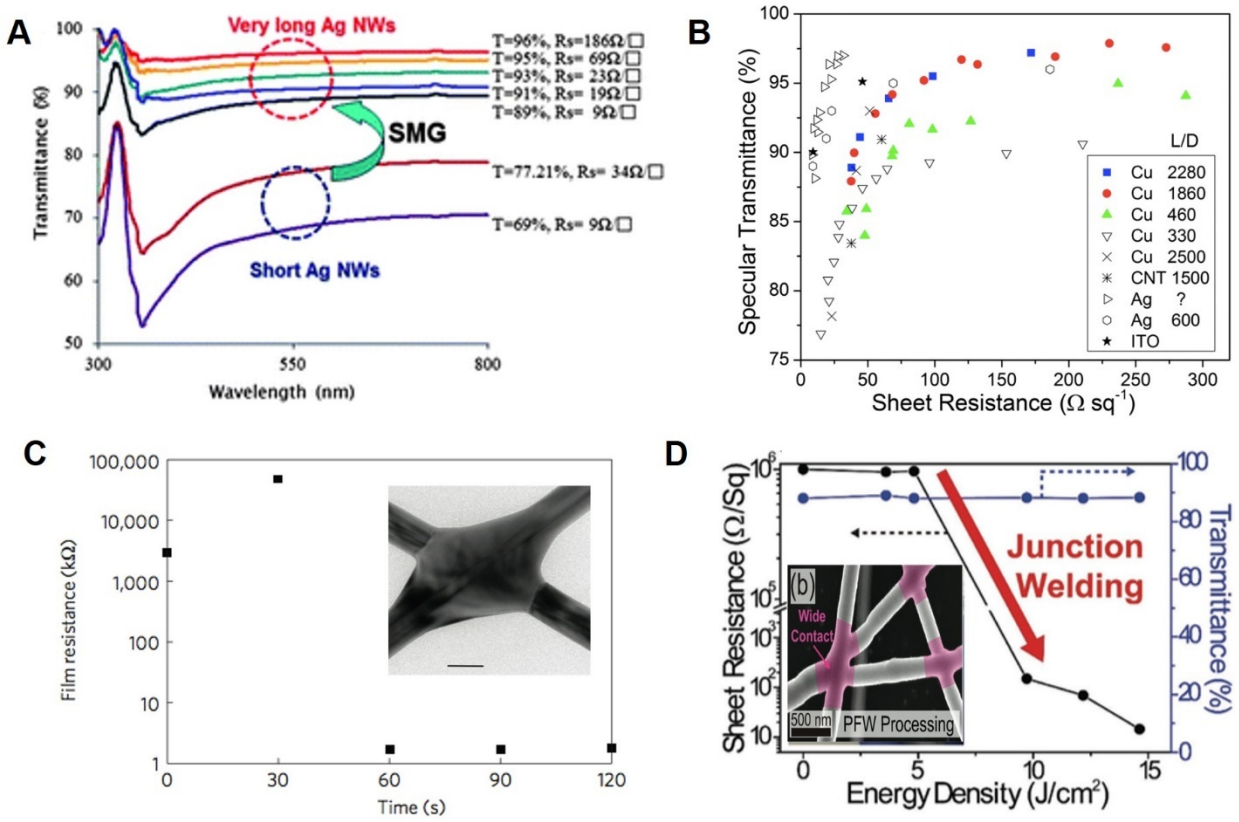

Figure 18. (A) The optical transmittance spectra and sheet resistance (R_s) of AgNW networks based on short AgNWs (average length = 10.2 μm) and very long AgNWs (average length = 95.1 μm). Reproduced with permission from Ref[104]. Copyright 2012 The Royal Society of Chemistry.

(B) Transmittance and sheet resistance of CuNW networks based on high aspect ratio Cu nanowires and comparison with other kinds of transparent electrodes. Reproduced with permission from Ref[403]. Copyright 2014 The Royal Society of Chemistry. (C) Resistance of AgNW network under light-induced plasmonic nanowelding process versus illumination time. The resistance dropped by more than three orders of magnitude after 60 s illumination. Adapted with permission from Ref[416]. Copyright 2012 Springer Nature. (D) The sheet resistance and transmittance of CuNW network before and after the PFW process with different flash energy density. Adapted with permission from Ref[417]. Copyright 2017 WILEY-VCH Verlag GmbH & Co. KGaA, Weinheim.

4.2 Transparent Conducting Oxides

TCOs including ITO, FTO, and aluminum-doped zinc oxide (AZO) are typically deposited via vacuum techniques such as thermal evaporation, and electromagnetic sputtering.[418,419] Whereas most of the transparent metal oxides show poor electrical conductivity due to the large bandgap, doping of the metal oxides could improve the carrier mobility, which results in higher electrical conductivity.[420,421] In principle, both *n*-type and *p*-type doping are effective for improving the carrier mobility of TCOs. However, *p*-type TCOs are rare compared to *n*-type TCOs because of the difficulties in material design.[422,423]

Solution-based spray pyrolysis deposition of TCOs has been developed for decades to replace the vacuum fabrication[424,425] In those methods, TCOs are deposited from precursor solutions containing metal and dopant salts,[426,427] or by coating or printing of TCO nanoparticles which are pre-synthesized via sol-gel method.[428,429] One advantage of the solution-based sol-gel method is the ability to control the nanostructures of nanoparticles. **Figure 19A** shows the SEM images of

ITO nanomaterials synthesized with different additives. The addition of ethanolamine and sodium acetate in the precursor solution resulted in ITO nanorods and nanospheres, respectively. The ITO nanorods exhibited higher specific surface area than the nanospheres, so the spin-coated nanorod films were rougher.[430] Another advantage of sol-gel method is that the doping concentration of TCOs can be tuned by adjusting the concentration of dopants in the precursor solution. Figure 19B shows the photographs of antimony-doped tin oxide nanoparticles synthesized via nonaqueous sol-gel with different doping ratio of Sb. The color of white SnO_2 particles changed to brownish-green once doped with Sb, indicating the existence of electrons in the conduction band.[431] Figure 19C shows the linear relationship between doping concentration of ITO nanoparticles and the concentration of dopant in initial solution. The different dopant concentration of precursor solutions had little impacts on the size of final ITO nanoparticles. However, the doping concentration affected the surface plasmon resonance (SPR) properties of the ITO nanoparticles. The λ_{SPR} occurred at 1,618 nm when the doping concentration of Sn was 10%. Higher or lower doping concentration would cause red shift of the λ_{SPR} peak.[432] Whereas the TCO nanoparticle dispersions can be coated or printed to form transparent films, the conductivity of the as-deposited films is always very low because of charge scattering at small nanoparticle grain boundaries.[433] Hence, a post-annealing process is necessary for higher crystallinity and lower boundary defects. Figure 19D shows the X-ray diffraction (XRD) patterns of solution-processed ITO films annealed at different temperatures in air. The thermal annealing at high temperature resulted in better crystallinity. However, the highest conductivity was obtained by 500 °C-annealed ITO films, and higher annealing temperature would lead to a decrease of hall mobility.[434]

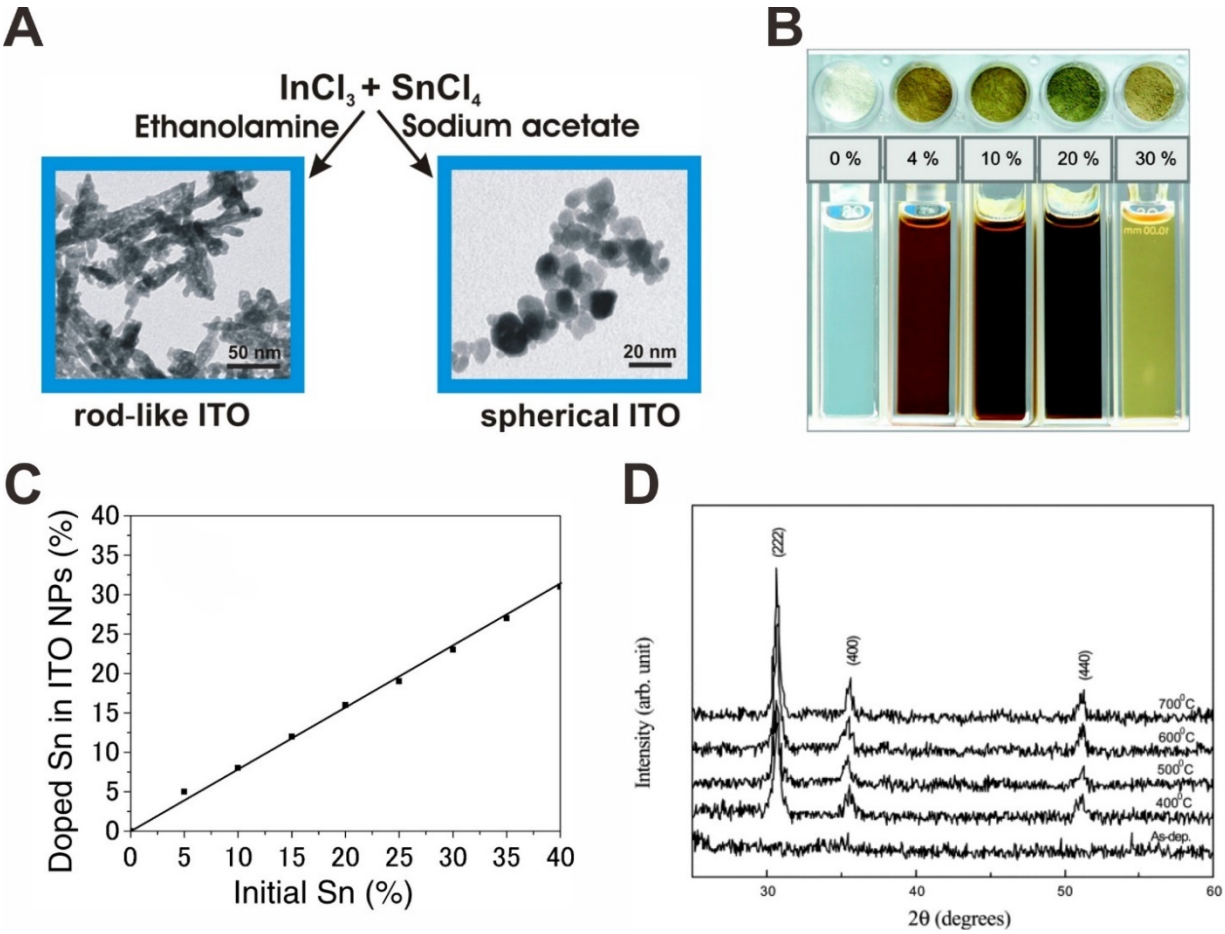

Figure 19. (A) SEM images of ITO nanorods and nanospheres. The nanorods and nanospheres were synthesized via sol-gel process with ethanolamine and sodium acetate as additives, respectively. Reproduced with permission from Ref[430]. Copyright 2014 Elsevier B.V. (B) Photograph of ATO nanoparticles (top) and colloids in tetrahydrofuran (THF) (bottom) with different doping ratio of Sb. Reproduced with permission from Ref[431]. Copyright 2009 American Chemical Society. (C) Relationship between doping ratio of Sn in ITO nanoparticles and the concentration of Sn in precursor solution. Reproduced with permission from Ref[432]. Copyright 2009 American Chemical Society. (D) The XRD patterns of solution-processed ITO films annealed at different temperatures. Reproduced with permission from Ref[434]. Copyright 2002 Elsevier Science B.V.

Nevertheless, 500 °C is too high for some electronic devices and certainly for most flexible substrates. To address this issue, laser annealing techniques are applied on solution-processed TCO thin films to reduce the surface roughness and R_{sh} without causing damage to the substrates.[435-437] Kim et al. developed a combustion process that can reduce the annealing temperature of metal oxides from > 400 °C to < 250 °C. **Figure 20A** illustrates the difference between the combustion process and conventional sol-gel process. The combustion process uses metal nitrates as oxidizer and acetylacetone/urea as "fuels". The redox reaction generates massive localized heat, and thus takes the place of high-temperature annealing processes. Figure 20B shows the differential thermal analysis (DTA) and thermogravimetric analysis (TGA) of ITO films synthesized via combustion process (red curves) and conventional process (blue curves). Both analyses indicate a complete conversion temperature of < 200 °C for the ITO films synthesized via combustion process. As a result, the combustion-processed ITO films showed 130 S/cm electrical conductivity with a low-temperature annealing process of 250 °C (Figure 20C).[438]

Generally, the optical transmittance of solution-processed TCOs for solar cells is > 80% over the entire visible spectrum. Figure 20D shows the optical transmittance of spin-coated ITO films with different layers. A red shift of the UV cut-off which was probably attributed to a quantum size effect that was observed as the films became thicker. Meanwhile, the difference in film thicknesses caused the interference of light at different wavelengths. As a result, maxima and minima can be observed on the transmittance spectra.[439] The post-treatment also has an impact on the optical transmittance of TCO films. Figure 20E, F, and G show the influence of post-annealing process on the optical transmittance of the brush-painted titanium-doped indium oxide (TIO) films. The

annealing process below 400 °C caused a decrease in optical transmittance at 550 nm, but higher annealing temperature could make the optical transmittance of the annealed films higher than as-deposited ones (Figure 14G).[105]

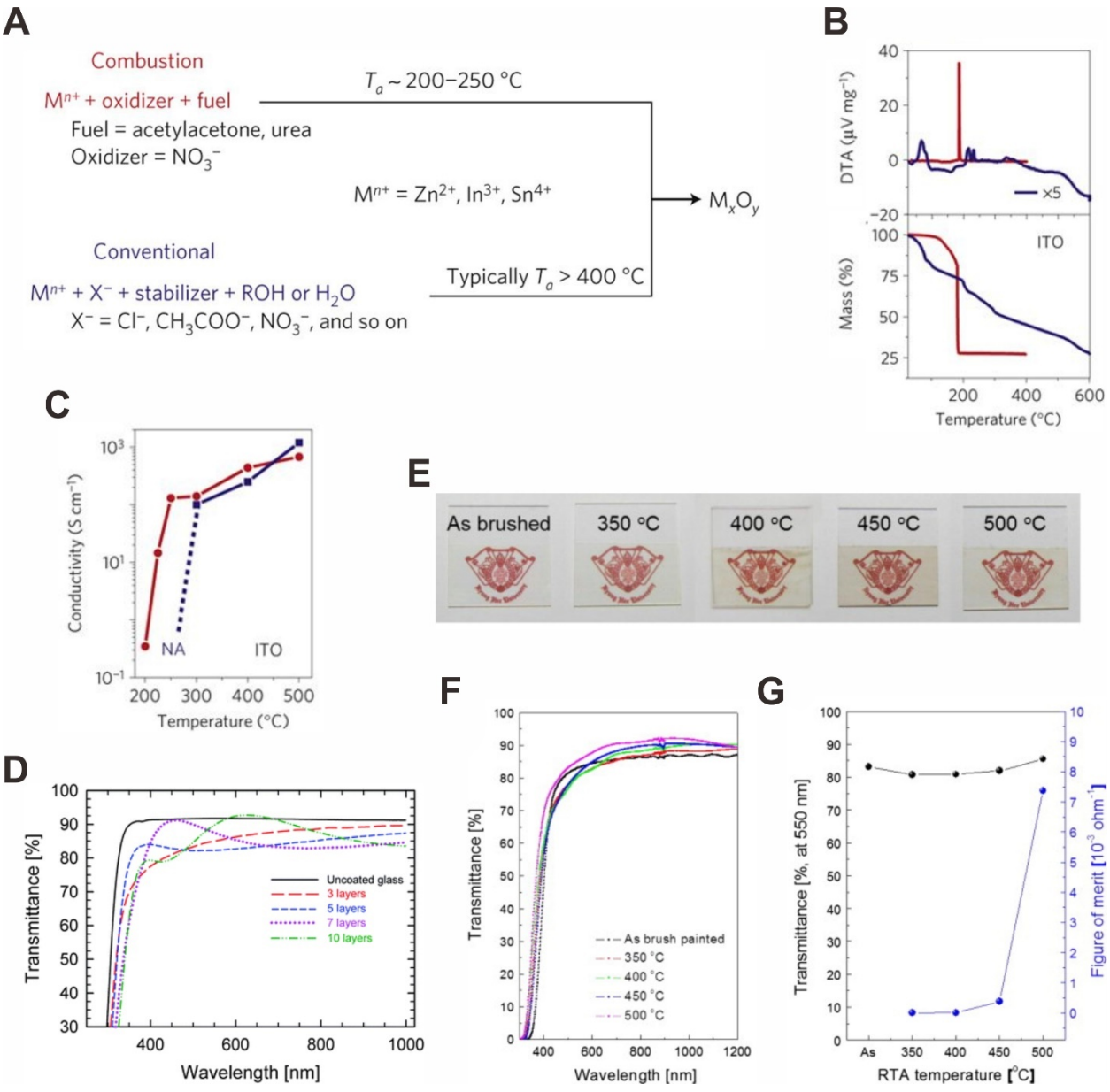

Figure 20. (A) Schematics of the combustion process compared to conventional sol-gel processes. (B) DTA (top) and TGA (bottom) analyses of ITO films synthesized via combustion (red curves)

and traditional process (blue curves). (C) The electrical conductivity of ITO films versus annealing temperature. Red and blue lines refer to ITO films synthesized via combustion and conventional processes, respectively. Reproduced with permission from Ref[438]. Copyright 2011 Springer Nature. (D) Optical transmittance of spin-coated ITO films with different layers compared to bare glass. Reproduced with permission from Ref[439]. Copyright 2012 The Royal Society of Chemistry. (E) Photograph, (F) optical transmittance spectra, and (G) specific transmittance at 500 nm of brush-painted TIO films with different post-annealing temperatures. The bottom right image also shows the change of figure of merit (FoM) of the TIO films as the temperature increases. Reproduced with permission from Ref[105]. Copyright 2013 Elsevier B.V.

5. Carbon Materials

5.1 Graphene

5.1.1 Material Synthesis

In 2004, Geim and Novoselov achieved the first experimental isolation of graphene via mechanical cleavage of graphite, and thus triggered the global research interest of graphene.[440] Up till now, the one-atom-thick graphene film has been well-reported as 2D material with unique physical and chemical properties, including excellent mechanical flexibility, good chemical stability, high optical transparency and charge carrier mobility. These features make the graphene materials especially promising for TEs of optoelectronic devices.[73,158,441]

Figure 21 summarizes the synthesis of various graphene for different applications.[442] To produce graphene sheets with high efficiency and low cost, chemical exfoliation approach is developed to

fabricate graphene oxide (GO) and reduced graphene oxide (rGO) sheets. GO sheets are mainly fabricated via oxidative treatments on graphite, such as Brodie method,[443] Hummers method[444-446] and Staudenmeier method.[447,448] Hummers method is the most adopted way nowadays, where the GO sheets are obtained through graphite oxidation in an anhydrous mixture of concentrated sulfuric acid, potassium permanganate and/or sodium nitrate. Furthermore, rGO sheets could be obtained by removing the oxygen-containing groups on GO surfaces. A number of reduction treatments on GO have been developed, which include the chemical reduction,[449-455] photothermal reduction,[456] thermal reduction[457-460], and microwave reduction.[461,462] The chemical reduction approach is the most versatile, with the availability of many different reduction agents such as hydrazine, strong alkaline media, ascorbic acid, sodium borohydride and poly (sodium 4-styrenesulfonate).

Compare to pristine graphene, rGO has lower conductivity caused by the residue oxygenated group and defective sites. Therefore, non-chemical exfoliation is developed as an alternative route to obtain graphene sheets from graphite without the oxidation process. Liquid-phase exfoliation of graphite is based on exposing the materials to a solvent with a surface tension that favors an increase in the total area of graphite crystallites.[463] Generally, there are two ways of the liquid phase exfoliation: using high surface tension solvents or using aqueous solutions with surfactant/polymers in water as stabilizers.[464] Through the sonication of graphite in these solutions, graphite is split into individual platelets and yields a significant fraction of monolayer graphene flakes in the suspension.[465,466]

Instead of solution processable graphene flakes, large-area and uniform graphene films are readily synthesized via vapor phase methods including chemical vapor deposition (CVD),[467-469] plasma-

enhanced chemical vapor deposition (PECVD),[470,471] and annealing SiC.[472,473] Among these methods, CVD is the most typical and readily accessible one that involves the decomposition of gaseous carbon source, such as methane,[467] hexane, toluene[474,475] and ethanol,[476] over a transition or polycrystalline metal substrate typically held at high temperature around 1000 °C.[477,478] The single-to-few-layer CVD graphene films are commonly grown on polycrystalline metals such as Ni[479] and Cu foils,[480] whereas CVD of graphene on transition metal substrates such as Pt,[481] Ru[482] and Ir[483] have also been explored. PECVD is developed to grow graphene at a lower temperature. Assisted by the remote-discharged radio-frequency plasma beam source (13.5 MHz), monolayer CVD graphene can be deposited on Cu foil in less than 5 minutes at ~ 650 °C.[470] Wafer-size single-to-few-layer graphene films can also be synthesized on carbon-containing substrates such as silicon carbide (SiC), where the graphene films were fabricated via the sublimation of silicon atoms and graphitization of remaining carbon atoms under very high temperature (1000 ~ 1600 °C).[484]

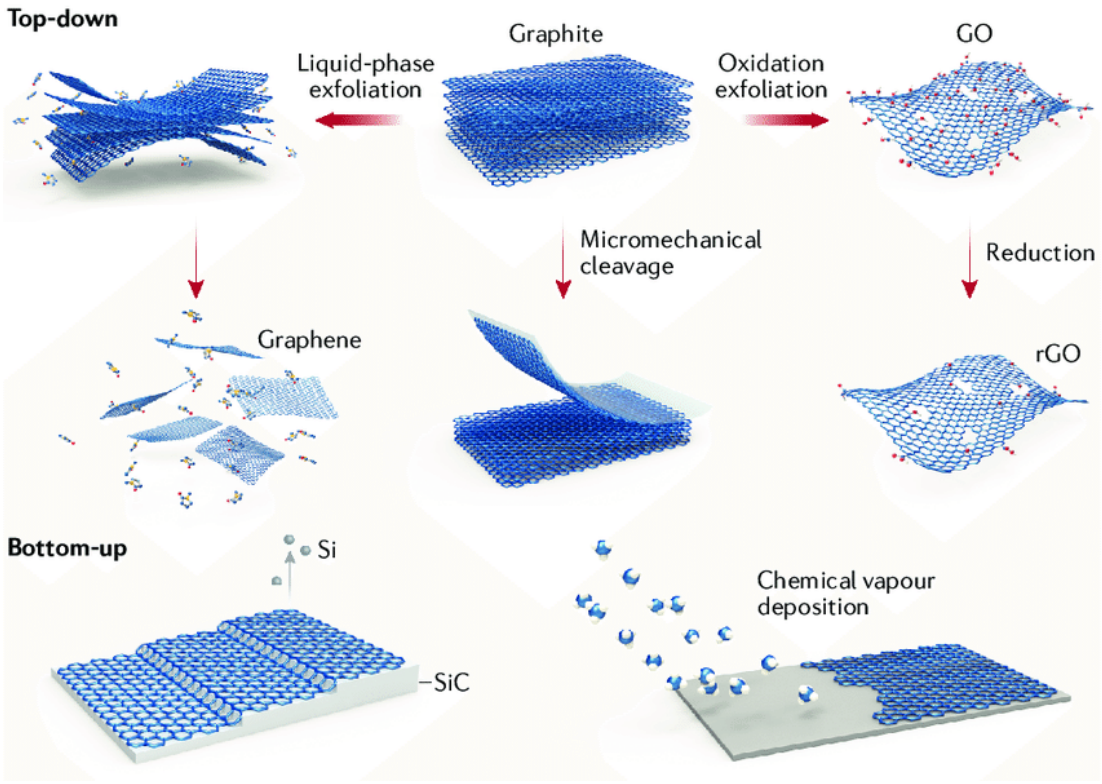

Figure 21. Major approaches of graphene synthesis. Fabrications of graphene could be categorized into four approaches: micromechanical cleavage of graphite, oxidation exfoliation, liquid-phase exfoliation, and chemical vapor deposition. Adapted with permission from Ref[442]. Copyright 2017 Springer Nature.

5.1.2 Optical and Electrical Properties

Graphene and its derivatives have unique physical properties and chemical stability that attract large research interest. Graphene film was first adopted as TE of a DSSC by Wang et al. in 2008. The rGO TE was ultrathin (~10 nm) and exhibited a large R_{sh} of 1.8 ± 0.08 kΩ/□ with a transparency > 70% under the wavelength of 1,000 ~ 3,000 nm.[118] Later in 2009, graphene TEs with different thicknesses (6-30 nm) were studied. The R_{sh} was reduced to 210 ~ 1,350 Ω/□ with

a transmittance of 72% ~91% in the visible range.[485] To date, rGO sheets that achieve the highest conductivity up to 6300 S/cm and a record-high mobility of 320 $cm^2 V^{-1} s^{-1}$ have been fabricated.[460] Large-area CVD graphene sheets up to 30 inches are shown in **Figure 22A**. Such graphene layers exhibited a low R_{sh} of ~125 Ω/□, high optical transmittance (~97.4%) and high mobilities up to 7350 cm^2 V^{-1} s^{-1} at low temperature (Figure 22B).[166] The extraordinary optical transparency, mechanical flexibility and electrical conductivity of graphene made them ideal candidates as TEs for flexible microelectronics.

Up till now, graphene-based electrodes have been applied in the photovoltaic devices extensively and reported with impressive performance and flexibility.[486,487] The hydrophobicity nature of graphene could be a problem for the subsequent solution-based deposition of other materials. Traditional surface modification methods such as plasma treatment may damage the very thin graphene, causing unwanted doping or a decrease in conductivity.[488,489] To improve the wettability of graphene while preserving its conductivity and transmittance, a self-assembled layer of pyrene buanoic acid succidymidyl ester (PBASE) was stacked on the graphene surface non-covalently via the pyrene group.[485] The PBASE modification barely affected the optical transmittance of the graphene film, as shown in Figure 22C, but greatly improved the wettability of PEDOT:PSS solution on the surface of graphene. On the other hand, appropriate surface modification could improve the performance of graphene TEs directly by improving the conductivity and tuning the work function.[490-492] For example, Sung et al. improved the conductivity of single-layer graphene TE by modifying the graphene surface with an evaporated MoO_3 layer. The R_{sh} of graphene film can be reduced from ~ 2000 Ω/□ to 780 Ω/□ by depositing 0.5 nm MoO_3 layer on top (Figure 22D). Moreover, this additional MoO_3 layer provides hydrophilicity to the graphene TE, and elevates the work function of graphene from 4.23 eV to 4.71 eV via the hole doping effect.[493]

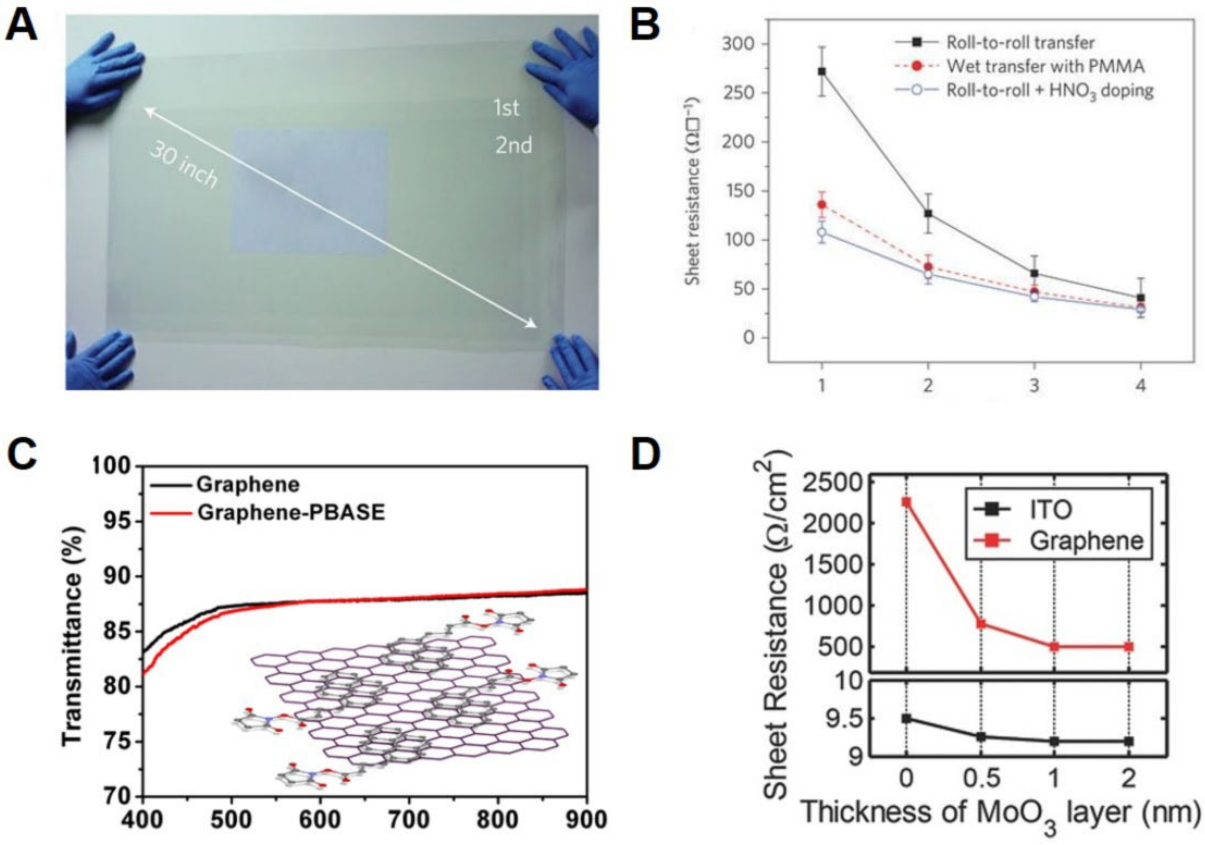

Figure 22. Optical and electrical properties of graphene electrodes applied on solar cells. (A) A transparent ultra-large-area graphene film transferred on a 35-inch PET sheet and (B) sheet resistances of transferred graphene films using a roll-to-roll (R2R) dry-transfer method combined with thermal release tapes and a PMMA-assisted wet-transfer method. Reproduced with permission from Ref[166]. 2010 Copyright Springer Nature. (C) Transmittance spectra of the graphene films before and after PBASE modification. (Inset: schematic diagram of the PBASE modified graphene film). Reproduced with permission from Ref[485]. Copyright 2009 American Institute of Physics. (D) Relationship between sheet resistance and MoO_3 thickness for graphene and ITO. Reproduced with permission from Ref[493]. Copyright 2015 WILEY-VCH Verlag GmbH & Co. KGaA, Weinheim.

5.2 Carbon Nanotubes

5.2.1 Material Synthesis

Apart from the two-dimensional (2D) carbon-based transparent conductive materials mentioned above, a lot of research efforts have also been put on the one-dimensional (1D) carbon nanotube (CNT) in the past few decades. The CNTs are commonly divided into two groups: single-wall CNT (SWCNT) and multi-wall CNT (MWCNT). The structure of SWCNT is considered as a rolled-up graphene sheet, while that of MWCNT consists of multiple graphene layers. The first experimental discovery of CNTs was about the MWCNTs fabricated through arc-discharge evaporation by Iijima et al. in 1991,[494] and the first SWCNT was synthesized by the same group two years later.[495]

In general, the presence of metal and/or metal oxide catalyst is found to be critical to control the structure of fabricated CNTs. Catalysts such as Co,[496,497] Ni,[498] Fe,[499-501] Ag[502], Ag,[503] Pd,[504,505] and MgO[506] are commonly adopted, and the effects lead by different mixtures of these catalysts have been widely studied. There are three approaches for CNTs fabrications nowadays: the plasma arc-discharge, pulsed laser ablation and CVD process. Among the three approaches, plasma arc-discharge and pulsed laser evaporation could produce CNTs with relatively high quality, but a harsher reaction condition involving high reaction pressure and temperature (1000 ~ 6000 K) is required.[507] For the arc-discharge technique, CNTs are produced from a chamber filled with inert gas at sub-atmospheric pressure (100 ~ 700 torr) as shown in **Figure 23A**.[508] The chamber contained a high-purity graphite cathode and anode, as well as filling with evaporated carbon molecules and metal catalysts. During such an arcing process, about half of the evaporated carbon solidified on the cathode tip and chamber wall, forming cigar-like structures that contain nanotubes

arranged randomly.[494,495,499,509]

Figure 23B shows the experimental setup for pulsed laser ablation, where a high-energy laser was used to vaporize the graphite placed in a quartz tube under ~ 1,200 °C in inert gas atmosphere.[510-512] Previous studies have demonstrated that this fabrication process allows an easier control of the diameter and yield of the resultant nanotubes when compared to the traditional arc discharge. Various parameters inside the reaction chamber could influence on the size of the CNTs, such as the laser power and wavelength,[513-515] pressure, temperature[516,517] and the chemical composition.[518] As demonstrated by Thess et al., the ultrafast (sub-picosecond) laser pulse vaporized carbon-nickel-cobalt mixture could enable the creation of large amounts of SWCNT under 1,200 °C with a yield of > 70%.[519]

On the other hand, CVD has been developed as the most widely used continuous production process of CNTs in a large scale.[520-522] CVD techniques allow precise control of experimental parameters, thus the chirality and morphologies of the resultant CNTs could be well-designed. Generally, the gaseous carbon source such as methane, ethanol, acetylene and carbon dioxide was deposited on a layer of metal and/or metal oxide catalyst supporting by a substrate under ~ 1,000 °C and ~ 1.25 atm (Figure 23C).[523] For instants, Kong et al. discovered that the catalyst substrate determines the growth of CNT as either an individual or a bundle. For example, individual SWCNTs were obtained when the Fe_2O_3 catalyst was supported by crystalline alumina nanoparticles, while only bundled SWCNTs were obtained when amorphous silica particles substrates were adopted.[524] A number of CVD processes including catalytic CVD (CCVD),[525-528] thermal CVD,[529-531] plasma enhanced (PE) CVD,[532] laser-assisted CVD,[533] water assisted CVD,[534]

microwave plasma (MPECVD),[535] and hot-filament (HFCVD)[536] have been adopted for improving the for the fabrication of CNTs.

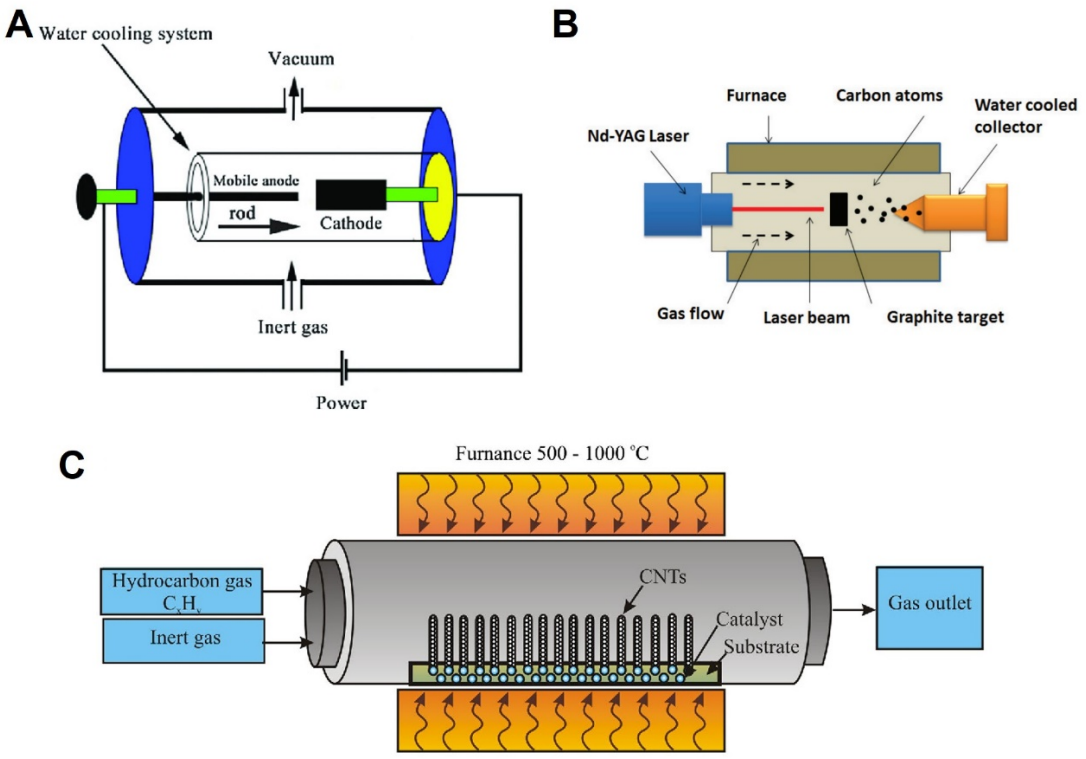

Figure 23. Major approaches for CNT synthesis. Fabrications of CNTs could be categorized into three major approaches: (A) arc discharge, reproduced with permission from Ref[508]. Copyright 1998 Springer-Verlag. (B) laser ablation, reproduced with permission from Ref[512]. Copyright 2018 AIP Publishing. (C) chemical vapor deposition. Reproduced with permission from Ref[523]. Copyright 2016 The Authors. http://creativecommons.org/licenses/by/4.0/

5.2.2 Optical and Electrical Properties

In 2004, Wu et al. reported transparent and conductive pure SWCNT films via filtration method, through which the resultant films possessed a transmittance and conductivity comparable to that

of ITO. The R_{sh} of the as-prepared 50 nm film was 30 Ω/□, with the corresponding transmittance over the visible spectrum and near-IR spectrum recorded as > 70% and > 90%, respectively.[71] Base on this technique, Pasquier et al. first applied the SWCNT films as TEs in OSCs. The films with thickness < 100 nm was found transparent to UV light, exhibiting a higher transparency than ITO-PET under the light with the wavelength from 250 to 850 nm.[537] **Figure 24A** shows a photograph of a free-standing CNT film which was used as top TE for PSCs.[538] The high work function (4.95 to 5.05 eV) of the CNT films makes them ideal as transparent anodes. The electrical conductivity of CNT can be further improved via acidic treatment, as reported by Geng et al.[106] The R_{sh} of CNTs films treated with 12 M HNO_3 for 60 min was reduced by a factor of about 2.5 times while the change in the transmittance was negligible in the visible region. The R_{sh} of the resulted films were ~ 40 Ω/□ and 70 Ω/□ at the corresponding transmittances of 70% and 80%, respectively (Figure 24B).

To serve as transparent cathodes, the work function of CNT should be reduced to facilitate the electron injection. In 2017, Luo et al. demonstrated SnO_2-coated cross-stacking carbon nanotube (CSCNT) films as efficient transparent cathodes for PSCs. The SnO_2-decorated CNT layers significantly reduced charge recombination of the device when compared to the bare-CNT-based ones because of the electron extracting nature of SnO_2. Meanwhile, the modified CNT exhibited a satisfactory R_{sh} of ~ 51 Ω/□.[539] On the other hand, many research works have been done on tuning the work function of CNTs films through doping processes.[540-542] Recently, Lee et al. reported the trifluoromethane-sulfonic acid (TFMS) vapor doping of the free-standing CNT sheet for PSCs (Figure 24C). As shown in Figure 24D, the R_{sh} of the doped CNT sheet was significantly reduced from 153 Ω/□ to 121 Ω/□ after 40 s TFMS doping, and the work function was increased from 4.75

to 4.96 eV.[108] Likewise, the conductivity and work function of CNTs sheets could be adjusted by polymer modification, such as the polyethyleneimine (PEI) modified cross-stacked super-aligned carbon nanotube (CSCNT) as demonstrated by Zhou et al. By drop-casting PEI/IPA solution on a CSCNT film fabricated via CVD process, a ~ 2- μm-thick CSCNT:PEI film with an R_{sh} of ~ 40.5 Ω/□ was obtained. Moreover, the work function of the CSCNT film was decreased from 4.68 eV to 4.45 eV. Thus, the charge transfer barrier between the electron transporting layer and CNT films was reduced as well as enhancing the performance of the photovoltaic devices.[543]

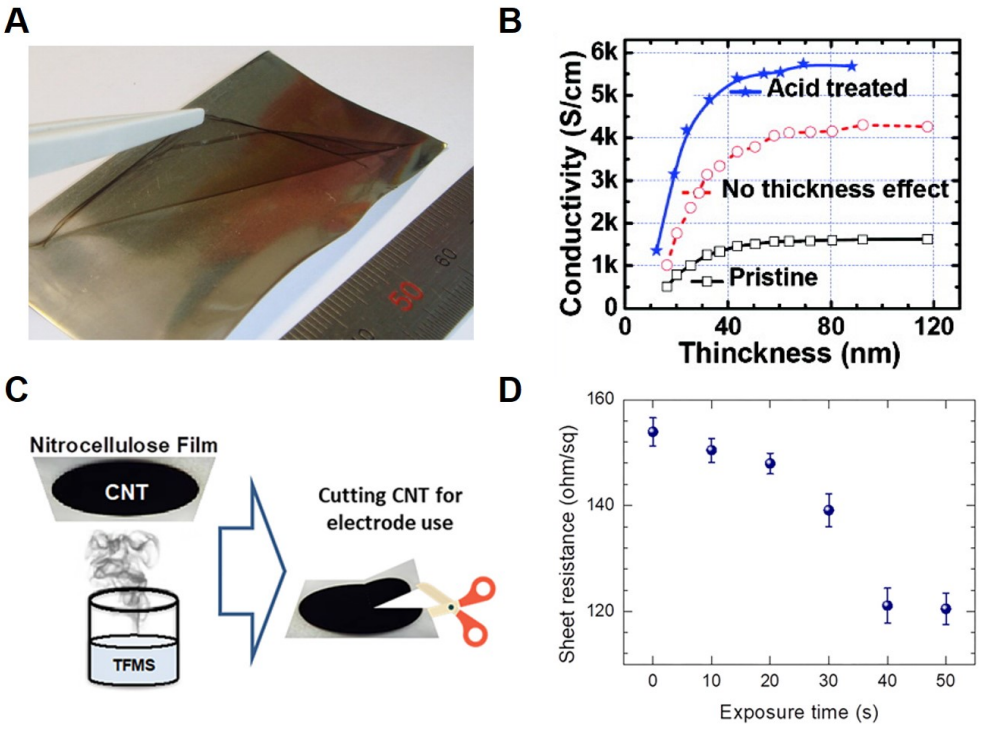

Figure 24. Optical and electrical properties of CNT electrodes applied on solar cells. (A) Photo of freestanding CNT film lifting by tweezers to transfer onto other substrates. Reproduced with permission from Ref[538]. Copyright 2014 American Chemical Society. (B) The corresponding conductivity as a function of film thickness before and after acid treatment. Reproduced with

permission from Ref[106]. Copyright 2007 American Chemical Society. (C) Schematic illustration showing ex-situ doping of CNT by using vaporized TFMS; and (D) measured sheet resistance with different exposure time to TFMS vapor. Reproduced with permission from Ref[108]. Copyright 2018 American Chemical Society.

6. Solution-based Coating and Printing Technologies for Fabrication of TEs

As mentioned above, solution-based thin-film deposition technologies are preferred by the photovoltaic industry because of high throughput, low material waste, and low cost compared with traditional vacuum deposition technologies.[544-546] However, achieving high-quality solution-deposited TEs is a challenge task because many aspects such as surface wettability, the volatility of solvents, the adhesion between TEs and substrates, and rheology of the solutions have to be considered and optimized.[547-550] **Figure 25** illustrates most frequently reported solution-based coating and printing techniques for TEs. Some examples of TEs fabricated via these techniques will be discussed in Section 6.1 to 6.6.

Spin coating is a facile approach to obtaining small-size (wafer scale) thin films.[551] It makes use of centrifugation force to spread materials uniformly on flat substrates. A solution or ink that contains the coating material is firstly drop-casted on top of the target substrate on the spin coater. To form a uniform film, the solution should have a certain degree of wettability on the target substrate. Most of the material and solvent is spun-off from the substrate during the spinning process, leaving a thin layer of material on the substrate. For a specific material, the thickness of the film is majorly determined by the concentration, volatility and viscosity of the solution, and

the spin speed.[552-554] There is a simplified model to illustrate the relationship between film thickness and spin speed when neglecting the effect of shear stress:

$$h \propto \omega^{-\frac{2}{3}} \quad (9)$$

where h is the final film thickness and ω is the rotation rate.[273] An annealing process is usually necessary after the spin coating of TE materials for multiple purposes such as evaporation of the residual solvent, sintering of the nanoparticles/nanowires, or conversion of the precursors to finally TEs.

Spray coating deposits droplets on the target substrate via the spray nozzle.[555] The spray nozzle generates an aerosol that contains droplets of TE material (or precursor), and directs the transport of materials to the target substrate with the aid of electrostatic charge or carrier gas.[22] A hotplate is usually necessary under the target substrate to evaporate the residual solvent, or to convert the precursor to the final TE. For example, transparent and conductive AZO thin films can be fabricated via the spray pyrolysis of a solution containing $Zn(Ac)_2$ and $AlCl_3$.[556]

Slot-die coating is a highly efficient one-dimensional coating technique that is commonly integrated into the R2R fabrication of solar cell modules.[557] As illustrated in Figure 25, the ink is pushed out of the slot-die head by a pressure system, and stripes of the ink is coated along the moving direction of the web. The thickness of the film is controlled by the pumping rate and concentration of the ink, while the coating speed is determined by the moving speed of the web. For R2R fabrication of OSCs, slot-die coating can provide a coating speed of ~ 2 m/min for the

deposition of TEs and electron/hole transport materials, whereas a much lower speed is adopted for the deposition of active materials.[558,559]

Inkjet printing employs printers that propel ink droplets on target substrate in a drop-on-demand manner, which is typically controlled with a computer program. Typically, the ink is pushed out of the nozzle by the piezoelectric printhead, but sometimes thermal printhead is adopted for forcing the ink to drop out of the nozzle by heat. Many different kinds of inkjet printers have been utilized for the deposition of active layers and electrodes for different types of solar cells in recent years.[34,560,561,562] The optimization of the surface wettability of the inks is critical for successful inkjet printing of uniform films.[563,564] Meanwhile, adjusting the viscosity of the inks to the "printable range" is also very important for successful inkjet printing.[565,566]

Screen printing is a commonly used low-cost printing technique for advertising, textiles and clothing, and printed electronics.[567-570] The screen is a mesh aperture that has part of the area to be ink-impermeable by the blocking stencil. The ink is pressed onto the target substrate by the squeegee (or blade) through the permeable areas, forming ink patterns on the selected areas. The screen printing system requires no delicate printing head or nozzle, but only a patterned silkscreen (typically polyester), a squeegee, and a holder. As a result, the equipment cost of screen printing is much lower than that of other printing techniques for solar cells. Besides, screen printing is a very high-throughput printing technique for solar cell fabrication. For example, the screen printing technique allows a throughput rate of 1,500 wafers per hour for the fabrication of Si selective

emitter solar cells.[571] The photovoltaic industry has adopted screen printing for the fabrication of silicon, CdS/CdTe solar cells for many years.[572,573]

Apart from the solution processes that are included in the dashed area in Figure 25, there has been some other R2R-compatible vacuum-free techniques for TE fabrication. Transfer printing is commonly adopted when the solution/ink of the material cannot be printed/coated on the target substrate directly. It is not exactly a "solution" process but is highly compatible with large-scale R2R fabrication. Figure 25 illustrates the transfer printing process of a TE thin film to target substrate. The TE film is firstly adhered or coated on the stamp, and then attached to the target substrate. The stamp is peeled-off from the substrate once the TE film has been released on the substrate.

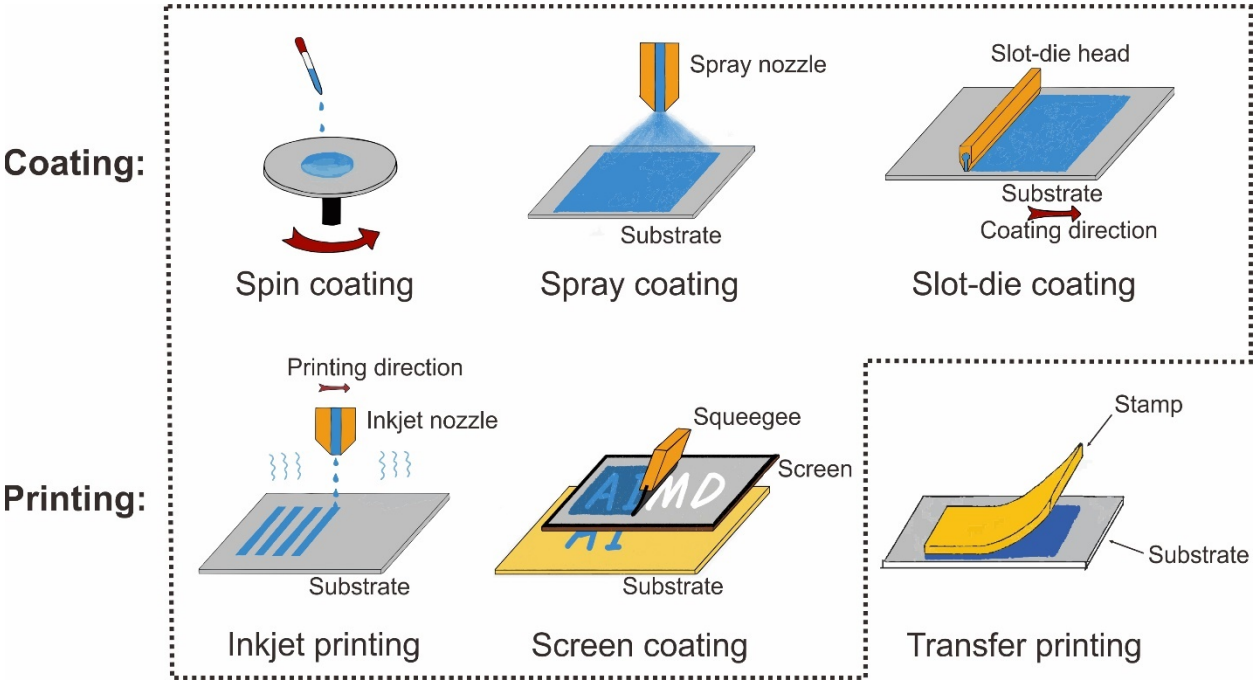

Figure 25. Typical coating and printing techniques for the fabrication of TEs of solar cells. The solution-based techniques are included in the dashed frame.

Table 3 compared the above-mentioned coating and printing technologies that are adopted for the deposition of TEs. Spin coating and spray coating are widely adopted for the lab-scale fabrication of thin-film solar cells since they only require simple equipment, and are easy to process. However, these technologies are not suitable for the industrial fabrication of solar modules because of the lack of scalability. In addition, spin coating wastes most of the raw materials, which is not acceptable for the industry. Other coating or printing technologies such as slot-die coating and screen printing are preferred by the industry for high throughput (> 10 m/min) and very low material waste.[574] Till now, fully printed organic solar modules have been available on the market for years, and high efficiency perovskite solar modules are expected to be on market very soon.[575,576] The following sections discuss the principles, advantages, and disadvantages of commonly used solution-based coating or printing techniques such as spin coating, spray coating, slot-die coating, inkjet printing, and screen printing for TEs of thin-film solar cells. For some specific applications, the R2R-processable transfer printing technique is employed. Apart from these techniques, some other solution-based methods such as electrospinning, self-assembly, doctor blading, flexographic printing, and etc. have been reported for the fabrication of TEs.[577-580]

Table 3. Comparison of typical coating or printing techniques that are adopted for the fabrication of solution-processed TEs.

Coating/ Printing Technique	Largest Reported Area	Film Thickness	Film Uniformity	Scalability	Material Utilization	Commonly Used Materials	Ref.
Spin Coating	5×5 cm	nanoscale	good	poor	< 5%	PEDOT:PSS, AgNW, rGO, TiO_2	581,582
Spray Coating	21×30 cm	nano- to microscale	good	limited	15~98%	AgNW, CNT, PEDOT:PSS, TiO_2	583,584
Slot-Die Coating	N.A.	nano- to microscale	good	good	very high	PEDOT:PSS	585
Inkjet Printing	N.A.	nano- to microscale	limited	good	very high	PEDOT:PSS, AgNP, AgNW	586
Screen Printing	> 88 m^2	nano- to microscale	good	good	~50%	PEDOT:PSS, AgNP	574
Transfer Printing	N.A	nano- to microscale	good	good	very high	Graphene, PEDOT:PSS, AgNW	166

6.1 Spin Coating

One major advantage of the spin coating technique is the ability of conformal coating of thin and uniform films on flat substrates. This feature very compatible with the request of high-quality TEs because the thickness of TEs should be well-controlled for a balance between electrical conductivity and optical transmittance. **Figure 26A** shows the AFM topographic images of PEDOT:PSS film deposited via spin coating with different rotation rate, solution concentration, and annealing temperature. The results indicate that the solution concentration, spin speed, annealing temperature, and annealing time played an important role in final film morphology and thickness.[587] Another research also suggested the necessity of thermal annealing after spin-coating of PEDOT:PSS for higher conductivity and better work function-alignment.[135]

Sometimes the uniformity of spin-coated TEs is not ideal due to the limitations of the material itself. For example, AgNW shows good dispersibility in water, isopropanol and some other commonly used solvents, and thus can be spin-coated on many substrates for electrode applications. However, the spin-coated AgNW usually forms a nanomesh on top of the substrates, which shows too high roughness for bottom TE applications.[217] Leem et al. addressed this issue by spin-coating a thick layer (200 nm) of the TiO_x buffer layer atop the AgNW to obtain a relatively uniform and smooth film, as shown in Figure 26B. The nanostructured TiO_x also served as an electron transporter for the inverted OSCs.[588] Apart from the roughness issue, the weak adhesion between AgNW and the substrates may lead to mechanical failure of devices, especially for flexible solar cells. Recently, Lee et al. reported AZO/AgNW/AZO sandwiched TEs fabricated via spin coating (Figure 26C). The AZO nanoparticles were obtained via a combustion sol-gel method, which provided better crystallinity compared with the traditional sol-gel method (Figure 26D). The spin-

coated AZO layer not only smoothened the surface of the AgNW but also protected the AgNW from the corrosion of perovskite active material. The adhesion between the sandwiched electrode and the substrate was also good that the flexible PSC based on it showed very little efficiency loss after repeated bending.[110]

For carbon-based TEs, the optical transmittance of the films will decrease significantly as the thickness increases. For example, every single layer of graphene (atomic level thickness) absorbs 2.3% of white light.[589] As a result, the thickness of graphene-based TEs should be very low to ensure sufficient optical transparency. Spin coating is an effective approach to obtaining a few nanometer-thick graphene thin films apart from the transfer printing technique. In 2008, Wu et al. reported OSCs based on spin-coated graphene TEs for the first time. The thickness of graphene films can be as thin as 3.1 nm after chemical reduction.[160] The unsatisfactory solar cell efficiency caused by the poor electrical conductivity of the thin rGO film can be addressed by mixing it with CNT to form a conductive nanocomposite. Figure 26E and F show the synthesis of rGO/CNT nanocomposite via solution process, and the AFM image of a spin-coated composite TE film, respectively. The spin-coated nanocomposite TEs exhibited good optical transmittance of > 80% while maintaining a decent R_{sh} of 600 Ω/□ (Figure 26G and H).[114]

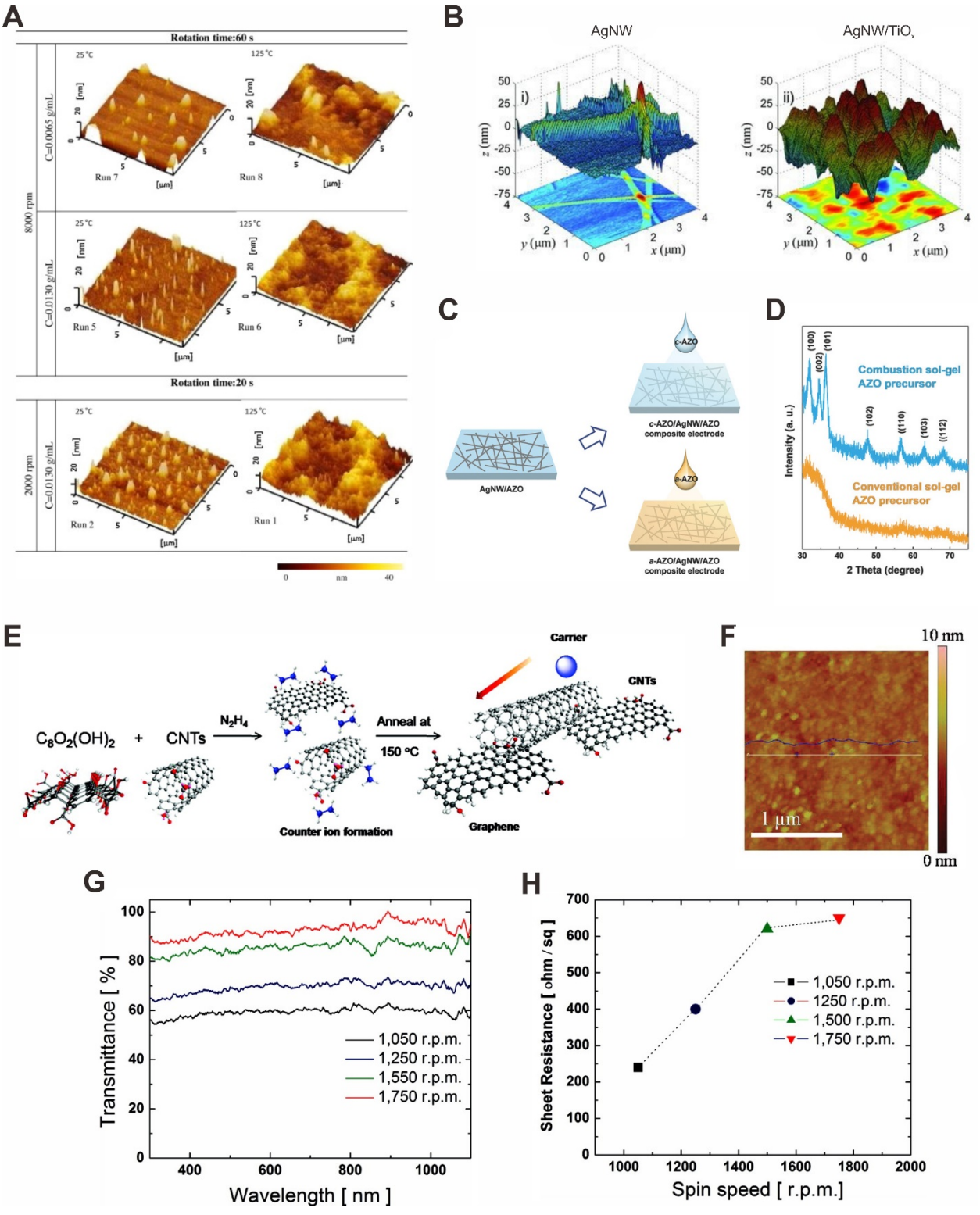

Figure 26. (A) AFM topographic images of spin-coated PEDOT:PSS films with different concentrations, spin speed and annealing temperature. Adapted with permission from Ref[587].

Copyright 2015 Elsevier B.V. (B) AFM topographic images of AgNW TEs with and without the TiO_x buffer layer. Reproduced with permission from Ref[588]. Copyright 2011 WILEY-VCH Verlag GmbH & Co. KGaA, Weinheim. (C) Schematics and (D) XRD patterns of AZO/AgNW/AZO composite TEs deposited via spin coating. Reproduced with permission from Ref[110]. Copyright 2017 WILEY-VCH Verlag GmbH & Co. KGaA, Weinheim. (E) Schematics, (F) AFM image, (G) optical transmittance, and (H) sheet resistance of rGO/CNT composite TEs fabricated via spin coating. Reproduced with permission from Ref[114]. Copyright 2009 American Chemical Society.

There are some limitations of the spin coating technique for the fabrication of TEs of thin-film solar cells. First, spin coating is material-wasting because most of the solution is spun-off. Considering that the material cost of TEs takes up a large part of the entire price of the raw materials of thin-film solar cell modules, the large amount of material waste caused by spin coating is not acceptable for large-scale fabrication, even if some may be recylced.[244,590] Second, the uniformity of spin-coated TEs is usually sensitive to substrate cleanness, humidity, spin speed, and etc. All these limitations will further increase the manufacturing cost of TEs via spin coating.[591,592] Third, spin coating on a large substrate is technically challenging. On one hand, it is difficult to hold a large substrate with a high spinning speed. The thickness of thin films at various locations over a large substrate is also different because of the difference of localized centrifugation speed.

6.2 Spray Coating

Compared with other solution-based coating technologies, the major advantage of spray coating is the ability of conformal deposition of materials on arbitrary surfaces. **Figure 27A** and B show

fiber-based organic photodetector based on PEDOT:PSS TE, which was deposited via spray coating of a PEDOT:PSS solution. The curved optical fiber substrate made it impossible to deposit uniform TE via spin coating, which is only applicable to smooth planar substrates. On the contrary, the uniform 140 nm-thick PEDOT:PSS film with > 90% optical transmittance and < 400 Ω/□ sheet resistance can be obtained via spray coating.[593] For other rough surfaces such as AgNW-coated glass substrate, direct spin-coating of PEDOT:PSS solution may also lead to non-uniform surface coverage. Thus, spray-coating PEDOT:PSS atop the AgNW film is a better choice for fabricating PEDOT:PSS/AgNW composite TE for planar solar cells.[594] Figure 27C shows the AFM image of a spray-coated AgNW film as the top TE for semi-transparent OSCs. The spray-coated AgNW top TEs exhibited a very low R_{sh} of < 10 Ω/□, resulting in a high fill factor of > 60% for the semi-transparent OSCs (Figure 27D).[102] Apart from PEDOT:PSS and AgNW, GO water dispersion is also suitable for spray coating. It can be reduced to graphene during spray coating when doped with a reductant such as hydrazine.[595] As a result, spray coating is regarded as a cost-effective approach to deposition graphene counter electrodes for DSSCs.[596] Whereas spray pyrolysis has become a conventional method for the deposition of the TiO_2 compact layer for DSSCs, TCOs for other thin-film solar cells can also be deposited via spray pyrolysis.[597,598] Apart from smooth and condense TCO films, spray coating is also capable for the deposition of nanostructured TCO films. Figure 27E introduces an electrospray system that is used for depositing nanostructured ZnO and AZO films for PSCs. A high voltage power supply system was incorporated with the spray coating system to adjust the morphology of ZnO or AZO films. The morphology of resulted films showed high dependence on deposition conditions such as applied voltage, annealing temperature, flow rate, substrate-to-nozzle distance, and deposition time.[599] Besides, the nanostructured TCOs can also be synthesized via the spray coating of a mixture of TCO precursor/nanoparticle and polymer

scaffold.[600] Figure 27F shows the schematics for the deposition of mesoporous TiO_2 electrodes for DSSCs via spray coating. The TiO_2 nanoparticles which were either pre-synthesized or synthesized in the mixed solution formed micelles with a block copolymer of polystyrene (PS) and poly(ethylene oxide) (PEO). The spray-coated TiO_2/PS-*b*-PEO film turned to a mesoporous TiO_2 film after the calcination process.

Similar to spin coating, the spray coating of TEs has the scalability issue when compared with other solution-based coating or printing technologies. For example, the printing speed is only 6 cm/min for an organic active material along the x-axis, which is very slow compared with other R2R processes.[601] As a result, spray coating is barely used for the fabrication of large-area thin-film solar modules.[22]

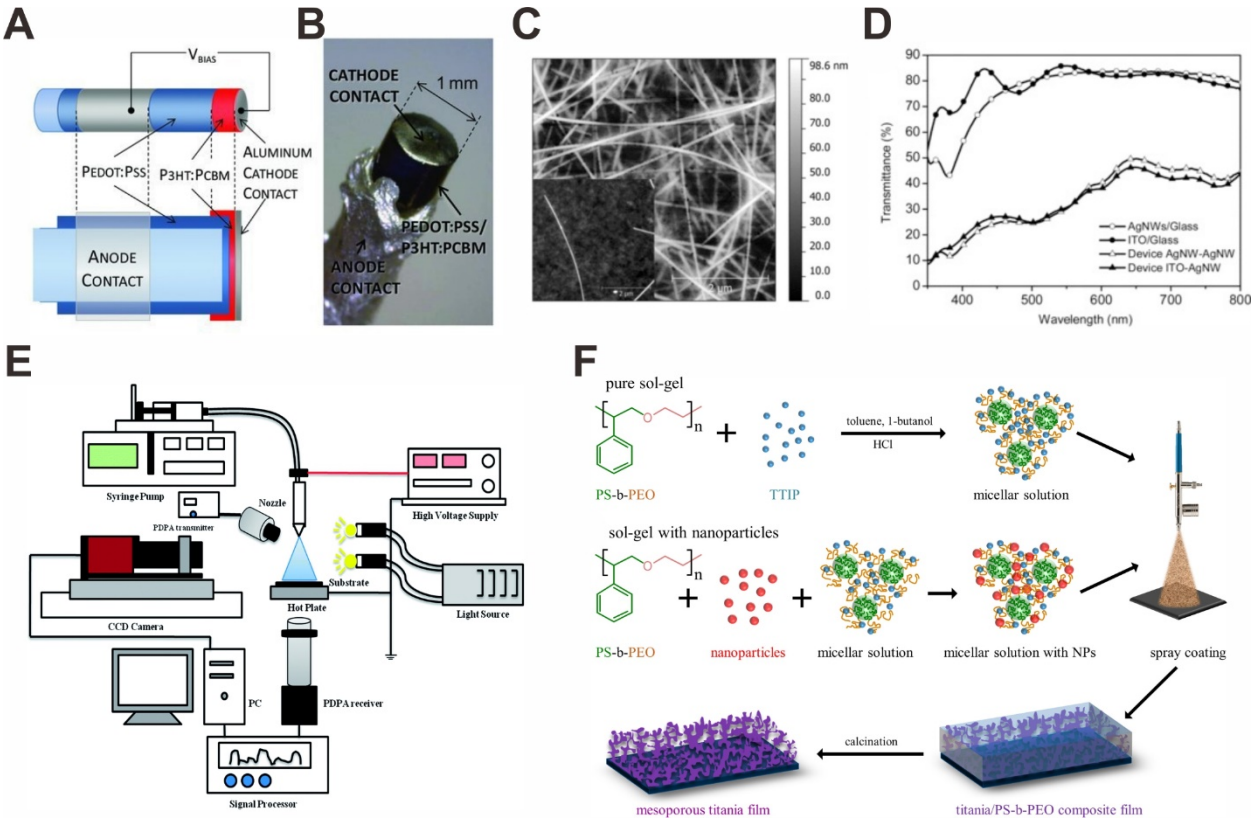

Figure 27. (A) Schematics and (B) photograph of fiber-shaped organic photodetector fabricated via spray coating. Reproduced with permission from Ref[593]. Copyright 2013 WILEY-VCH Verlag GmbH & Co. KGaA, Weinheim. (C) AFM image, and (D) optical transmittance of semi-transparent OSC with spray-coated AgNW top electrode. Reproduced with permission from Ref[102]. Copyright 2013 WILEY-VCH Verlag GmbH & Co. KGaA, Weinheim. (E) Schematics of an electrospray system with a high voltage supply to control film morphology. Reproduced with permission from Ref[599]. Copyright 2014 The Royal Society of Chemistry. (F) Schematics of the deposition of mesoporous TiO_2 electrodes via spray coating of TiO_2/PS-*b*-PEO micellar solution. Reproduced with permission Ref[602]. Copyright 2017 Elsevier Ltd.

6.3 Slot-Die Coating

Figure 28A and B show the roller slot-die coating system that was used to fabricate flexible organic LEDs.[603] The coating system employs a material-saving small slot-die head, which is suitable for the deposition of expensive active materials. The surface roughness of anodic interface for a 2 × 2 μm area was 20 nm, such roughness is higher than typical results of spin-coated or spray-coated films (Figure 28C).[603] Despite the relatively high surface roughness, the scalability of slot-die coating is significantly higher than that of spin coating and spray coating. Figure 28D shows flexible large-area organic solar modules with an active area of 1 cm^2 for every single solar cell. The organic active material and the PEDOT:PSS TEs were both deposited via slot-die coating.[604] Another advantage of slot-die coating is the high utilization rate of the substrate area. The significant edge-to-center thickness variation caused by the spin coating process is negligible on slot-die coated films.[605] Thus, large-area organic solar modules with a 98.5% geometric fill factor were fabricated by combining slot-die-coating with fast laser patterning, as shown in Figure 28E.[606]

The most frequently used ink for slot-die coating of TEs is the water solution of PEDOT:PSS, which is similar to that for spin-coated and spray-coated TEs. However, the R2R processing feature of slot-die coating provides the opportunity for *in-situ* studying of PEDOT:PSS film formation mechanism. Figure 28F shows an *in-situ* grazing incidence wide-angle X-ray scattering (GIWAXS) setup that is incorporated with a slot-die coating system. The time-resolved data of GIWAXS indicate different solvent evaporation and crystallization mechanism for pristine PEDOT:PSS, ED-doped PEDOT:PSS, and PEDOT:PSS post-treated by EG. The EG doping of post-treatment was found helpful for reducing the π-π stacking distance between PEDOT chains,

which strengthens the interchain coupling and thus results in higher electrical conductivity.[607] The R2R slot-die coating has been found compatible with other conductive inks such as graphene, CNT, and AgNW.[558,608,609] Figure 28G compares a R2R-coated ZnO/PEDOT:PSS/Ag grid/PET flextrode (left) and a slot-die coated ZnO/AgNW/PET TE (right). The optical transmittance of optimized AgNW TE was 10% higher than that of the flextrode, and the R_{sh} of the AgNW TE (10 ~ 20 Ω/□) was lower than that of commercial ITO/PET. The superior optical transmittance of slot-die coated AgNW TEs resulted in higher efficiency of organic tandem solar cells compared with the flextrode-based solar cells.[610] Recently, Jeong et al. optimized the solvent, concentration, and flow rate of AgNW solution for large-area slot-die coating on PET substrate for the touch panel application. By adjusting the flow rate of AgNW ink, the R_{sh} and optical transmittance of the AgNW films fell within the range of 12.9 ~ 149 Ω/□ and 77.3 ~ 92.2%, respectively. The surface roughness of the AgNW TE was reduced after a calendaring process. In principle, such optimized AgNW films are also promising for solar cell applications.[611]

The limitation of slot-die coating includes 1) the strict requirement of rheology of the inks of slot-die coating for high-quality thin films.[612,613] and 2) the high-density coating defects such as ribbing, rivulet, and dripping phenomena may occur, which damage the uniformity of the coated films.[614]

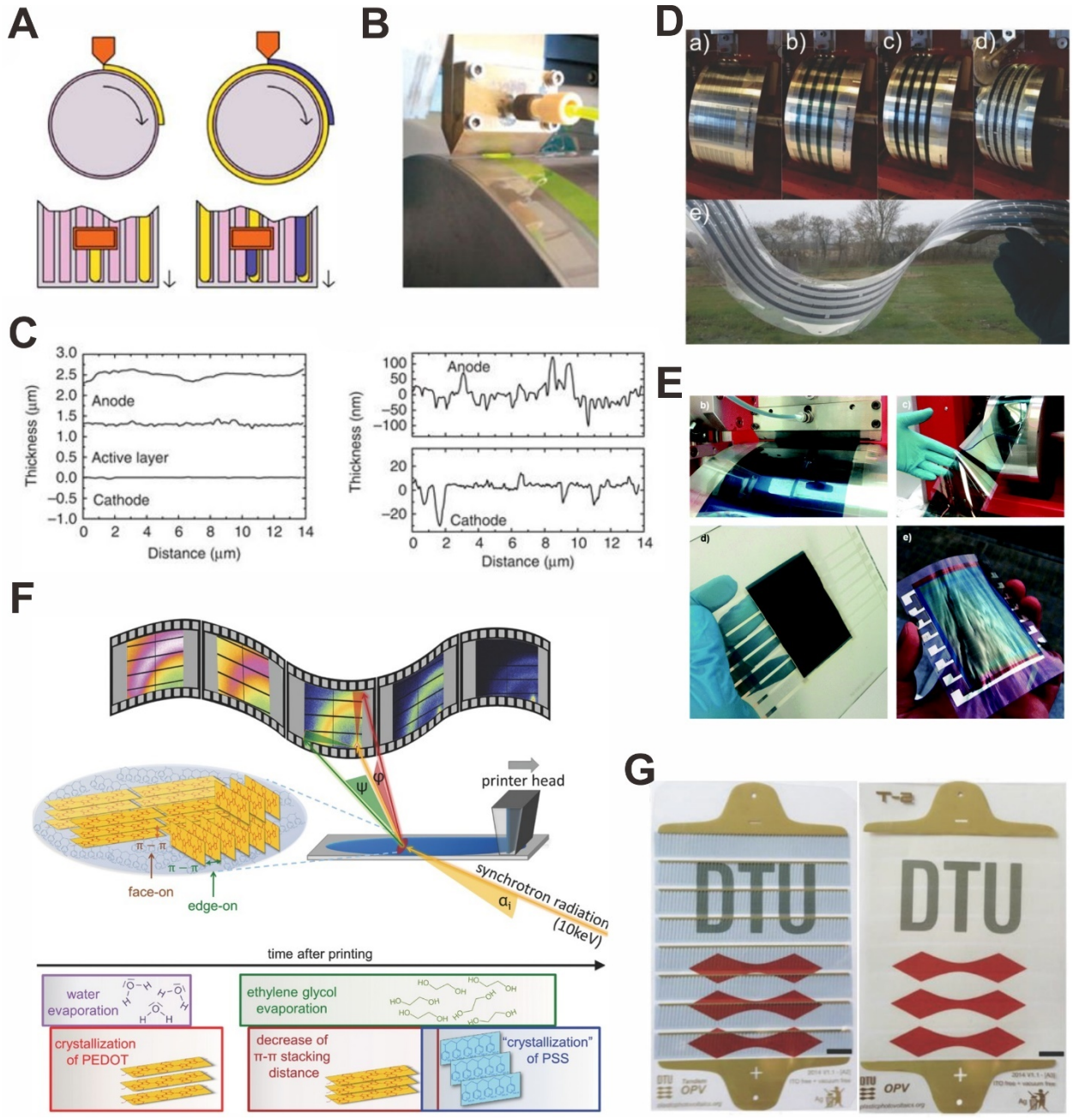

Figure 28. (A) Schematics and (B) photographs of roller slot-die coating system for OLED module fabrication, and (C) the surface topography of slot-die coated films. Reproduced with permission from Ref[603]. Copyright 2012 Springer Nature. (D) Large-area flexible organic solar modules with slot-die coated PEDOT:PSS TEs. Reproduced with permission from Ref[604]. Copyright 2016 The Authors. Published by WILEY‐VCH Verlag GmbH & Co. KGaA, Weinheim. (E) Slot-die coated

organic solar modules with high geometric fill factor. Reproduced with permission from Ref[606]. Copyright 2016 The Royal Society of Chemistry. (F) A R2R slot-die coating system integrating with an *in-situ* GIWAXS system that tracks the crystalline data of PEDOT:PSS film in real-time. Reproduced with permission from Ref[607]. Copyright 2015 WILEY-VCH Verlag GmbH & Co. KGaA, Weinheim. (G) large-area R2R-printed flextrode (left) and slot-die coated ZnO/AgNW TE on PET substrate. Reproduced with permission from Ref[610]. Copyright 2015 WILEY-VCH Verlag GmbH & Co. KGaA, Weinheim.

6.4 Inkjet Printing

One of the features of the inkjet printing technique is the direct printing of high-resolution patterns without the lithography process. **Figure 29A** shows a large-area OSC with inkjet-printed Ag current collecting grids. The printed Ag grids only covered 8% of the surface area thanks to the fine width (~ 160 μm) of the printed grid lines. The thickness of printed Ag grid lines was > 2,000 nm, which induced too large height difference for the spin-coating of PEDOT:PSS TE and active material (Figure 29B). This problem can be solved by embedding the Ag grids into an additional barrier layer. The large-area OSCs with PEDOT:PSS/Ag grid TEs exhibited superior photovoltaic performance compared with that of ITO-based control device thanks to the very low sheet resistance (1 Ω/□) of the inkjet-printed Ag grids.[216]

Inkjet printing is also an effective approach to producing large-area continuous TE films. Figure 29C and D show solution-processed OSC with inkjet-printed PEDOT:PSS TE, ZnO electron transport layer (ETL), and P3HT:PCBM active material. The films exhibited good uniformity over

the entire area, resulting in a good photovoltaic performance for large-area solar cells (Figure 29E). There was a surface coverage issue of inkjet-printed ZnO films atop the PEDOT:PSS TEs. Such problem has been overcome by repeated printing of multiple ZnO layers.[615]

One major challenge for obtaining smooth inkjet-printed thin films is the coffee-ring effect, which originates from the capillary flow during the solvent drying process.[616,617] However, such effect can be helpful for fabrication TEs with specific ring patterns.[618] Figure 29F shows a CNT transparent conductive film with connected ring structures, which was formed by printing the CNT dispersion on a heated PET substrate. The diameter and height of the CNT rings were found relevant to the temperature of the substrate, and a post-annealing process can further reduce the R_{sh} of the CNT films.[619] GO and few-layered graphene oxide (FGO) can also be inkjet-printed for TE applications. Huang et al. reported inkjet-printed GO and FGO patterns on PI, PET, and paper for electrical circuit and chemical sensor applications. For the polymeric substrates, simple surface treatment with PSS and PEI was conducted before the inkjet printing of GO and FGO to improve the wetting of the inks.[620]

Another category of promising inkjet-printable material is the TCO dispersion or precursor solution. The solution-processed TCOs always show limited electrical conductivity due to poor crystallinity, which can be improved to a certain degree by post-sintering processes.[621] Jeong et al. addressed this issue by sandwiching Ag grids between two layers of inkjet-printed ITO TEs. Figure 29G and H show the optical and SEM images of inkjet-printed ITO/Ag grids/ITO composite TEs. The participation of Ag grids reduced the R_{sh} of the TE significantly to 2.86 Ω/□ while maintaining

an optical transmittance of 74.06%. Such result is even better than that of commercial vacuum-deposited ITO/glass TEs.[112]

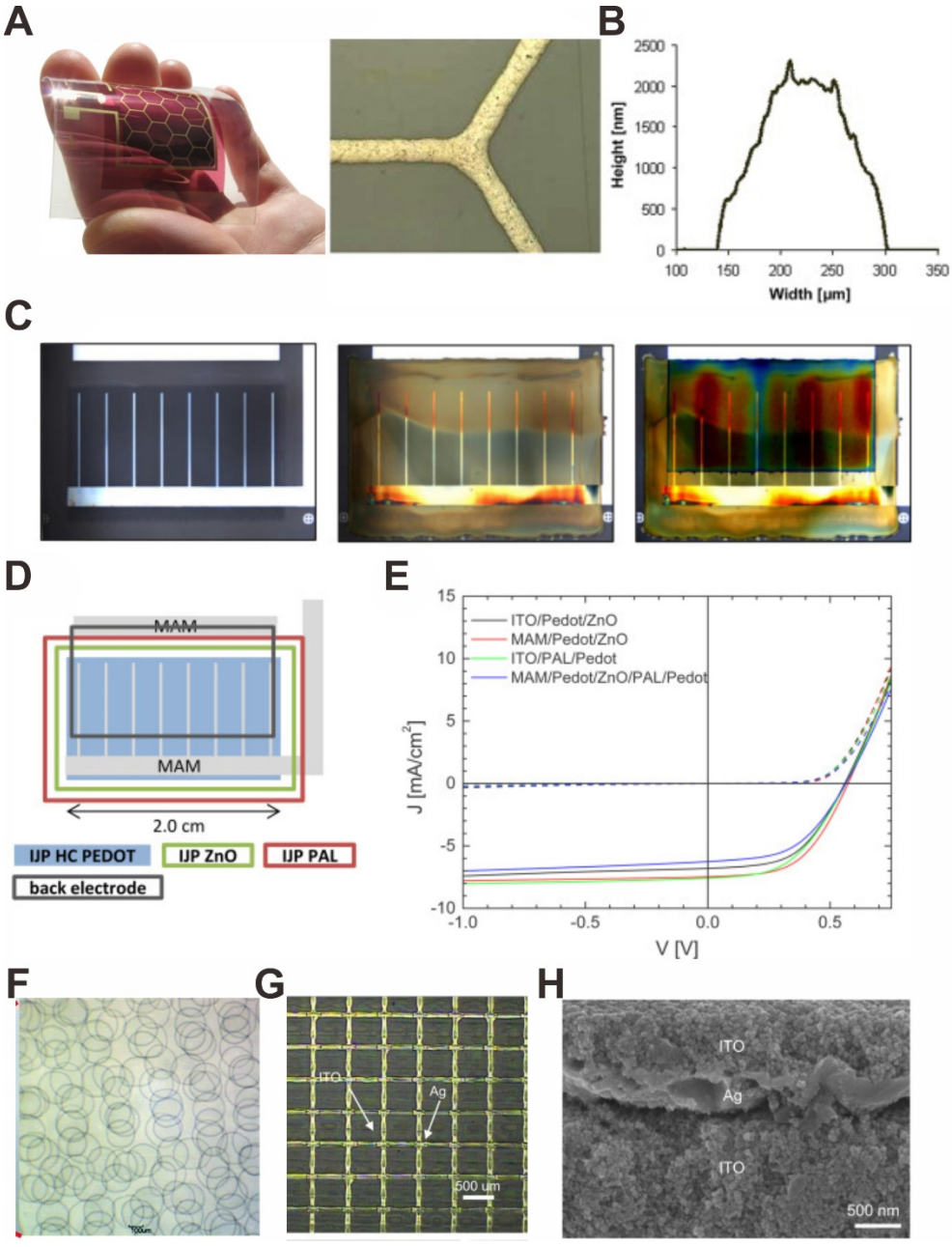

Figure 29. (A) Optical images and (B) surface profile of inkjet-printed Ag current collecting grids for flexible OSCs. Reproduced with permission from Ref[216]. Copyright 2010 Elsevier B.V. (C)

Optical images with inkjet-printed PEDOT:PSS TE, ZnO ETL, and P3HT:PCBM active layer. (D) Schematics and (E) J-V curves of the fully printed OSCs. Reproduced with permission from Ref[615]. Copyright 2014 Elsevier B.V. (F) Flexible transparent conductive film constructed with connected "coffee rings" of CNTs. Reproduced with permission from Ref[619]. Copyright 2014 The Royal Society of Chemistry. (G) optical and (H) SEM images of ITO/Ag grids/ITO composite TEs fabricated via inkjet printing. Reproduced with permission from Ref[112]. Copyright 2011 Elsevier B.V.

6.5 Screen Printing

Screen printing have attracted great attention for the fabrication of solution-processed thin-film solar cells in recent years. **Figure 30A** shows R2R-processed flexible organic solar modules with screen-printed ZnO ETLs, PEDOT:PSS TEs, and hole transport layers (HTLs). The highly efficient rotary screen printing system provided very fast printing speeds of > 10 m/min and 10 m/min for PEDOT:PSS films and ZnO films, respectively.[622] The screen-printed PEDOT:PSS can obtain an R_{sh} of 60 Ω/□ on PET substrates, which is comparable with that of ITO/PET TEs. The mesh structure of the screen aperture can be an advantage for TE fabrication because the mesh-structured TEs show higher optical transmittance than homogeneous thin films. Figure 30B and C depict the schematic of a screen printing process for mesh-structured PEDOT:PSS TEs, and the microscopic images of PEDOT:PSS meshes, respectively.[95] The PEDOT:PSS meshes with different width/period (W:T) ratios can be obtained by adjusting the mesh count, wire diameter, and photoresist thickness of the stainless steel mask. The OLED devices with such screen-printed PEDOT:PSS TEs showed a peak power efficiency of 1.83 lm/W and a peak current efficiency of 3.40 cd/A, which is comparable or better than that of ITO-based devices. The resolution of

traditional screen printing techniques is not so high, but the feature size can be improved to ~ 30 μm by a modified screen-offset technique.[623] Figure 30D shows screen-printed GO patterns on flexible PET substrate (left), which was further reduced to rGO (right) with HI under moderate conditions. Such a method provided a facile approach to producing large-scale patterned graphene TEs with hundreds of nanometer thickness (Figure 30E).[624] Apart from PEDOT:PSS and graphene materials, screen printing is also adopted for the deposition of TiO_2 TEs for DSSCs.[35] For optimal solar cell performance, TiO_2 nanocrystals with different particle sizes can be printed for electrode and light scattering purposes.[625] The screen printing technique also provided a facile approach to obtaining stripe-type TEs, which improve the efficiency of large-area solar cells significantly compared with pain-type devices.[626]

Another feature of screen printing technique is the low dependence on the target surface because the highly viscous printed inks/pastes slow down both wetting and dewetting behaviors.[627,628] Figure 30F illustrates the structure of solution-processed OSC with printed Ag grids as TEs. Figure 30G compares the printed Ag grids on PEDOT:PSS top TEs with different printing techniques for the solution-processed TCO-free OSCs. The uniformity of flatbed screen-printed and rotary screen-printed Ag grids was much better than that of flexographic-printed and inkjet-printed grids, which suffered from a severe de-wetting issue in PEDOT:PSS surface. As a result, the OSCs with screen-printed Ag grids exhibited superior efficiency compared with flexographic-printed and inkjet-printed devices.[629]

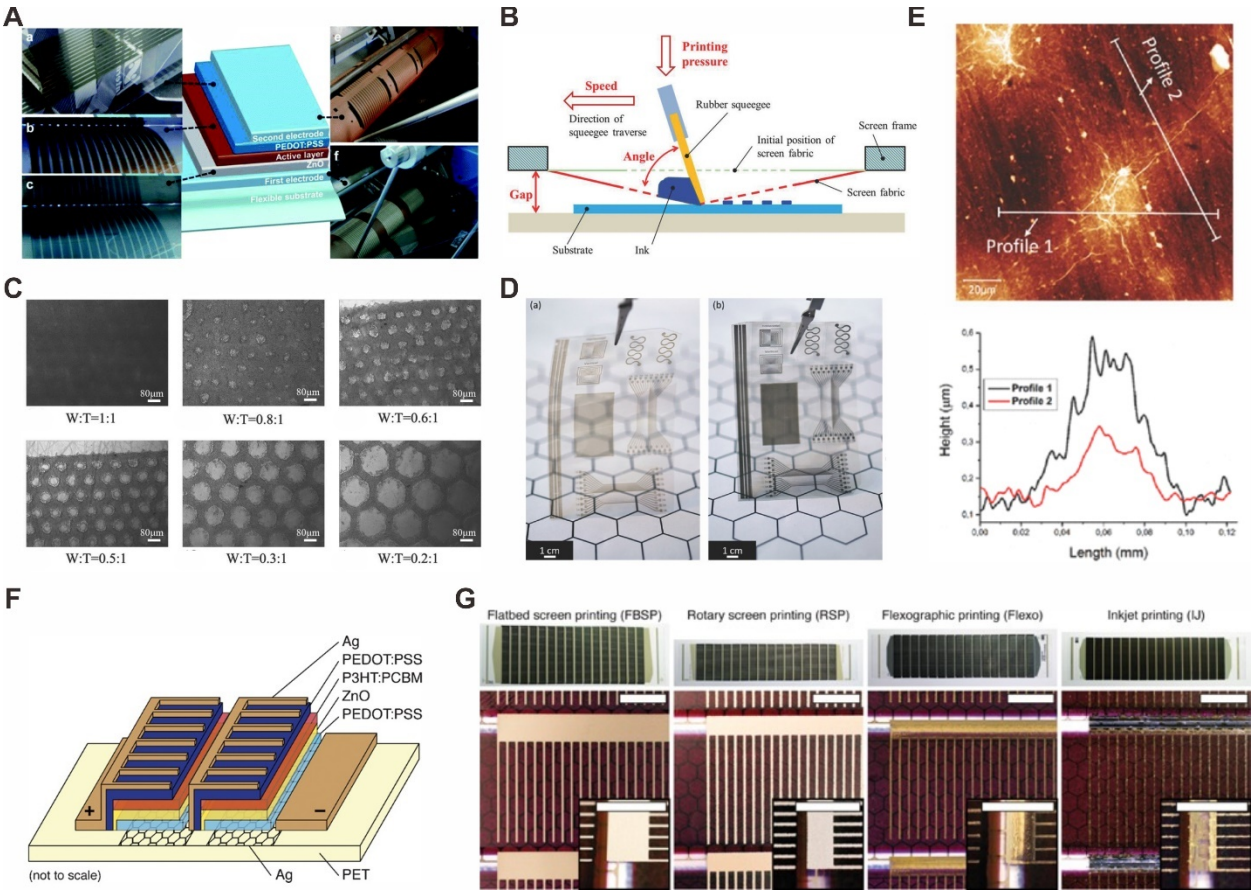

Figure 30. (A) R2R-processed organic solar modules with screen-printed PEDOT:PSS TEs. Reproduced with permission from Ref[622]. Copyright 2012 The Royal Society of Chemistry. (B) Schematics of the screen printing process of PEDOT:PSS meshes, and (C) microscopic images of screen-printed PEDOT:PSS meshes with different width/period ratios. Reproduced with permission from Ref[95]. Copyright 2018 WILEY-VCH Verlag GmbH & Co. KGaA, Weinheim. (D) Optical images of screen-printed GO (left) and rGO (right) films on PET substrate, and (E) AFM topographic image (top) and profile (bottom) of rGO grid line. Reproduced with permission from Ref[624]. Copyright 2017 WILEY-VCH Verlag GmbH & Co. KGaA, Weinheim. (F) Schematics of solution-processed organic solar modules, and (G) optical images of Ag grids printed with flatbed screen printing, rotary screen printing, flexographic printing, and inkjet printing on top

PEDOT:PSS TEs. Reproduced with permission from Ref[629]. Copyright 2013 WILEY-VCH Verlag GmbH & Co. KGaA, Weinheim.

6.6 Transfer Printing

High-quality graphene thin films are usually deposited on Cu or Ni foils via the CVD process.[630] For TE applications, the CVD graphene thin films have to be transfer-printed on either transparent substrates or the top of the devices. Suk et al. developed two versatile transfer printing methods to print CVD graphene on multiple substrates, as illustrated in **Figure 31A** and B. The graphene film was firstly protected by a spin-coated PMMA thin film, followed by an etching process in $FeCl_3$ to remove the underlying Cu foil. The PMMA-protected graphene film was then either picked up with a polydimethylsiloxane (PDMS) stamp to laminate on the target substrate or scooped up with the target substrate directly.[631] For large-scale production, an R2R transfer printing technique has been developed for the fabrication of 30-inch large graphene TEs on flexible substrates. Such transfer-printed monolayer graphene showed a low R_{sh} of 125 Ω/□ and high optical transmittance of 97.4%, and thus are ideal candidates for solar cell applications.[166] The optimized flexible PSC with transfer-printed graphene TE on polyethylene naphthalate (PEN) substrate exhibited a maximum efficiency ~ 17%, and the device was very robust under repeated bending at a small radius of 2 mm thanks to the ultrahigh flexibility of graphene.[632] Recently, Heo et al. reported > 18% efficiency flexible PSCs with bis(trifluoromethanesulfonyl)-amide (TFSA)-doped graphene TEs, whose efficiency is one of the highest among all-reported flexible PSCs.[109]

However, such a “wet” transfer printing technique is limited for the deposition of graphene top TEs for PSCs because the perovskite materials are very sensitive to moisture.[633] You et al. developed a transfer-printable graphene/PEDOT:PSS composite electrodes for semi-transparent PSCs as top TEs, and the device structure is illustrated in Figure 31C. The D-sorbitol doped PEDOT:PSS not only reduced the R_{sh} of the TEs from > 1,000 Ω/□ to < 200 Ω/□, but also served as a binder to improve the contact between graphene and N2,N2,N2′,N2′,N7,N7,N7′,N7′-octakis(4-methoxyphenyl)-9,9′-spirobi[9H-fluorene]-2,2′,7,7′-tetramine (spiro-OMeTAD) HTL. The optimized devices employed double-layered graphene/PEDOT:PSS TEs, showing an efficiency of > 12% when illuminated from either FTO side or the composite TE side (Figure 31D).[111] The standalone PEDOT:PSS films can also be transfer-printed by a PDMS stamp. Such a transfer-printing technique overcomes the wettability issue of PEDOT:PSS solution/ink on hydrophobic materials, generating more possibilities for top-illuminated device architectures. For example, Wang et al. reported transfer-printable PEDOT:PSS TEs deposited on PDMS stamps via VPP as top TEs for OSCs in 2012.[634] Later in 2013, Gupta et al. reported top-illuminated OSCs with transfer-printed PEDOT:PSS TEs, which were spin-coated on PDMS stamps directly before transfer.[635]

In Section 3, we have introduced the effect of strong acid treatment for improving the electrical conductivity of PEDOT:PSS TEs. A bonus of such acid treatment is the impaired adhesion between PEDOT:PSS and substrates, which results from the removal of PSS. In 2015, Kim et al. reported transfer-printed highly conductive PEDOT:PSS TEs by making use of the weakened adhesion between acid-treated PEDOT:PSS and the substrate. The PEDOT:PSS films were peeled-off by PDMS stamps directly after treating with concentrated H_2SO_4. The transfer-printed

PEDOT:PSS TEs served as bottom TEs for OSCs, resulting in an efficiency of 7.7% which was slightly higher than that of ITO-based control device.[157] Such facile transfer-printing technique is ideal for the fabrication of top-illuminated PSCs, as it avoids the degradation of perovskite active materials caused by PEDOT:PSS solution. In 2017, a fully solution-based approach to obtain TCO-free semi-transparent PSCs was report (Figure 31E). The PSCs employed HNO_3-treated PEDOT:PSS as both top and bottom TEs. Figure 31F shows a SEM cross-sectional image that suggests a conformable contact between the transfer-printed PEDOT:PSS and the spiro-OMeTAD HTL. The HNO_3 treatment reduced the R_{sh} of PEDOT:PSS films from megaohm scale to < 40 Ω/□, and the PEDOT:PSS films can be transfer-printed after the treatment as well. Such a transfer-printing process required only < 70 °C for successful printing on top of the spiro-OMeTAD HTL of the PSCs, so the performance of the device would not be influenced by the printing process.[636]

Another well-studied transfer-printable material for TEs is the AgNW thin film, which typically shows very poor adhesion to substrates. The weak adhesion between AgNW films and substrates makes it very easy to pick the AgNW films up with the PDMS or other polymeric stamps.[637,638] The superior conductivity and high optical transmittance of transfer-printed AgNW TEs guarantee the high efficiency of opaque and semi-transparent OSCs that is comparable to ITO-based devices.[631,639] For large-scale R2R fabrication, an adhesive layer is necessary for the lamination of high-quality AgNW TEs. For example, D. Spyropoulos et al. reported an R2R transfer-printing process of AgNW TEs on top of flexible organic and perovskite solar modules. A mixture of PEDOT:PSS solution and D-sorbitol served as a transparent conductive adhesive (TCA) for the AgNW TEs. The TCA improved the interfacial contact between AgNW and the active materials,

resulting in > 5% and > 9% efficiencies for semi-transparent organic and perovskite solar modules, respectively.[640]

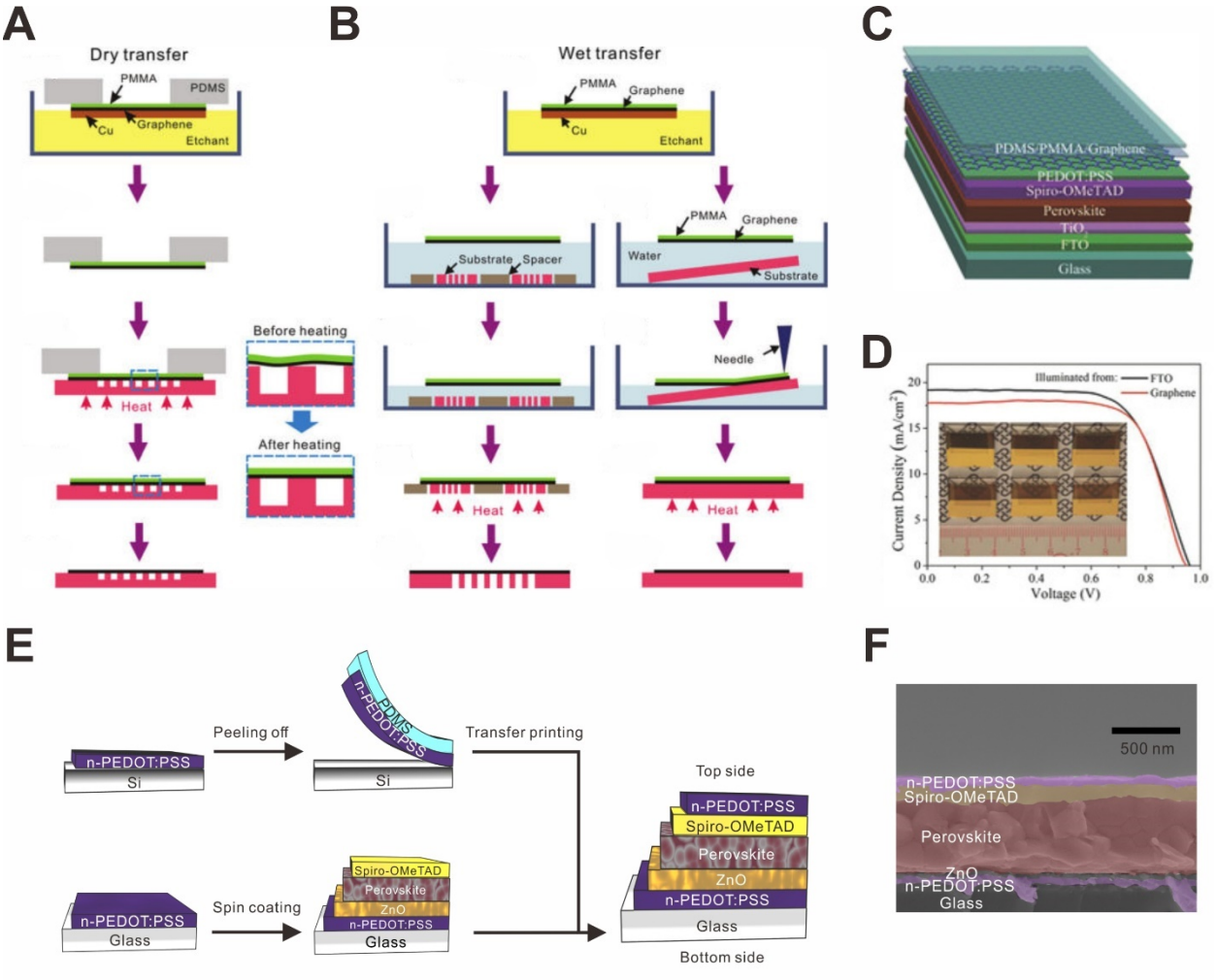

Figure 31. Schematics of (A) dry and (B) wet transfer-printing process of graphene TEs on multiple substrates. Reproduced with permission from Ref[631]. Copyright 2011 American Chemical Society. (C) Schematics and (D) J-V curves of semi-transparent PSCs with transfer-printed graphene/PEDOT:PSS composite top TEs. Inset is the photograph of the semi-transparent devices. Reproduced with permission from Ref[111]. Copyright 2015 WILEY-VCH Verlag GmbH & Co. KGaA, Weinheim. (E) Fabrication process of fully solution-processed TCO-free semi-transparent PSC. (F) SEM cross-sectional image of theTCO-free semi-transparent PSC with HNO_3-treated

PEDOT:PSS as both top and bottom TEs. Reproduced with permission from Ref[636]. Copyright 2017 WILEY-VCH Verlag GmbH & Co. KGaA, Weinheim.

7. Applications on Emerging Thin-film Solar Cells

The solution-processed TEs are low-cost and highly scalable compared with traditional vacuum-deposited TCOs. However, such an advantage does not necessarily make them preferred substitutes for vacuum-deposited TCOs. In this section, we introduce and discuss the application of different solution-processed TEs on different thin-film solar cells. The flexible thin-film solar cells with solution-processed TEs are highlighted.

7.1 Organic Solar Cells

OSCs are thin-film photovoltaics that use photoactive semiconducting polymers or small organic molecules as active materials.[182,641] The progress in OSCs is very rapid recent years. The record efficiencies of OSCs have reached 16.5% and 17.3%, for single-junction and tandem solar cells, respectively.[145,642] Currently, the organic active layer is dominated by a BHJ type that consists of a blend of p-type electron donor and an n-type acceptor.[643,644] Photons are absorbed by the BHJ active material under illumination, generating bounded electron-hole pairs (i.e., excitons). The electrons and holes that dissociated from the excitons at the interfaces between donor and acceptor diffuse to the LUMO energy level of acceptor and the HOMO energy level of the donor, respectively (**Figure 32**). One advantage of organic active materials is the very high absorption coefficient ($> 1 \times 10^5$ cm^{-1}), which results in sufficient light absorption even at very low film thickness.[645,646] Besides, most of the reported organic active materials are soluble in common

solvents such as chlorobenzene, dichlorobenzene, and toluene, and thus are suitable for R2R solution coating and printing. As a result, the organic active materials are promising for large-scale R2R-printable solar modules.[647,648]

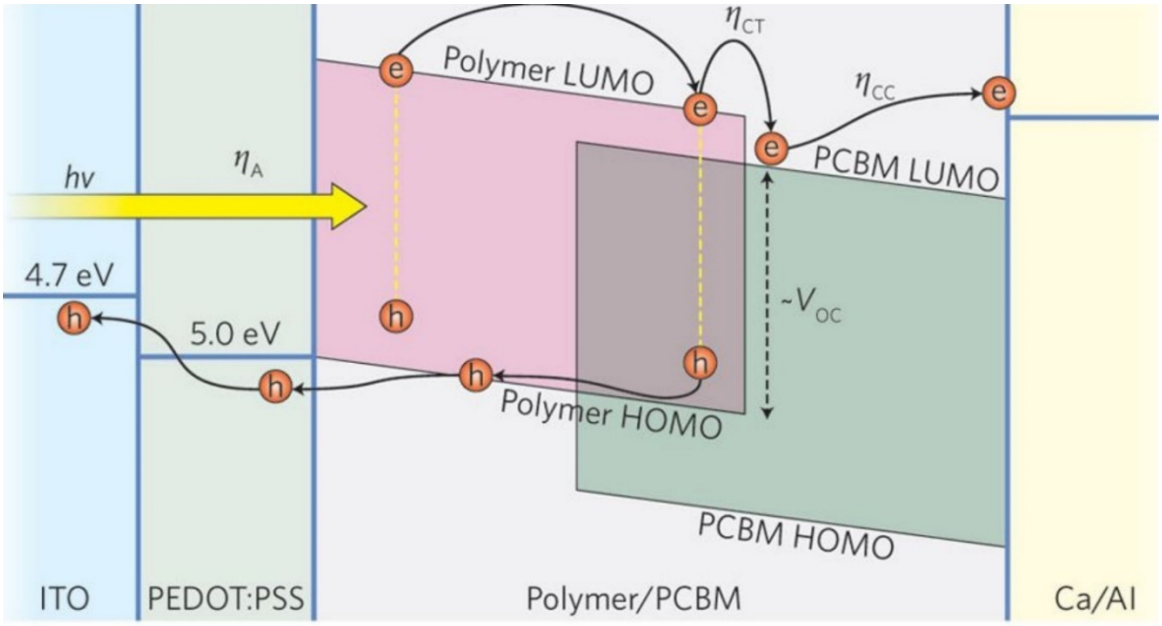

Figure 32. Exciton generation and charge separation mechanism of BHJ OSCs. Reproduced with permission from Ref[649]. Copyright 2012 Springer Nature.

The state-of-the-art OSCs with solution-processed TEs employ high FoM materials such as doped or post-treated PEDOT:PSS, AgNW, PEDOT:PSS/Ag meshes, and TCO/AgNW composites. Very recently, Peng et al. reported highly efficient solution-processed flexible OSCs with an efficiency of 12.35% with D-maltose doped PEDOT:PSS, which is comparable to the best-reported flexible OSC with vacuum-deposited ITO TEs.[650,651] **Figure 33A** and B show a sulfuric acid post-treated PEDOT:PSS TE and its application on solution-processed OSC. The 4,380 S/cm

conductivity of treated PEDOT:PSS TEs provide a comparable J-V performance of the OSCs to the ITO-based control devices (Figure 33C).[294] Even with this high conductivity, it is still considered not adequate for large-size solar modules.[652] Thus, further reducing the serial resistance caused by PEDOT:PSS is important for fully solution-processed organic solar modules. One commonly adopted method is incorporating highly conductive transparent metal grids with PEDOT:PSS films. Ag grids are preferred as current collecting grids because of the high electrical conductivity of Ag metal (6.30×10^9 S/cm), and the ease of solution-based coating or printing.[653] Figure 33D shows a photograph of large-scale fully printed organic solar modules consisting of 16,000 serial-connected OSCs. The solar modules employed flexo-printed Ag grids and rotary screen-printed PEDOT:PSS TEs as bottom electrodes, and rotary screen-printed PEDOT:PSS and Ag grids as top electrodes. The 80 m-long solar modules exhibited a V_{OC} of 8.12 kV under full sun illumination, and > 1.5% overall PCE was obtained for 1,856 serial-connected cells (Figure 33E).[654] The ease of large-scale printing makes the combination of Ag grids and PEDOT:PSS very promising for the industrialization of large-area low-cost organic solar modules. However, the hygroscopic nature of PEDOT:PSS films may accelerate the degradation rate of the OSCs based on PEDOT:PSS TEs or HTLs. Despite the stability issue can also be by doping of post-treatment which partly remove the hydrophilic PSS moieties, the long-term stability of PEDOT:PSS TE-based OSCs remains to be studied.[245,655-657]

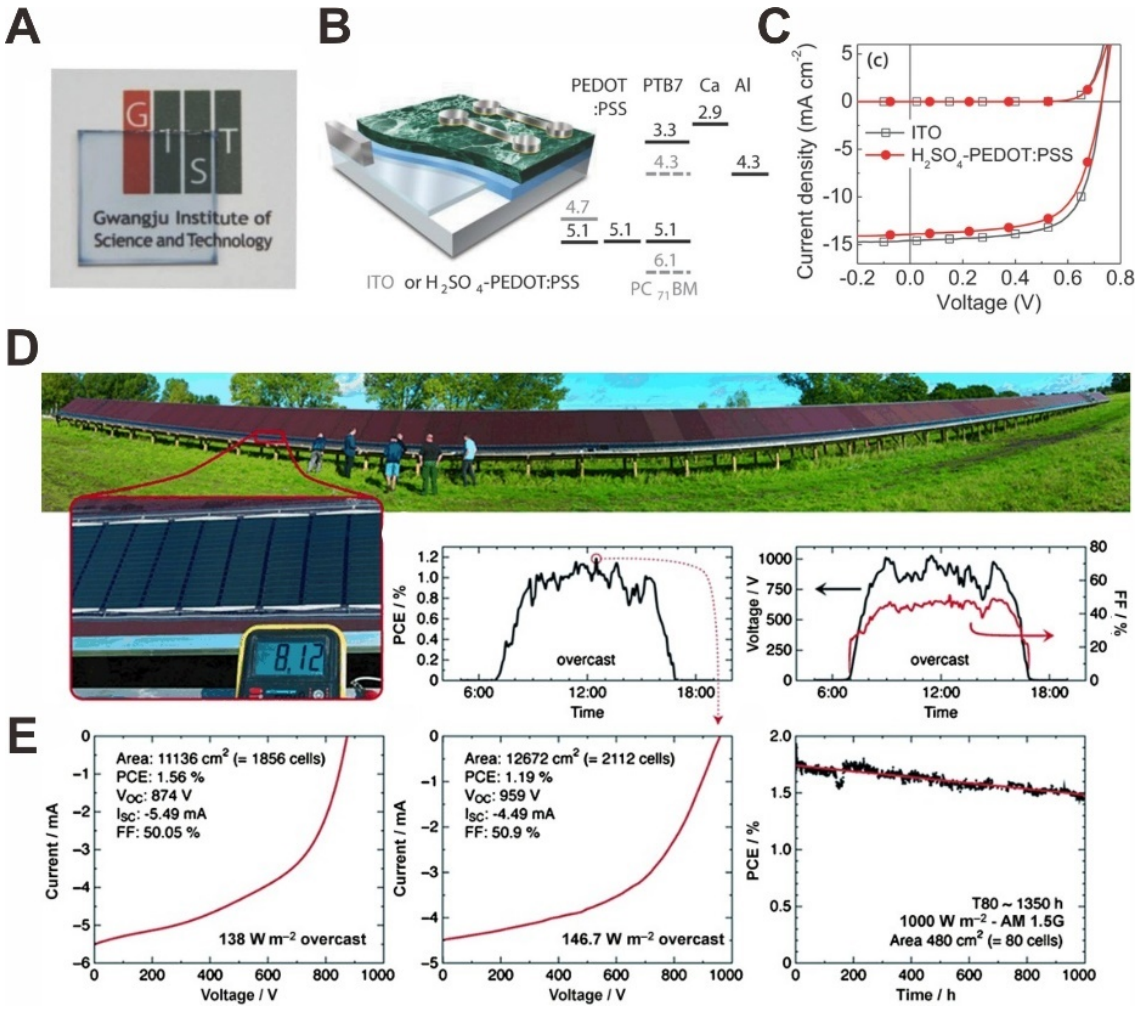

Figure 33. (A) Sulfuric acid-treated PEDOT:PSS film as TEs for solution-processed OSCs. (B) Schematics and energy diagram of the solar cell, and (C) J-V curves of the solution-processed device compared with the ITO-based control device. Reproduced with permission from Ref[294]. Copyright 2014 American Chemical Society. (D) Photograph of 80 m-long organic solar modules with printed PEDOT:PSS/Ag grid TEs as both top and bottom TEs. (E) The J-V curves and PCE of different areas of the solar module. Reproduced with permission from Ref[654]. Copyright 2013 WILEY-VCH Verlag GmbH & Co. KGaA, Weinheim.

Nano- or micro-scale meshes consisted of AgNWs are ideal for small-area OSCs as they show very high FoM that is even superior to that of vacuum-deposited ITO (Table 1). However, AgNW films are rarely used as bottom TEs for OSCs alone due to the roughness issue, as mentioned in previous sections. In real practice, AgNW films are combined either with high work function conducting polymers as anodes or with low work function TCOs as cathodes.[658,659] **Figure 34A** and B illustrate the structure and J-V curve of a solution-processed OSC with PEDOT:PSS/AgNW anode. Another layer of PEDOT:PSS was coated on top of the composite TE as an HTL. The doping ratio of PEDOT:PSS and the thickness of the composite electrode were optimized to obtain an optimum balance between conductivity and transmittance. In the meantime, the surface roughness of the TEs has been found relevant to the doping ratio of PEDOT:PSS solution. The optimized OSC on flexible PET substrate showed a PCE > 10%, which is comparable to a rigid control device on ITO/glass substrate.[660] For cathode applications, AgNW TEs are often combined with TCOs such as ITO, AZO, and ZnO.[162,579,661] Figure 34C shows an example combining AgNW and ZnO together as high-performance cathodes for solution-processed OSCs. The ZnO thin films not only smoothened the surface of AgNW TEs, but also functioned as an ETL for efficient charge separation of the OSCs (Figure 34D). A multi-length scaled structure which further improves the FoM of AgNW films was adopted for the AgNW TEs.[662] The patterned AgNW TEs allowed more light to pass through, and thus resulted in a higher PCE of the OSCs (9.02%) compared with that of plain AgNW-based OSCs (8.55%).[663] For top TE applications, the AgNW films can be spray-coated on top of the devices directly as the roughness issue of AgNW films becomes less prominent for top-illuminated devices.[664,665] Figure 34E illustrates a semi-transparent OSC with inkjet-printed AgNW TE as the top electrode. The doctor-bladed phosphomolybdic acid (PMA):PEDOT:PSS composite HTL ensured good wettability of AgNW dispersion for spray

coating. Such fabrication method is versatile for different active materials (P3HT:$PC_{61}BM$, PTB7-Th:$PC_{71}BM$, or PffBT4T-2OD:$PC_{71}BM$) with different deposition process (spin coating or doctor blading). The fully printed semi-transparent OSC with PTB7-Th:$PC_{71}BM$ active layer and AgNW top TEs showed > 5% PCE while maintaining > 50% average transmittance of 400 ~ 780 nm (Figure 34F).[666]

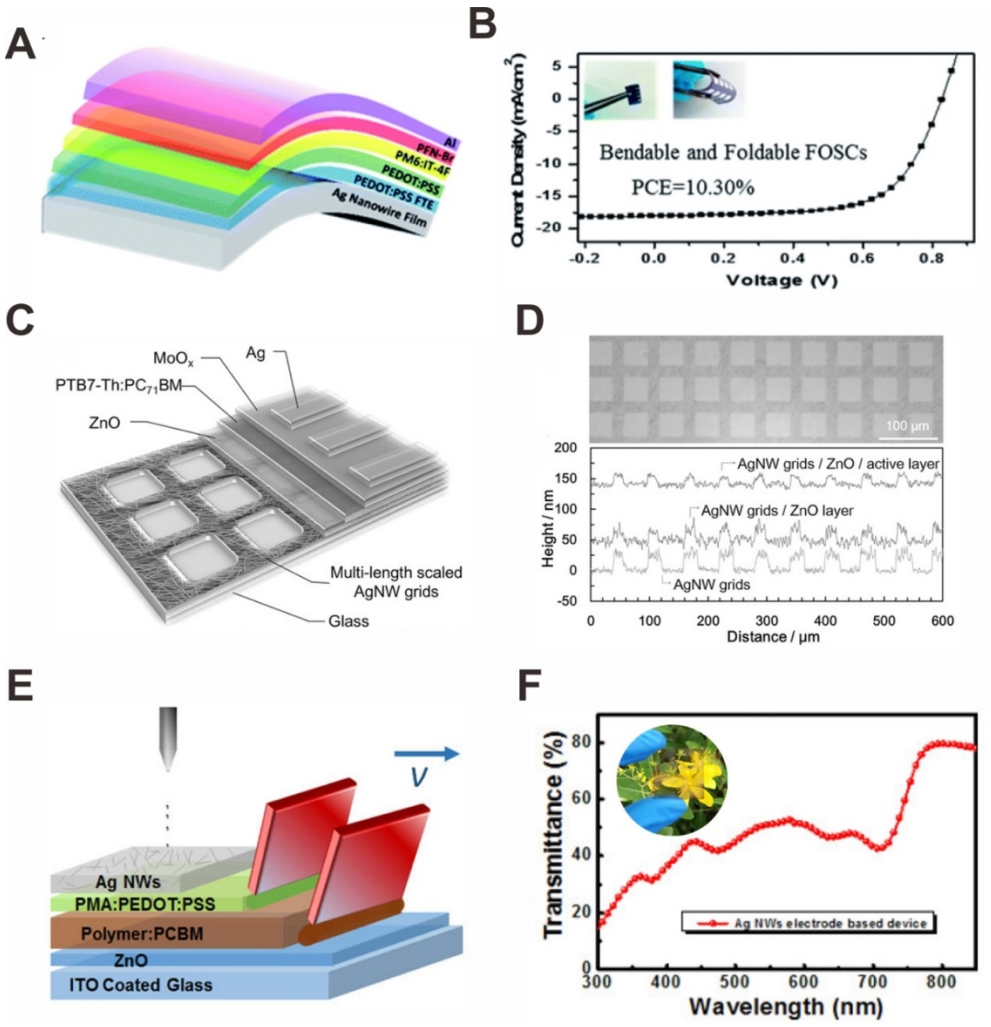

Figure 34. (A) Structure and (B) J-V curve of flexible OSC with PEEDOT:PSS/AgNW anode as TE. Adapted with permission from Ref[660]. Copyright 2019 The Royal Society of Chemistry. (C)

Structure of a solution-processed OSC with ZnO/AgNW cathode as TE. (C) Optical image and (D) surface profile of the AgNW mesh electrodes. Adapted with permission from Ref[663]. Copyright 2016 WILEY‐VCH Verlag GmbH & Co. KGaA, Weinheim. (E) Schematics of fully solution-processed semi-transparent OSC with spray-coated AgNW top TE. (F) The optical transmittance spectrum of the semi-transparent OSC from 300 to 850 nm. Inset shows a photograph of the semi-transparent device. Adapted with permission from Ref[666]. Copyright 2017 American Chemical Society.

The R2R processability of graphene has attracted great attention in the field of solution-processed OSCs.[74,160] However, the unsatisfactory conductivity of pristine graphene limits the efficiency of graphene TE-based OSCs. In 2011, Wang et al. reported 2.5% OSC with 4 layer-stacked graphene TE and MoO_3/PEDOT:PSS surface modification. The stacking of multi-layered graphene was realized by repeated wet-transfer printing of CVD graphene films.[667] Later on, tetracyanoquinodimethane (TCNQ) and PEDOT:PSS were combined with multiple-layered graphene TEs for higher electrical conductivity.[668,669] **Figure 35A** shows a graphene-based transparent cathode for inverted OSCs. The n-type graphene was obtained by spin-coating of a fluorocarbon surfactant (Zonyl) doped ZnO solution on top of the graphene TE. The surfactant improved the wettability of ZnO solution on the hydrophobic graphene surface, and thus increased the uniformity and smoothness of the ZnO film. Thanks to the ideal work function and high optical transmittance of the n-type graphene TEs, the PCE (7.5%) of OSCs made with graphene TEs was the same as that of ITO control devices.[670]

Apart from the transfer-printing of CVD graphene sheets, direct solution coating or printing of graphene or graphene derivatives is an approach to obtaining low-cost graphene TEs.[671-673] Figure 35B shows solution-processed graphene TEs by direct spray-coating a dispersion of graphene nanosheets. The graphene nanosheets were synthesized by a simple electrochemical exfoliation of graphite. The OSCs with spray-coated graphene TEs showed an efficiency of 4.23%. Although the performance of the spray-coated graphene TE was notably worse than that of CVD graphene due to limited conductivity, the electrochemical synthesis and spray coating process may significantly lower the cost of TEs.[674] The high optical transmittance feature of graphene is favorable for some specific applications such as "colorless" OSCs, which is promising for building-integrated photovoltaic devices.[675] Figure 35C shows the structure and photograph of colorless OSCs with graphene TEs as both top and bottom TEs. The graphene electrodes showed > 95% optical transmittance, resulting in a 69% transmittance at 550 nm for the entire OSC. Meanwhile, the full-graphene-TE-based OSCs showed PCE values of > 4% and > 3.7% on glass and PET substrates, respectively.[676]

Apart from graphene, CNTs are also promising carbon materials for OSC applications. For example, Jeon et al. demonstrated dry-deposited SWCNT as TE anode for OSCs, which showed PCE values of > 6% and ~ 4% for rigid and flexible devices, respectively.[677] Figure 35D illustrates R2R-processed CNT/PEDOT:PSS composite TEs and the OSCs based on them. The composite TEs were found significantly more conductive than pristine PEDOT:PSS films because the highly oriented CNT arrays enriched the pathways for efficient electron transport. As a result, the electrical conductivity and optical transmittance of the composite TE were comparable to those of vacuum deposited ITO electrode.[113] **Table 4** lists some of the best-reported OSCs with solution-

processed TEs. Note that the efficiency of OSCs is highly relevant to the active material, some solution processed TE-based OSCs with low-efficiency active materials (e.g., P3HT:PCBM) are not listed in the Table although their efficiencies are comparable or even higher than the ITO-based control devices.[125,245]

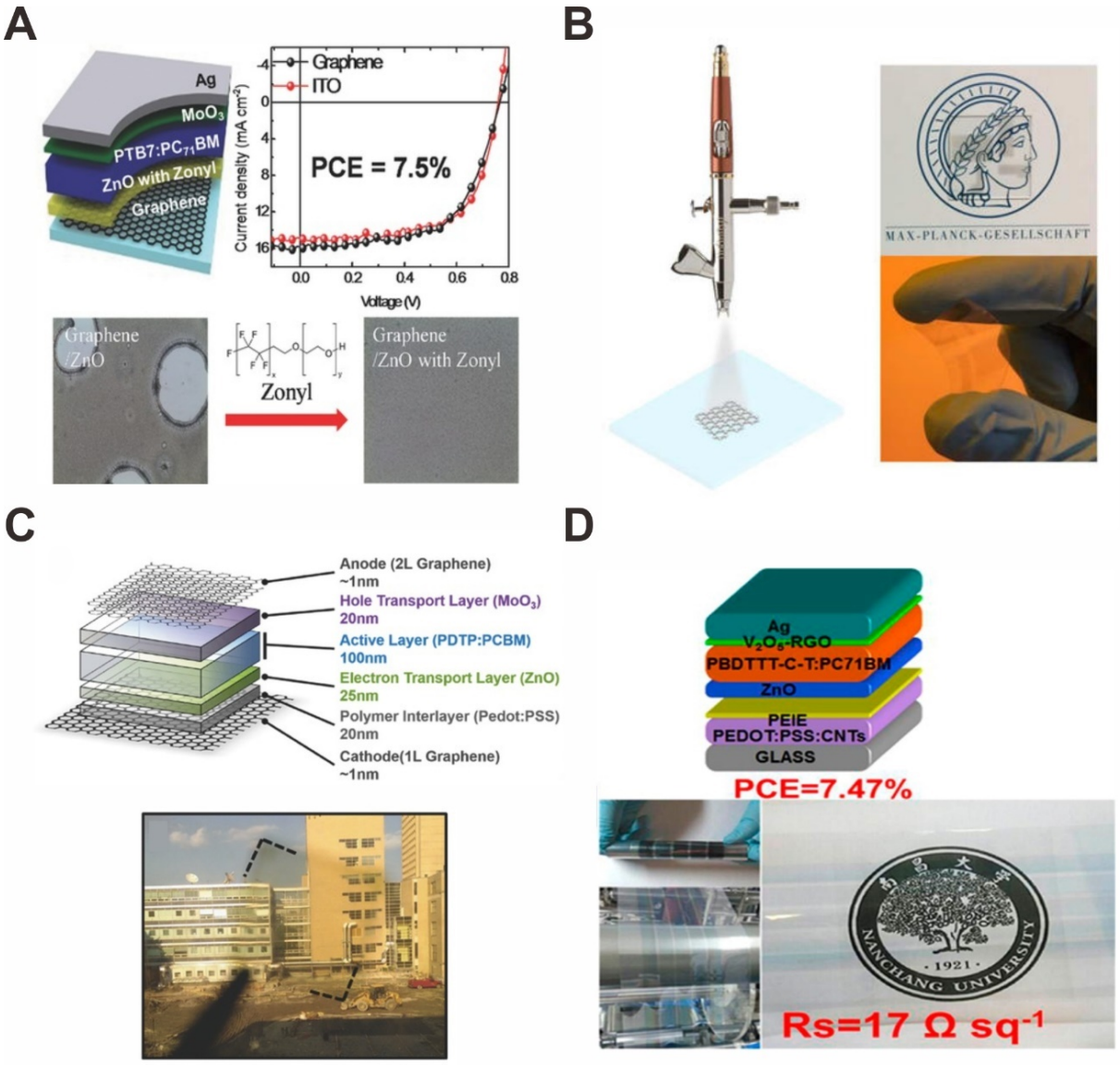

Figure 35. (A) Schematics (top left) and J-V curves of OSCs with solution-processed n-type graphene TE. The graphene film was deposited via wet-transfer printing of the CVD graphene sheet. Bottom image shows the effect of Zonyl surfactant for the uniform coating of ZnO on top of the graphene TEs. Reproduced with permission from Ref[670]. Copyright 2016 WILEY‐VCH Verlag GmbH & Co. KGaA, Weinheim. (B) Spray-coated graphene nanosheets as anode TEs for OSCs. The graphene nanosheets were synthesized by electrochemical exfoliation of graphite. Reproduced with permission from Ref[674]. Copyright 2017 American Chemical Society. (C) Schematics (top) and photograph (bottom) of neutral-color semi-transparent OSCs with graphene thin films as both top and bottom TEs. Adapted with permission from Ref[676]. Copyright 2016 WILEY-VCH Verlag GmbH & Co. KGaA, Weinheim. (D) Solution-processed OSCs with R2R-processed CNT/PEDOT:PSS composite TEs. Reproduced with permission from Ref[113]. Copyright 2014 American Chemical Society.

Table 4. Examples of highly efficient OSCs with solution-processed TEs.

TE	Processing Method	Active Material	V_{OC} (V)	J_{SC} (mA/cm^2)	FF (%)	PCE (%)	Ref.
PEDOT:PSS	Spin coating	PBDB-T-2Cl:IT-4F	0.885	19.13	72.92	12.35[a]	[650]
PEDOT:PSS/ AgNW	Spin coating	PM6:IT-4F	0.825	19.17	65.08	10.30[a]	[660]
PEDOT:PSS/ Embedded-Ag mesh	Spin coating /Nano-imprinting	PBDB-T:PTB7-Th:IHIC	0.74	20.48	67.54	10.20	[678]
PEDOT:PSS	Transfer printing	PTB7-Th:$PC_{71}BM$	0.77	14.22	70	7.7[a]	[157]
Graphene[b]	Transfer printing	SMPV1:PC_{71}BM, and PTTBDT-FTT:PC_{71}BM	1.56 ± 0.01	8.45 ± 0.02	64.32 ± 0.02	8.48 ± 0.01	[679]
Graphene	Transfer printing	PTB7:PC_{71}BM	0.72	14.1	69.5	7.1[a]	[680]
PEDOT:PSS/ CNT	Spin coating	PBDTTT-C-T:$PC_{71}BM$	0.77 ± 0.02	15.76 ± 0.62	61.97 ± 1.88	7.47 ± 0.66 (8.16[a])	[113]
rGO mesh// AgNW[c]	Spin coating/ Transfer printing	PSEHTT:IC_{60}BA and BDTT-DPP:$PC_{71}BM$	1.62	7.62	64.21	8.02[a]	[681]
PEDOT:PSS/ Ag grid	Spin coating/ Rod Coating	PTB7:$PC_{71}BM$	0.718	14.11	68.60	6.955[a]	[682]
AZO/AgNW	Doctor blading	PCDTBT:$PC_{71}BM$	0.88 ± 0.01	9.89 ± 0.33	61.29 ± 1.59	5.40 ± 0.14	[683]
ZnO/AgNW	Spin coating	PTB7-Th:$PC_{71}BM$	0.759 ± 0.016	17.8 ± 0.2	63.5 ± 0.7	8.58 (8.94[a])	[221]
ZnO/AgNW	Spin coating/ Nano-imprinting	PM6:IT4F	0.84	22.26	64.66	12.02[a]	[684]
ZnO/AgNW grid	Spin coating/ Photo-lithography	TB7-Th:$PC_{71}BM$	0.78	17.8	65	9.02[a]	[663]
ZnO/Ag nanomesh	Spin coating/ Transfer printing	PTB7:$PC_{71}BM$	0.74 ± 0.01	15.97 ± 0.09	61.37 ± 0.42	7.25 ± 0.14	[685]

[a]Champion device PCE. [b]Tandem cell. [c]Semi-transparent tandem cell.

7.2 Dye-Sensitized Solar Cells

DSSC is a non-conventional type of solar cell that utilizes dye sensitizer as the light absorber. The DSSCs have emerged as promising highly efficient thin-film solar cells when improved by O'Regan and Grätzel in 1991.[686] As illustrated in **Figure 36**, a typical Grätzel cell consists of TCO, working electrode, dye sensitizer, electrolyte, and a counter electrode. Unlike traditional solar cells using semiconductors as the absorber, photoexcited electrons are generated in the dye sensitizer from its HOMO to LUMO under light irradiation for DSSCs. The electrons are injected to the conduction band of the working electrode (e.g., TiO_2 nanoparticles) which the dye sensitizer is anchored on, followed by a regeneration process which reduces the oxidized dye sensitizer to its original state with the reducing component (e.g., I^-) of the redox couple (e.g., I_3^-/I^-) in the electrolyte. Finally, the oxidized component is reduced by the electrons from the external load at the counter electrode.[687] DSSCs are regarded as low-cost thin-film solar cells because the working electrode, dye sensitizer and electrolyte used for DSSCs are basically cheap materials. However, the conventional Grätzel cells require expensive vacuum-deposited TCOs and Pt islands for transparent electrodes and counter electrodes, so the large-scale production of DSSCs remains to be challenging.[688,689]

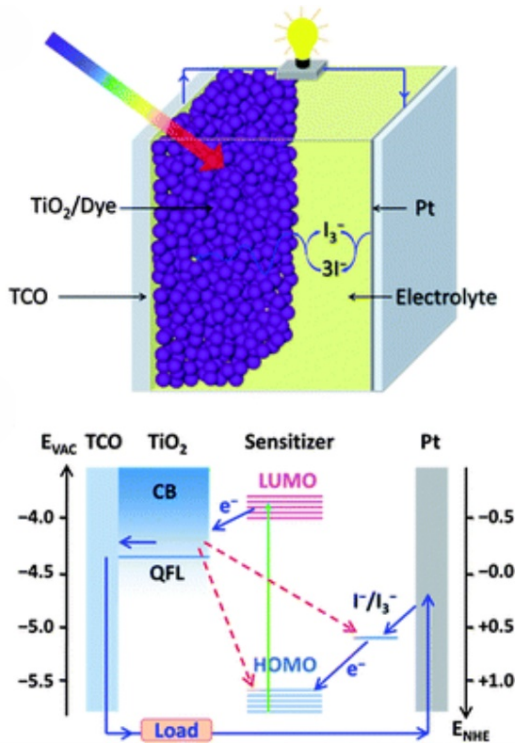

Figure 36. Structure (top) and charge transfer process (bottom) of a typical DSSC. Reproduced with permission from Ref[687]. Copyright 2013 The Royal Society of Chemistry.

To overcome the high-cost issue of vacuum-deposited TCO and Pt electrodes, efforts have been put on developing solution-processed TEs and Pt-free counter electrodes for DSSCs.[690-692] Conducting polymers such as PANI and PEDOT are good substitutes for Pt nanoparticles because of their high electrochemical activity.[332] **Figure 37A** shows the structure of DSSC with *in-situ* deposited PEDOT thin-film as the counter electrode. The cyclic voltammograms (CV) of the PEDOT and Pt films showed a higher reduction current density of PEDOT than Pt, indicating stronger electrochemical activity of the PEDOT electrodes (Figure 37B). In the meantime, the counter electrode was free from TCOs due to the good electrical conductivity of the PEDOT film (800 S/cm).[693] The post-treatment of PEDOT or PEDOT:PSS films may further improve the

efficiency of Pt/TCO-free DSSCs. Figure 37C and D show the structure and J-V curves of the DSSC with HNO_3-treated PEDOT:PSS counter electrodes, respectively. The thickness of the PEDOT:PSS films for counter electrode applications can be relatively thick because the light is normally illuminated from the other side. A thick (220 nm) HNO_3-treated PEDOT:PSS counter electrode exhibited a comparable R_{sh} (11 Ω/□) to that of Pt/FTO (7 Ω/□), resulting in a high efficiency (8.59%) of the Pt/FTO-free DSSC.[694] Other PTh derivatives such as poly(3,4-propylenedioxythiophene) (PProDOT) have been developed as efficient counter electrodes for Pt-free DSSCs.[695] For example, Yum et al. reported > 10 % efficiency Pt-free DSSCs using electrochemically polymerized nano-porous PProDOT counter electrodes.[696]

Apart from PTh derivatives, other conducting polymers such as PANI and PPy are competitive candidates for counter electrode applications owing to their good electrochemical properties.[332,349] Figure 37E depicts the structure of bifacial DSSC with chemically deposited micro-porous PANI counter electrodes. The chemically deposited PANI counter electrodes with 4-aminothiophenol (4-ATP) bridging agent exhibited superior electrochemical activity to electrochemically deposited PANI counter electrodes and Pt counter electrodes. Meanwhile, the optical transmittance of the PANI/4-ATP counter electrodes was much higher than that of electrochemically deposited PANI counter electrodes. As a result, the PCE of PANI/4-ATP counter electrode-based DSSC (8.35%) was much higher than that of control devices with chemically deposited PANI (5.90%) or Pt (7.44%) counter electrodes.[697] Oxidized PPy is another promising material for counter electrode applications because of its good conductivity, high optical transmittance, ease of synthesis, and good electrochemical activity.[698] Figure 37F compares the CV curves of chemically deposited PPy and vacuum-deposited Pt counter electrodes on FTO/glass substrates. The larger current density

of I_3^- reduction peak on CV curves indicated a lower charge-transfer resistance in the reaction of I_2/I^- redox for PPy counter electrodes. Hence, the PPy thin films were supposed to be better catalysts for the redox reaction in DSSCs than Pt islands. The higher PCE of PPy counter electrode-based DSSC (7.66%) than that of Pt counter electrode-based control device (6.90%) was an evidence of the superior electrocatalytic activity of PPy.[699]

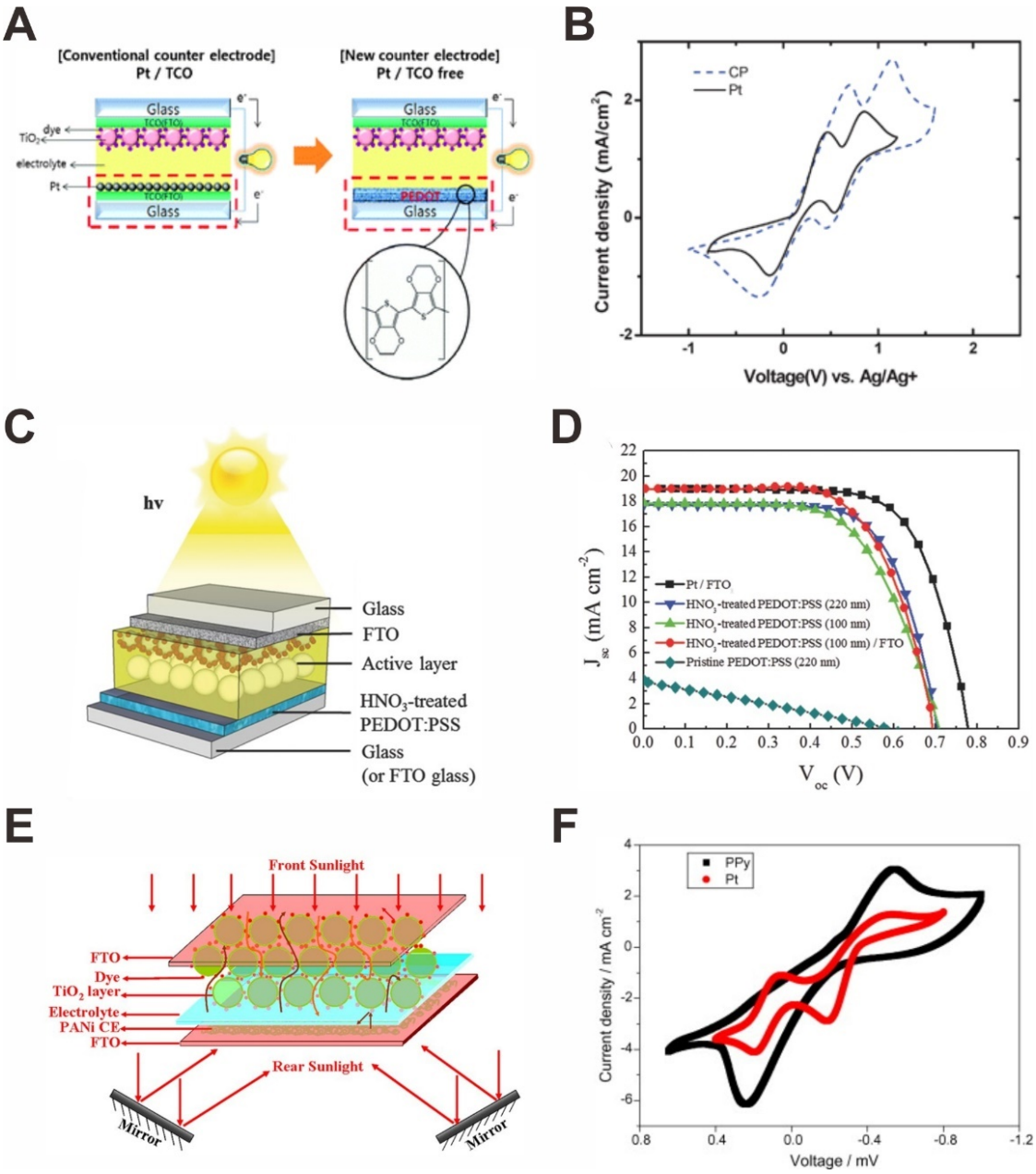

Figure 37. (A) Structure of PEDOT counter electrode-based DSSC, and (B) CV curves of PEDOT and Pt counter electrodes (bottom). Reproduced with permission from Ref[693]. Copyright 2010 The Royal Society of Chemistry. (C) Structure and (D) J-V curves of DSSC with HNO_3-treated PEDOT:PSS counter electrode. Reproduced with permission from Ref[694]. Copyright 2015 WILEY-VCH Verlag GmbH & Co. KGaA, Weinheim. (E) Schematics of bifacial DSSC with a

micro-porous PANI counter electrode. Reproduced with permission from Ref[697]. Copyright 2014 Jihuai Wu, Yan Li, Qunwei Tang, Gentian Yue, Jianming Lin, Miaoliang Huang and Lijian Meng. https://creativecommons.org/licenses/by/3.0/. (F) Comparison of CV curves of PPy counter electrode and Pt counter electrode. Reproduced with permission from Ref[699]. Copyright 2008 Published by Elsevier B.V.

Solution-processed metal oxides such as TiO_2 and ZnO are conventional photoanodes for DSSCs.[213,700,701] These metal oxide photoanodes are usually deposited on vacuum-deposited TCOs which serve as a current collector to improve the conductivity. Yoo et al. reported TCO-free flexible solid-state DSSC employing transfer-printed TiO_2 photoanode and spin-coated AgNW current collector, as illustrated in **Figure 38A**. The transfer printing process of TiO_2 avoided thermal-induced damage of flexible PEN substrate during the high-temperature annealing process of TiO_2. The spin-coated AgNW films functioned as a highly conductive back contact layer while providing sufficient porous paths for the infiltration of spiro-OMeTAD HTL into mesoporous TiO_2 electrodes. Figure 38B compares the J-V curves of solid-state DSSCs with TiO_2/FTO TE and AgNW/TiO_2 TE. The PCE of the TCO-free flexible solid-state DSSC was 3.36%, which was very high compared with other reported flexible solid-state DSSCs.[702-704] Solution-processed metal or metal compounds with high electrochemical activity are also investigated to replace Pt/FTO transparent counter electrodes for lower material and manufacturing cost.[705-707] For example, Pt-free DSSC with $NiSe_2$ counter electrode that was deposited via a hydrothermal method exhibited superior PCE (8.69%) to that of Pt-based device (8.04%).[708] Lin et al. reported a solution-based approach to depositing Ni_3S_2/Ni-P on flexible PI substrates for Pt/TCO-free DSSCs. The Ni-P film was deposited via electroless deposition (ELD), followed by an electrochemical oxidation process

and a chemical displacement to obtain Ni_3S_2/Ni-P bilayer counter electrodes. However, the Ni_3S_2/Ni-P bilayer counter electrode deposited via this method cannot function as TE because it is optically opaque.[709] Figure 38C illustrates the fabrication of free-standing transparent CuS nanosheet with the aid of an electro-spun polymer scaffold. A transparent Cu network was firstly obtained by depositing Cu thin film on an electro-spun polyvinyl alcohol (PVA) frame, followed by the etching of PVA, and then the chemical reaction between Cu and S which converted the Cu network to transparent CuS nanosheet. The CuS nanosheet TEs showed good electrical conductivity at high optical transmittance, as illustrated in Figure 38D. The high FoM and good electrochemical activity of CuS TE resulted in 6.38% PCE of the DSSC, which was 14% higher than that of the Pt/FTO control device.[710] For DSSCs using liquid electrolytes, the surface smoothness of the laminated top counter electrode is not very important compared with other thin-film solar cells. For example, FTO-free DSSCs with laminated W fabric as transparent counter electrodes have been demonstrated, showing a high PCE of 8.4% when illuminated under 1 Sun.[711]

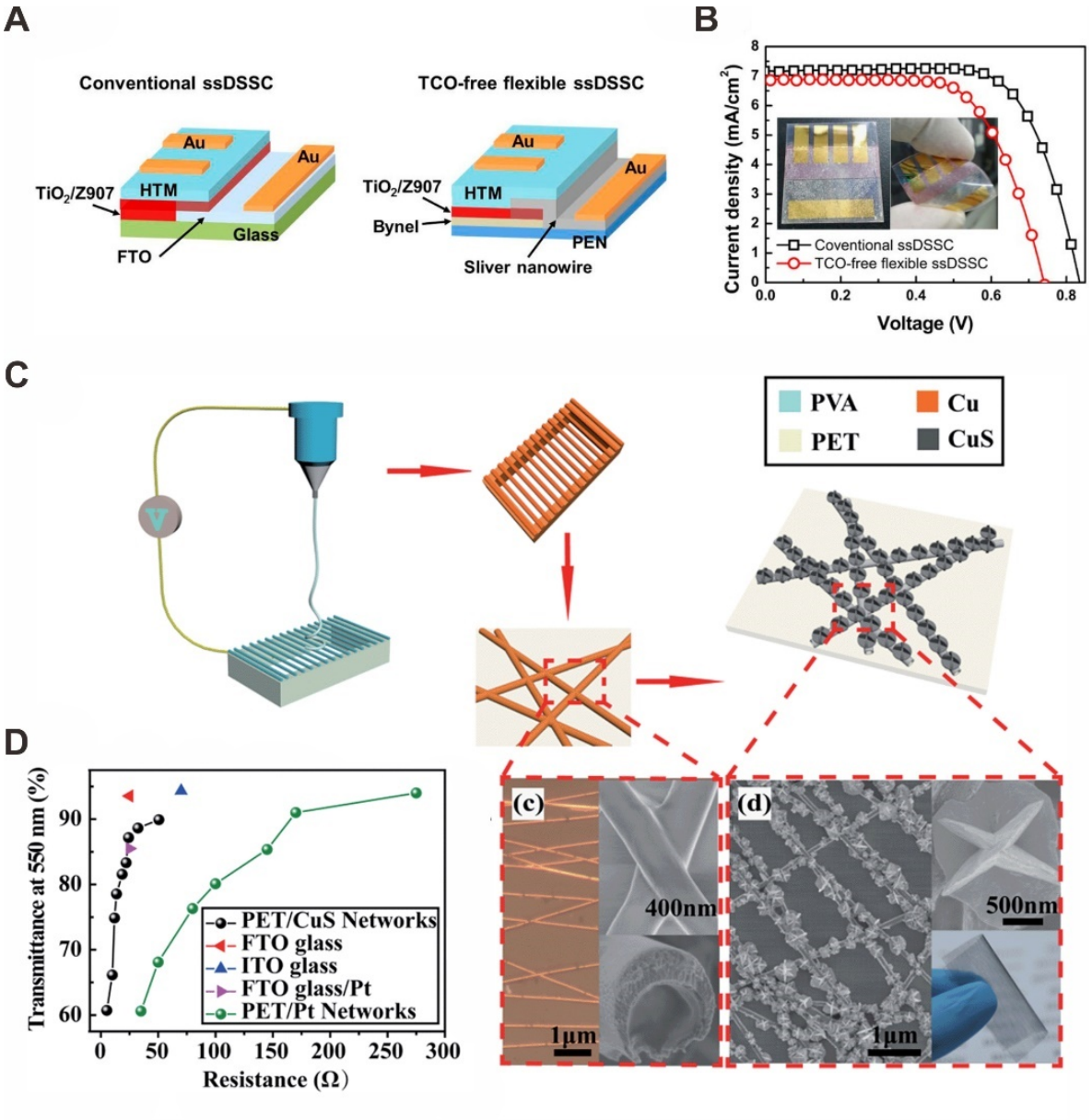

Figure 38. (A) Schematics of conventional solid-state DSSC and TCO-free solid-state DSSC with AgNW current collector, and (B) J-V curves of the DSSCs. Reproduced with permission from Ref[702]. Copyright 2015 American Chemical Society. (C) Schematics of the CuS nanosheet fabrication process, and optical/SEM images of the deposited Cu network and CuS nanosheet. (D) Optical transmittance (@550 nm) versus sheet resistance of the CuS TE and other control samples. Reproduced with permission from Ref[710]. Copyright 2016 The Royal Society of Chemistry.

The high surface area and good electrical conductivity of carbon materials show great advantages for counter electrode applications.[712,713] However, the dense carbon film consisted of carbon powders or particles is optically opaque, and thus is not suitable for transparent counter electrodes. Graphene is known for its high optical transmittance and good electrical conductivity. In addition, the ease of modifying graphene materials with functional groups is beneficial for counter electrode application because the catalytic activity of the graphene material can be improved by defects and oxygen-containing functional groups.[714,715] **Figure 39A** illustrates the synthesis of FeN/N-doped graphene nano-composite counter electrode for Pt-free DSSCs. The nano-composite was obtained by the chemical reaction between GO/$FeCl_3$ mixture and cyanamide. The FeN/N-doped graphene counter electrode offered a higher catalytic activity than both standalone N-doped graphene nanosheet and Pt counter electrodes. Figure 39B compares the J-V curves of DSSCs with 4 different counter electrodes, among which the FeN/N-doped graphene-based devices exhibited the highest short-circuit current density and fill factor. The 10.86% PCE of the composite counter electrode-based DSSC suggested the composite material to be promising low-cost and high-performance substitute for conventional Pt counter electrodes.[716] In general, CVD graphene exhibits inferior catalytic activity of the redox reaction to GO or doped GO due to less functional groups and defects. As a result, CVD graphene is usually incorporated with other high activity materials for counter electrode applications.[717] Figure 39C illustrates the fabrication process of PEDOT/graphene composite counter electrode for Pt/TCO-free DSSCs. The CVD graphene was transfer-printed onto PET substrate, followed by an N-doping process to improve the conductivity of graphene via HNO_3 post-treatment. The PEDOT film was synthesized on transfer-printed CVD graphene via *in-situ* polymerization. The graphene film not only improved the conductivity of the

transparent counter electrode, but also provided extra catalytic activity compared with standalone PEDOT film. Both factors contributed to the superior PCE of PEDOT/graphene counter electrode-based DSSC (6.26%) than that of the PEDOT-based control device (5.62%).[718]

Another approach to improving the catalytic activity of the graphene counter electrodes is constructing 3D nanostructure to improve the surface area.[719] For example, Wu et al. reported a 3D honeycomb-like graphene counter electrode for DSSCs synthesized via the reaction between Li_2O and CO. The optimized device showed 7.8% high PCE, which is significantly higher than that of a control device using exfoliated graphene nanosheet as the counter electrode (0.64%).[720] The unique structure and high surface area of CNT, especially multi-walled CNT (MWCNT) have been proved to be beneficial for counter electrode applications.[721,722] However, the CNT films are either too thick to be transparent or coated on FTO current collectors for higher electrical conductivity in most situations.[723-726] Figure 39D shows a photograph of a semi-transparent DSSC using spray-coated SWCNT as the top transparent counter electrode. The SWCNT films were treated with H_2PtCl_6 to load Pt nanoparticles on the CNT surface, which further improve the catalytic activity of the transparent counter electrodes. The optimized semi-transparent DSSC exhibited 25% optical transmittance at 550 nm. In the meantime, the rigid device showed a PCE of 5.11%, which was slightly inferior to that of the control device with a Pt/FTO counter electrode (5.42%). However, the performance of Pt/CNT/PEN-based flexible DSSC was almost identical to that of Pt/ITO/PEN-based control device, as shown in Figure 39E. Such results indicated that solution-processed CNT films are promising substitutes for vacuum-deposited TCOs when applied to flexible DSSCs.[727] Apart from the counter electrode, there has been reported on using carbon materials for photoanode applications by mixing graphene or CNT with ZnO or TiO_2 to form

composite working electrodes for DSSCs. However, highly conductive TCO substrates are still required for high-efficiency devices with such composite photoanodes.[728-731]

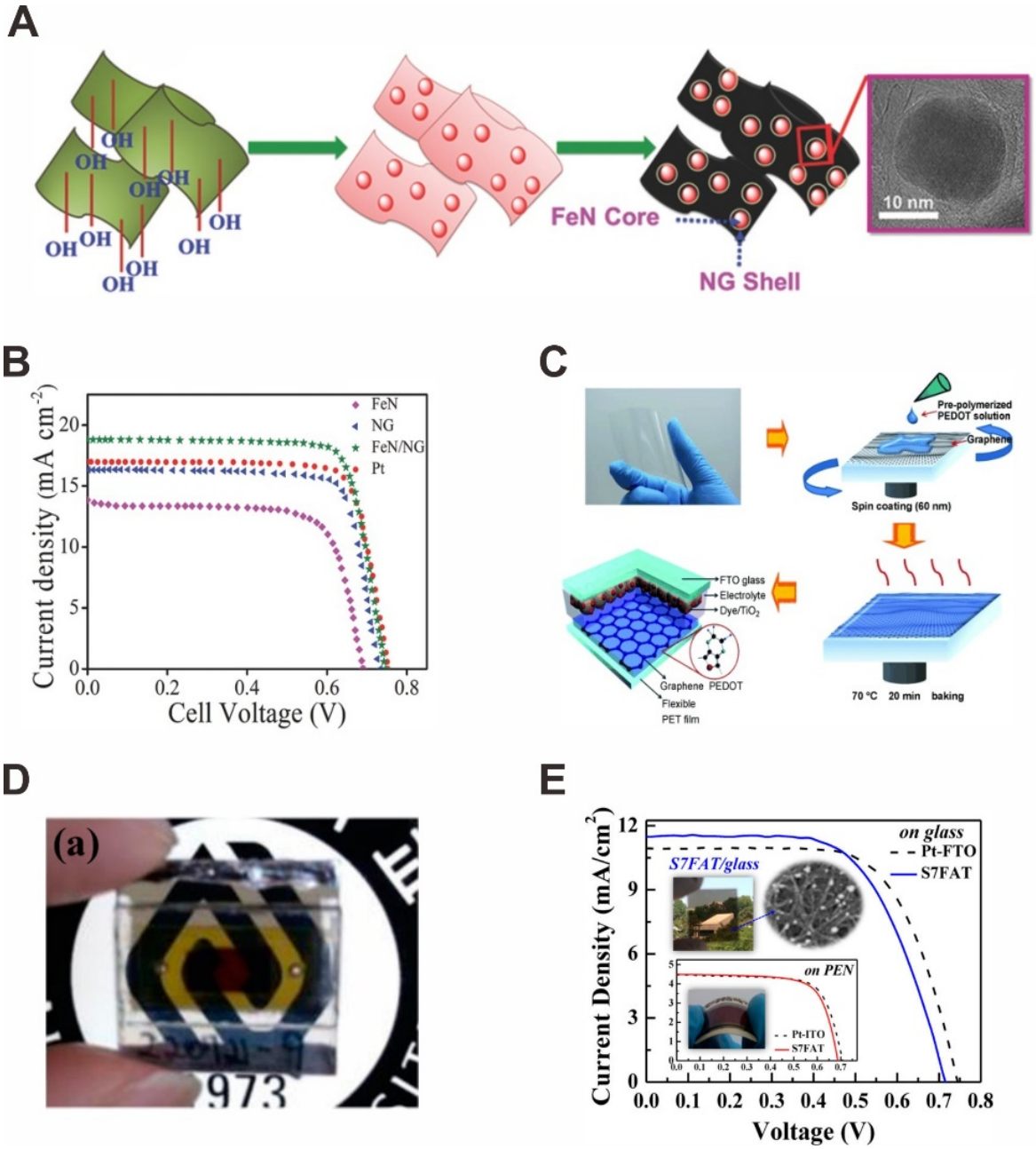

Figure 39. (A) Schematics of the synthesis of FeN/N-doped graphene nano-composites as counter electrodes for DSSCs. (B) J-V curves of DSSCs with Pt, standalone FeN, standalone N-doped

graphene, and FeN/N-doped graphene counter electrodes. Reproduced with permission from Ref[716]. Copyright 2015 WILEY‐VCH Verlag GmbH & Co. KGaA, Weinheim. (C) Schematics of the fabrication of solution-processed PEDOT/graphene transparent counter electrodes for DSSCs. Reproduced with permission from Ref[718]. Copyright 2012 WILEY‐VCH Verlag GmbH & Co. KGaA, Weinheim. (D) Photograph of a semi-transparent DSSC with solution-processed Pt/SWCNT transparent counter electrode. (E) The J-V curves of the semi-transparent DSSC with Pt/SWCNT and Pt/FTO counter electrodes. Inset shows the J-V curves of flexible DSSCs with Pt/SWCNT and Pt/ITO counter electrodes on PEN substrates. Reproduced with permission from Ref[727]. Copyright 2014 American Chemical Society.

Table 5 lists some of the best-performing DSSCs with solution-processed TEs and current collectors. Although best-reported DSSC has reached a PCE ~ 13%, the high-efficiency devices still require vacuum-deposited TCOs as current collectors for working electrodes or counter electrodes.[732] Meanwhile, there have been few studies on fully solution-processed transparent anodes (photoanode + current collector) for DSSCs.

Table 5. Examples of best-performing DSSCs with solution-processed TEs and current collectors.

TE	Processing Method	Electrode Type	V_{OC} (V)	J_{SC} (mA/cm^2)	FF (%)	PCE (%)	Ref.
PEDOT:PSS	Spin coating	Counter electrode	0.696	18.99	65.0	8.59[a]	[694]
PEDOT	Nanoimprinting/Spin coating	Counter electrode	0.692	15.4	66.6	7.1[a]	[690]
PANI-CSA	Spin coating	Counter electrode	0.80	12.4	67	6.23[a]	[733]
PANI	Chemical deposition	Counter electrode	0.730	17.51	65.3	8.35[a]	[697]
Pt/Ni mesh	Electrochemical deposition	Counter electrode	0.79	13.19	67.3	6.91[a]	[734]
AgNW/TiO_2	Spin coating/transfer printing	Working electrode (photoanode)	0.74	6.88	66	3.36[a]	[702]
CuS network	Electro-spinning/transfer lamination	Counter electrode	0.66	18.10	53.4	6.38[a]	[710]
PEDOT/graphene	*in-situ* polymerization/transfer printing	Counter electrode	0.77	12.9	63	6.26[a]	[718]
Pt/SWCNT	Chemical deposition/spray coating	Counter electrode	0.720 ± 0.007	11.3 ± 0.17	62.8 ± 0.7	5.11 ± 0.07	[727]

[a]Champion device PCE.

7.3 Perovskite Solar Cells

The rapid development of organometal halide-based PSCs has attracted great attention from both researchers and the photovoltaic industry.[735] The device configuration of PSCs is illustrated in **Figure 40**.[736] Evolved from DSSCs in 2009, the early PSCs employed a mesoscopic structure regarding the perovskite materials as sensitized for the mesoporous TiO_2 anode.[737,738] Later in 2013, planar-structured PSC with > 15% PCE was developed, indicating a great potential of organolead halide as active materials.[739,740] To date, the record efficiency of lab-scale single-junction PSC has reached 25.2%, which is the highest among all the thin-film solar cells.[741] The PSCs are also promising for tandem solar cell applications, as the bandgap of the perovskite active material can be tuned easily by doping.[742,743] The tunable bandgap from ~1.2 eV to ~1.8 eV makes the perovskite solar cells suitable for both top cell and bottom cell applications.[744,745] In 2018, 28% certified PCE of perovskite/Si tandem solar cell was reported by Oxford PV, indicating that the perovskite/Si tandem solar cells have great potential to break through the limitations of single-junction Si solar cells.[746] Moreover, perovskite-perovskite tandem solar cells with > 25% PCE for 4-terminal cell and > 23% PCE for 2-terminal (monolithic) cell was reported very recently.[747] Apart from the high photovoltaic efficiency, the low-cost and solution-processable perovskite materials are highly compatible with the R2R process, and thus is promising for low-cost solar modules and flexible solar cells.[748,749]

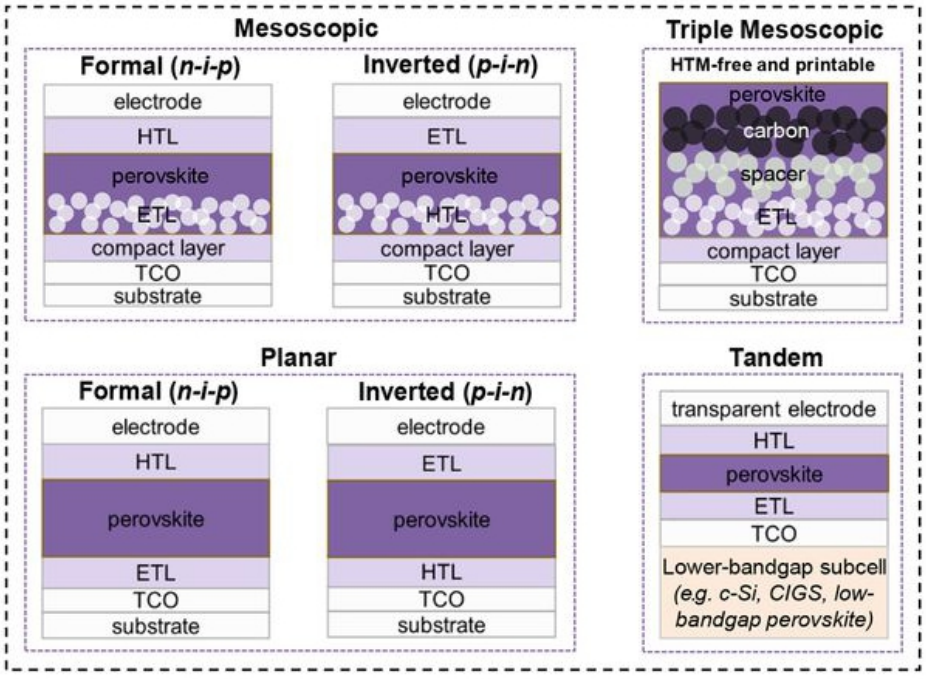

Figure 40. Schematics of PSC configurations: mesoscopic, triple mesoscopic, planar, and tandem structure. It is worth noting that the "formal" and "inverted" concept of PSCs is opposite to that of OSCs. Reproduced with permission from Ref[736]. 2018 The Authors, some rights reserved; exclusive licensee American Association for the Advancement of Science. No claim to original U.S. Government Works. http://www.sciencemag.org/about/science-licenses-journal-article-reuse. This is an article distributed under the terms of the Science Journals Default License.

Although most of the reported PSCs still employ vacuum-deposited FTO or ITO as TEs, there have been increasing number of works on solution-processed TEs in recent years.[49,227,750] The composite electrode structure combining current collecting grid and PEDOT:PSS, which is very effective on OSCs, also works well on PSCs. Very recently, Hu et al. reported highly efficient PEDOT:PSS-based PSCs with 19.4% and 19.0% efficiencies on rigid glass and flexible PET substrates, respectively. The doping of zinc di[bis(trifluoromenthylsulfonyl) imide] ($Zn(TFSI)_2$)

not only improved the conductivity of PEDOT:PSS to > 4,100 S/cm, but also enhanced the mechanical robustness of PEDOT:PSS TEs.[96] **Figure 41A**, B and C show the schematics, SEM images, and energy diagram of flexible PSC with PEDOT:PSS/embedded-Ag mesh TE, respectively. The transmittance of the Ag mesh was optimized that only 3.9% of transmittance loss was observed on Ag mesh/PET compared with bare PET film. The R_{sh} of the optimized TE was 3 Ω/□, while maintaining a high optical transmittance of 86% and low surface roughness of 2 nm. As a result, the champion PSCs showed 14.2% PCE with 80% high fill factor.[49] The ease of transfer printing for the PEDOT:PSS-based TEs provides the possibility of constructing top-illuminated PSCs.

To avoid the damage of perovskite materials by moisture or solvents, the transfer-printing of PEDOT:PSS employs dry-transfer or "half-dry" transfer with adhesives.[111,751] Figure 41D and E show the structure and photograph of a top-illuminated flexible PSC using titanium foil as the bottom electrode and flexible substrate, respectively. To form the transparent conductive adhesive layer, PEDOT:PSS solution was doped with a pressure sensitive acrylic adhesive before doctor-blading on top of the Ni meshed-embedded PET substrate. The transfer-printed composite TE exhibited good contact with the HTL, resulting in an efficiency of > 10%.[752] Such transfer printing technique is compatible with the R2R process, and thus is suitable for the high throughput fabrication of self-encapsulated PSC modules.[640]

The high-work function PDEOT:PSS TEs are occasionally employed as cathodes in "formal" PSCs with proper surface modifications. For example, the PEI thin films that are commonly

adopted as surface modifiers in OSCs are also suitable for PSCs (Figure 41F). The work function of PEDOT:PSS decreased from 5.08 eV to 4.08 eV after coating of 10 nm-thick PEI. The significant change in work function turned the PEDOT:PSS TEs ideal cathodes for PSCs, as illustrated by the device structure. As a result, the formal-structured PSC performed well on both rigid and flexible substrates (Figure 41G). Such configuration avoided using of ETLs which are either expensive or high-temperature requiring in most of the circumstances.[753]

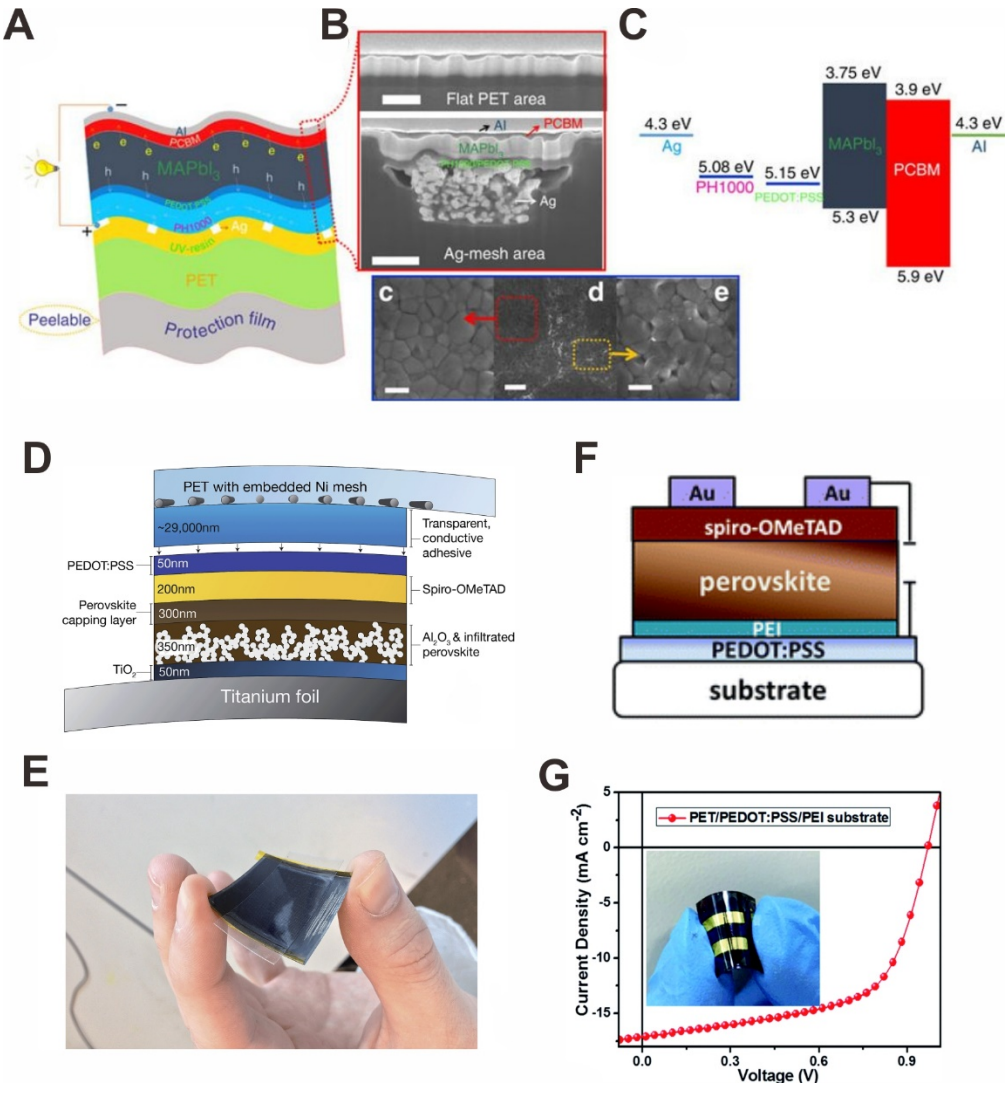

Figure 41. (A) Schematics, (B) SEM images, and (C) energy diagram of flexible PSCs with solution-processed PEDOT:PSS/embedded-Ag mesh composite TEs. Reproduced with

permission from Ref[49]. Copyright 2016 The authors. http://creativecommons.org/licenses/by/4.0/. (D) Schematics and (E) photograph of top-illuminated flexible PSC with transfer-printed PEDOT:PSS/embedded-Ni mesh top TE on titanium foil. Reproduced with permission from Ref[752]. Copyright 2015 The Royal Society of Chemistry. (F) Schematics of formal-structured ETL-free PSC with PEDOT:PSS transparent cathode. (G) J-V curve and photograph (inset) of the flexible PSC. Reproduced with permission from Ref[753]. Copyright 2017 The Royal Society of Chemistry.

The high FoM of TEs made of metal nanowires provide sufficient conductivity while maintaining high optical transmittance, which is important for semi-transparent top cell in tandem solar cells. **Figure 42A** and B are the SEM cross-sectional images and schematics of semi-transparent PSCs with AgNW top TEs for tandem applications with crystalline Si bottom cells, respectively. Although denser AgNW film resulted in a higher photovoltaic performance of the PSC top cell, the transmittance of the top cell should not be too low to ensure a high overall efficiency of the tandem cell. As a compromise between top cell efficiency and transmittance, the optimum AgNW TE had an R_{sh} of 16 Ω/□ and an average optical transmittance of 88%. The optimized top PSC cell exhibited a high PCE of 17.1%, and the overall efficiency of the 4-terminal tandem solar cell was as high as 26.7%.[754] The metal materials are also eligible for bottom TE applications, but the stability issue should be addressed for metal electrodes in PSCs because the organolead halide (especially iodide) perovskite materials may react with metals, which leads to degradation of the devices.[755] Figure 42C and D show the structure and SEM cross-sectional image of AZO/AgNW/AZO composite TEs on rigid and flexible PSCs. The top AZO layer not only worked as a smooth compact layer, but also a barrier to prevent the direct contact between the perovskite layer and AgNWs. An additional layer of ZnO served as an ETL between the composite TE and

the perovskite active layer. The FoM of the composite TE was as high as 25.1×10^{-3} Ω^{-1}, which is comparable to that of the commercial FTO/glass (30.9×10^{-3} Ω^{-1}) that is used in conventional PSCs. As a result, the PSC with composite TE exhibited comparable performance to the FTO-based control device (Figure 42E). In addition, because the solution-processed TEs exhibited superior flexibility to vacuum-deposited ITO/PET, the devices showed much better performance stability under repeated bending (Figure 42F).[110] Apart from metal and TCOs, some other metal element-based materials have been reported for solution-processed TEs.[756] Figure 42G depicts the fabrication process of solution-processed transparent and conductive 2D metal-organic framework (MOF) as TEs for PSCs. The Cu-benzenehexathiol (Cu-BHT) MOF was deposited *in-situ* on the transparent substrates via a liquid-liquid interface reaction. The obtained Cu-BHT TEs exhibited a decent conductivity of 2,500 S/cm and an optical transmittance of 82%. The MOF TE-based PSC exhibited almost identical performance compared with the ITO-based control devices.[757]

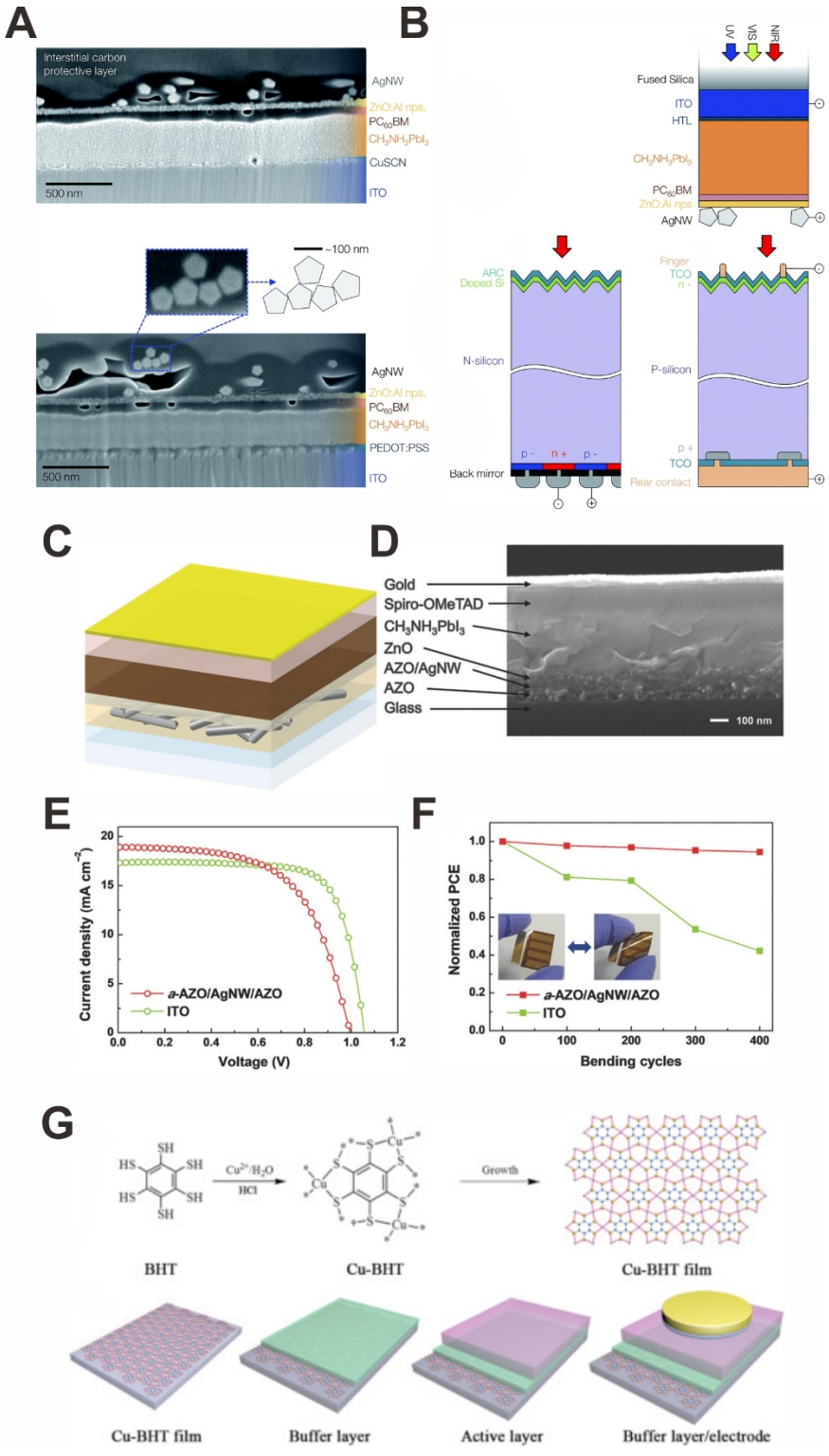

Figure 42. (A) SEM cross-sectional images of semi-transparent PSCs with AgNW top TEs, and (B) schematics of the 4-terminal tandem solar cells (right). Reproduced with permission from

Ref[754]. Copyright 2018 The Royal Society of Chemistry. (C) Schematics and (D) SEM image of AZO/AgNW/AZO composite TE-based PSC. (E) J-V curves of the composite TE-based and FTO-based PSCs. (F) Normalized PCE of the composite TE-based PSC and FTO-based control device under repeated bending. Reproduced with permission from Ref[110]. Copyright 2017 WILEY-VCH Verlag GmbH & Co. KGaA, Weinheim. (G) Schematics of the solution-deposited Cu-BHT thin film TE. Reproduced with permission from Ref[757]. Copyright 2017 Elsevier Ltd.

The application of carbon electrodes on PSCs is of great interests because the carbon materials are chemically stable.[758-760] **Figure 43A** compares the J-V curves of graphene and CNT TE-based PSCs with an ITO-based control device.[542] For SWCNTs, the HNO_3 post-treatment improved the conductivity of the TEs significantly, resulting in 15.3% high efficiency for the champion device.[761] Successful post-treatment also plays an important role in high-performance graphene-based TEs. A recent study by Heo et al. suggested that bis(trifluoromethanesulfonyl)-amide (TFSA)-doped graphene is ideal for TE applications on PSCs. Figure 43B, C and D show the structure, energy diagram, and SEM cross-sectional image of the graphene-based PSC, respectively. The transfer-printed monolayer graphene exhibited an R_{sh} of 116 Ω/□ and an ultrahigh optical transmittance of 96.80% after the treatment of TFSA. In comparison, the pristine graphene without doping showed a large R_{sh} of 650 Ω/□. As a result, the graphene-based PSCs showed very high efficiencies of 18.9% and 18.3% for rigid and flexible devices, respectively.[109]

The high transmittance of graphene TEs also shows advantages for semi-transparent and tandem PSCs. Figure 43E shows an example of perovskites/Si tandem solar cells using graphene TEs. The

devices made use of transfer-printed graphene TEs as top electrodes of the PSCs during fabrication. It is worth noting that the parasitic absorption of spiro-OMeTAD HTL at short wavelength reduced the efficiency of the semi-transparent PSCs when illuminated from the graphene side, so the higher overall efficiency of the tandem solar cells appeared when the FTO side of the PSCs facing up.[762,763]

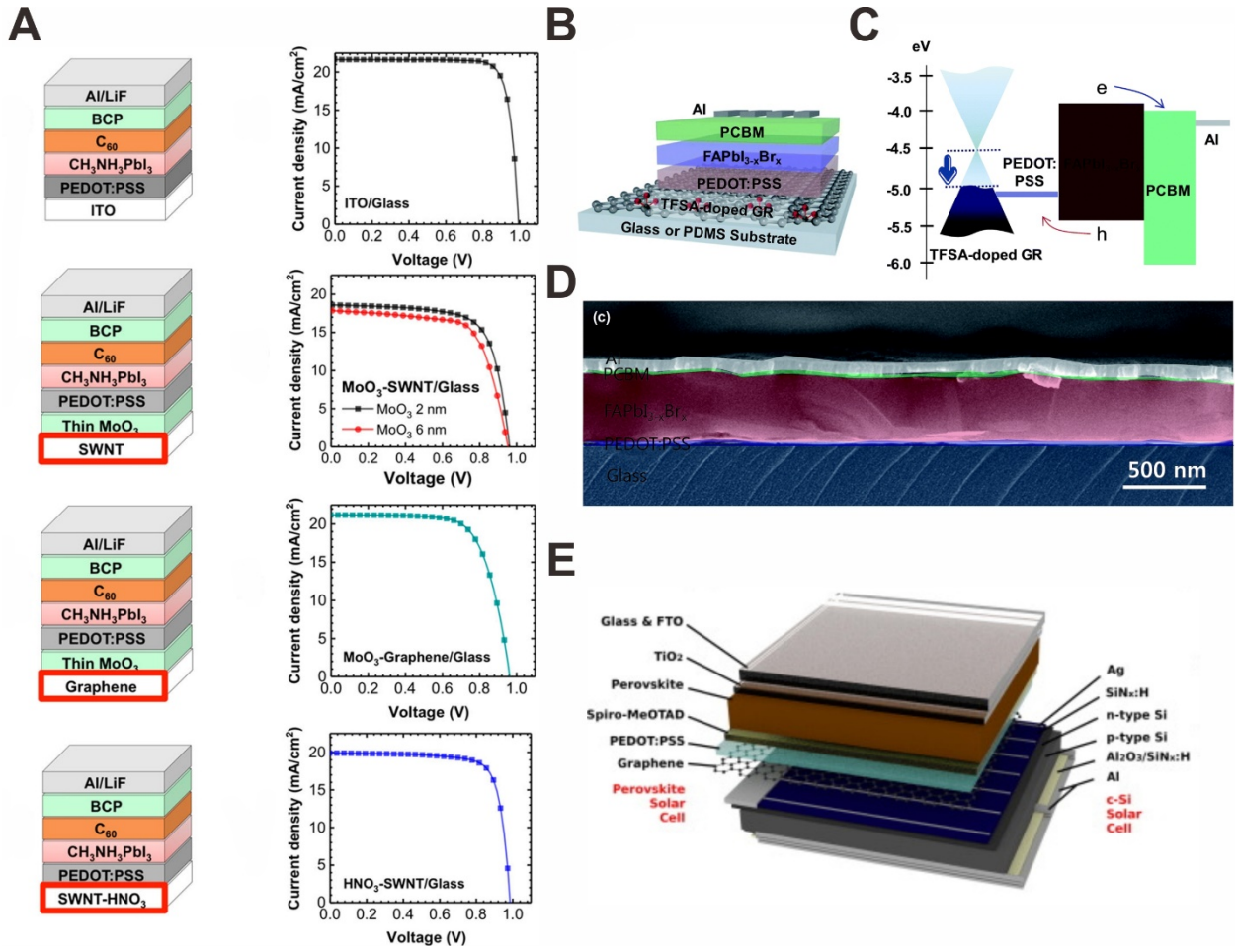

Figure 43. (A) Comparison of the structure (left) and J-V curves (right) of ITO control, MoO_3/SWCNT, MoO_3/graphene, and HNO_3-treated SWCNT PSCs. Reproduced with permission from Ref[761]. Copyright 2017 American Chemical Society. (B) Structure, (C) energy diagram, and (D) SEM cross-sectional image of TFSA-graphene-based PSC. Reproduced with permission from

Ref[109]. Copyright 2018 The Royal Society of Chemistry. (E) Schematics of 4-terminal perovskite/Si tandem solar cells with graphene TEs. Reproduced with permission from Ref[763]. Copyright 2018 Elsevier B.V.

Table 6 summarizes some of the best-reported PSCs with solution-processed TEs. The state-of-the-art PSCs with solution-processed TEs exhibited a PCE of ~ 14% or even higher, which is far beyond that of the solution-processed thin-film solar cells with other active materials. The good solution-processability of perovskite active materials also provides great possibilities for large-scale R2R printing of perovskite solar modules.[37,748]

Table 6. Examples of highly efficient PSCs with solution-processed TEs.

TE	Method	Active Material	V_{OC} (V)	J_{SC} (mA/cm^2)	FF (%)	PCE (%)	Ref.
PEDOT:PSS:CFE	Slot-die coating	Mixed-cation perovskite	1.07 (1.08)	21.96 (22.51)	78 (80)	18.4 (19.4[a)])	96
PEDOT:PSS//PEDOT:PSS[b]	Spin coating//Transfer printing	Mixed-cation perovskite	1.06	19.3	68	13.9[a]	636
PEDOT:PSS//PEDOT:PSS[c]	Spin coating//Transfer printing	Mixed-cation perovskite	1.07	18.7	78	15.61[a]	98
PEDOT:PSS/Ag mesh[d]	Spin coating/Nano-imprinting	$MAPbI_3$	0.91	19.5	80	14.2[a]	49
CNT	Transfer printing	$MAPbI_3$	0.81	18.3	66	9.8[a]	107
PEDOT:PSS/CNT	Spin coating/Transfer printing	$MAPbI_3$	0.98	19.9	78	15.3[a]	761
$AuCl_3$-doped Graphene	Transfer printing	$MAPbI_3$	1.09	21.0	78.3	17.9[a]	764
TFSA-doped Graphene	Transfer printing	$FAPbI_{3-x}Br_x$	1.05 ± 0.017	22.15 ± 0.437	75.0 ± 1.64	17.4 ± 0.80 (18.9[a])	109
AgNW[b]	Spray coating	$MAPbI_3$	1.098	21.0	74.1	17.1[a]	754
AgNW[b]	Transfer printing	Mixed-cation	1.12	20.68	69.2	16.03[a]	765
Cu-BHT	Interface reaction		0.985 ± 0.023	20.47 ± 0.65	70.1 ± 2.4	14.13 ± 1.24	757

[a]Champion device PCE. [b]Semi-transparent PSC. [c]Stretchable PSC. [d]Flexible PSC.

7.4 Flexible Solar Cells

Lightweight and flexible solar cells are important energy harvesting devices for further wearable and portable electronics, vehicles, and building-integrated energy harvesting systems.[766-770] The thin-film solar cells are ideal candidates for flexible solar cells because of the solution processability and intrinsic flexibility of the materials.[771-773] For flexible thin-film solar cells, the commonly adopted substrates include polymeric thin films (PET, PEN, PDMS, and etc.), metal foils, and natural or artificial textiles.[774-780] Whereas most of the reported flexible solar cells employ a planar thin-film configuration, there has been an increasing interest in non-planar textile-based solar cells for their superior mechanical flexibility and good compatibility to wearable applications.[781-783] This section reviews solution-processed flexible thin-film solar cells from both material and mechanical design point-of-view.

For planar thin-film devices, the stress applied on each layer during bending is relevant to the Young's modulus of the material, the thickness of each layer, and the bending radius.[784] For example, the relationship between stress σ and bending radius r for a bilayer system is described by Stoney's equation:

$$\sigma = \frac{E_s t_s^2}{6 t_f r} \qquad (9)$$

where E_s is Young's modulus of the substrate, t_s is the thickness of the substrate, and t_f is the thickness of the film.[785] For a multi-layer system, the outermost layer undertakes the largest tensile strain during bending, while the innermost layer sustains the largest compressive strain.

Accordingly, there will be a mechanical neutral plane that sustains neither tensile strain nor compressive strain inside the multi-layer system. Thus, one design principle for flexible thin-film solar cells is applying the most brittle layer (e.g., metal oxides) nearest the mechanical neutral plane.

Figure 44 illustrates the impact of mechanical design on the resistance change of ITO thin films after bending at different curvature. There have been reports on employing a soft middle layer to obtain multiple mechanical neutral planes for flexible electronics.[786,787] Figure 44A and B show 2 symmetric structures with hard (E = 255 MPa) and soft (E = 0.1 MPa) middle layers, respectively. The neutral plane (N.P.) for A structure was inside the hard middle layer, which was far away from the ITO film. As a result, the outer and inner ITO films sustained tensile and compressive strains, respectively. The large tensile strain at < 9 mm bending radius induced cracks on outer ITO film, which led to a dramatic increase of the electrical resistance (Figure 44C). On the contrary, the B structure had 2 neutral planes that are near ITO films, resulting in very low strain on ITO films during bending. Hence, the resistance of both ITO films almost remained unchanged after the bending test (Figure 44D).[788]

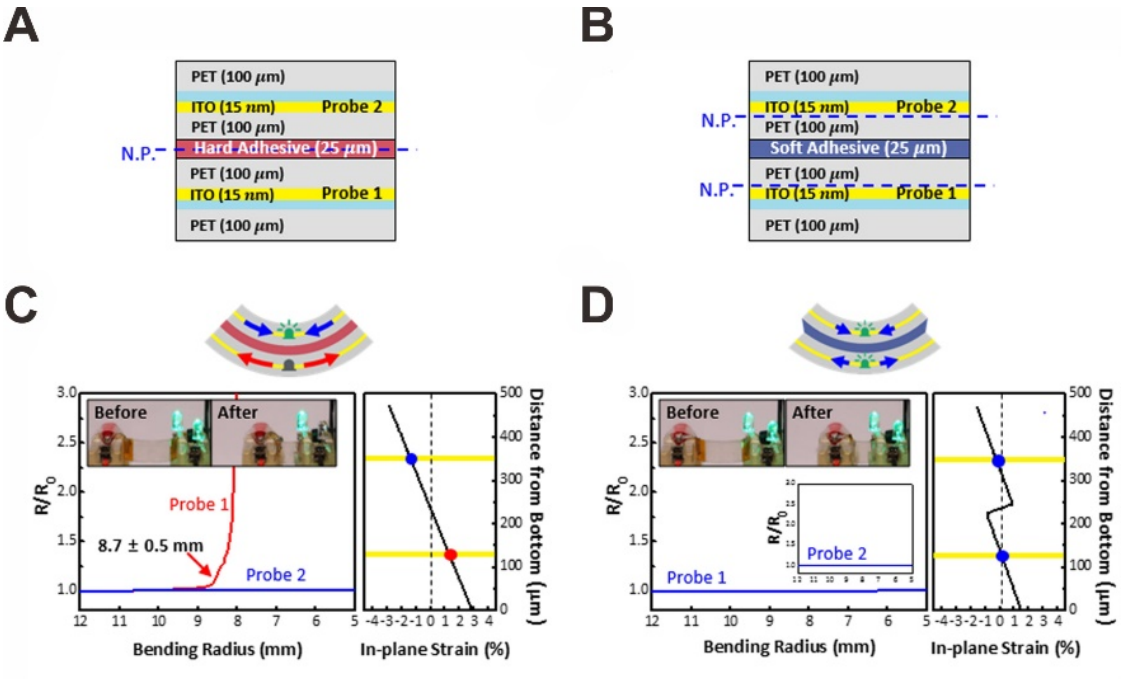

Figure 44. Illustration of sandwiched ITO films with (A) hard and (B) soft middle layers. (C) and (D) Resistance change versus bending radius, and in-plane strain of the ITO films in (A) and (B), respectively. Reproduced with permission from Ref[788]. Copyright 2017 IOP Publishing Ltd.

PET and PEN are common substrates for flexible thin-film solar cells because of their high optical transmittance, good mechanical flexibility, and good thermal stability.[789,790] **Figure 45A** depicts the structure of a solution-processed flexible OSC with PEDOT:PSS TE. The solar cell avoided the use of brittle TCOs and metal oxide ETL/HTL materials, and thus resulted in good mechanical flexibility on the PET substrate. The device maintained > 95% of their initial efficiency after 1,000 cycles of bending at a radius of 5.6 mm (Figure 45B). For comparison, the control devices with ITO showed 50% degradation after repeated bending under the same condition. In the meantime, the average initial efficiency of the PEDOT:PSS -based devices (10.03%) was higher than that of the ITO-based control devices (7.80%).[97]

To obtain higher flexibility, Yoon et al. reported graphene-based PSCs on PEN substrates that were mechanically stable at a very small bending radius (2 mm). The very high flexibility of graphene TEs endorsed mechanical stability for the flexible PSCs that > 90% of the solar cell efficiency was maintained after 10,000 cycles of bending at 4 mm-radius.[632] For fully solution-processed PSCs, the organometal halide perovskite active materials are the relatively brittle components.[791]

Recently, Hu et al. reported mechanically optimized PSCs that were intrinsically stretchable. The superb flexibility of perovskite films was obtained via both chemical and physical engineering. On the one hand, poly(styrene-co-butadiene) (SBS) and polyurethane (PU) were doped in the perovskite solution to obtain a "brick-mortar structure" during film formation. The polymer mixture improved the crystalline quality of the perovskite film while suppressing the "cask effect" that originated form the brittleness of perovskite film (Figure 45C). On the other hand, the perovskite layer was sandwiched between two PDMS substrate, which shifted the mechanical neutral plane inside the perovskite film (Figure 45D). As a result, the optimized flexible PSC with polymer mixture showed superior mechanical stability during bending and stretching tests. As shown in Figure 45E, the efficiency of PSCs based on SBS-PU mixture maintained stable at different bending curvature, whereas the control devices showed different degrees of degradation after bending. Moreover, the PSC survived from 5,000 cycles of stretching test at a strain of 20%, maintaining ~ 80% of its initial efficiency (Figure 45F).[98]

Another approach to obtaining stretchable solar cells is introducing a "wavy" structure via a pre-stretch strategy.[792,793] Figure 45G to P show the application of pre-stretch strategy to ultrathin OSCs and PSCs. In 2012, Kaltenbrunner et al. reported flexible OSCs that were fabricated on 1.4 μm thick ultrathin PET substrates (Figure 45G). Spin-coated PEDOT:PSS films were adopted for avoiding strain-induced cracks under severe compression. The ultrathin OSCs were highly flexible that they could be conformally attached on arbitrarily curved surfaces such as the surface of a human hair (Figure 45H). When attached to a pre-stretched elastomer, buckles will form on the surface of the OSCs once the strain has been released as shown in Figure 45I. Figure 45J and K show the J-V curves and photovoltaic performance of the OSC under different compressive strain, respectively. The output current of the OSC decreased under compression state because the actual active area of the device was reduced. However, the stable V_{OC} and FF indicated that the OSC was functioning normally under compression.[46] Later in 2015, the authors demonstrated ultrathin PSCs with similar device configuration on ultrathin PET substrates. The PEDOT:PSS-based flexible PSC exhibited a PCE of 12%, which was almost identical to that of the control device with ITO TE. Meanwhile, the solution-processed PSC showed good mechanical stability even under radial compressive strain. Figure 45L and M exhibit the schematic and photograph of stretchable PSC on a radially pre-stretched elastomer. Figure 45N shows the photographs of the PSC before and after 44% radial compression. The current of the PSC decreased as the active area shrunk, whereas the V_{OC} and FF maintained almost unchanged (Figure 45O and P). In addition, the PSC was high power-per-weight (23 W/g) thanks to the lightweight and high-efficiency perovskite active material and the ultrathin PET substrate. Such a feature made the ultrathin PSC very promising for aircraft and spacecraft, which require high power and lightweight energy supplies.[7]

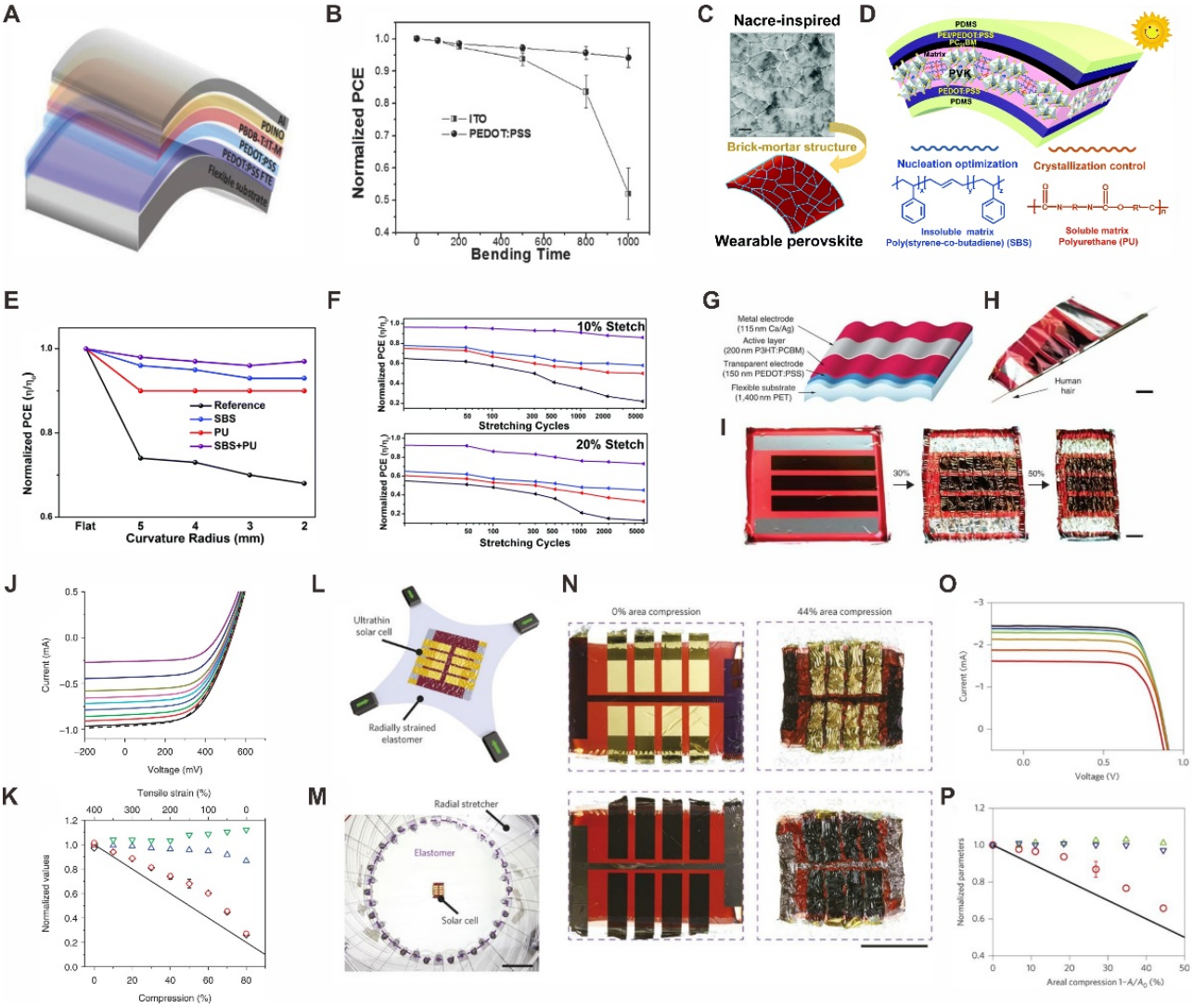

Figure 45. (A) Schematic of solution-processed OSC with PEDOT:PSS TE, and (B) normalized PCE of the flexible PSC and ITO-based control PSC under repeated bending at a radius of 5.6 mm. Reproduced with permission from Ref[97]. Copyright 2018 WILEY-VCH Verlag GmbH & Co. KGaA, Weinheim. (C) SEM image and schematics of the brick-mortar structure perovskite film obtained via doping of SBS and PU. (D) Schematics of the semi-transparent stretchable PSC and the chemical structure of SBS and PU. Normalized PCE of SBS+PU doped PSC, SBS doped PSC, PU doped PSC and doping-free control PSC under (E) different bending curvature, and (F) repeated stretching at a strain of 10% or 20%. Reproduced with permission from Ref[98]. Copyright

2019 The Royal Society of Chemistry. (G) Schematics of ultrathin OSC on 1.4 μm-thick PET substrate. (H) Photograph of an ultrathin OSC wrapped on a human hair, the radius of which was 35 μm. (I) Photographs of the OSC during compression. The OSC was attached to a 50% pre-stretched elastomer. (J) The I-V curves of the OSC under different degrees of compression from 0 (black line) to 80% (purple line). (K) Normalized V_{OC} (upward triangle), I_{SC} (circle), FF (downward triangle), and PCE (diamond) of the OSC at different compressive strain. Reproduced with permission from Ref[46]. Copyright 2012 Springer Nature. (L) Schematics and (M) photograph of a stretchable ultrathin PSC on a radially pre-stretched elastomer. (N) Top view and bottom view photographs of the PSC at 0 strain and 44% areal compressive strain. (O) I-V curves of the ultrathin PSC under radial compression from 0 strain (black line) to 44% strain (red line). (P) V_{OC} (downward triangle), I_{SC} (upward triangle), and FF (circle) of the PSC under different compressive strain. Reproduced with permission from Ref[7]. Copyright 2015 Springer Nature.

Textile-based electronics are promising for wearable applications because textile structures accommodate the motions of the human body without inducing mechanical failure.[794-796] In 2007, Liu et al. demonstrated optical fiber-based OSC with solution-processed ITO TE. The OSC exhibited poor PCE due to non-perpendicular light incidence.[797] Later in 2008, O'Connor et al. improved the OSC structure by employing semi-transparent metal top TE, which allowed light incidence from the outer surface of the OSC. However, the fabrication of the solar cell required vacuum deposition of metal on fiber substrate, which is technically complicated and high cost.[798] **Figure 46A** depicts the structure of an OSC fiber based on two wire electrodes and transparent cladding. The primary electrode was a stainless steel wire on which the organic active layer was coated. The secondary electrode was also a stainless steel wire but coated with Ag paste which

enhanced the conductivity of the electrode and smoothened the surface of stainless steel wire. The secondary electrode was wrapped on the core wire to form close contact with the PEDOT:PSS HTL. Since the secondary electrode was an opaque metal wire, the incident light would be partially shaded by the secondary electrode as illustrated in Figure 46A. To address this issue, transparent polymer cladding was employed to focus shaded light onto the active area of the OSC. Figure 46B shows the dependence of power absorbed by the active layer on the light incident angle with and without the transparent polymer cladding. The cladding provided significant light absorption enhancement that light absorption has been observed even when the active layer was completely shaded. As a result, the fiber-based OSCs exhibited decent PCE ranging from 2.79% to 3.27%.[799]

Whereas most of the solution-based coating and printing techniques are not applicable to curved fiber substrates, solution-based chemical and electrochemical deposition show less dependence on surface morphology. Figure 46C shows the schematics and SEM image of fiber-shaped DSSC with electrochemically deposited TiO_2 nanotube photoanode on Ti wire. The counter electrode which was twisted on TiO_2/Ti core consisted of wet-spun graphene and electrochemical-deposited Pt. The twisted structure of the fiber-shaped DSSC exhibited a very high efficiency of 8.45%, which was independent from the light incident angle.[800] Previous researches have demonstrated that highly oriented CNT sheet can be obtained by drawing from a CNT forest.[801,802] Figure 46D illustrates the fabrication process of fiber-shaped PSC using wrapped CNT sheet as TE. The PSC employed solution-deposited TiO_2 on Ti wire, which was similar to the photoanode of the fiber-shaped DSSC. The perovskite active layer was deposited via a cathodic deposition process, which provided uniform surface coverage on TiO_2 nanotube. Instead of the wrapped opaque metal counter electrode, a transparent CNT sheet was wrapped onto the perovskite layer directly. The

CNT sheet functioned as TE as well as HTL, resulting in a 7.1% efficiency PSC without an additional layer of HTL. Whereas the efficiency of the fiber-shaped PSC was lower than that of DSSC, the PSC was free from liquid electrolyte which is more desirable for wearable applications.[803] For wearable applications, the fiber-based solar cells should be assembled on cloth via weaving, knitting, embroidery, and etc.[40,804-806]

Figure 46E shows a simple approach to fabricate fabric-based DSSC by stacking of CNT and TiO_2/Ti fabrics. Instead of weaving the fabricated fiber-shaped DSSCs, the researchers stacked the woven fabrics of the photoanode and counter electrode, followed by the injecting of the liquid electrolyte. An additional sealing process was necessary for such liquid-state DSSC to prevent leaking of electrolyte. The sealed device (Figure 46F inset) exhibited a decent PCE of 3.67%, and the solar cell performance was very stable under bending. The DSSC textiles were further integrated on fabrics as shown in Figure 46G, demonstrating good compatibility with conventional textiles and cloths.[779]

As flexible energy harvesters, the textile-based solar cells are supposed to combine with other textile-based energy harvesting and storage devices for real-world practice. For example, Chai et al. combined fiber-based DSSCs and supercapacitors together for energy harvesting textiles, which was fully charged to 1.2 V in 17 s under AM1.5 solar simulator.[807] Same year in 2016, Wen et al. demonstrated self-powered textile that integrated DSSC, nanogenerator, and supercapacitor together. The textile-based device collected solar energy and mechanical energy with DSSC and nanogenerator, respectively. Thus, the hybridized device was rechargeable under both indoor and

outdoor conditions.[783] The fabric construction such as weaving structure and thread counts impacts on the performance of these textile-integrated devices. Figure 46H and I show the structure of the textile-based triboelectric nanogenerator (TENG) and DSSC, respectively. For DSSCs, the photoanode was fabricated via a full-solution process on polybutylene terephthalate (PBT) substrate. The Mn/Cu conductor was deposited on the fiber substrate via chemical and electrochemical deposition, followed by the chemical growth of ZnO nanowire arrays. Meanwhile, the Cu counter electrode was also fabricated via chemical deposition of Cu on PBT wire. Instead of liquid electrolytes, the DSSC adopted solid CuI HTL which avoided the risk of electrolyte leaking and contamination. The weaving structure of fabric was found relevant to the efficiency of the DSSC textile, as shown in Figure 46J. The highest current density was achieved with conventional plain weave structure. Figure 46K shows a photograph of the energy harvesting textile integrated on a colored fabric. The flexibility of the device was demonstrated to be satisfactory for wearable applications.[781]

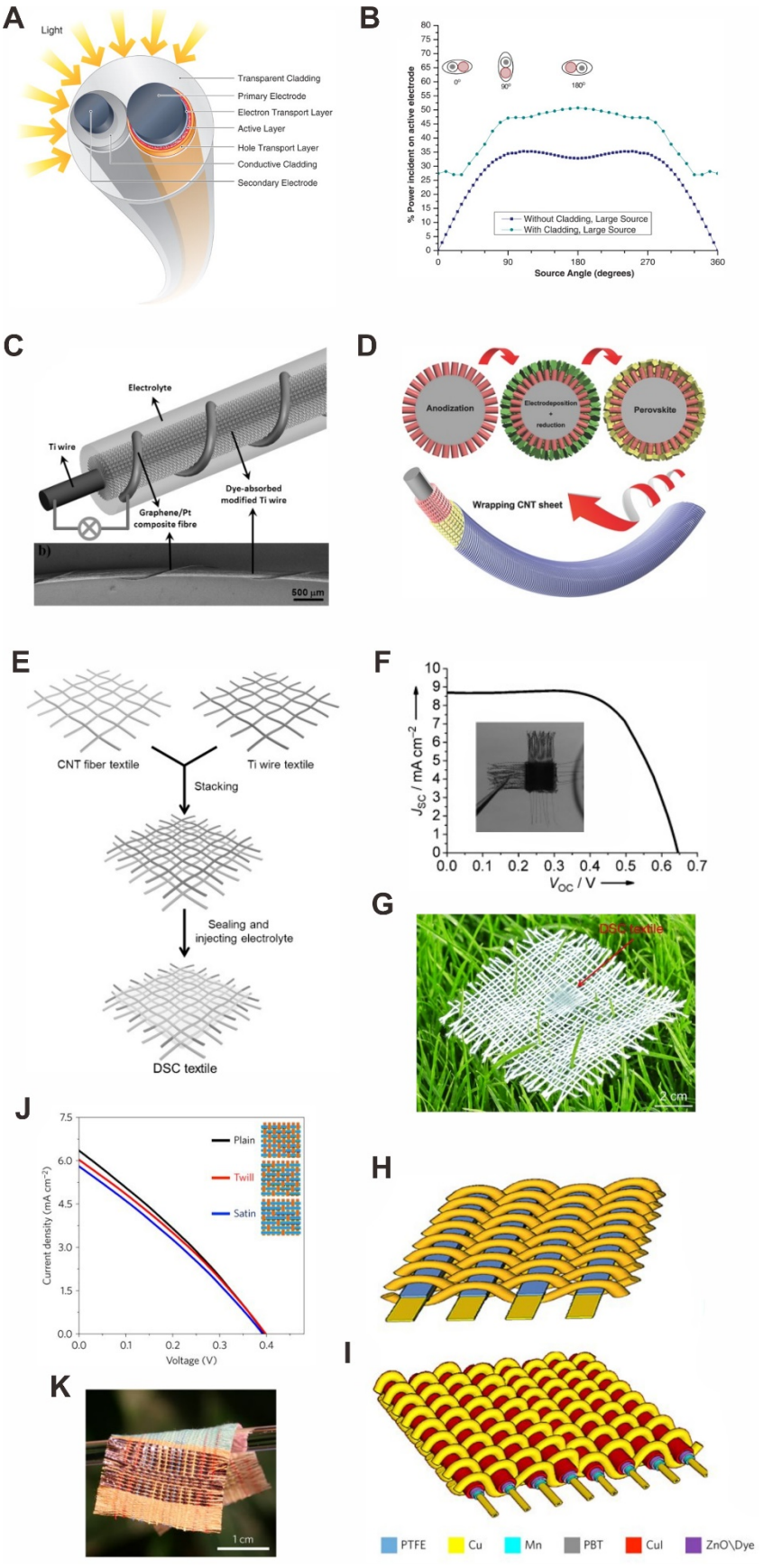
A
Light
Transparent Cladding
Primary Electrode
Electron Transport Layer
Active Layer
Hole Transport Layer
Conductive Cladding
Secondary Electrode
B
% Power incident on active electrode
Source Angle (degrees)
Without Cladding, Large Source
With Cladding, Large Source
C
Electrolyte
Ti wire
Dye-absorbed modified Ti wire
Graphene/Pt composite fibre
b)
500 μm
D
Anodization
Electrodeposition + reduction
Perovskite
Wrapping CNT sheet
E
CNT fiber textile
Ti wire textile
Stacking
Sealing and injecting electrolyte
DSC textile
F
J_{SC} / mA cm^{-2}
V_{OC} / V
G
DSC textile
2 cm
H
I
PTFE
Cu
Mn
PBT
CuI
ZnO\Dye
J
Current density (mA cm^{-2})
Voltage (V)
Plain
Twill
Satin
K
1 cm

Figure 46. (A) Schematics of fiber-shaped OSC using stainless steel wires as electrodes. A transparent polymer cladding was employed as encapsulation and solar concentrator. (B) Estimated power absorbed by the active layer-coated primary electrode versus light incident angle. Reproduced with permission from Ref[799]. Copyright 2009 American Association for the Advancement of Science. (C) Schematics and SEM image of fiber-shaped DSSC with solution-processed Pt/graphene counter electrode and TiO_2 photoanode. Reproduced with permission from Ref[800]. Copyright 2013 WILEY‐VCH Verlag GmbH & Co. KGaA, Weinheim. (D) Schematics of the fabrication process for fiber-based PSC with CNT sheet TE. Reproduced with permission from Ref[803]. Copyright 2016 WILEY‐VCH Verlag GmbH & Co. KGaA, Weinheim. (E) Illustration of the fabrication process for stacked DSSC textile. The liquid electrolyte was filled and encapsulated between CNT and Ti fabrics. (F) J-V curve and photograph (inset) of the DSSC textile, and (G) photograph of the DSSC textile integrated on a large size fabric. Reproduced with permission from Ref[779]. Copyright 2014 WILEY‐VCH Verlag GmbH & Co. KGaA, Weinheim. (H) and (I) Schematics of woven TENG and DSSC, respectively. The conductive Cu-coated yarns were obtained via chemical and electrochemical metal plating. (J) J-V curves of woven DSSC fabric with plain (black), twill (red) and satin (blue) structure. (K) Photograph of the energy harvesting textile woven on colored fabrics. Reproduced with permission from Ref[781]. Copyright 2016 Springer Nature.

Table 7 lists some of the best-reported flexible thin-film solar cells on different substrates in recent years. For planar devices on flexible thin-film substrates, the state-of-the-art OSCs and PSCs exhibited > 12% PCE while maintaining good mechanical robustness. Noting that the performance

of the solar cells is also closely related to other factors such as active materials, ETLs/HTLs, processing methods, active area, and etc., the performance of solution-processed TEs should not be evaluated by comparing efficiencies of solar cells with different configurations. For example, the PEDOT:PSS/Ag mesh-based PSC exhibited 14.2% efficiency, which was not the highest among all reported solar cells with solution-processed TEs. However, such efficiency was slightly higher than that of the ITO-based control device with the same configuration, indicating a better performance of PEDOT:PSS/Ag mesh than that of ITO in this case.[49] The substrate's impact on solar cell efficiencies should also be considered for flexible solar cells. For example, the average efficiency of PEDOT:PSS:CFE-based PSCs on PET substrates (18.0%) was significantly higher than that of ITO-based control devices on PET (14.7%). However, the opposite situation happened on rigid devices with the same device structures (18.4% and 19.5% for PEDOT:PSS:CFE and ITO devices, respectively).[96] Bi et al. suggested that the significant mismatch between ITO/PET and ITO glass for PSCs could be attributed from the poor coverage of perovskite films on ITO/PET, which could be improved by tailoring the composition of perovskite precursor solutions.[808] Whereas PET and PEN films are eligible for low temperature-processed solar cells, some metal oxide-based TE, ETL or HTL requires > 200 °C annealing temperature. Thus, PI or very thin glass films that can sustain high temperature are adopted as alternatives for those polyesters.[809] In brief, using high performance TE is only a necessary condition for high efficiency flexible solar cells, because other factors such as active materials, processing methods, and substrates also play an important role.

Table 7. Typical flexible thin-film solar cells with solution-processed TEs on different substrates.

TE	Substrate	Device Type	V_{OC} (V)	J_{SC} (mA/cm^2)	FF (%)	PCE (%)	Ref.
ZnO/AgNW	PET film	OSC	0.84	22.26	64.66	12.02[a]	[684]
PEDOT:PSS	PET film	OSC	0.885	19.13	72.92	12.35[a]	[650]
PEDOT:PSS	1.4 μm PET film	OSC	0.58	11.9	61	4.2[a]	[46]
Transfer printed ITO	Colorless PI film	OSC	0.821	8.90	68.99	5.04[a]	[810]
PEDOT:PSS	100 μm glass film	OSC	0.86 ± 0.01	14.2 ± 0.5	63.6 ± 0.02	7.7 ± 0.4 (8.0[a])	[811]
CuS	Ti foil	DSSC	0.66	18.10	53.4	6.38[a]	[710]
AgNW/TiO_2[b]	PEN film	DSSC	0.74	6.88	66	3.36[a]	[702]
PEDOT:PSS	PET	PSC	1.07	21.79	77	18.0 (19.0[a])	[96]
PEDOT:PSS/ Ag mesh	PET film	PSC	0.91	19.5	80	14.2[a]	[49]
PEDOT:PSS[c]	1.4 μm PET film	PSC	0.95 ± 0.02	17±0.5	75	12±1	[7]
PEDOT:PSS// PEDOT:PSS[d]	PDMS film	PSC	1.07	18.7	78	15.61[a]	[98]
AZO/AgNW/ AZO	PES film	PSC	0.99	18.9	59.7	11.23[a]	[110]
Graphene	PDMS film	PSC	1.05 ± 0.014	21.45 ± 0.682	74.7 ± 1.31	16.9 ± 0.96 (18.3[a])	[109]
Cu-BHT	PI film	PSC	0.978 ± 0.043	19.26 ± 1.13	64.1 ± 3.6	12.07 ± 1.44	[757]
Graphene	Stainless steel	OSC	0.570	8.14	54.5	2.53[a]	[812]
PEDOT:PSS	Cu-coated PET fabric	OSC	0.58	12.1	41	2.90[a]	[40]
TiO_2 nanotube arrays	Ti wire/Pt wire	DSSC	0.66	18.8	73	9.1[a]	[813]
TiO_2	Stainless steel-Ti fabric	DSSC	0.69	19.70	43	5.83[a]	[814]

CNT	Ti wire	PSC	0.85	14.5	56	7.1[a]	[803]

[a]Champion device PCE. [b]Solid-state cell. [c]Stretchable. [d]Stretchable and semitransparent.

8. Conclusions and Outlook

The progress of the development of solution-processed TEs for thin-film solar cells in recent years has been encouraging. Various categories of materials including conducting polymers, metals and metal oxides, and carbon materials have been incorporated with multiple coating and printing techniques such as spin coating, spray coating, slot-die coating, inkjet printing, screen printing, and transfer printing. In this article, we have reviewed the synthesis and properties of each material, and compared some typical solution-based fabrication processes for TEs with examples. The use of solution-processed TEs for solar cells has the following advantages. 1) The solution-based coating and printing techniques are usually much more cost-effective than traditional vacuum deposition processes because of higher material utilization, higher throughput, and lower energy consumption. 2) The solution-based techniques enable the uniform deposition of TEs on flexible and curved substrates with good adhesion and high mechanical robustness.

From the materials point-of-view, transparent conducting polymers, especially PEDOT and its derivatives, are well-balanced candidates for solution-processed TEs. The state-of-the-art PEDOT-based TEs exhibit comparable FoM to vacuum-deposited ITO on flexible substrates but a notably superior mechanical flexibility. Meanwhile, many cost analyses have suggested a significant lower cost of the solar cells once replacing vacuum-deposited TCOs with solution-processed PEDOT:PSS films. Some other conducting polymers such as PANI and PPy are particularly suitable for semi-transparent DSSCs because of their high electrochemical activity. The conducting polymer can be synthesized as printable inks easily, and thus is versatile for most

of the solution processes. In addition, the conducting polymer based TEs require no high temperature (> 150 °C) post-treatment. These advantages make conducting polymers very promising for large scale R2R fabrication of fully solution-processed thin-film solar cells. However, current conducting polymer based TEs cannot meet the requirements (> 90% optical transmittance and < 10 Ω/□ R_{sh}) for large area commercial solar modules due to the limited conductivity of the polymers. The high electrical conductivity of metals is a huge advantage for electrodes. The solution-processed metal nanomeshes/grids address the issue of poor optical transmittance of conventional vacuum-deposited metal thin films, and provide better electrical conductivity than conventional TCOs for large area applications. As a result, metal-based TEs now become competitive candidates for optoelectronic applications such as solar cells, OLEDs, and touch screens.[149] A remaining issue for most metal/metal oxide nanomaterial based TEs is the requirement of a post-treating process to sinter nanomaterials or to remove the non-conductive residuals. Carbon materials are potentially very high-performance candidates for solution-processed TEs. Whereas a substantial gap between the theoretical values and the experimental performance still exist, the development of large-scale CVD and solution-based synthesis has made it possible for large-area and low-cost carbon-based TEs. It is also worth noting that the combination of two or more materials could further improve the performance of solution-processed TEs. For example, incorporating metal nanowires with conducting polymers or metal oxides reduces the surface roughness of metal nanomeshes/grids while maintaining high electrical conductivity. For large-area solar modules (e.g., 88 m^2 organic solar modules), composite TEs have been proved to be very effective.

From the fabrication point-of-view, the choice of solution-based coating and printing techniques is determined by the application scenarios. Spin coating is widely adopted for the deposition of high-quality TEs with small areas, and thus is ubiquitous in lab-scale fabrication. Among all the solution-based coating and printing techniques mentioned above, the R2R-compatible slot-die coating and screen printing techniques are very promising for the large-scale fabrication of TEs and solar modules.[815] Inkjet printing is a versatile technique for depositing both uniform films and high-resolution meshes/grids. Such advantage lowers the cost of patterned TEs by avoiding additional lithographic processes. In addition, some other R2R techniques such as flexographic printing and gravure printing have also been reported for the deposition of TEs in recent years. Whereas more efforts are required for optimized equipment design and ink formulation, both techniques have revealed promising features[816,817]

In the device part, we have summarized the state-of-the-art OSCs, DSSCs, and PSCs fabricated with solution-processed TEs. The best-performing thin-film solar cells showed comparable efficiency (e.g., > 19% PCE PSCs with PEDOT:PSS) to conventional lab-scale devices fabricated with vacuum-deposited TCOs. The R2R-processability of the solution-processed TEs also generates possibilities for large-scale direct printing of thin-film solar modules. In addition, solution-processed polymer, carbon, and metal TEs show unique advantages for flexible solar cells because of their mechanical robustness and good adhesion to substrates. State-of-the-art flexible solar cells with solution-processed TEs maintain > 90% of their initial PCE after thousands of cycles of bending at small bending radii. Some solution-based coating techniques are compatible with complicated curved surfaces such as textile fabrics, and thus are ideal for the fabrication of textile-based wearable solar cells. Although the development of the solution-processed emerging

thin-film solar cells is still in early stage, we see efforts from both the research community and the industry to commercialize these emerging energy harvesting devices. Up till now, organic solar modules fabricated via these techniques have been available on market, and commercially available perovskite solar modules are believed to be realized very soon.[818]

However, there are still quite a few of challenges of these solution-processed TEs toward large-scale solar modules. The first challenge is the long-term stability of the electrode materials and the devices. For example. the lifetime of commercial Si solar cells is 25 years, which is much longer than that of the best-reported PSC.[819,820] It is estimated that a 30-year lifetime is necessary for 15% PCE perovskite solar modules to meet the target levelized cost of energy (LCOE) of 0.06 USD/kWh (Sunshot 2020 utility-scale solar cost target).[821] For the polymeric TEs, the long-term stability has always been the weakness. The instability may attribute to either the intrinsic property of the TE material itself or the interface between the TE and other layers of the solar cells. For example, the degradation of PEDOT:PSS may be caused by the moisture absorption of PEDOT:PSS, or the interfacial corrosion of the active materials by the acidic PEDOT.[657,822,823] Although the issue can be partially addressed by post treatment and surface modification of the electrodes, the long-term stability of the polymer electrodes still requires comprehensive and detailed studies in the future.[824-826] Similar issue also occurs on metal nanomaterials which show higher chemical reactivity than their bulks. A study of the failure mechanism of AgNW TEs found that the Joule heating generated by the current flow in solar cells could lead to the electrode failure.[827] Another study suggested that light and humidity also have a significant impact on the stability of AgNW TEs.[828] Whereas some research indicated that mixing carbon materials such as graphene and CNTs with AgNWs improves the stability of AgNW, long term study of these

composite TEs remains to be studied.[829,830] Another challenge is the uniformity of solution-processed TEs over large areas. The uniformity, issue which is not important for small-area devices, can be profound for large-area devices. Although there have been some reports demonstrating R2R-processed films with good uniformity, the impact of materials, solvents, coating/printing methods, and the environment on the uniformity of large-area solution-processed TE films remains to be studied.[831,832]

Despite all these challenges, we remain optimistic that the solution-processed TEs shall play important roles in solar cell and optoelectronic industries in the future. In 2013, TEs made of vacuum-deposited ITO dominated 93% of the transparent conductor market.[833] However, this market is changing rapidly as the demand for flexible and wearable optoelectronics keeps increasing. A report from IDTechEx claimed that 25.6% of the manufactured OLED displays were based on plastic substrates in 2017, and this proportion would increase to 35.3% in 2020.[834] The commercialization of flexible solar cells and OLEDs will create more opportunities for the solution-processed flexible TEs. AgNW-based TEs will become a very large market that is comparable to ITO-based TEs in 2028 according to another research report from the same company.[835]

Acknowledgement

We acknowledge the financially support from General Research Fund of Hong Kong (PolyU 153202/16P), and Collaborative Research Fund of Hong Kong (C5037-18G).

References

(1) Cheng, Y.-J.; Yang, S.-H.; Hsu, C.-S. Synthesis of Conjugated Polymers for Organic Solar Cell Applications. *Chem. Rev.* **2009,** *109*, 5868-5923.
(2) Kalowekamo, J.; Baker, E. Estimating the Manufacturing Cost of Purely Organic Solar Cells. *Sol. Energy* **2009,** *83*, 1224-1231.
(3) Machui, F.; Hösel, M.; Li, N.; Spyropoulos, G. D.; Ameri, T.; Søndergaard, R. R.; Jørgensen, M.; Scheel, A.; Gaiser, D.; Kreul, K. Cost Analysis of Roll-To-Roll Fabricated ITO Free Single and Tandem Organic Solar Modules Based on Data from Manufacture. *Energy Environ. Sci.* **2014,** *7*, 2792-2802.
(4) Lee, M. M.; Teuscher, J.; Miyasaka, T.; Murakami, T. N.; Snaith, H. J. Efficient Hybrid Solar Cells Based on Meso-Superstructured Organometal Halide Perovskites. *Science* **2012,** *338*, 643-647.
(5) Li, Z.; Klein, T. R.; Kim, D. H.; Yang, M.; Berry, J. J.; van Hest, M. F.; Zhu, K. Scalable Fabrication of Perovskite Solar Cells. *Nat. Rev. Mater.* **2018,** *3*, 18017.
(6) Cai, M.; Wu, Y.; Chen, H.; Yang, X.; Qiang, Y.; Han, L. Cost-performance Analysis of Perovskite Solar Modules. *Adv. Sci.* **2017,** *4*, 1600269.
(7) Kaltenbrunner, M.; Adam, G.; Głowacki, E. D.; Drack, M.; Schwödiauer, R.; Leonat, L.; Apaydin, D. H.; Groiss, H.; Scharber, M. C.; White, M. S.et al. Flexible High Power-per-weight Perovskite Solar Cells with Chromium Oxide–metal Contacts for Improved Stability in Air. *Nat. Mater.* **2015,** *14*, 1032.
(8) Carr, G. Sunny Uplands: Alternative Energy Will No Longer Be Alternative. https://www.economist.com/news/2012/11/21/sunny-uplands (accessed Nov 06, 2019).
(9) Swanson, R. M. A Vision for Crystalline Silicon Photovoltaics. *Prog. Photovoltaics Res. Appl.* **2006,** *14*, 443-453.
(10) Khan, J.; Arsalan, M. H. Solar Power Technologies for Sustainable Electricity Generation – A Review. *Renewable Sustainable Energy Rev.* **2016,** *55*, 414-425.
(11) Sheats, J. R. Manufacturing and Commercialization Issues in Organic Electronics. *J. Mater. Res.* **2004,** *19*, 1974-1989.
(12) Burke, D. J.; Lipomi, D. J. Green Chemistry for Organic Solar Cells. *Energy Environ. Sci.* **2013,** *6*, 2053-2066.
(13) Brenner, T. M.; Egger, D. A.; Kronik, L.; Hodes, G.; Cahen, D. Hybrid Organic—inorganic Perovskites: Low-cost Semiconductors with Intriguing Charge-transport Properties. *Nat. Rev. Mater.* **2016,** *1*, 15007.

(14) Park, N.-G.; Grätzel, M.; Miyasaka, T.; Zhu, K.; Emery, K. Towards stable and commercially available perovskite solar cells. *Nat. Energy* **2016,** *1*, 16152.
(15) Elangovan, E.; Ramamurthi, K. Studies on Micro-structural and Electrical Properties of Spray-deposited Fluorine-doped Tin Oxide Thin Films from Low-cost Precursor. *Thin Solid Films* **2005,** *476*, 231-236.
(16) Minami, T. Transparent Conducting Oxide Semiconductors for Transparent Electrodes. *Semicond. Sci. Technol.* **2005,** *20*, S35.
(17) Gordon, R. G. Criteria for Choosing Transparent Conductors. *MRS Bull.* **2011,** *25*, 52-57.
(18) Zheng, M.; Horowitz, K.; Woodhouse, M.; Battaglia, C.; Kapadia, R.; Javey, A. III-Vs at Scale: A PV Manufacturing Cost Analysis of the Thin Film Vapor–Liquid–Solid Growth Mode. *Prog. Photovoltaics Res. Appl.* **2016,** *24*, 871-878.
(19) Espinosa, N.; Garcia-Valverde, R.; Urbina, A.; Krebs, F. C. A Life Cycle Analysis of Polymer Solar Cell Modules Prepared Using Roll-to-roll Methods under Ambient Conditions. *Sol. Energy Mater. Sol. Cells* **2011,** *95*, 1293-1302.
(20) Krebs, F. C.; Jørgensen, M.; Norrman, K.; Hagemann, O.; Alstrup, J.; Nielsen, T. D.; Fyenbo, J.; Larsen, K.; Kristensen, J. A Complete Process for Production of Flexible Large Area Polymer Solar Cells Entirely Using Screen Printing—First Public Demonstration. *Sol. Energy Mater. Sol. Cells* **2009,** *93*, 422-441.
(21) Jeon, N. J.; Noh, J. H.; Kim, Y. C.; Yang, W. S.; Ryu, S.; Seok, S. I. Solvent Engineering for High-performance Inorganic–organic Hybrid Perovskite Solar Cells. *Nat. Mater.* **2014,** *13*, 897.
(22) Krebs, F. C. Fabrication and Processing of Polymer Solar Cells: A Review of Printing and Coating Techniques. *Sol. Energy Mater. Sol. Cells* **2009,** *93*, 394-412.
(23) Barrows, A. T.; Pearson, A. J.; Kwak, C. K.; Dunbar, A. D.; Buckley, A. R.; Lidzey, D. G. Efficient Planar Heterojunction Mixed-halide Perovskite Solar Cells Deposited via Spray-deposition. *Energy Environ. Sci.* **2014,** *7*, 2944-2950.
(24) Girotto, C.; Rand, B. P.; Genoe, J.; Heremans, P. Exploring Spray Coating as a Deposition Technique for the Fabrication of Solution-processed Solar Cells. *Sol. Energy Mater. Sol. Cells* **2009,** *93*, 454-458.
(25) Ramasamy, E.; Lee, W. J.; Lee, D. Y.; Song, J. S. Spray Coated Multi-Wall Carbon Nanotube Counter Electrode for Tri-Iodide (I3-) Reduction In Dye-Sensitized Solar Cells. *Electrochem. Commun.* **2008,** *10*, 1087-1089.
(26) Deng, Y.; Peng, E.; Shao, Y.; Xiao, Z.; Dong, Q.; Huang, J. Scalable Fabrication of Efficient Organolead Trihalide Perovskite Solar Cells with Doctor-bladed Active Layers. *Energy Environ. Sci.* **2015,** *8*, 1544-1550.
(27) Tang, S.; Deng, Y.; Zheng, X.; Bai, Y.; Fang, Y.; Dong, Q.; Wei, H.; Huang, J. Composition Engineering in Doctor‐Blading of Perovskite Solar Cells. *Adv. Energy Mater.* **2017,** *7*, 1700302.
(28) Joshi, P.; Xie, Y.; Ropp, M.; Galipeau, D.; Bailey, S.; Qiao, Q. Dye-sensitized Solar Cells Based on Low Cost Nanoscale Carbon/TiO 2 Composite Counter Electrode. *Energy Environ. Sci.* **2009,** *2*, 426-429.
(29) Alstrup, J.; Jørgensen, M.; Medford, A. J.; Krebs, F. C. Ultra Fast and Parsimonious Materials Screening for Polymer Solar Cells Using Differentially Pumped Slot-die Coating. *ACS Appl. Mater. Interfaces* **2010,** *2*, 2819-2827.

(30) Vak, D.; Hwang, K.; Faulks, A.; Jung, Y. S.; Clark, N.; Kim, D. Y.; Wilson, G. J.; Watkins, S. E. 3D Printer Based Slot-Die Coater as a Lab-To-Fab Translation Tool for Solution-Processed Solar Cells. *Adv. Energy Mater.* **2015,** *5*, 1401539.

(31) Hwang, K.; Jung, Y. S.; Heo, Y. J.; Scholes, F. H.; Watkins, S. E.; Subbiah, J.; Jones, D. J.; Kim, D. Y.; Vak, D. Toward large scale roll-to-roll production of fully printed perovskite solar cells. *Adv. Mater.* **2015,** *27*, 1241-1247.

(32) Wei, Z.; Chen, H.; Yan, K.; Yang, S. Inkjet Printing and Instant Chemical Transformation of a CH3NH3PbI3/Nanocarbon Electrode and Interface for Planar Perovskite Solar Cells. *Angew. Chem. Int. Ed.* **2014,** *53*, 13239-13243.

(33) Hoth, C. N.; Choulis, S. A.; Schilinsky, P.; Brabec, C. J. High Photovoltaic Performance of Inkjet Printed Polymer: Fullerene Blends. *Adv. Mater.* **2007,** *19*, 3973-3978.

(34) Hoth, C. N.; Schilinsky, P.; Choulis, S. A.; Brabec, C. J. Printing Highly Efficient Organic Solar Vells. *Nano Lett.* **2008,** *8*, 2806-2813.

(35) Ito, S.; Chen, P.; Comte, P.; Nazeeruddin, M. K.; Liska, P.; Péchy, P.; Grätzel, M. Fabrication of Screen-Printing Pastes from TiO2 Powders for Dye-sensitised Solar Cells. *Prog. Photovoltaics Res. Appl.* **2007,** *15*, 603-612.

(36) Krebs, F. C.; Alstrup, J.; Spanggaard, H.; Larsen, K.; Kold, E. Production of Large-area Polymer Solar Cells by Industrial Silk Screen Printing, Lifetime Considerations and Lamination with Polyethyleneterephthalate. *Sol. Energy Mater. Sol. Cells* **2004,** *83*, 293-300.

(37) Schmidt, T. M.; Larsen-Olsen, T. T.; Carlé, J. E.; Angmo, D.; Krebs, F. C. Upscaling of Perovskite Solar Cells: Fully Ambient Roll Processing of Flexible Perovskite Solar Cells with Printed Back Electrodes. *Adv. Energy Mater.* **2015,** *5*, 1500569.

(38) Lee, C. H.; Kim, D. R.; Cho, I. S.; William, N.; Wang, Q.; Zheng, X. Peel-and-stick: Fabricating Thin Film Solar cell on Universal Substrates. *Sci. Rep.* **2012,** *2*, 1000.

(39) Wang, X.; Ishwara, T.; Gong, W.; Campoy-Quiles, M.; Nelson, J.; Bradley, D. D. C. High-Performance Metal-Free Solar Cells Using Stamp Transfer Printed Vapor Phase Polymerized Poly(3,4-Ethylenedioxythiophene) Top Anodes. *Adv. Funct. Mater.* **2012,** *22*, 1454-1460.

(40) Zhen, H.; Li, K.; Chen, C.; Yu, Y.; Zheng, Z.; Ling, Q. Water-Borne Foldable Polymer Solar Cells: One-Step Transferring Free-Standing Polymer Films onto Woven Fabric Electrodes. *J. Mater. Chem. A* **2017,** *5*, 782-788.

(41) Zhou, Y.; Li, F.; Barrau, S.; Tian, W.; Inganäs, O.; Zhang, F. Inverted and Transparent Polymer Solar Cells Prepared with Vacuum-Free Processing. *Sol. Energy Mater. Sol. Cells* **2009,** *93*, 497-500.

(42) Lee, D.; Paeng, D.; Park, H. K.; Grigoropoulos, C. P. Vacuum-Free, Maskless Patterning of Ni Electrodes by Laser Reductive Sintering of NiO Nanoparticle Ink and Its Application to Transparent Conductors. *ACS Nano* **2014,** *8*, 9807-9814.

(43) Peh, R. J.; Lu, Y.; Zhao, F.; Lee, C.-L. K.; Kwan, W. L. Vacuum-free processed transparent inverted organic solar cells with spray-coated PEDOT: PSS anode. *Sol. Energy Mater. Sol. Cells* **2011,** *95*, 3579-3584.

(44) Van De Lagemaat, J.; Barnes, T. M.; Rumbles, G.; Shaheen, S. E.; Coutts, T. J.; Weeks, C.; Levitsky, I.; Peltola, J.; Glatkowski, P. Organic Solar Cells with Carbon Nanotubes Replacing In 2 O 3: Sn as the Transparent Electrode. *Appl. Phys. Lett.* **2006,** *88*, 233503.

(45) You, J.; Hong, Z.; Yang, Y.; Chen, Q.; Cai, M.; Song, T.-B.; Chen, C.-C.; Lu, S.; Liu, Y.; Zhou, H. Low-Temperature Solution-Processed Perovskite Solar Cells with High Efficiency and Flexibility. *ACS Nano* **2014,** *8*, 1674-1680.
(46) Kaltenbrunner, M.; White, M. S.; Głowacki, E. D.; Sekitani, T.; Someya, T.; Sariciftci, N. S.; Bauer, S. Ultrathin and lightweight organic solar cells with high flexibility. *Nature Communications* **2012,** *3*, 770.
(47) Feng, J.; Zhu, X.; Yang, Z.; Zhang, X.; Niu, J.; Wang, Z.; Zuo, S.; Priya, S.; Liu, S.; Yang, D. Record Efficiency Stable Flexible Perovskite Solar Cell Using Effective Additive Assistant Strategy. *Adv. Mater.* **2018,** *30*, 1801418.
(48) Yoon, J.; Baca, A. J.; Park, S.-I.; Elvikis, P.; GEDDES III, J. B.; Li, L.; Kim, R. H.; Xiao, J.; Wang, S.; Kim, T.-H. In *Materials For Sustainable Energy: A Collection of Peer-Reviewed Research and Review Articles from Nature Publishing Group*; World Scientific, 2011.
(49) Li, Y.; Meng, L.; Yang, Y. M.; Xu, G.; Hong, Z.; Chen, Q.; You, J.; Li, G.; Yang, Y.; Li, Y. High-Efficiency Robust Perovskite Solar Cells on Ultrathin Flexible Substrates. *Nat. Commun.* **2016,** *7*, 10214.
(50) Watson, B. L.; Rolston, N.; Printz, A. D.; Dauskardt, R. H. Scaffold-Reinforced Perovskite Compound Solar Cells. *Energy Environ. Sci.* **2017,** *10*, 2500-2508.
(51) Nathan, A.; Ahnood, A.; Cole, M. T.; Lee, S.; Suzuki, Y.; Hiralal, P.; Bonaccorso, F.; Hasan, T.; Garcia-Gancedo, L.; Dyadyusha, A.et al. Flexible Electronics: The Next Ubiquitous Platform. *Proc. IEEE* **2012,** *100*, 1486-1517.
(52) Lee, M.-W.; Lee, M.-Y.; Choi, J.-C.; Park, J.-S.; Song, C.-K. Fine Patterning of Glycerol-Doped PEDOT: PSS on Hydrophobic PVP Dielectric with Ink Jet for Source and Drain Electrode ff OTFTs. *Org. Electron.* **2010,** *11*, 854-859.
(53) Wei, W.; Wang, H.; Hu, Y. H. A Review on PEDOT-Based Counter Electrodes for Dye-Sensitized Solar Cells. *Int. J. Energy Res.* **2014,** *38*, 1099-1111.
(54) Liang, J.; Tong, K.; Pei, Q. A Water-Based Silver-Nanowire Screen-Print Ink for the Fabrication of Stretchable Conductors and Wearable Thin-Film Transistors. *Adv. Mater.* **2016,** *28*, 5986-5996.
(55) Kim, S.; Kim, S. Y.; Chung, M. H.; Kim, J.; Kim, J. H. A One-step Roll-to-roll Process of Stable AgNW/PEDOT: PSS Solution Using Imidazole as a Mild Base for Highly Conductive and Transparent Films: Optimizations and Mechanisms. *J. Mater. Chem. C* **2015,** *3*, 5859-5868.
(56) Moon, I. K.; Kim, J. I.; Lee, H.; Hur, K.; Kim, W. C.; Lee, H. 2D Graphene Oxide Nanosheets as an Adhesive Over-Coating Layer for Flexible Transparent Conductive Electrodes. *Sci. Rep.* **2013,** *3*, 1112.
(57) Ouyang, J.; Yang, Y. Conducting Polymer as Transparent Electric Glue. *Adv. Mater.* **2006,** *18*, 2141-2144.
(58) Cao, Y.; Treacy, G. M.; Smith, P.; Heeger, A. J. Solution-cast Films of Polyaniline: Optical-quality Transparent Electrodes. *Appl. Phys. Lett.* **1992,** *60*, 2711-2713.
(59) Elschner, A.; Kirchmeyer, S.; Lovenich, W.; Merker, U.; Reuter, K. *PEDOT: Principles and Applications of an Intrinsically Conductive Polymer*; CRC Press, 2010.
(60) Wu, C. G.; Lu, M. I.; Chang, S. J.; Wei, C. S. A Solution-Processable High-Coloration-Efficiency Low-Switching-Voltage Electrochromic Polymer Based on Polycyclopentadithiophene. *Adv. Funct. Mater.* **2007,** *17*, 1063-1070.

(61) Gustafsson-Carlberg, J.; Inganäs, O.; Andersson, M.; Booth, C.; Azens, A.; Granqvist, C. Tuning the Bandgap for Polymeric Smart Windows and Displays. *Electrochim. Acta* **1995,** *40*, 2233-2235.
(62) Lee, S.; Gleason, K. K. Enhanced Optical Property with Tunable Band Gap of Cross-linked PEDOT Copolymers via Oxidative Chemical Vapor Deposition. *Adv. Funct. Mater.* **2015,** *25*, 85-93.
(63) Bredas, J.; Scott, J.; Yakushi, K.; Street, G. Polarons and Bipolarons in Polypyrrole: Evolution of the Band Structure and Optical Spectrum Upon Doing. *Phys. Rev. B* **1984,** *30*, 1023.
(64) Kang, M. G.; Kim, M. S.; Kim, J.; Guo, L. J. Organic Solar Cells Using Nanoimprinted Transparent Metal Electrodes. *Adv. Mater.* **2008,** *20*, 4408-4413.
(65) Hu, L.; Wu, H.; Cui, Y. Metal Nanogrids, Nanowires, and Nanofibers for Transparent Electrodes. *MRS Bull.* **2011,** *36*, 760-765.
(66) Xia, Y.; Sun, K.; Ouyang, J. Solution-Processed Metallic Conducting Polymer Films as Transparent Electrode of Optoelectronic Devices. *Adv. Mater.* **2012,** *24*, 2436-2440.
(67) Hong, S.; Yeo, J.; Kim, G.; Kim, D.; Lee, H.; Kwon, J.; Lee, H.; Lee, P.; Ko, S. H. Nonvacuum, Maskless Fabrication of a Flexible Metal Grid Transparent Conductor by Low-temperature Selective Laser Sintering of Nanoparticle Ink. *ACS Nano* **2013,** *7*, 5024-5031.
(68) Djaoued, Y.; Vu Hong, P.; Badilescu, S.; Ashrit, P. V.; Girouard, F. E.; Vo-Van, T. Sol-gel-prepared ITO Films for Electrochromic Systems. *Thin Solid Films* **1997,** *293*, 108-112.
(69) Lee, K. E.; Wang, M.; Kim, E. J.; Hahn, S. H. Structural, Electrical and Optical Properties of Sol–Gel AZO Thin Films. *Curr. Appl Phys.* **2009,** *9*, 683-687.
(70) Hecht, D. S.; Hu, L.; Irvin, G. Emerging Transparent Electrodes Based on Thin Films of Carbon Nanotubes, Graphene, and Metallic Nanostructures. *Adv. Mater.* **2011,** *23*, 1482-1513.
(71) Wu, Z.; Chen, Z.; Du, X.; Logan, J. M.; Sippel, J.; Nikolou, M.; Kamaras, K.; Reynolds, J. R.; Tanner, D. B.; Hebard, A. F.et al. Transparent, Conductive Carbon Nanotube Films. *Science* **2004,** *305*, 1273-1276.
(72) Wang, X.; Zhi, L.; Tsao, N.; Tomović, Ž.; Li, J.; Müllen, K. Transparent Carbon Films as Electrodes in Organic Solar Cells. *Angew. Chem. Int. Ed.* **2008,** *47*, 2990-2992.
(73) Kim, K. S.; Zhao, Y.; Jang, H.; Lee, S. Y.; Kim, J. M.; Kim, K. S.; Ahn, J.-H.; Kim, P.; Choi, J.-Y.; Hong, B. H. Large-scale Pattern Growth of Graphene Films for Stretchable Transparent Electrodes. *Nature* **2009,** *457*, 706.
(74) Kobayashi, T.; Bando, M.; Kimura, N.; Shimizu, K.; Kadono, K.; Umezu, N.; Miyahara, K.; Hayazaki, S.; Nagai, S.; Mizuguchi, Y. Production of a 100-m-long High-quality Graphene Transparent Conductive Film by Roll-to-roll Chemical Vapor Deposition and Transfer Process. *Appl. Phys. Lett.* **2013,** *102*, 023112.
(75) Bae, S.; Kim, H.; Lee, Y.; Xu, X.; Park, J.-S.; Zheng, Y.; Balakrishnan, J.; Lei, T.; Kim, H. R.; Song, Y. I. Roll-to-roll production of 30-inch graphene films for transparent electrodes. *Nat. Nanotechnol.* **2010,** *5*, 574.
(76) Chandrashekar, B. N.; Deng, B.; Smitha, A. S.; Chen, Y.; Tan, C.; Zhang, H.; Peng, H.; Liu, Z. Roll-to-roll Green Transfer of CVD Graphene onto Plastic for a Transparent and Flexible Triboelectric Nanogenerator. *Adv. Mater.* **2015,** *27*, 5210-5216.

(77) Muhsin, B.; Roesch, R.; Gobsch, G.; Hoppe, H. Flexible ITO-Free Polymer Solar Cells Based on Highly Conductive PEDOT: PSS and a Printed Silver Grid. *Sol. Energy Mater. Sol. Cells* **2014,** *130*, 551-554.
(78) Galagan, Y.; Zimmermann, B.; Coenen, E. W.; Jørgensen, M.; Tanenbaum, D. M.; Krebs, F. C.; Gorter, H.; Sabik, S.; Slooff, L. H.; Veenstra, S. C. Current Collecting Grids for ITO-Free Solar Cells. *Adv. Energy Mater.* **2012,** *2*, 103-110.
(79) Xie, F. X.; Choy, W. C.; Wang, C. C.; Sha, W. E.; Fung, D. D. Improving the Efficiency of Polymer Solar Cells by Incorporating Gold Nanoparticles into All Polymer Layers. *Appl. Phys. Lett.* **2011,** *99*, 219.
(80) Choi, H.; Lee, J.-P.; Ko, S.-J.; Jung, J.-W.; Park, H.; Yoo, S.; Park, O.; Jeong, J.-R.; Park, S.; Kim, J. Y. Multipositional Silica-coated Silver Nanoparticles for High-performance Polymer Solar Cells. *Nano Lett.* **2013,** *13*, 2204-2208.
(81) Notarianni, M.; Vernon, K.; Chou, A.; Aljada, M.; Liu, J.; Motta, N. Plasmonic Effect of Gold Nanoparticles in Organic Solar Cells. *Sol. Energy* **2014,** *106*, 23-37.
(82) Bidan, G. Electroconducting Conjugated Polymers: New Sensitive Matrices to Build up Chemical or Electrochemical Sensors. A Review. *Sens. Actuators, B* **1992,** *6*, 45-56.
(83) Heeger, A. J.; Kivelson, S.; Schrieffer, J. R.; Su, W. P. Solitons in Conducting Polymers. *Rev. Mod. Phys.* **1988,** *60*, 781-850.
(84) Brédas, J. L. Relationship Between Band Gap and Bond Length Alternation in Organic Conjugated Polymers. *The Journal of Chemical Physics* **1985,** *82*, 3808-3811.
(85) Ahlskog, M.; Reghu, M.; Noguchi, T.; Ohnishi, T. Doping and Conductivity Studies on Poly(p-phenylene vinylene). *Synth. Met.* **1997,** *89*, 11-15.
(86) Tsukamoto, J.; Takahashi, A.; Kawasaki, K. Structure and Electrical Properties of Polyacetylene Yielding a Conductivity of 105 S/cm. *Jpn. J. Appl. Phys.* **1990,** *29*, 125.
(87) Naarmann, H.; Theophilou, N. New Process for the Production of Metal-like, Stable Polyacetylene. *Synth. Met.* **1987,** *22*, 1-8.
(88) Deprez, N.; McLachlan, D. S. The Analysis of the Electrical Conductivity of Graphite Conductivity of Graphite Powders During Compaction. *J. Phys. D: Appl. Phys.* **1988,** *21*, 101-107.
(89) Chen, J.-H.; Jang, C.; Xiao, S.; Ishigami, M.; Fuhrer, M. S. Intrinsic and Extrinsic Performance Limits of Graphene Devices on SiO2. *Nat. Nanotechnol.* **2008,** *3*, 206.
(90) Ebbesen, T. W.; Lezec, H. J.; Hiura, H.; Bennett, J. W.; Ghaemi, H. F.; Thio, T. Electrical Conductivity of Individual Carbon Nanotubes. *Nature* **1996,** *382*, 54-56.
(91) Edwards, P. P.; Porch, A.; Jones, M. O.; Morgan, D. V.; Perks, R. M. Basic Materials Physics of Transparent Conducting Oxides. *Dalton Trans.* **2004**, DOI:10.1039/B408864F 10.1039/B408864F2995-3002.
(92) Rao, C. N. R.; Subba Rao, G. V. Electrical Conduction in Metal Oxides. *Phys. Status Solidi A* **1970,** *1*, 597-652.
(93) Polman, A.; Atwater, H. A. Photonic Design Principles for Ultrahigh-Efficiency Photovoltaics. *Nat. Mater.* **2012,** *11*, 174-177.
(94) Lee, U. J.; Lee, S.-H.; Yoon, J. J.; Oh, S. J.; Lee, S. H.; Lee, J. K. Surface Interpenetration Between Conducting Polymer and PET Substrate for Mechanically Reinforced ITO-Free Flexible Organic Solar Cells. *Sol. Energy Mater. Sol. Cells* **2013,** *108*, 50-56.
(95) Zhou, L.; Yu, M.; Chen, X.; Nie, S.; Lai, W.-Y.; Su, W.; Cui, Z.; Huang, W. Screen-Printed Poly(3,4-Ethylenedioxythiophene):Poly(Styrenesulfonate) Grids as ITO-Free

Anodes for Flexible Organic Light-Emitting Diodes. *Adv. Funct. Mater.* **2018,** *28*, 1705955.
(96) Hu, X.; Meng, X.; Zhang, L.; Zhang, Y.; Cai, Z.; Huang, Z.; Su, M.; Wang, Y.; Li, M.; Li, F.et al. A Mechanically Robust Conducting Polymer Network Electrode for Efficient Flexible Perovskite Solar Cells. *Joule* **2019,** *3*, 2205-2218.
(97) Song, W.; Fan, X.; Xu, B.; Yan, F.; Cui, H.; Wei, Q.; Peng, R.; Hong, L.; Huang, J.; Ge, Z. All-Solution-Processed Metal-Oxide-Free Flexible Organic Solar Cells with Over 10% Efficiency. *Adv. Mater.* **2018,** *30*, 1800075.
(98) Hu, X.; Huang, Z.; Li, F.; Su, M.; Huang, Z.; Zhao, Z.; Cai, Z.; Yang, X.; Meng, X.; Li, P.et al. Nacre-inspired Crystallization and Elastic "Brick-and-mortar" Structure for a Wearable Perovskite Solar Module. *Energy Environ. Sci.* **2019,** *12*, 979-987.
(99) Mengistie, D. A.; Ibrahem, M. A.; Wang, P.-C.; Chu, C.-W. Highly Conductive PEDOT:PSS Treated with Formic Acid for ITO-Free Polymer Solar Cells. *ACS Appl. Mater. Interfaces* **2014,** *6*, 2292-2299.
(100) Meng, W.; Ge, R.; Li, Z.; Tong, J.; Liu, T.; Zhao, Q.; Xiong, S.; Jiang, F.; Mao, L.; Zhou, Y. Conductivity Enhancement of PEDOT:PSS Films via Phosphoric Acid Treatment for Flexible All-Plastic Solar Cells. *ACS Appl. Mater. Interfaces* **2015,** *7*, 14089-14094.
(101) Kumar, D.; Stoichkov, V.; Brousseau, E.; Smith, G. C.; Kettle, J. High Performing AgNW Transparent Conducting Electrodes with a Sheet Resistance of 2.5 Ω Sq−1 Based upon a Roll-to-roll Compatible Post-processing Technique. *Nanoscale* **2019,** *11*, 5760-5769.
(102) Guo, F.; Zhu, X.; Forberich, K.; Krantz, J.; Stubhan, T.; Salinas, M.; Halik, M.; Spallek, S.; Butz, B.; Spiecker, E.et al. ITO-Free and Fully Solution-Processed Semitransparent Organic Solar Cells with High Fill Factors. *Adv. Energy Mater.* **2013,** *3*, 1062-1067.
(103) Chen, Z.; Li, W.; Li, R.; Zhang, Y.; Xu, G.; Cheng, H. Fabrication of Highly Transparent and Conductive Indium–Tin Oxide Thin Films with a High Figure of Merit via Solution Processing. *Langmuir* **2013,** *29*, 13836-13842.
(104) Lee, J.; Lee, P.; Lee, H.; Lee, D.; Lee, S. S.; Ko, S. H. Very Long Ag Nanowire Synthesis and Its Application in a Highly Transparent, Conductive and Flexible Metal Electrode Touch Panel. *Nanoscale* **2012,** *4*, 6408-6414.
(105) Jeong, J.-A.; Jeon, Y.-J.; Kim, S.-S.; Kyoung Kim, B.; Chung, K.-B.; Kim, H.-K. Simple Brush-painting of Ti-doped In2O3 Transparent Conducting Electrodes from Nano-particle Solution for Organic Solar Cells. *Sol. Energy Mater. Sol. Cells* **2014,** *122*, 241-250.
(106) Geng, H.-Z.; Kim, K. K.; So, K. P.; Lee, Y. S.; Chang, Y.; Lee, Y. H. Effect of Acid Treatment on Carbon Nanotube-Based Flexible Transparent Conducting Films. *J. Am. Chem. Soc.* **2007,** *129*, 7758-7759.
(107) Jeon, I.; Seo, S.; Sato, Y.; Delacou, C.; Anisimov, A.; Suenaga, K.; Kauppinen, E. I.; Maruyama, S.; Matsuo, Y. Perovskite Solar Cells Using Carbon Nanotubes Both as Cathode and as Anode. *J. Phys. Chem. C* **2017,** *121*, 25743-25749.
(108) Lee, J.-W.; Jeon, I.; Lin, H.-S.; Seo, S.; Han, T.-H.; Anisimov, A.; Kauppinen, E. I.; Matsuo, Y.; Maruyama, S.; Yang, Y. Vapor-Assisted Ex-Situ Doping of Carbon Nanotube toward Efficient and Stable Perovskite Solar Cells. *Nano Lett.* **2019,** *19*, 2223-2230.
(109) Heo, J. H.; Shin, D. H.; Song, D. H.; Kim, D. H.; Lee, S. J.; Im, S. H. Super-flexible Bis(trifluoromethanesulfonyl)-amide Doped Graphene Transparent Conductive

Electrodes for Photo-stable Perovskite Solar Cells. *J. Mater. Chem. A* **2018,** *6*, 8251-8258.
(110) Lee, E.; Ahn, J.; Kwon, H.-C.; Ma, S.; Kim, K.; Yun, S.; Moon, J. All-Solution-Processed Silver Nanowire Window Electrode-Based Flexible Perovskite Solar Cells Enabled with Amorphous Metal Oxide Protection. *Adv. Energy Mater.* **2018,** *8*, 1702182.
(111) You, P.; Liu, Z.; Tai, Q.; Liu, S.; Yan, F. Efficient Semitransparent Perovskite Solar Cells with Graphene Electrodes. *Adv. Mater.* **2015,** *27*, 3632-3638.
(112) Jeong, J.-A.; Kim, J.; Kim, H.-K. Ag Grid/ITO Hybrid Transparent Electrodes Prepared by Inkjet Printing. *Sol. Energy Mater. Sol. Cells* **2011,** *95*, 1974-1978.
(113) Hu, X.; Chen, L.; Zhang, Y.; Hu, Q.; Yang, J.; Chen, Y. Large-Scale Flexible and Highly Conductive Carbon Transparent Electrodes via Roll-to-Roll Process and Its High Performance Lab-Scale Indium Tin Oxide-Free Polymer Solar Cells. *Chem. Mater.* **2014,** *26*, 6293-6302.
(114) Tung, V. C.; Chen, L.-M.; Allen, M. J.; Wassei, J. K.; Nelson, K.; Kaner, R. B.; Yang, Y. Low-Temperature Solution Processing of Graphene−Carbon Nanotube Hybrid Materials for High-Performance Transparent Conductors. *Nano Lett.* **2009,** *9*, 1949-1955.
(115) Barnes, T. M.; Reese, M. O.; Bergeson, J. D.; Larsen, B. A.; Blackburn, J. L.; Beard, M. C.; Bult, J.; van de Lagemaat, J. Comparing the Fundamental Physics and Device Performance of Transparent, Conductive Nanostructured Networks with Conventional Transparent Conducting Oxides. *Adv. Energy Mater.* **2012,** *2*, 353-360.
(116) Hauger, T. C.; Zeberoff, A.; Worfolk, B. J.; Elias, A. L.; Harris, K. D. Real-time Resistance, Transmission and Figure-of-merit Analysis for Transparent Conductors under Stretching-mode Strain. *Sol. Energy Mater. Sol. Cells* **2014,** *124*, 247-255.
(117) O'Connor, B.; Haughn, C.; An, K.-H.; Pipe, K. P.; Shtein, M. Transparent and Conductive Electrodes Based on Unpatterned, Thin Metal Films. *Appl. Phys. Lett.* **2008,** *93*, 223304.
(118) Wang, X.; Zhi, L.; Müllen, K. Transparent, Conductive Graphene Electrodes for Dye-Sensitized Solar Cells. *Nano Lett.* **2008,** *8*, 323-327.
(119) Choi, K. H.; Kim, J. Y.; Lee, Y. S.; Kim, H. J. ITO/Ag/ITO Multilayer Films for the Application of a Very Low Resistance Transparent Electrode. *Thin Solid Films* **1999,** *341*, 152-155.
(120) Axelevitch, A.; Gorenstein, B.; Golan, G. Investigation of Optical Transmission in Thin Metal Films. *Physics Procedia* **2012,** *32*, 1-13.
(121) Kaiser, N. Review of the Fundamentals of Thin-film Growth. *Appl. Opt.* **2002,** *41*, 3053-3060.
(122) Schneider, J.; Rohner, P.; Thureja, D.; Schmid, M.; Galliker, P.; Poulikakos, D. Electrohydrodynamic NanoDrip Printing of High Aspect Ratio Metal Grid Transparent Electrodes. *Adv. Funct. Mater.* **2016,** *26*, 833-840.
(123) Ohsawa, M.; Hashimoto, N. Flexible Transparent Electrode of Gravure Offset Printed Invisible Silver-Grid Laminated with Conductive Polymer. *Mater. Res. Express* **2018,** *5*, 085030.
(124) Wu, H.; Kong, D.; Ruan, Z.; Hsu, P.-C.; Wang, S.; Yu, Z.; Carney, T. J.; Hu, L.; Fan, S.; Cui, Y. A Transparent Electrode Based on a Metal Nanotrough Network. *Nat. Nanotechnol.* **2013,** *8*, 421.
(125) Ajuria, J.; Ugarte, I.; Cambarau, W.; Etxebarria, I.; Tena-Zaera, R.; Pacios, R. Insights on The Working Principles of Flexible and Efficient ITO-free Organic Solar Cells Based on

Solution Processed Ag Nanowire Electrodes. *Sol. Energy Mater. Sol. Cells* **2012,** *102*, 148-152.
(126) Liu, C.-H.; Yu, X. Silver Nanowire-Based Transparent, Flexible, and Conductive Thin Film. *Nanoscale Res. Lett.* **2011,** *6*, 75.
(127) Chen, P.-Y.; Li, C.-T.; Lee, C.-P.; Vittal, R.; Ho, K.-C. PEDOT-decorated Nitrogen-doped Graphene as the Transparent Composite Film for the Counter Electrode of a Dye-sensitized Solar Cell. *Nano Energy* **2015,** *12*, 374-385.
(128) Kovacik, P.; Hierro, G. d.; Livernois, W.; Gleason, K. K. Scale-up of oCVD: Large-area Conductive Polymer Thin Films for Next-Generation Electronics. *Mater. Horiz.* **2015,** *2*, 221-227.
(129) Smolin, Y. Y.; Van Aken, K. L.; Boota, M.; Soroush, M.; Gogotsi, Y.; Lau, K. K. S. Engineering Ultrathin Polyaniline in Micro/Mesoporous Carbon Supercapacitor Electrodes Using Oxidative Chemical Vapor Deposition. *Adv. Mater. Interfaces* **2017,** *4*, 1601201.
(130) Bonaccorso, F.; Sun, Z.; Hasan, T.; Ferrari, A. C. Graphene Photonics and Optoelectronics. *Nat. Photonics* **2010,** *4*, 611.
(131) De, S.; King, P. J.; Lotya, M.; O'Neill, A.; Doherty, E. M.; Hernandez, Y.; Duesberg, G. S.; Coleman, J. N. Flexible, Transparent, Conducting Films of Randomly Stacked Graphene from Surfactant-Stabilized, Oxide-Free Graphene Dispersions. *Small* **2010,** *6*, 458-464.
(132) Hecht, D. S.; Heintz, A. M.; Lee, R.; Hu, L.; Moore, B.; Cucksey, C.; Risser, S. High Conductivity Transparent Carbon Nanotube Films Deposited from Superacid. *Nanotechnology* **2011,** *22*, 075201.
(133) Gamerith, S.; Klug, A.; Scheiber, H.; Scherf, U.; Moderegger, E.; List, E. J. W. Direct Ink-Jet Printing of Ag–Cu Nanoparticle and Ag-Precursor Based Electrodes for OFET Applications. *Adv. Funct. Mater.* **2007,** *17*, 3111-3118.
(134) Kim, A.; Lee, H.; Kwon, H.-C.; Jung, H. S.; Park, N.-G.; Jeong, S.; Moon, J. Fully Solution-processed Transparent Electrodes Based on Silver Nanowire Composites for Perovskite Solar Cells. *Nanoscale* **2016,** *8*, 6308-6316.
(135) Kim, Y.; Ballantyne, A. M.; Nelson, J.; Bradley, D. D. C. Effects of Thickness and Thermal Annealing of the PEDOT:PSS Layer on the Performance of Polymer Solar Cells. *Org. Electron.* **2009,** *10*, 205-209.
(136) Alam, M. J.; Cameron, D. C. Characterization of Transparent Conductive ITO Thin Films Deposited on Titanium Dioxide Film by a Sol–gel Process. *Surf. Coat. Technol.* **2001,** *142-144*, 776-780.
(137) Lee, S. J.; Kim, Y.-H.; Kim, J. K.; Baik, H.; Park, J. H.; Lee, J.; Nam, J.; Park, J. H.; Lee, T.-W.; Yi, G.-R.et al. A Roll-To-Roll Welding Process for Planarized Silver Nanowire Electrodes. *Nanoscale* **2014,** *6*, 11828-11834.
(138) Im, H.-G.; Jin, J.; Ko, J.-H.; Lee, J.; Lee, J.-Y.; Bae, B.-S. Flexible Transparent Conducting Composite Films Using a Monolithically Embedded AgNW Electrode with Robust Performance Stability. *Nanoscale* **2014,** *6*, 711-715.
(139) Krebs, F. C.; Søndergaard, R.; Jørgensen, M. Printed Metal Back Electrodes for R2R Fabricated Polymer Solar Cells Studied Using the LBIC Technique. *Sol. Energy Mater. Sol. Cells* **2011,** *95*, 1348-1353.

(140) Groenendaal, L.; Jonas, F.; Freitag, D.; Pielartzik, H.; Reynolds, J. R. Poly(3,4-ethylenedioxythiophene) and Its Derivatives: Past, Present, and Future. *Adv. Mater.* **2000,** *12*, 481-494.
(141) You, J.; Meng, L.; Song, T.-B.; Guo, T.-F.; Yang, Y.; Chang, W.-H.; Hong, Z.; Chen, H.; Zhou, H.; Chen, Q.et al. Improved Air Stability of Perovskite Solar Cells via Solution-Processed Metal Oxide Transport Layers. *Nat. Nanotechnol.* **2016,** *11*, 75-81.
(142) Jung, E. H.; Jeon, N. J.; Park, E. Y.; Moon, C. S.; Shin, T. J.; Yang, T.-Y.; Noh, J. H.; Seo, J. Efficient, Stable and Scalable Perovskite Solar Cells Using Poly(3-hexylthiophene). *Nature* **2019,** *567*, 511-515.
(143) Kirchartz, T.; Rau, U. What Makes a Good Solar Cell? *Adv. Energy Mater.* **2018,** *8*, 1703385.
(144) Luo, D.; Yang, W.; Wang, Z.; Sadhanala, A.; Hu, Q.; Su, R.; Shivanna, R.; Trindade, G. F.; Watts, J. F.; Xu, Z.et al. Enhanced Photovoltage for Inverted Planar Heterojunction Perovskite Solar Cells. *Science* **2018,** *360*, 1442-1446.
(145) Meng, L.; Zhang, Y.; Wan, X.; Li, C.; Zhang, X.; Wang, Y.; Ke, X.; Xiao, Z.; Ding, L.; Xia, R.et al. Organic and Solution-Processed Tandem Solar Cells with 17.3% Efficiency. *Science* **2018,** *361*, 1094-1098.
(146) Niesen, B.; Rand, B. P.; Van Dorpe, P.; Cheyns, D.; Tong, L.; Dmitriev, A.; Heremans, P. Plasmonic Efficiency Enhancement of High Performance Organic Solar Cells with a Nanostructured Rear Electrode. *Adv. Energy Mater.* **2013,** *3*, 145-150.
(147) Xu, X.; Liu, Z.; Zuo, Z.; Zhang, M.; Zhao, Z.; Shen, Y.; Zhou, H.; Chen, Q.; Yang, Y.; Wang, M. Hole Selective NiO Contact for Efficient Perovskite Solar Cells with Carbon Electrode. *Nano Lett.* **2015,** *15*, 2402-2408.
(148) Rowell, M. W.; McGehee, M. D. Transparent Electrode Requirements for Thin Film Solar Cell Modules. *Energy Environ. Sci.* **2011,** *4*, 131-134.
(149) Sannicolo, T.; Lagrange, M.; Cabos, A.; Celle, C.; Simonato, J.-P.; Bellet, D. Metallic Nanowire-Based Transparent Electrodes for Next Generation Flexible Devices: A Review. *Small* **2016,** *12*, 6052-6075.
(150) Haacke, G. Transparent Conducting Coatings. *Annu. Rev. Mater. Sci.* **1977,** *7*, 73-93.
(151) Ellmer, K. Past achievements and future challenges in the development of optically transparent electrodes. *Nature Photonics* **2012,** *6*, 809.
(152) Luther, J. M.; Jain, P. K.; Ewers, T.; Alivisatos, A. P. Localized Surface Plasmon Resonances Arising from Free Carriers in Doped Quantum Dots. *Nat. Mater.* **2011,** *10*, 361.
(153) Haacke, G. New Figure of Merit for Transparent Vonductors. *J. Appl. Phys.* **1976,** *47*, 4086-4089.
(154) Chu, H.-C.; Chang, Y.-C.; Lin, Y.; Chang, S.-H.; Chang, W.-C.; Li, G.-A.; Tuan, H.-Y. Spray-Deposited Large-Area Copper Nanowire Transparent Conductive Electrodes and Their Uses for Touch Screen Applications. *ACS Appl. Mater. Interfaces* **2016,** *8*, 13009-13017.
(155) Wald, G. The Receptors of Human Color Vision. *Science* **1964,** *145*, 1007-1016.
(156) Dressel, M.; Grüner, G. *Electrodynamics of Solids: Optical Properties of Electrons in Matter*; Cambridge University Press: Cambridge, 2002.
(157) Kim, N.; Kang, H.; Lee, J.-H.; Kee, S.; Lee, S. H.; Lee, K. Highly Conductive All-Plastic Electrodes Fabricated Using a Novel Chemically Controlled Transfer-Printing Method. *Adv. Mater.* **2015,** *27*, 2317-2323.

(158) Wu, J.; Agrawal, M.; Becerril, H. A.; Bao, Z.; Liu, Z.; Chen, Y.; Peumans, P. Organic Light-Emitting Diodes on Solution-Processed Graphene Transparent Electrodes. *ACS Nano* **2010,** *4*, 43-48.
(159) Rowell, M. W.; Topinka, M. A.; McGehee, M. D.; Prall, H.-J.; Dennler, G.; Sariciftci, N. S.; Hu, L.; Gruner, G. Organic Solar Cells with Carbon Nanotube Network Electrodes. *Appl. Phys. Lett.* **2006,** *88*, 233506.
(160) Wu, J.; Becerril, H. A.; Bao, Z.; Liu, Z.; Chen, Y.; Peumans, P. Organic Solar Cells with Solution-Processed Graphene Transparent Electrodes. *Appl. Phys. Lett.* **2008,** *92*, 263302.
(161) Fraser, D.; Cook, H. Highly Conductive, Transparent Films of Sputtered In2− x Sn x O 3− y. *J. Electrochem. Soc.* **1972,** *119*, 1368-1374.
(162) Kim, A.; Won, Y.; Woo, K.; Jeong, S.; Moon, J. All-Solution-Processed Indium-Free Transparent Composite Electrodes based on Ag Nanowire and Metal Oxide for Thin-Film Solar Cells. *Adv. Funct. Mater.* **2014,** *24*, 2462-2471.
(163) José Andrés, L.; Fe Menéndez, M.; Gómez, D.; Luisa Martínez, A.; Bristow, N.; Paul Kettle, J.; Menéndez, A.; Ruiz, B. Rapid Synthesis of Ultra-long Silver Nanowires for Tailor-made Transparent Conductive Electrodes: Proof of Concept in Organic Solar Cells. *Nanotechnology* **2015,** *26*, 265201.
(164) Vosgueritchian, M.; Lipomi, D. J.; Bao, Z. Highly Conductive and Transparent PEDOT:PSS Films with a Fluorosurfactant for Stretchable and Flexible Transparent Electrodes. *Adv. Funct. Mater.* **2012,** *22*, 421-428.
(165) Cai, G.; Darmawan, P.; Cui, M.; Wang, J.; Chen, J.; Magdassi, S.; Lee, P. S. Highly Stable Transparent Conductive Silver Grid/PEDOT:PSS Electrodes for Integrated Bifunctional Flexible Electrochromic Supercapacitors. *Adv. Energy Mater.* **2016,** *6*, 1501882.
(166) Bae, S.; Kim, H.; Lee, Y.; Xu, X.; Park, J.-S.; Zheng, Y.; Balakrishnan, J.; Lei, T.; Ri Kim, H.; Song, Y. I.et al. Roll-to-roll Production of 30-inch Graphene Films for Transparent Electrodes. *Nat. Nanotechnol.* **2010,** *5*, 574.
(167) Ricciardulli, A. G.; Yang, S.; Wetzelaer, G.-J. A. H.; Feng, X.; Blom, P. W. M. Hybrid Silver Nanowire and Graphene-Based Solution-Processed Transparent Electrode for Organic Optoelectronics. *Adv. Funct. Mater.* **2018,** *28*, 1706010.
(168) Deng, B.; Hsu, P.-C.; Chen, G.; Chandrashekar, B. N.; Liao, L.; Ayitimuda, Z.; Wu, J.; Guo, Y.; Lin, L.; Zhou, Y.et al. Roll-to-Roll Encapsulation of Metal Nanowires between Graphene and Plastic Substrate for High-Performance Flexible Transparent Electrodes. *Nano Lett.* **2015,** *15*, 4206-4213.
(169) Jiang, S.; Hou, P.-X.; Chen, M.-L.; Wang, B.-W.; Sun, D.-M.; Tang, D.-M.; Jin, Q.; Guo, Q.-X.; Zhang, D.-D.; Du, J.-H.et al. Ultrahigh-performance Transparent Conductive Films of Carbon-welded Isolated Single-wall Carbon Nanotubes. *Sci. Adv.* **2018,** *4*, eaap9264.
(170) Mirri, F.; Ma, A. W. K.; Hsu, T. T.; Behabtu, N.; Eichmann, S. L.; Young, C. C.; Tsentalovich, D. E.; Pasquali, M. High-Performance Carbon Nanotube Transparent Conductive Films by Scalable Dip Coating. *ACS Nano* **2012,** *6*, 9737-9744.
(171) Sorel, S.; Lyons, P. E.; De, S.; Dickerson, J. C.; Coleman, J. N. The Dependence of the Optoelectrical Properties of Silver Nanowire Networks on Nanowire Length and Diameter. *Nanotechnology* **2012,** *23*, 185201.

(172) De, S.; King, P. J.; Lyons, P. E.; Khan, U.; Coleman, J. N. Size Effects and the Problem with Percolation in Nanostructured Transparent Conductors. *ACS Nano* **2010,** *4*, 7064-7072.
(173) Muzzillo, C. P. Metal Nano-Grids for Transparent Conduction in Solar Cells. *Sol. Energy Mater. Sol. Cells* **2017,** *169*, 68-77.
(174) Müller, J.; Rech, B.; Springer, J.; Vanecek, M. TCO and Light Trapping in Silicon Thin Film Solar Cells. *Sol. Energy* **2004,** *77*, 917-930.
(175) Krč, J.; Zeman, M.; Kluth, O.; Smole, F.; Topič, M. Effect of Surface Roughness of ZnO:Al Films on Light Scattering in Hydrogenated Amorphous Silicon Solar Cells. *Thin Solid Films* **2003,** *426*, 296-304.
(176) Kang, G.; Bae, K.; Nam, M.; Ko, D.-H.; Kim, K.; Padilla, W. J. Broadband and Ultrahigh Optical Haze Thin Films with Self-Aggregated Alumina Nanowire Bundles for Photovoltaic Applications. *Energy Environ. Sci.* **2015,** *8*, 2650-2656.
(177) Preston, C.; Xu, Y.; Han, X.; Munday, J. N.; Hu, L. Optical Haze of Transparent and Conductive Silver Nanowire Films. *Nano Res.* **2013,** *6*, 461-468.
(178) Wang, B.-Y.; Yoo, T.-H.; Lim, J. W.; Sang, B.-I.; Lim, D.-S.; Choi, W. K.; Hwang, D. K.; Oh, Y.-J. Enhanced Light Scattering and Trapping Effect of Ag Nanowire Mesh Electrode for High Efficient Flexible Organic Solar Cell. *Small* **2015,** *11*, 1905-1911.
(179) Li, K.; Zhang, Y.; Zhen, H.; Wang, H.; Liu, S.; Yan, F.; Zheng, Z. Versatile Biomimetic Haze Films for Efficiency Enhancement of Photovoltaic Devices. *J. Mater. Chem. A* **2017,** *5*, 969-974.
(180) Morales-Masis, M.; De Wolf, S.; Woods-Robinson, R.; Ager, J. W.; Ballif, C. Transparent Electrodes for Efficient Optoelectronics. *Adv. Electron. Mater.* **2017,** *3*, 1600529.
(181) He, Z.; Zhong, C.; Su, S.; Xu, M.; Wu, H.; Cao, Y. Enhanced Power-conversion Efficiency in Polymer Solar Cells using an Inverted Device Structure. *Nat. Photonics* **2012,** *6*, 591.
(182) Wöhrle, D.; Meissner, D. Organic Solar Cells. *Adv. Mater.* **1991,** *3*, 129-138.
(183) Biswas, P. K.; De, A.; Dua, L. K.; Chkoda, L. Work Function of Sol–gel Indium Tin Oxide (ITO) Films on Glass. *Appl. Surf. Sci.* **2006,** *253*, 1953-1959.
(184) Shi, Y.; Kim, K. K.; Reina, A.; Hofmann, M.; Li, L.-J.; Kong, J. Work Function Engineering of Graphene Electrode via Chemical Doping. *ACS Nano* **2010,** *4*, 2689-2694.
(185) Michaelson, H. B. The Work Function of the Elements and Its Periodicity. *J. Appl. Phys.* **1977,** *48*, 4729-4733.
(186) Sugiyama, K.; Ishii, H.; Ouchi, Y.; Seki, K. Dependence of Indium–Tin–Oxide Work Function on Surface Cleaning Method as Studied by Ultraviolet and X-Ray Photoemission Spectroscopies. *J. Appl. Phys.* **2000,** *87*, 295-298.
(187) Nardes, A. M.; Kemerink, M.; De Kok, M.; Vinken, E.; Maturova, K.; Janssen, R. Conductivity, Work Function, and Environmental Stability of PEDOT:PSS Thin Films Treated with Sorbitol. *Org. Electron.* **2008,** *9*, 727-734.
(188) Benor, A.; Takizawa, S.-y.; Pérez-Bolívar, C.; Anzenbacher, P. Efficiency Improvement of Fluorescent OLEDs by Tuning the Working Function of PEDOT:PSS Using UV–ozone Exposure. *Org. Electron.* **2010,** *11*, 938-945.
(189) Zhou, T.; Xie, G.; Gong, S.; Huang, M.; Luo, J.; Yang, C. Simple InCl3 Doped PEDOT:PSS and UV–Ozone Treatment Strategy: External Quantum Efficiency up to

21% for Solution-Processed Organic Light-Emitting Devices with a Thermally Activated Delayed Fluorescence Emitter. *ACS Appl. Mater. Interfaces* **2017,** *9*, 34139-34145.
(190) de Boer, B.; Hadipour, A.; Mandoc, M. M.; van Woudenbergh, T.; Blom, P. W. M. Tuning of Metal Work Functions with Self-Assembled Monolayers. *Adv. Mater.* **2005,** *17*, 621-625.
(191) Li, Z.; Liang, Y.; Zhong, Z.; Qian, J.; Liang, G.; Zhao, K.; Shi, H.; Zhong, S.; Yin, Y.; Tian, W. A Low-Work-Function, High-Conductivity PEDOT:PSS Electrode for Organic Solar Cells with a Simple Structure. *Synth. Met.* **2015,** *210*, 363-366.
(192) Zhou, Y.; Fuentes-Hernandez, C.; Shim, J.; Meyer, J.; Giordano, A. J.; Li, H.; Winget, P.; Papadopoulos, T.; Cheun, H.; Kim, J.et al. A Universal Method to Produce Low–Work Function Electrodes for Organic Electronics. *Science* **2012,** *336*, 327-332.
(193) Li, K.; Zhen, H.; Niu, L.; Fang, X.; Zhang, Y.; Guo, R.; Yu, Y.; Yan, F.; Li, H.; Zheng, Z. Full-Solution Processed Flexible Organic Solar Cells Using Low-Cost Printable Copper Electrodes. *Adv. Mater.* **2014,** *26*, 7271-7278.
(194) Zhang, Y.; Chen, L.; Hu, X.; Zhang, L.; Chen, Y. Low Work-function Poly(3,4-ethylenedioxylenethiophene): Poly(styrene sulfonate) as Electron-transport Layer for High-efficient and Stable Polymer Solar Cells. *Sci. Rep.* **2015,** *5*, 12839.
(195) Zhou, H.; Chen, Q.; Li, G.; Luo, S.; Song, T.-b.; Duan, H.-S.; Hong, Z.; You, J.; Liu, Y.; Yang, Y. Interface Engineering of Highly Efficient Perovskite Solar Cells. *Science* **2014,** *345*, 542-546.
(196) Ahn, S.; Jeong, S.-H.; Han, T.-H.; Lee, T.-W. Conducting Polymers as Anode Buffer Materials in Organic and Perovskite Optoelectronics. *Advanced Optical Materials* **2017,** *5*, 1600512.
(197) Abdulrazzaq, O.; Bourdo, S. E.; Saini, V.; Watanabe, F.; Barnes, B.; Ghosh, A.; Biris, A. S. Tuning the work function of polyaniline via camphorsulfonic acid: an X-ray photoelectron spectroscopy investigation. *RSC Adv.* **2015,** *5*, 33-40.
(198) Gupta, R.; Misra, S. C. K.; Malhotra, B. D.; Beladakere, N. N.; Chandra, S. Metal/semiconductive Polymer Schottky Device. *Appl. Phys. Lett.* **1991,** *58*, 51-52.
(199) Yu, Y.-J.; Zhao, Y.; Ryu, S.; Brus, L. E.; Kim, K. S.; Kim, P. Tuning the Graphene Work Function by Electric Field Effect. *Nano Lett.* **2009,** *9*, 3430-3434.
(200) Shiraishi, M.; Ata, M. Work Function of Carbon Nanotubes. *Carbon* **2001,** *39*, 1913-1917.
(201) Yang, L.; Zhang, T.; Zhou, H.; Price, S. C.; Wiley, B. J.; You, W. Solution-Processed Flexible Polymer Solar Cells with Silver Nanowire Electrodes. *ACS Appl. Mater. Interfaces* **2011,** *3*, 4075-4084.
(202) Chen, J.; Zhou, W.; Chen, J.; Fan, Y.; Zhang, Z.; Huang, Z.; Feng, X.; Mi, B.; Ma, Y.; Huang, W. Solution-processed Copper Nanowire Flexible Transparent Electrodes with PEDOT:PSS as Binder, Protector and Oxide-layer Scavenger for Polymer Solar Cells. *Nano Res.* **2015,** *8*, 1017-1025.
(203) Sheats, J. R.; Antoniadis, H.; Hueschen, M.; Leonard, W.; Miller, J.; Moon, R.; Roitman, D.; Stocking, A. Organic Electroluminescent Devices. *Science* **1996,** *273*, 884-888.
(204) Zhao, J.; Xie, S.; Han, S.; Yang, Z.; Ye, L.; Yang, T. Organic Light-Emitting Diodes with AZO Films as Electrodes. *Synth. Met.* **2000,** *114*, 251-254.
(205) Bulliard, X.; Ihn, S.-G.; Yun, S.; Kim, Y.; Choi, D.; Choi, J.-Y.; Kim, M.; Sim, M.; Park, J.-H.; Choi, W.et al. Enhanced Performance in Polymer Solar Cells by Surface Energy Control. *Adv. Funct. Mater.* **2010,** *20*, 4381-4387.

(206) Zuo, L.; Gu, Z.; Ye, T.; Fu, W.; Wu, G.; Li, H.; Chen, H. Enhanced Photovoltaic Performance of CH3NH3PbI3 Perovskite Solar Cells through Interfacial Engineering Using Self-Assembling Monolayer. *J. Am. Chem. Soc.* **2015,** *137*, 2674-2679.
(207) Zheng, Z.; Hu, Q.; Zhang, S.; Zhang, D.; Wang, J.; Xie, S.; Wang, R.; Qin, Y.; Li, W.; Hong, L.et al. A Highly Efficient Non-Fullerene Organic Solar Cell with a Fill Factor over 0.80 Enabled by a Fine-Tuned Hole-Transporting Layer. *Adv. Mater.* **2018,** *30*, 1801801.
(208) Dahou, F. Z.; Cattin, L.; Garnier, J.; Ouerfelli, J.; Morsli, M.; Louarn, G.; Bouteville, A.; Khellil, A.; Bernède, J. C. Influence of Anode Roughness and Buffer Layer Nature on Organic Solar Cells Performance. *Thin Solid Films* **2010,** *518*, 6117-6122.
(209) Steirer, K. X.; Berry, J. J.; Reese, M. O.; van Hest, M. F. A. M.; Miedaner, A.; Liberatore, M. W.; Collins, R. T.; Ginley, D. S. Ultrasonically Sprayed and Inkjet Printed Thin Film Electrodes for Organic Solar Cells. *Thin Solid Films* **2009,** *517*, 2781-2786.
(210) Xu, Y.; Long, G.; Huang, L.; Huang, Y.; Wan, X.; Ma, Y.; Chen, Y. Polymer Photovoltaic Devices with Transparent Graphene Electrodes Produced by Spin-Casting. *Carbon* **2010,** *48*, 3308-3311.
(211) Wu, Z.; Bai, S.; Xiang, J.; Yuan, Z.; Yang, Y.; Cui, W.; Gao, X.; Liu, Z.; Jin, Y.; Sun, B. Efficient Planar Heterojunction Perovskite Solar Cells Employing Graphene Oxide as Hole Conductor. *Nanoscale* **2014,** *6*, 10505-10510.
(212) Richardson, B. J.; Wang, X.; Almutairi, A.; Yu, Q. High Efficiency PTB7-Based Inverted Organic Photovoltaics on Nano-Ridged and Planar Zinc Oxide Electron Transport Layers. *J. Mater. Chem. A* **2015,** *3*, 5563-5571.
(213) Chen, D.; Huang, F.; Cheng, Y.-B.; Caruso, R. A. Mesoporous Anatase TiO2 Beads with High Surface Areas and Controllable Pore Sizes: A Superior Candidate for High-Performance Dye-Sensitized Solar Cells. *Adv. Mater.* **2009,** *21*, 2206-2210.
(214) Zukalová, M.; Zukal, A.; Kavan, L.; Nazeeruddin, M. K.; Liska, P.; Grätzel, M. Organized Mesoporous TiO2 Films Exhibiting Greatly Enhanced Performance in Dye-Sensitized Solar Cells. *Nano Lett.* **2005,** *5*, 1789-1792.
(215) Zheng, L.; Ma, Y.; Chu, S.; Wang, S.; Qu, B.; Xiao, L.; Chen, Z.; Gong, Q.; Wu, Z.; Hou, X. Improved Light Absorption and Charge Transport for Perovskite Solar Cells with Rough Interfaces by Sequential Deposition. *Nanoscale* **2014,** *6*, 8171-8176.
(216) Galagan, Y.; J.M. Rubingh, J.-E.; Andriessen, R.; Fan, C.-C.; W.M. Blom, P.; C. Veenstra, S.; M. Kroon, J. ITO-free Flexible Organic Solar Cells with Printed Current Collecting Grids. *Sol. Energy Mater. Sol. Cells* **2011,** *95*, 1339-1343.
(217) Lee, J.-Y.; Connor, S. T.; Cui, Y.; Peumans, P. Solution-Processed Metal Nanowire Mesh Transparent Electrodes. *Nano Lett.* **2008,** *8*, 689-692.
(218) Yim, J. H.; Joe, S.-y.; Pang, C.; Lee, K. M.; Jeong, H.; Park, J.-Y.; Ahn, Y. H.; de Mello, J. C.; Lee, S. Fully Solution-Processed Semitransparent Organic Solar Cells with a Silver Nanowire Cathode and a Conducting Polymer Anode. *ACS Nano* **2014,** *8*, 2857-2863.
(219) Hauger, T. C.; Al-Rafia, S. M. I.; Buriak, J. M. Rolling Silver Nanowire Electrodes: Simultaneously Addressing Adhesion, Roughness, and Conductivity. *ACS Appl. Mater. Interfaces* **2013,** *5*, 12663-12671.
(220) Tokuno, T.; Nogi, M.; Karakawa, M.; Jiu, J.; Nge, T. T.; Aso, Y.; Suganuma, K. Fabrication of Silver Nanowire Transparent Electrodes at Room Temperature. *Nano Res.* **2011,** *4*, 1215-1222.

(221) Seo, J. H.; Hwang, I.; Um, H.-D.; Lee, S.; Lee, K.; Park, J.; Shin, H.; Kwon, T.-H.; Kang, S. J.; Seo, K. Cold Isostatic-Pressured Silver Nanowire Electrodes for Flexible Organic Solar Cells via Room-Temperature Processes. *Adv. Mater.* **2017,** *29*, 1701479.
(222) Meng, Y.; Hu, Z.; Ai, N.; Jiang, Z.; Wang, J.; Peng, J.; Cao, Y. Improving the Stability of Bulk Heterojunction Solar Cells by Incorporating pH-Neutral PEDOT:PSS as the Hole Transport Layer. *ACS Appl. Mater. Interfaces* **2014,** *6*, 5122-5129.
(223) Wang, Q.; Chueh, C.-C.; Eslamian, M.; Jen, A. K. Y. Modulation of PEDOT:PSS pH for Efficient Inverted Perovskite Solar Cells with Reduced Potential Loss and Enhanced Stability. *ACS Appl. Mater. Interfaces* **2016,** *8*, 32068-32076.
(224) Wang, R.; Mujahid, M.; Duan, Y.; Wang, Z.-K.; Xue, J.; Yang, Y. A Review of Perovskites Solar Cell Stability. *Adv. Funct. Mater. 0*, 1808843.
(225) Han, Y.; Meyer, S.; Dkhissi, Y.; Weber, K.; Pringle, J. M.; Bach, U.; Spiccia, L.; Cheng, Y.-B. Degradation Observations of Encapsulated Planar CH3NH3PbI3 Perovskite Solar Cells at High Temperatures and Humidity. *J. Mater. Chem. A* **2015,** *3*, 8139-8147.
(226) Bi, E.; Chen, H.; Xie, F.; Wu, Y.; Chen, W.; Su, Y.; Islam, A.; Grätzel, M.; Yang, X.; Han, L. Diffusion Engineering of Ions and Charge Carriers for Stable Efficient Perovskite Solar Cells. *Nat. Commun.* **2017,** *8*, 15330.
(227) Sears, K. K.; Fievez, M.; Gao, M.; Weerasinghe, H. C.; Easton, C. D.; Vak, D. ITO-Free Flexible Perovskite Solar Cells Based on Roll-to-Roll, Slot-Die Coated Silver Nanowire Electrodes. *Sol. RRL* **2017,** *1*, 1700059.
(228) Huo, D.; Kim, M. J.; Lyu, Z.; Shi, Y.; Wiley, B. J.; Xia, Y. One-Dimensional Metal Nanostructures: From Colloidal Syntheses to Applications. *Chem. Rev.* **2019,** *119*, 8972-9073.
(229) Dou, L.; Cui, F.; Yu, Y.; Khanarian, G.; Eaton, S. W.; Yang, Q.; Resasco, J.; Schildknecht, C.; Schierle-Arndt, K.; Yang, P. Solution-Processed Copper/Reduced-Graphene-Oxide Core/Shell Nanowire Transparent Conductors. *ACS Nano* **2016,** *10*, 2600-2606.
(230) Niu, Z.; Cui, F.; Yu, Y.; Becknell, N.; Sun, Y.; Khanarian, G.; Kim, D.; Dou, L.; Dehestani, A.; Schierle-Arndt, K.et al. Ultrathin Epitaxial Cu@Au Core–Shell Nanowires for Stable Transparent Conductors. *J. Am. Chem. Soc.* **2017,** *139*, 7348-7354.
(231) Chen, Z.; Ye, S.; Stewart, I. E.; Wiley, B. J. Copper Nanowire Networks with Transparent Oxide Shells That Prevent Oxidation without Reducing Transmittance. *ACS Nano* **2014,** *8*, 9673-9679.
(232) Hsu, P.-C.; Wu, H.; Carney, T. J.; McDowell, M. T.; Yang, Y.; Garnett, E. C.; Li, M.; Hu, L.; Cui, Y. Passivation Coating on Electrospun Copper Nanofibers for Stable Transparent Electrodes. *ACS Nano* **2012,** *6*, 5150-5156.
(233) Chu, C. R.; Lee, C.; Koo, J.; Lee, H. M. Fabrication of Sintering-Free Flexible Copper Nanowire/Polymer Composite Transparent Electrodes with Enhanced Chemical and Mechanical Stability. *Nano Res.* **2016,** *9*, 2162-2173.
(234) Sajjad, M. T.; Park, J.; Gaboriau, D.; Harwell, J. R.; Odobel, F.; Reiss, P.; Samuel, I. D. W.; Aldakov, D. CuSCN Nanowires as Electrodes for p-Type Quantum Dot Sensitized Solar Cells: Charge Transfer Dynamics and Alumina Passivation. *J. Phys. Chem. C* **2018,** *122*, 5161-5170.
(235) Adhyaksa, G. W. P.; Veldhuizen, L. W.; Kuang, Y.; Brittman, S.; Schropp, R. E. I.; Garnett, E. C. Carrier Diffusion Lengths in Hybrid Perovskites: Processing, Composition, Aging, and Surface Passivation Effects. *Chem. Mater.* **2016,** *28*, 5259-5263.

(236) Kaneto, K.; Kohno, Y.; Yoshino, K.; Inuishi, Y. Electrochemical Preparation of a Metallic Polythiophene Film. *J. Chem. Soc., Chem. Commun.* **1983,** 382-383.
(237) Ofer, D.; Crooks, R. M.; Wrighton, M. S. Potential Dependence of the Conductivity of Highly Oxidized Polythiophenes, Polypyrroles, and Polyaniline: Finite Windows of High Conductivity. *J. Am. Chem. Soc.* **1990,** *112*, 7869-7879.
(238) Sato, M.-a.; Tanaka, S.; Kaeriyama, K. Soluble Conducting Polythiophenes. *J. Chem. Soc., Chem. Commun.* **1986,** 873-874.
(239) Chang, Y. T.; Hsu, S. L.; Su, M. H.; Wei, K. H. Soluble Phenanthrenyl-Imidazole-Presenting Regioregular Poly (3-octylthiophene) Copolymers Having Tunable Bandgaps for Solar Cell Applications. *Adv. Funct. Mater.* **2007,** *17*, 3326-3331.
(240) Cui, Y.; Yang, C.; Yao, H.; Zhu, J.; Wang, Y.; Jia, G.; Gao, F.; Hou, J. Efficient Semitransparent Organic Solar Cells with Tunable Color enabled by an Ultralow-Bandgap Nonfullerene Acceptor. *Adv. Mater.* **2017,** *29*, 1703080.
(241) Lam, J. W.; Tang, B. Z. Functional Polyacetylenes. *Acc. Chem. Res.* **2005,** *38*, 745-754.
(242) Masuda, T.; Tang, B. Z.; Higashimura, T.; Yamaoka, H. Thermal Degradation of Polyacetylenes Carrying Substituents. *Macromolecules* **1985,** *18*, 2369-2373.
(243) Drillet, J.-F.; Dittmeyer, R.; Jüttner, K. Activity and Long-term Stability of PEDOT as Pt Catalyst Support for the DMFC Anode. *J. Appl. Electrochem.* **2007,** *37*, 1219-1226.
(244) Crispin, X.; Jakobsson, F.; Crispin, A.; Grim, P.; Andersson, P.; Volodin, A.; Van Haesendonck, C.; Van der Auweraer, M.; Salaneck, W. R.; Berggren, M. The Origin of the High Conductivity of Poly (3, 4-ethylenedioxythiophene)− poly (styrenesulfonate)(PEDOT− PSS) Plastic Electrodes. *Chem. Mater.* **2006,** *18*, 4354-4360.
(245) Kim, Y. H.; Sachse, C.; Machala, M. L.; May, C.; Müller-Meskamp, L.; Leo, K. Highly Conductive PEDOT:PSS Electrode with Optimized Solvent and Thermal Post-Treatment for ITO-Free Organic Solar Cells. *Adv. Funct. Mater.* **2011,** *21*, 1076-1081.
(246) Alemu, D.; Wei, H.-Y.; Ho, K.-C.; Chu, C.-W. Highly Conductive PEDOT: PSS Electrode by Simple Film Treatment with Methanol for ITO-free Polymer Solar Cells. *Energy Environ. Sci.* **2012,** *5*, 9662-9671.
(247) Krebs, F. C. All Solution Roll-to-roll Processed Polymer Solar Cells Free from Indium-tin-oxide and Vacuum Coating Steps. *Org. Electron.* **2009,** *10*, 761-768.
(248) Krebs, F. C.; Fyenbo, J.; Jørgensen, M. Product Integration of Compact Roll-to-roll Processed Polymer Solar Cell Modules: Methods and Manufacture Using Flexographic Printing, Slot-die Coating and Rotary Screen Printing. *J. Mater. Chem.* **2010,** *20*, 8994-9001.
(249) Emmott, C. J.; Urbina, A.; Nelson, J. Environmental and Economic Assessment of ITO-free Electrodes for Organic Solar Cells. *Sol. Energy Mater. Sol. Cells* **2012,** *97*, 14-21.
(250) Gogte, V.; Shah, L.; Tilak, B.; Gadekar, K.; Sahasrabudhe, M. Synthesis of Potential Anticancer Agents—I: Synthesis of Substituted Thiophenes. *Tetrahedron* **1967,** *23*, 2437-2441.
(251) Caras-Quintero, D.; Bäuerle, P. Synthesis of the First Enantiomerically Pure and Chiral, Disubstituted 3, 4-ethylenedioxythiophenes (EDOTs) and Corresponding Stereo-and Regioregular PEDOTs. *Chem. Commun. (Camb.)* **2004,** 926-927.
(252) Coffey, M.; McKellar, B.; Reinhardt, B.; Nijakowski, T.; Feld, W. A Facile Synthesis of 3, 4-dialkoxythiophenes. *Synth. Commun.* **1996,** *26*, 2205-2212.
(253) Wynberg, H.; Kooreman, H. The Mechanism of the Hinsberg Thiophene Ring Synthesis1, 2. *J. Am. Chem. Soc.* **1965,** *87*, 1739-1742.

(254) Caras-Quintero, D.; Bäuerle, P. Efficient Synthesis of 3, 4-ethylenedioxythiophenes (EDOT) by Mitsunobu Reaction. *Chem. Commun. (Camb.)* **2002,** 2690-2691.
(255) von Kieseritzky, F.; Allared, F.; Dahlstedt, E.; Hellberg, J. Simple One-Step Synthesis of 3, 4-Dimethoxythiophene and Its Conversion into 3, 4-Ethylenedioxythiophene (EDOT). *Tetrahedron Lett.* **2004,** *45*, 6049-6050.
(256) Das, S.; Dutta, P. K.; Panda, S.; Zade, S. S. 3, 4-Ethylenedioxythiophene and 3, 4-Ethylenedioxyselenophene: Synthesis and Reactivity of Cα− Si Bond. *J. Org. Chem.* **2010,** *75*, 4868-4871.
(257) Jang, J.; Chang, M.; Yoon, H. Chemical Sensors Based on Highly Conductive Poly (3, 4-ethylenedioxythiophene) Nanorods. *Adv. Mater.* **2005,** *17*, 1616-1620.
(258) Ajjan, F.; Casado, N.; Rębiś, T.; Elfwing, A.; Solin, N.; Mecerreyes, D.; Inganäs, O. High Performance PEDOT/lignin Biopolymer Composites for Electrochemical Supercapacitors. *J. Mater. Chem. A* **2016,** *4*, 1838-1847.
(259) Zhang, S.; Zhang, W.; Zhang, G.; Bai, Y.; Chen, S.; Xu, J.; Yu, Z.; Sun, K. p-Toluenesulfonic Acid Catalytic Polymerization of EDOT without Oxidants. *Mater. Lett.* **2018,** *222*, 105-108.
(260) Damlin, P.; Kvarnström, C.; Ivaska, A. Electrochemical Synthesis and In Situ Spectroelectrochemical Characterization of Poly (3, 4-ethylenedioxythiophene)(PEDOT) in oom Temperature Ionic Liquids. *J. Electroanal. Chem.* **2004,** *570*, 113-122.
(261) Xiao, Y.-M.; Lin, J.-Y.; Wu, J.-H.; Tai, S.-Y.; Yue, G.-T. Pulse Potentiostatic Electropolymerization of High Performance PEDOT Counter Electrodes for Pt-Free Dye-Sensitized Solar Cells. *Electrochim. Acta* **2012,** *83*, 221-226.
(262) Syritski, V.; Idla, K.; Öpik, A. Synthesis and Redox Behavior of PEDOT/PSS and PPy/DBS Structures. *Synth. Met.* **2004,** *144*, 235-239.
(263) Jönsson, S.; Birgerson, J.; Crispin, X.; Greczynski, G.; Osikowicz, W.; Van Der Gon, A. D.; Salaneck, W. R.; Fahlman, M. The Effects of Solvents on the Morphology and Sheet Resistance in Poly (3, 4-ethylenedioxythiophene)–polystyrenesulfonic Acid (PEDOT–PSS) Films. *Synth. Met.* **2003,** *139*, 1-10.
(264) Łapkowski, M.; Proń, A. Electrochemical Oxidation of Poly (3, 4-ethylenedioxythiophene)—"in situ" Conductivity and Spectroscopic Investigations. *Synth. Met.* **2000,** *110*, 79-83.
(265) Cho, B.; Park, K. S.; Baek, J.; Oh, H. S.; Koo Lee, Y.-E.; Sung, M. M. Single-crystal poly (3, 4-ethylenedioxythiophene) nanowires with ultrahigh conductivity. *Nano Lett.* **2014,** *14*, 3321-3327.
(266) Bolin, M. H.; Svennersten, K.; Wang, X.; Chronakis, I. S.; Richter-Dahlfors, A.; Jager, E. W.; Berggren, M. Nano-fiber Scaffold Electrodes Based on PEDOT for Cell Stimulation. *Sens. Actuators, B* **2009,** *142*, 451-456.
(267) Bhandari, S.; Deepa, M.; Srivastava, A. K.; Lal, C.; Kant, R. Poly (3, 4-ethylenedioxythiophene)(PEDOT)-Coated MWCNTs Tethered to Conducting Substrates: Facile Electrochemistry and Enhanced Coloring Efficiency. *Macromol. Rapid Commun.* **2008,** *29*, 1959-1964.
(268) Gueye, M. N.; Carella, A.; Massonnet, N.; Yvenou, E.; Brenet, S.; Faure-Vincent, J.; Pouget, S.; Rieutord, F.; Okuno, H.; Benayad, A.et al. Structure and Dopant Engineering in PEDOT Thin Films: Practical Tools for a Dramatic Conductivity Enhancement. *Chem. Mater.* **2016,** *28*, 3462-3468.

(269) McFarlane, S. L.; Deore, B. A.; Svenda, N.; Freund, M. S. A One-Step, Organic-Solvent Processable Synthesis of PEDOT Thin Films via In Situ Metastable Chemical Polymerization. *Macromolecules* **2010,** *43*, 10241-10245.
(270) Hofmann, A. I.; Smaal, W. T.; Mumtaz, M.; Katsigiannopoulos, D.; Brochon, C.; Schütze, F.; Hild, O. R.; Cloutet, E.; Hadziioannou, G. An Alternative Anionic Polyelectrolyte for Aqueous PEDOT Dispersions: Toward Printable Transparent Electrodes. *Angew. Chem.* **2015,** *127*, 8626-8630.
(271) Winther-Jensen, B.; West, K. Vapor-Phase Polymerization of 3, 4-Ethylenedioxythiophene: A Route to Highly Conducting Polymer Surface Layers. *Macromolecules* **2004,** *37*, 4538-4543.
(272) Winther-Jensen, B.; Winther-Jensen, O.; Forsyth, M.; MacFarlane, D. R. High Rates of Oxygen Reduction over a Vapor Phase–Polymerized PEDOT Electrode. *Science* **2008,** *321*, 671-674.
(273) Zuber, K.; Fabretto, M.; Hall, C.; Murphy, P. Improved PEDOT Conductivity via Suppression of Crystallite Formation in Fe (III) Tosylate During Vapor Phase Polymerization. *Macromol. Rapid Commun.* **2008,** *29*, 1503-1508.
(274) Ma, F.; Boo, J.-H.; Sohn, H.; Kim, S. Feasibility Test of Spray-Coating Method for Patterning of Vapor Phase-Polymerized Poly (3, 4-Ethylenedioxythiophene) Thin Film. *Mater. Res. Bull.* **2014,** *57*, 197-202.
(275) Laforgue, A.; Robitaille, L. Production of Conductive PEDOT Nanofibers by the Combination of Electrospinning and Vapor-phase Polymerization. *Macromolecules* **2010,** *43*, 4194-4200.
(276) Wang, X.; Zhang, X.; Sun, L.; Lee, D.; Lee, S.; Wang, M.; Zhao, J.; Shao-Horn, Y.; Dincă, M.; Palacios, T.et al. High Electrical Conductivity and Carrier Mobility in oCVD PEDOT Thin Films by Engineered Crystallization and Acid Treatment. *Sci. Adv.* **2018,** *4*, eaat5780.
(277) Krebs, F. C. Roll-to-roll Fabrication of Monolithic Large-area Polymer Solar Cells Free from Indium-tin-oxide. *Sol. Energy Mater. Sol. Cells* **2009,** *93*, 1636-1641.
(278) Roth, B.; dos Reis Benatto, G. A.; Corazza, M.; Søndergaard, R. R.; Gevorgyan, S. A.; Jørgensen, M.; Krebs, F. C. The Critical Choice of PEDOT: PSS Additives for Long Term Stability of Roll‐to‐Roll Processed OPVs. *Adv. Energy Mater.* **2015,** *5*, 1401912.
(279) Gevorgyan, S. A.; Madsen, M. V.; Dam, H. F.; Jørgensen, M.; Fell, C. J.; Anderson, K. F.; Duck, B. C.; Mescheloff, A.; Katz, E. A.; Elschner, A. Interlaboratory Outdoor Stability Studies of Flexible Roll-to-roll Coated Organic Photovoltaic Modules: Stability over 10,000 h. *Sol. Energy Mater. Sol. Cells* **2013,** *116*, 187-196.
(280) Huang, J.; Miller, P. F.; Wilson, J. S.; de Mello, A. J.; de Mello, J. C.; Bradley, D. D. Investigation of the Effects of Doping and Post‐deposition Treatments on the Conductivity, Morphology, and Work Function of Poly (3, 4-ethylenedioxythiophene)/poly (styrene sulfonate) films. *Adv. Funct. Mater.* **2005,** *15*, 290-296.
(281) Snaith, H. J.; Kenrick, H.; Chiesa, M.; Friend, R. H. Morphological and Electronic Consequences of Modifications to the Polymer Anode 'PEDOT: PSS'. *Polymer* **2005,** *46*, 2573-2578.
(282) Cho, C.-K.; Hwang, W.-J.; Eun, K.; Choa, S.-H.; Na, S.-I.; Kim, H.-K. Mechanical Flexibility of Transparent PEDOT: PSS Electrodes Prepared by Gravure Printing for Flexible Organic Solar Cells. *Sol. Energy Mater. Sol. Cells* **2011,** *95*, 3269-3275.

(283) Shi, H.; Liu, C.; Jiang, Q.; Xu, J. Effective Approaches to Improve the Electrical Conductivity of PEDOT: PSS: A Review. *Adv. Electron. Mater.* **2015,** *1*, 1500017.
(284) Granlund, T.; Nyberg, T.; Stolz Roman, L.; Svensson, M.; Inganäs, O. Patterning of Polymer Light-emitting Diodes with Soft Lithography. *Adv. Mater.* **2000,** *12*, 269-273.
(285) Kim, J.; Jung, J.; Lee, D.; Joo, J. Enhancement of Electrical Conductivity of Poly (3, 4-ethylenedioxythiophene)/poly (4-styrenesulfonate) by a Change of Solvents. *Synth. Met.* **2002,** *126*, 311-316.
(286) Na, S. I.; Kim, S. S.; Jo, J.; Kim, D. Y. Efficient and Flexible ITO-Free Organic Solar Cells Using Highly Conductive Polymer Anodes. *Adv. Mater.* **2008,** *20*, 4061-4067.
(287) Kim, N.; Kee, S.; Lee, S. H.; Lee, B. H.; Kahng, Y. H.; Jo, Y. R.; Kim, B. J.; Lee, K. Highly Conductive PEDOT:PSS Nanofibrils Induced by Solution-Processed Crystallization. *Adv. Mater.* **2014,** *26*, 2268-2272.
(288) Zhang, Y.; Wu, Z.; Li, P.; Ono, L. K.; Qi, Y.; Zhou, J.; Shen, H.; Surya, C.; Zheng, Z. Fully Solution-Processed TCO-Free Semitransparent Perovskite Solar Cells for Tandem and Flexible Applications. *Adv. Energy Mater.* **2018,** *8*, 1701569.
(289) Okuzaki, H.; Harashina, Y.; Yan, H. Highly Conductive PEDOT/PSS Microfibers Fabricated by Wet-Spinning and Dip-Treatment in Ethylene Glycol. *Eur. Polym. J.* **2009,** *45*, 256-261.
(290) Badre, C.; Marquant, L.; Alsayed, A. M.; Hough, L. A. Highly Conductive Poly (3, 4-ethylenedioxythiophene): poly (styrenesulfonate) Films Using 1-ethyl-3-methylimidazolium tetracyanoborate Ionic Liquid. *Adv. Funct. Mater.* **2012,** *22*, 2723-2727.
(291) Alemu, D.; Wei, H.-Y.; Ho, K.-C.; Chu, C.-W. Highly conductive PEDOT:PSS electrode by simple film treatment with methanol for ITO-free polymer solar cells. *Energy Environ. Sci.* **2012,** *5*, 9662-9671.
(292) Ouyang, J. Solution-Processed PEDOT:PSS Films with Conductivities as Indium Tin Oxide through a Treatment with Mild and Weak Organic Acids. *ACS Appl. Mater. Interfaces* **2013,** *5*, 13082-13088.
(293) Yeo, J.-S.; Yun, J.-M.; Kim, D.-Y.; Kim, S.-S.; Na, S.-I. Successive Solvent-Treated PEDOT:PSS Electrodes for Flexible ITO-Free Organic Photovoltaics. *Sol. Energy Mater. Sol. Cells* **2013,** *114*, 104-109.
(294) Kim, N.; Kee, S.; Lee, S. H.; Lee, B. H.; Kahng, Y. H.; Jo, Y.-R.; Kim, B.-J.; Lee, K. Highly Conductive PEDOT:PSS Nanofibrils Induced by Solution-Processed Crystallization. *Adv. Mater.* **2014,** *26*, 2268-2272.
(295) Yu, Z.; Xia, Y.; Du, D.; Ouyang, J. PEDOT:PSS Films with Metallic Conductivity through a Treatment with Common Organic Solutions of Organic Salts and Their Application as a Transparent Electrode of Polymer Solar Cells. *ACS Appl. Mater. Interfaces* **2016,** *8*, 11629-11638.
(296) Worfolk, B. J.; Andrews, S. C.; Park, S.; Reinspach, J.; Liu, N.; Toney, M. F.; Mannsfeld, S. C. B.; Bao, Z. Ultrahigh Electrical Conductivity in Solution-Sheared Polymeric Transparent Films. *Proc. Natl. Acad. Sci.* **2015,** *112*, 14138-14143.
(297) Howden, R. M.; McVay, E. D.; Gleason, K. K. oCVD Poly(3,4-ethylenedioxythiophene) Conductivity and Lifetime Enhancement via Acid Rinse Dopant Exchange. *J. Mater. Chem. A* **2013,** *1*, 1334-1340.

(298) Ouyang, J.; Xu, Q.; Chu, C.-W.; Yang, Y.; Li, G.; Shinar, J. On the Mechanism of Conductivity Enhancement in Poly (3, 4-Ethylenedioxythiophene): Poly (Styrene Sulfonate) Film Through Solvent Treatment. *Polymer* **2004,** *45*, 8443-8450.
(299) Suchand Sangeeth, C. S.; Jaiswal, M.; Menon, R. Correlation of Morphology and Charge Transport in Poly(3,4-ethylenedioxythiophene)–Polystyrenesulfonic Acid (PEDOT–PSS) Films. *J. Phys.: Condens. Matter* **2009,** *21*, 072101.
(300) Im, S. G.; Gleason, K. K.; Olivetti, E. A. Doping Level and Work Function Control in Oxidative Chemical Vapor Deposited Poly (3,4-ethylenedioxythiophene). *Appl. Phys. Lett.* **2007,** *90*, 152112.
(301) Petrosino, M.; Vacca, P.; Miscioscia, R.; Nenna, G.; Minarini, C.; Rubino, A. *Effect of PEDOT:PSS ratio on the electrical and optical properties of OLEDs*; SPIE, 2007.
(302) Chen, Y.; Kang, K. S.; Han, K. J.; Yoo, K. H.; Kim, J. Enhanced Optical and Electrical Properties of PEDOT: PSS Films by the Addition of MWCNT-sorbitol. *Synth. Met.* **2009,** *159*, 1701-1704.
(303) Cruz-Cruz, I.; Reyes-Reyes, M.; Aguilar-Frutis, M. A.; Rodriguez, A. G.; López-Sandoval, R. Study of the Effect of DMSO Concentration on the Thickness of the PSS Insulating Barrier in PEDOT:PSS Thin Films. *Synth. Met.* **2010,** *160*, 1501-1506.
(304) Fan, X.; Wang, J.; Wang, H.; Liu, X.; Wang, H. Bendable ITO-free Organic Solar Cells with Highly Conductive and Flexible PEDOT:PSS Electrodes on Plastic Substrates. *ACS Appl. Mater. Interfaces* **2015,** *7*, 16287-16295.
(305) Saghaei, J.; Fallahzadeh, A.; Saghaei, T. ITO-free Organic Solar Cells Using Highly Conductive Phenol-Treated PEDOT:PSS Anodes. *Org. Electron.* **2015,** *24*, 188-194.
(306) Vaagensmith, B.; Reza, K. M.; Hasan, M. D. N.; Elbohy, H.; Adhikari, N.; Dubey, A.; Kantack, N.; Gaml, E.; Qiao, Q. Environmentally Friendly Plasma-Treated PEDOT:PSS as Electrodes for ITO-Free Perovskite Solar Cells. *ACS Appl. Mater. Interfaces* **2017,** *9*, 35861-35870.
(307) Jiang, Y.; Luo, B.; Jiang, F.; Jiang, F.; Fuentes-Hernandez, C.; Liu, T.; Mao, L.; Xiong, S.; Li, Z.; Wang, T.et al. Efficient Colorful Perovskite Solar Cells Using a Top Polymer Electrode Simultaneously as Spectrally Selective Antireflection Coating. *Nano Lett.* **2016,** *16*, 7829-7835.
(308) Das, T. K.; Prusty, S. Review on Conducting Polymers and Their Applications. *Polym.-Plast. Technol. Eng.* **2012,** *51*, 1487-1500.
(309) Gangopadhyay, R.; De, A. Conducting Polymer Nanocomposites: A Brief Overview. *Chem. Mater.* **2000,** *12*, 608-622.
(310) Gustafsson, G.; Cao, Y.; Treacy, G. M.; Klavetter, F.; Colaneri, N.; Heeger, A. J. Flexible Light-emitting Diodes Made from Soluble Conducting Polymers. *Nature* **1992,** *357*, 477-479.
(311) Gao, J.; Heeger, A. J.; Lee, J. Y.; Kim, C. Y. Soluble Polypyrrole as the Transparent Anode in Polymer Light-emitting Diodes. *Synth. Met.* **1996,** *82*, 221-223.
(312) Yang, Y.; Heeger, A. J. Polyaniline as a Transparent Electrode for Polymer Light-Emitting Diodes: Lower Operating Voltage and Higher Efficiency. *Appl. Phys. Lett.* **1994,** *64*, 1245-1247.
(313) Salvatierra, R. V.; Cava, C. E.; Roman, L. S.; Zarbin, A. J. G. ITO-Free and Flexible Organic Photovoltaic Device Based on High Transparent and Conductive Polyaniline/Carbon Nanotube Thin Films. *Adv. Funct. Mater.* **2013,** *23*, 1490-1499.

(314) Tai, Q.; Chen, B.; Guo, F.; Xu, S.; Hu, H.; Sebo, B.; Zhao, X.-Z. In Situ Prepared Transparent Polyaniline Electrode and Its Application in Bifacial Dye-Sensitized Solar Cells. *ACS Nano* **2011,** *5*, 3795-3799.
(315) Ćirić-Marjanović, G. Recent Advances in Polyaniline Research: Polymerization Mechanisms, Structural Aspects, Properties and Applications. *Synth. Met.* **2013,** *177*, 1-47.
(316) Kupila, E. L.; Kankare, J. Electropolymerization of Pyrrole: Effects of pH and Anions on the Conductivity and Growth Kinetics of Polypyrrole. *Synth. Met.* **1993,** *55*, 1402-1405.
(317) Li, W.; Wang, H.-L. Oligomer-Assisted Synthesis of Chiral Polyaniline Nanofibers. *J. Am. Chem. Soc.* **2004,** *126*, 2278-2279.
(318) Khulbe, K. C.; Mann, R. S.; Khulbe, C. P. Polymerization of Pyrrole by Potassium Persulfate. *Journal of Polymer Science: Polymer Chemistry Edition* **1982,** *20*, 1089-1095.
(319) Yasuda, A.; Shimidzu, T. Chemical and Electrochemical Analyses of Polyaniline Prepared with FeCl3. *Synth. Met.* **1993,** *61*, 239-245.
(320) Planche, M. F.; Thiéblemont, J. C.; Mazars, N.; Bidan, G. Kinetic Study of Pyrrole Polymerization with Iron (III) Chloride in Water. *J. Appl. Polym. Sci.* **1994,** *52*, 1867-1877.
(321) Ballav, N. High-conducting Polyaniline via Oxidative Polymerization of Aniline by MnO2, PbO2 and NH4VO3. *Mater. Lett.* **2004,** *58*, 3257-3260.
(322) Chao, T. H.; March, J. A Study of Polypyrrole Synthesized with Oxidative Transition Metal Ions. *J. Polym. Sci., Part A: Polym. Chem.* **1988,** *26*, 743-753.
(323) Mallick, K.; Witcomb, M. J.; Dinsmore, A.; Scurrell, M. S. Polymerization of Aniline by Auric Acid: Formation of Gold Decorated Polyaniline Nanoballs. *Macromol. Rapid Commun.* **2005,** *26*, 232-235.
(324) Blinova, N. V.; Stejskal, J.; Trchová, M.; Sapurina, I.; Ćirić-Marjanović, G. The Oxidation of Aniline With Silver Nitrate to Polyaniline–silver Composites. *Polymer* **2009,** *50*, 50-56.
(325) Pringle, J. M.; Winther-Jensen , O.; Lynam, C.; Wallace, G. G.; Forsyth, M.; MacFarlane, D. R. One-Step Synthesis of Conducting Polymer–Noble Metal Nanoparticle Composites using an Ionic Liquid. *Adv. Funct. Mater.* **2008,** *18*, 2031-2040.
(326) Rao, P. S.; Sathyanarayana, D. N.; Palaniappan, S. Polymerization of Aniline in an Organic Peroxide System by the Inverted Emulsion Process. *Macromolecules* **2002,** *35*, 4988-4996.
(327) Saravanan, C.; Shekhar, R. C.; Palaniappan, S. Synthesis of Polypyrrole Using Benzoyl Peroxide as a Novel Oxidizing Agent. *Macromol. Chem. Phys.* **2006,** *207*, 342-348.
(328) Tan, S.; Tieu, J. H.; Bélanger, D. Chemical Polymerization of Aniline on a Poly(styrene sulfonic acid) Membrane: Controlling the Polymerization Site Using Different Oxidants. *J. Phys. Chem. B* **2005,** *109*, 14085-14092.
(329) Stejskal, J.; Sapurina, I.; Trchová, M.; Konyushenko, E. N. Oxidation of Aniline: Polyaniline Granules, Nanotubes, and Oligoaniline Microspheres. *Macromolecules* **2008,** *41*, 3530-3536.
(330) Stejskal, J.; Sapurina, I.; Trchová, M.; Konyushenko, E. N.; Holler, P. The Genesis of Polyaniline Nanotubes. *Polymer* **2006,** *47*, 8253-8262.
(331) Liang, L.; Liu, J.; Windisch, J., Charles F.; Exarhos, G. J.; Lin, Y. Direct Assembly of Large Arrays of Oriented Conducting Polymer Nanowires. *Angew. Chem. Int. Ed.* **2002,** *41*, 3665-3668.

(332) Li, Q.; Wu, J.; Tang, Q.; Lan, Z.; Li, P.; Lin, J.; Fan, L. Application of Microporous Polyaniline Counter Electrode for Dye-Sensitized Solar Cells. *Electrochem. Commun.* **2008,** *10*, 1299-1302.
(333) Pan, L.; Chortos, A.; Yu, G.; Wang, Y.; Isaacson, S.; Allen, R.; Shi, Y.; Dauskardt, R.; Bao, Z. An Ultra-Sensitive Resistive Pressure Sensor Based on Hollow-Sphere Microstructure Induced Elasticity in Conducting Polymer Film. *Nat. Commun.* **2014,** *5*, 3002.
(334) Park, K.-H.; Kim, S. J.; Gomes, R.; Bhaumik, A. High performance dye-sensitized solar cell by using porous polyaniline nanotubes as counter electrode. *Chem. Eng. J.* **2015,** *260*, 393-398.
(335) Peng, T.; Sun, W.; Huang, C.; Yu, W.; Sebo, B.; Dai, Z.; Guo, S.; Zhao, X.-Z. Self-Assembled Free-Standing Polypyrrole Nanotube Membrane as an Efficient FTO- and Pt-Free Counter Electrode for Dye-Sensitized Solar Cells. *ACS Appl. Mater. Interfaces* **2014,** *6*, 14-17.
(336) Wang, H.; Feng, Q.; Gong, F.; Li, Y.; Zhou, G.; Wang, Z.-S. In Situ Growth of Oriented Polyaniline Nanowires Array for Efficient Cathode of Co(Iii)/Co(Ii) Mediated Dye-Sensitized Solar Cell. *J. Mater. Chem. A* **2013,** *1*, 97-104.
(337) Ćirić-Marjanović, G. Recent Advances in Polyaniline Composites with Metals, Metalloids and Nonmetals. *Synth. Met.* **2013,** *170*, 31-56.
(338) Zhou, C.; Zhang, Y.; Li, Y.; Liu, J. Construction of High-Capacitance 3D CoO@Polypyrrole Nanowire Array Electrode for Aqueous Asymmetric Supercapacitor. *Nano Lett.* **2013,** *13*, 2078-2085.
(339) Lee, H.; Choi, T. K.; Lee, Y. B.; Cho, H. R.; Ghaffari, R.; Wang, L.; Choi, H. J.; Chung, T. D.; Lu, N.; Hyeon, T.et al. A Graphene-Based Electrochemical Device with Thermoresponsive Microneedles for Diabetes Monitoring and Therapy. *Nat. Nanotechnol.* **2016,** *11*, 566.
(340) Stejskal, J.; Hlavatá, D.; Holler, P.; Trchová, M.; Prokeš, J.; Sapurina, I. Polyaniline Prepared in the Presence of Various Acids: A Conductivity Study. *Polym. Int.* **2004,** *53*, 294-300.
(341) Krukiewicz, K.; Katunin, A. The Effect of Reaction Medium on the Conductivity and Morphology of Polyaniline Doped with Camphorsulfonic Acid. *Synth. Met.* **2016,** *214*, 45-49.
(342) Chiang, J.-C.; MacDiarmid, A. G. 'Polyaniline': Protonic Acid Doping of the Emeraldine Form to the Metallic Regime. *Synth. Met.* **1986,** *13*, 193-205.
(343) Dimitriev, O. P. Doping of Polyaniline by Transition-Metal Salts. *Macromolecules* **2004,** *37*, 3388-3395.
(344) Jeon, S. S.; Kim, C.; Lee, T. H.; Lee, Y. W.; Do, K.; Ko, J.; Im, S. S. Camphorsulfonic Acid-Doped Polyaniline Transparent Counter Electrode for Dye-Sensitized Solar Cells. *J. Phys. Chem. C* **2012,** *116*, 22743-22748.
(345) Lee, K.; Cho, S.; Kim, M.; Kim, J.; Ryu, J.; Shin, K.-Y.; Jang, J. Highly Porous Nanostructured Polyaniline/Carbon Nanodots as Efficient Counter Electrodes for Pt-Free Dye-Sensitized Solar Cells. *J. Mater. Chem. A* **2015,** *3*, 19018-19026.
(346) Lee, K.; Cho, S.; Heum Park, S.; Heeger, A. J.; Lee, C.-W.; Lee, S.-H. Metallic Transport in Polyaniline. *Nature* **2006,** *441*, 65-68.

(347) Izumi, C. M. S.; Constantino, V. R. L.; Ferreira, A. M. C.; Temperini, M. L. A. Spectroscopic Characterization of Polyaniline Doped with Transition Metal Salts. *Synth. Met.* **2006,** *156*, 654-663.
(348) Pillalamarri, S. K.; Blum, F. D.; Tokuhiro, A. T.; Bertino, M. F. One-Pot Synthesis of Polyaniline−Metal Nanocomposites. *Chem. Mater.* **2005,** *17*, 5941-5944.
(349) Bu, C.; Tai, Q.; Liu, Y.; Guo, S.; Zhao, X. A Transparent and Stable Polypyrrole Counter Electrode for Dye-Sensitized Solar Cell. *J. Power Sources* **2013,** *221*, 78-83.
(350) Kim, D. H.; Lu, N. S.; Ma, R.; Kim, Y. S.; Kim, R. H.; Wang, S. D.; Wu, J.; Won, S. M.; Tao, H.; Islam, A.et al. Epidermal Electronics. *Science* **2011,** *333*, 838-843.
(351) Ellmer, K. Past Achievements and Future Challenges in the Development of Optically Transparent Electrodes. *Nat. Photonics* **2012,** *6*, 808-816.
(352) Kang, H.; Jung, S.; Jeong, S.; Kim, G.; Lee, K. Polymer-metal Hybrid Transparent Electrodes for Flexible Electronics. *Nat. Commun.* **2015,** *6*, 6503.
(353) Zhao, G. Q.; Kim, S. M.; Lee, S. G.; Bae, T. S.; Mun, C.; Lee, S.; Yu, H. S.; Lee, G. H.; Lee, H. S.; Song, M.et al. Bendable Solar Cells from Stable, Flexible, and Transparent Conducting Electrodes Fabricated Using a Nitrogen-Doped Ultrathin Copper Film. *Adv. Funct. Mater.* **2016,** *26*, 4180-4191.
(354) Zhang, C.; Zhao, D. W.; Gu, D. E.; Kim, H.; Ling, T.; Wu, Y. K. R.; Guo, L. J. An Ultrathin, Smooth, and Low-Loss Al-Doped Ag Film and Its Application as a Transparent Electrode in Organic Photovoltaics. *Adv. Mater.* **2014,** *26*, 5696-5701.
(355) Gu, D.; Zhang, C.; Wu, Y. K.; Guo, L. J. Ultrasmooth and Thermally Stable Silver-Based Thin Films with Subnanometer Roughness by Aluminum Doping. *ACS Nano* **2014,** *8*, 10343-10351.
(356) Zhao, G.; Wang, W.; Bae, T. S.; Lee, S. G.; Mun, C.; Lee, S.; Yu, H. S.; Lee, G. H.; Song, M.; Yun, J. Stable Ultrathin Partially Oxidized Copper Film Electrode for Highly Efficient Flexible Solar Cells. *Nat. Commun.* **2015,** *6*,
(357) Zhao, J.; Brinkmann, K.; Hu, T.; Pourdavoud, N.; Becker, T.; Gahlmann, T.; Heiderhoff, R.; Polywka, A.; Görrn, P.; Chen, Y. Self‐Encapsulating Thermostable and Air‐Resilient Semitransparent Perovskite Solar Cells. *Adv. Energy Mater.* **2017,**
(358) Yun, J. Ultrathin Metal films for Transparent Electrodes of Flexible Optoelectronic Devices. *Adv. Funct. Mater.* **2017,** 1606641.
(359) Mahenderkar, N. K.; Chen, Q.; Liu, Y.-C.; Duchild, A. R.; Hofheins, S.; Chason, E.; Switzer, J. A. Epitaxial Lift-Off of Electrodeposited Single-Crystal Gold Foils for Flexible Electronics. *Science* **2017,** *355*, 1203-1206.
(360) Wang, D.; Zhang, Y.; Lu, X.; Ma, Z.; Xie, C.; Zheng, Z. Chemical Formation of Soft Metal Electrodes for Flexible and Wearable Electronics. *Chem. Soc. Rev.* **2018,** *47*, 4611-4641.
(361) Yin, Y.; Li, Z.-Y.; Zhong, Z.; Gates, B.; Xia, Y.; Venkateswaran, S. Synthesis and Characterization of Stable Aqueous Dispersions of Silver Nanoparticles Through the Tollens Process. *J. Mater. Chem.* **2002,** *12*, 522-527.
(362) Xia, Y.; Xia, X.; Wang, Y.; Xie, S. Shape-Controlled Synthesis of Metal Nanocrystals. *MRS Bull.* **2013,** *38*, 335-344.
(363) Xia, Y.; Xia, X.; Peng, H.-C. Shape-Controlled Synthesis of Colloidal Metal Nanocrystals: Thermodynamic versus Kinetic Products. *J. Am. Chem. Soc.* **2015,** *137*, 7947-7966.

(364) Raveendran, P.; Fu, J.; Wallen, S. L. A Simple and "Green" Method for the Synthesis of Au, Ag, and Au–Ag Alloy Nanoparticles. *Green Chem.* **2006,** *8*, 34-38.
(365) Mulfinger, L.; Solomon, S. D.; Bahadory, M.; Jeyarajasingam, A. V.; Rutkowsky, S. A.; Boritz, C. Synthesis and Study of Silver Nanoparticles. *J. Chem. Educ.* **2007,** *84*, 322.
(366) Jia, Z.; Sun, H.; Gu, Q. Preparation of Ag Nanoparticles with Triethanolamine as Reducing Agent and Their Antibacterial Property. *Colloids Surf., A* **2013,** *419*, 174-179.
(367) Zeng, J.; Zheng, Y.; Rycenga, M.; Tao, J.; Li, Z.-Y.; Zhang, Q.; Zhu, Y.; Xia, Y. Controlling the Shapes of Silver Nanocrystals with Different Capping Agents. *J. Am. Chem. Soc.* **2010,** *132*, 8552-8553.
(368) Gawande, M. B.; Goswami, A.; Felpin, F.-X.; Asefa, T.; Huang, X.; Silva, R.; Zou, X.; Zboril, R.; Varma, R. S. Cu and Cu-Based Nanoparticles: Synthesis and Applications in Catalysis. *Chem. Rev.* **2016,** *116*, 3722-3811.
(369) Vitulli, G.; Bernini, M.; Bertozzi, S.; Pitzalis, E.; Salvadori, P.; Coluccia, S.; Martra, G. Nanoscale Copper Particles Derived from Solvated Cu Atoms in the Activation of Molecular Oxygen. *Chem. Mater.* **2002,** *14*, 1183-1186.
(370) Park, B. K.; Jeong, S.; Kim, D.; Moon, J.; Lim, S.; Kim, J. S. Synthesis and Size Control of Monodisperse Copper Nanoparticles by Polyol Method. *J. Colloid Interface Sci.* **2007,** *311*, 417-424.
(371) Sun, Y.; Gates, B.; Mayers, B.; Xia, Y. Crystalline Silver Nanowires by Soft Solution Processing. *Nano Lett.* **2002,** *2*, 165-168.
(372) Sun, Y.; Xia, Y. Large-Scale Synthesis of Uniform Silver Nanowires Through a Soft, Self-Seeding, Polyol Process. *Adv. Mater.* **2002,** *14*, 833-837.
(373) Sun, Y.; Yin, Y.; Mayers, B. T.; Herricks, T.; Xia, Y. Uniform Silver Nanowires Synthesis by Reducing AgNO3 with Ethylene Glycol in the Presence of Seeds and Poly(Vinyl Pyrrolidone). *Chem. Mater.* **2002,** *14*, 4736-4745.
(374) Chang, Y.; Lye, M. L.; Zeng, H. C. Large-Scale Synthesis of High-Quality Ultralong Copper Nanowires. *Langmuir* **2005,** *21*, 3746-3748.
(375) Shi, Y.; Li, H.; Chen, L.; Huang, X. Obtaining Ultra-Long Copper Nanowires via a Hydrothermal Process. *Sci. Technol. Adv. Mater.* **2005,** *6*, 761-765.
(376) Jin, M.; He, G.; Zhang, H.; Zeng, J.; Xie, Z.; Xia, Y. Shape-Controlled Synthesis of Copper Nanocrystals in an Aqueous Solution with Glucose as a Reducing Agent and Hexadecylamine as a Capping Agent. *Angew. Chem. Int. Ed.* **2011,** *50*, 10560-10564.
(377) Guo, H.; Lin, N.; Chen, Y.; Wang, Z.; Xie, Q.; Zheng, T.; Gao, N.; Li, S.; Kang, J.; Cai, D.et al. Copper Nanowires as Fully Transparent Conductive Electrodes. *Sci. Rep.* **2013,** *3*, 2323.
(378) Sachse, C.; Weiß, N.; Gaponik, N.; Müller-Meskamp, L.; Eychmüller, A.; Leo, K. ITO-Free, Small-Molecule Organic Solar Cells on Spray-Coated Copper-Nanowire-Based Transparent Electrodes. *Adv. Energy Mater.* **2014,** *4*, 1300737.
(379) Stewart, I. E.; Rathmell, A. R.; Yan, L.; Ye, S.; Flowers, P. F.; You, W.; Wiley, B. J. Solution-Processed Copper–Nickel Nanowire Anodes for Organic Solar Cells. *Nanoscale* **2014,** *6*, 5980-5988.
(380) Sun, Y.; Mayers, B.; Herricks, T.; Xia, Y. Polyol Synthesis of Uniform Silver Nanowires: A Plausible Growth Mechanism and the Supporting Evidence. *Nano Lett.* **2003,** *3*, 955-960.
(381) Ahn, B. Y.; Lorang, D. J.; Lewis, J. A. Transparent Conductive Grids Via Direct Writing of Silver Nanoparticle Inks. *Nanoscale* **2011,** *3*, 2700-2702.

(382) Park, J. H.; Lee, D. Y.; Seung, W.; Sun, Q.; Kim, S. W.; Cho, J. H. Metallic Grid Electrode Fabricated via Flow Coating for High-Performance Flexible Piezoelectric Nanogenerators. *J. Phys. Chem. C* **2015,** *119*, 7802-7808.
(383) Jin, W.-Y.; Ginting, R. T.; Ko, K.-J.; Kang, J.-W. Ultra-Smooth, Fully Solution-Processed Large-Area Transparent Conducting Electrodes for Organic Devices. *Sci. Rep.* **2016,** *6*, 36475.
(384) Lee, Y.; Jin, W. Y.; Cho, K. Y.; Kang, J. W.; Kim, J. Thermal Pressing of a Metal-Grid Transparent Electrode into a Plastic Substrate for Flexible Electronic Devices. *J. Mater. Chem. C* **2016,** *4*, 7577-7583.
(385) Zhou, L.; Xiang, H. Y.; Shen, S.; Li, Y. Q.; De Chen, J.; Xie, H. J.; Goldthorpe, I. A.; Chen, L. S.; Lee, S. T.; Tang, J. X. High-Performance Flexible Organic Light-Emitting Diodes Using Embedded Silver Network Transparent Electrodes. *ACS Nano* **2014,** *8*, 12796-12805.
(386) Oh, Y. S.; Choi, D. Y.; Sung, H. J. Direct Imprinting of Thermally Reduced Silver Nanoparticles via Deformation-Driven Ink Injection for High-Performance, Flexible Metal Grid Embedded Transparent Conductors. *RSC Adv.* **2015,** *5*, 64661-64668.
(387) Lu, S. D.; Lin, J.; Liu, K.; Yue, S. Z.; Ren, K. K.; Tan, F. R.; Wang, Z. J.; Jin, P.; Qu, S. C.; Wang, Z. G. Large Area Flexible Polymer Solar Cells with High Efficiency Enabled by Imprinted Ag Grid and Modified Buffer Layer. *Acta Mater.* **2017,** *130*, 208-214.
(388) Kang, J.; Park, C. G.; Lee, S. H.; Cho, C.; Choi, D. G.; Lee, J. Y. Fabrication of High Aspect Ratio Nanogrid Transparent Electrodes via Capillary Assembly of Ag Nanoparticles. *Nanoscale* **2016,** *8*, 11217-11223.
(389) Hu, A.; Guo, J.; Alarifi, H.; Patane, G.; Zhou, Y.; Compagnini, G.; Xu, C. Low Temperature Sintering of Ag Nanoparticles for Flexible Electronics Packaging. *Appl. Phys. Lett.* **2010,** *97*, 153117.
(390) Alarifi, H.; Hu, A.; Yavuz, M.; Zhou, Y. N. Silver Nanoparticle Paste for Low-Temperature Bonding of Copper. *J. Electron. Mater.* **2011,** *40*, 1394-1402.
(391) Sciacca, B.; van de Groep, J.; Polman, A.; Garnett, E. C. Solution-Grown Silver Nanowire Ordered Arrays as Transparent Electrodes. *Adv. Mater.* **2016,** *28*, 905-909.
(392) Park, J. H.; Jeong, S.; Lee, E. J.; Lee, S. S.; Seok, J. Y.; Yang, M.; Choi, Y.; Kang, B. Transversally Extended Laser Plasmonic Welding for Oxidation-Free Copper Fabrication toward High-Fidelity Optoelectronics. *Chem. Mater.* **2016,** *28*, 4151-4159.
(393) Kwon, J.; Cho, H.; Suh, Y. D.; Lee, J.; Lee, H.; Jung, J.; Kim, D.; Lee, D.; Hong, S.; Ko, S. H. Flexible and Transparent Cu Electronics by Low-Temperature Acid-Assisted Laser Processing of Cu Nanoparticles. *Adv. Mater. Technol.* **2017,** *2*, 1600222.
(394) Lee, C.; Kim, C.; Jeong, M.; Kim, J.; Lee, J.; Oh, J. W.; Lee, J.; Kim, S. H.; Park, S. S.; Kim, J. M. Highly Flexible and Transparent Metal Grids Made of Metal Nanowire Networks. *RSC Adv.* **2015,** *5*, 77288-77295.
(395) Maurer, J. H. M.; Gonzalez-Garcia, L.; Reiser, B.; Kanelidis, I.; Kraus, T. Templated Self-Assembly of Ultrathin Gold Nanowires by Nanoimprinting for Transparent Flexible Electronics. *Nano Lett.* **2016,** *16*, 2921-2925.
(396) Yu, Z.; Li, L.; Zhang, Q.; Hu, W.; Pei, Q. Silver Nanowire-Polymer Composite Electrodes for Efficient Polymer Solar Cells. *Adv. Mater.* **2011,** *23*, 4453-4457.
(397) Guo, F.; Azimi, H.; Hou, Y.; Przybilla, T.; Hu, M.; Bronnbauer, C.; Langner, S.; Spiecker, E.; Forberich, K.; Brabec, C. J. High-performance Semitransparent Perovskite

Solar Cells with Solution-processed Silver Nanowires as Top Electrodes. *Nanoscale* **2015,** *7*, 1642-1649.
(398) Hsu, P. C.; Kong, D. S.; Wang, S.; Wang, H. T.; Welch, A. J.; Wu, H.; Cui, Y. Electrolessly Deposited Electrospun Metal Nanowire Transparent Electrodes. *J. Am. Chem. Soc.* **2014,** *136*, 10593-10596.
(399) Hu, L.; Hecht, D. S.; Grüner, G. Percolation in Transparent and Conducting Carbon Nanotube Networks. *Nano Lett.* **2004,** *4*, 2513-2517.
(400) Hu, L. B.; Kim, H. S.; Lee, J. Y.; Peumans, P.; Cui, Y. Scalable Coating and Properties of Transparent, Flexible, Silver Nanowire Electrodes. *ACS Nano* **2010,** *4*, 2955-2963.
(401) Li, B.; Ye, S. R.; Stewart, I. E.; Alvarez, S.; Wiley, B. J. Synthesis and Purification of Silver Nanowires To Make Conducting Films with a Transmittance of 99%. *Nano Lett.* **2015,** *15*, 6722-6726.
(402) Zhang, Y.; Guo, J. N.; Xu, D.; Sun, Y.; Yan, F. One-Pot Synthesis and Purification of Ultralong Silver Nanowires for Flexible Transparent Conductive Electrodes. *ACS Appl. Mater. Interfaces* **2017,** *9*, 25465-25473.
(403) Ye, S.; Rathmell, A. R.; Stewart, I. E.; Ha, Y.-C.; Wilson, A. R.; Chen, Z.; Wiley, B. J. A Rapid Synthesis of High Aspect Ratio Copper Nanowires for High-Performance Transparent Conducting Films. *Chem. Commun. (Camb.)* **2014,** *50*, 2562-2564.
(404) O'Callaghan, C.; Gomes da Rocha, C.; Manning, H. G.; Boland, J. J.; Ferreira, M. S. Effective Medium Theory for the Conductivity of Disordered Metallic Nanowire Networks. *Phys. Chem. Chem. Phys.* **2016,** *18*, 27564-27571.
(405) Bellew, A. T.; Manning, H. G.; Gomes da Rocha, C.; Ferreira, M. S.; Boland, J. J. Resistance of Single Ag Nanowire Junctions and Their Role in the Conductivity of Nanowire Networks. *ACS Nano* **2015,** *9*, 11422-11429.
(406) Mutiso, R. M.; Sherrott, M. C.; Rathmell, A. R.; Wiley, B. J.; Winey, K. I. Integrating Simulations and Experiments To Predict Sheet Resistance and Optical Transmittance in Nanowire Films for Transparent Conductors. *ACS Nano* **2013,** *7*, 7654-7663.
(407) Garnett, E. C.; Cai, W.; Cha, J. J.; Mahmood, F.; Connor, S. T.; Greyson Christoforo, M.; Cui, Y.; McGehee, M. D.; Brongersma, M. L. Self-limited Plasmonic Welding of Silver Nanowire Junctions. *Nat. Mater.* **2012,** *11*, 241.
(408) Park, J. H.; Hwang, G. T.; Kim, S.; Seo, J.; Park, H. J.; Yu, K.; Kim, T. S.; Lee, K. J. Flash-Induced Self-Limited Plasmonic Welding of Silver Nanowire Network for Transparent Flexible Energy Harvester. *Adv. Mater.* **2017,** *29*, 1603473.
(409) Park, J. H.; Han, S.; Kim, D.; You, B. K.; Joe, D. J.; Hong, S.; Seo, J.; Kwon, J.; Jeong, C. K.; Park, H.-J.et al. Plasmonic-Tuned Flash Cu Nanowelding with Ultrafast Photochemical-Reducing and Interlocking on Flexible Plastics. *Adv. Funct. Mater.* **2017,** *27*, 1701138.
(410) Lee, J. G.; Kim, D. Y.; Lee, J. H.; Sinha-Ray, S.; Yarin, A. L.; Swihart, M. T.; Kim, D.; Yoon, S. S. Production of Flexible Transparent Conducting Films of Self-Fused Nanowires via One-Step Supersonic Spraying. *Adv. Funct. Mater.* **2017,** *27*, 1602548.
(411) Kang, H. S.; Choi, J.; Cho, W.; Lee, H.; Lee, D.; Lee, D. G.; Kim, H. T. Silver Nanowire Networks Embedded in a Cure-controlled Optical Adhesive Film for a Transparent and Highly Conductive Electrode. *J. Mater. Chem. C* **2016,** *4*, 9834-9840.
(412) Kim, J.; Nam, Y. S.; Song, M. H.; Park, H. W. Large Pulsed Electron Beam Welded Percolation Networks of Silver Nanowires for Transparent and Flexible Electrodes. *ACS Appl. Mater. Interfaces* **2016,** *8*, 20938-20945.

(413) Xiong, W.; Liu, H.; Chen, Y.; Zheng, M.; Zhao, Y.; Kong, X.; Wang, Y.; Zhang, X.; Kong, X.; Wang, P. Highly Conductive, Air‐Stable Silver Nanowire@ Iongel Composite Films toward Flexible Transparent Electrodes. *Adv. Mater.* **2016,** *28*, 7167-7172.
(414) Chen, T. L.; Ghosh, D. S.; Mkhitaryan, V.; Pruneri, V. Hybrid Transparent Conductive Film on Flexible Glass Formed by Hot-Pressing Graphene on a Silver Nanowire Mesh. *ACS Appl. Mater. Interfaces* **2013,** *5*, 11756-11761.
(415) An, S.; Jo, H. S.; Kim, D. Y.; Lee, H. J.; Ju, B. K.; Al-Deyab, S. S.; Ahn, J. H.; Qin, Y.; Swihart, M. T.; Yarin, A. L.et al. Self-Junctioned Copper Nanofiber Transparent Flexible Conducting Film via Electrospinning and Electroplating. *Adv. Mater.* **2016,** *28*, 7149-7154.
(416) Garnett, E. C.; Cai, W.; Cha, J. J.; Mahmood, F.; Connor, S. T.; Christoforo, M. G.; Cui, Y.; McGehee, M. D.; Brongersma, M. L. Self-limited plasmonic welding of silver nanowire junctions. *Nat. Mater.* **2012,** *11*, 241-249.
(417) Park, J. H.; Han, S.; Kim, D.; You, B. K.; Joe, D. J.; Hong, S.; Seo, J.; Kwon, J.; Jeong, C. K.; Park, H.-J.et al. Plasmonic‐Tuned Flash Cu Nanowelding with Ultrafast Photochemical‐Reducing and Interlocking on Flexible Plastics. *Adv. Funct. Mater.* **2017,** *27*, 1701138.
(418) Stadler, A. Transparent Conducting Oxides-An Up-To-Date Overview. *Materials* **2012,** *5*, 661-683.
(419) George, J.; Menon, C. S. Electrical and Optical Properties of Electron Beam Evaporated ITO Thin Films. *Surf. Coat. Technol.* **2000,** *132*, 45-48.
(420) Herranz, G.; Basletić, M.; Bibes, M.; Carrétéro, C.; Tafra, E.; Jacquet, E.; Bouzehouane, K.; Deranlot, C.; Hamzić, A.; Broto, J. M.et al. High Mobility in LaAlO3/SrTiO3 Heterostructures: Origin, Dimensionality, and Perspectives. *Phys. Rev. Lett.* **2007,** *98*, 216803.
(421) Calnan, S.; Tiwari, A. N. High Mobility Transparent Conducting Oxides for Thin Film Solar Cells. *Thin Solid Films* **2010,** *518*, 1839-1849.
(422) Kawazoe, H.; Yasukawa, M.; Hyodo, H.; Kurita, M.; Yanagi, H.; Hosono, H. P-type Electrical Conduction in Transparent Thin Films of CuAlO2. *Nature* **1997,** *389*, 939-942.
(423) Sato, H.; Minami, T.; Takata, S.; Yamada, T. Transparent Conducting p-Type NiO Thin Films Prepared by Magnetron Sputtering. *Thin Solid Films* **1993,** *236*, 27-31.
(424) Köstlin, H.; Jost, R.; Lems, W. Optical and Electrical Properties of Doped In2O3 Films. *Phys. Status Solidi A* **1975,** *29*, 87-93.
(425) Mooney, J. B.; Radding, S. B. Spray Pyrolysis Processing. *Annu. Rev. Mater. Sci.* **1982,** *12*, 81-101.
(426) Kawashima, T.; Matsui, H.; Tanabe, N. New Transparent Conductive Films: FTO Coated ITO. *Thin Solid Films* **2003,** *445*, 241-244.
(427) Aouaj, M. A.; Diaz, R.; Belayachi, A.; Rueda, F.; Abd-Lefdil, M. Comparative study of ITO and FTO thin films grown by spray pyrolysis. *Mater. Res. Bull.* **2009,** *44*, 1458-1461.
(428) Mattox, D. M. Sol-Gel Derived, Air-Baked Indium and Tin Oxide Films. *Thin Solid Films* **1991,** *204*, 25-32.
(429) Tahar, R. B. H.; Ban, T.; Ohya, Y.; Takahashi, Y. Tin Doped Indium Oxide Thin Films: Electrical Properties. *J. Appl. Phys.* **1998,** *83*, 2631-2645.

(430) Kőrösi, L.; Scarpellini, A.; Petrik, P.; Papp, S.; Dékány, I. Sol–gel Synthesis of Nanostructured Indium Tin Oxide with Controlled Morphology and Porosity. *Appl. Surf. Sci.* **2014,** *320*, 725-731.
(431) Müller, V.; Rasp, M.; Štefanić, G.; Ba, J.; Günther, S.; Rathousky, J.; Niederberger, M.; Fattakhova-Rohlfing, D. Highly Conducting Nanosized Monodispersed Antimony-Doped Tin Oxide Particles Synthesized via Nonaqueous Sol−Gel Procedure. *Chem. Mater.* **2009,** *21*, 5229-5236.
(432) Kanehara, M.; Koike, H.; Yoshinaga, T.; Teranishi, T. Indium Tin Oxide Nanoparticles with Compositionally Tunable Surface Plasmon Resonance Frequencies in the Near-IR Region. *J. Am. Chem. Soc.* **2009,** *131*, 17736-17737.
(433) Němec, H.; Kužel, P.; Sundström, V. Far-Infrared Response of Free Charge Carriers Localized in Semiconductor Nanoparticles. *Phys. Rev. B* **2009,** *79*, 115309.
(434) Alam, M. J.; Cameron, D. C. Investigation of Annealing Effects on Sol–gel Deposited Indium Tin Oxide Thin Films in Different Atmospheres. *Thin Solid Films* **2002,** *420-421*, 76-82.
(435) Chen, M.-F.; Lin, K.-m.; Ho, Y.-S. Laser Annealing Process of ITO Thin Films Using Beam Shaping Technology. *Opt. Lasers Eng.* **2012,** *50*, 491-495.
(436) Tsang, W. M.; Wong, F. L.; Fung, M. K.; Chang, J. C.; Lee, C. S.; Lee, S. T. Transparent Conducting Aluminum-Doped Zinc Oxide Thin Film Prepared by Sol–Gel Process Followed by Laser Irradiation Treatment. *Thin Solid Films* **2008,** *517*, 891-895.
(437) Lee, D.; Pan, H.; Ko, S. H.; Park, H. K.; Kim, E.; Grigoropoulos, C. P. Non-Vacuum, Single-Step Conductive Transparent ZnO Patterning by Ultra-Short Pulsed Laser Annealing of Solution-Deposited Nanoparticles. *Appl. Phys. A* **2012,** *107*, 161-171.
(438) Kim, M.-G.; Kanatzidis, M. G.; Facchetti, A.; Marks, T. J. Low-temperature Fabrication of High-performance Metal Oxide Thin-film Electronics via Combustion Processing. *Nat. Mater.* **2011,** *10*, 382.
(439) Sunde, T. O. L.; Garskaite, E.; Otter, B.; Fossheim, H. E.; Sæterli, R.; Holmestad, R.; Einarsrud, M.-A.; Grande, T. Transparent and Conducting ITO Thin Films by Spin Coating of an Aqueous Precursor Solution. *J. Mater. Chem.* **2012,** *22*, 15740-15749.
(440) Geim, A. K.; Novoselov, K. S. The Rise of Graphene. *Nat. Mater.* **2007,** *6*, 183.
(441) Li, X.; Zhu, Y.; Cai, W.; Borysiak, M.; Han, B.; Chen, D.; Piner, R. D.; Colombo, L.; Ruoff, R. S. Transfer of Large-Area Graphene Films for High-Performance Transparent Conductive Electrodes. *Nano Lett.* **2009,** *9*, 4359-4363.
(442) Wang, X.-Y.; Narita, A.; Müllen, K. Precision Synthesis Versus Bulk-Scale Fabrication of Graphenes. *Nat. Rev. Chem.* **2017,** *2*, 0100.
(443) Botas, C.; Álvarez, P.; Blanco, P.; Granda, M.; Blanco, C.; Santamaría, R.; Romasanta, L. J.; Verdejo, R.; López-Manchado, M. A.; Menéndez, R. Graphene Materials with Different Structures Prepared from the Same Graphite by the Hummers and Brodie Methods. *Carbon* **2013,** *65*, 156-164.
(444) Hummers Jr, W. S.; Offeman, R. E. Preparation of Graphitic Oxide. *J. Am. Chem. Soc.* **1958,** *80*, 1339-1339.
(445) Marcano, D. C.; Kosynkin, D. V.; Berlin, J. M.; Sinitskii, A.; Sun, Z.; Slesarev, A.; Alemany, L. B.; Lu, W.; Tour, J. M. Improved Synthesis of Graphene Oxide. *ACS Nano* **2010,** *4*, 4806-4814.
(446) Gao, W.; Alemany, L. B.; Ci, L.; Ajayan, P. M. New Insights into the Structure and Reduction of Graphite Oxide. *Nat. Chem.* **2009,** *1*, 403.

(447) Stankovich, S.; Dikin, D. A.; Piner, R. D.; Kohlhaas, K. A.; Kleinhammes, A.; Jia, Y.; Wu, Y.; Nguyen, S. T.; Ruoff, R. S. Synthesis of Graphene-Based Nanosheets via Chemical Reduction of Exfoliated Graphite Oxide. *Carbon* **2007,** *45*, 1558-1565.
(448) Hermanová, S.; Zarevúcká, M.; Bouša, D.; Pumera, M.; Sofer, Z. Graphene Oxide Immobilized Enzymes Show High Thermal and Solvent Stability. *Nanoscale* **2015,** *7*, 5852-5858.
(449) Shin, H. J.; Kim, K. K.; Benayad, A.; Yoon, S. M.; Park, H. K.; Jung, I. S.; Jin, M. H.; Jeong, H. K.; Kim, J. M.; Choi, J. Y. Efficient Reduction of Graphite Oxide by Sodium Borohydride and Its Effect on Electrical Conductance. *Adv. Funct. Mater.* **2009,** *19*, 1987-1992.
(450) Park, S.; An, J.; Potts, J. R.; Velamakanni, A.; Murali, S.; Ruoff, R. S. Hydrazine-reduction of graphite-and graphene oxide. *Carbon* **2011,** *49*, 3019-3023.
(451) Dreyer, D. R.; Murali, S.; Zhu, Y.; Ruoff, R. S.; Bielawski, C. W. Reduction of Graphite Oxide Using Alcohols. *J. Mater. Chem.* **2011,** *21*, 3443-3447.
(452) Eda, G.; Fanchini, G.; Chhowalla, M. Large-area Ultrathin Films of Reduced Graphene Oxide As a Transparent and Flexible Electronic Material. *Nat. Nanotechnol.* **2008,** *3*, 270.
(453) Zhang, J.; Yang, H.; Shen, G.; Cheng, P.; Zhang, J.; Guo, S. Reduction of Graphene Oxide via L-Ascorbic Acid. *Chem. Commun. (Camb.)* **2010,** *46*, 1112-1114.
(454) Zhou, T.; Chen, F.; Liu, K.; Deng, H.; Zhang, Q.; Feng, J.; Fu, Q. A Simple and Efficient Method to Prepare Graphene by Reduction of Graphite Oxide with Sodium Hydrosulfite. *Nanotechnology* **2010,** *22*, 045704.
(455) Fan, X.; Peng, W.; Li, Y.; Li, X.; Wang, S.; Zhang, G.; Zhang, F. Deoxygenation of Exfoliated Graphite Oxide under Alkaline Conditions: a Green Route to Graphene Preparation. *Adv. Mater.* **2008,** *20*, 4490-4493.
(456) Cote, L. J.; Cruz-Silva, R.; Huang, J. Flash Reduction and Patterning of Graphite Oxide and Its Polymer Composite. *J. Am. Chem. Soc.* **2009,** *131*, 11027-11032.
(457) Zhu, Y.; Stoller, M. D.; Cai, W.; Velamakanni, A.; Piner, R. D.; Chen, D.; Ruoff, R. S. Exfoliation of Graphite Oxide in Propylene Carbonate and Thermal Reduction of the Resulting Graphene Oxide Platelets. *ACS Nano* **2010,** *4*, 1227-1233.
(458) Lin, Z.; Yao, Y.; Li, Z.; Liu, Y.; Li, Z.; Wong, C.-P. Solvent-Assisted Thermal Reduction of Graphite Oxide. *J. Phys. Chem. C* **2010,** *114*, 14819-14825.
(459) Le, L. T.; Ervin, M. H.; Qiu, H.; Fuchs, B. E.; Lee, W. Y. Graphene Supercapacitor Electrodes Fabricated by Inkjet Printing and Thermal Reduction of Graphene Oxide. *Electrochem. Commun.* **2011,** *13*, 355-358.
(460) Wang, Y.; Chen, Y.; Lacey, S. D.; Xu, L.; Xie, H.; Li, T.; Danner, V. A.; Hu, L. Reduced Graphene Oxide Film with Record-High Conductivity and Mobility. *Mater. Today* **2018,** *21*, 186-192.
(461) Zhu, Y.; Murali, S.; Stoller, M. D.; Velamakanni, A.; Piner, R. D.; Ruoff, R. S. Microwave Assisted Exfoliation and Reduction of Graphite Oxide for Ultracapacitors. *Carbon* **2010,** *48*, 2118-2122.
(462) Voiry, D.; Yang, J.; Kupferberg, J.; Fullon, R.; Lee, C.; Jeong, H. Y.; Shin, H. S.; Chhowalla, M. High-Quality Graphene via Microwave Reduction of Solution-Exfoliated Graphene Oxide. *Science* **2016,** *353*, 1413-1416.
(463) Novoselov, K. S.; Fal, V.; Colombo, L.; Gellert, P.; Schwab, M.; Kim, K. A Roadmap for Graphene. *Nature* **2012,** *490*, 192.

(464) Coleman, J. N.; Lotya, M.; O'Neill, A.; Bergin, S. D.; King, P. J.; Khan, U.; Young, K.; Gaucher, A.; De, S.; Smith, R. J. Two-dimensional Nanosheets Produced by Liquid Exfoliation of Layered Materials. *Science* **2011,** *331*, 568-571.
(465) Coleman, J. N. Liquid Exfoliation of Defect-free Graphene. *Acc. Chem. Res.* **2012,** *46*, 14-22.
(466) Ciesielski, A.; Samorì, P. Graphene via Sonication Assisted Liquid-phase Exfoliation. *Chem. Soc. Rev.* **2014,** *43*, 381-398.
(467) Li, X.; Cai, W.; An, J.; Kim, S.; Nah, J.; Yang, D.; Piner, R.; Velamakanni, A.; Jung, I.; Tutuc, E. Large-Area Synthesis of High-Quality and Uniform Graphene Films on Copper Foils. *Science* **2009,** *324*, 1312-1314.
(468) Obraztsov, A. N. Chemical Vapour Deposition: Making Graphene on a Large Scale. *Nat. Nanotechnol.* **2009,** *4*, 212.
(469) Reina, A.; Jia, X.; Ho, J.; Nezich, D.; Son, H.; Bulovic, V.; Dresselhaus, M. S.; Kong, J. Large Area, Few-Layer Graphene Films on Arbitrary Substrates by Chemical Vapor Deposition. *Nano Lett.* **2008,** *9*, 30-35.
(470) Wang, Y.; Xu, X.; Lu, J.; Lin, M.; Bao, Q.; Ozyilmaz, B.; Loh, K. P. Toward High Throughput Interconvertible Graphane-To-Graphene Growth and Patterning. *ACS Nano* **2010,** *4*, 6146-6152.
(471) Boyd, D.; Lin, W.-H.; Hsu, C.-C.; Teague, M.; Chen, C.-C.; Lo, Y.-Y.; Chan, W.-Y.; Su, W.-B.; Cheng, T.-C.; Chang, C.-S. Single-step Deposition of High-mobility Graphene at Reduced Temperatures. *Nat. Commun.* **2015,** *6*, 6620.
(472) Göckeritz, R.; Schmidt, D.; Beleites, M.; Seifert, G.; Krischok, S. P.; Himmerlich, M.; Pezoldt, J. Mater. Sci. Forum, 2011; p 785-788.
(473) Emtsev, K. V.; Bostwick, A.; Horn, K.; Jobst, J.; Kellogg, G. L.; Ley, L.; McChesney, J. L.; Ohta, T.; Reshanov, S. A.; Röhrl, J. Towards Wafer-size Graphene Layers by Atmospheric Pressure Graphitization of Silicon Carbide. *Nat. Mater.* **2009,** *8*, 203.
(474) Srivastava, A.; Galande, C.; Ci, L.; Song, L.; Rai, C.; Jariwala, D.; Kelly, K. F.; Ajayan, P. M. Novel Liquid Precursor-Based Facile Synthesis of Large-Area Continuous, Single, and Few-Layer Graphene Films. *Chem. Mater.* **2010,** *22*, 3457-3461.
(475) Zhang, B.; Lee, W. H.; Piner, R.; Kholmanov, I.; Wu, Y.; Li, H.; Ji, H.; Ruoff, R. S. Low-Temperature Chemical Vapor Deposition Growth of Graphene from Toluene on Electropolished Copper Foils. *ACS Nano* **2012,** *6*, 2471-2476.
(476) Dong, X.; Wang, P.; Fang, W.; Su, C.-Y.; Chen, Y.-H.; Li, L.-J.; Huang, W.; Chen, P. Growth of Large-sized Graphene Thin-films by Liquid Precursor-based Chemical Vapor Deposition Under Atmospheric Pressure. *Carbon* **2011,** *49*, 3672-3678.
(477) Li, X.; Magnuson, C. W.; Venugopal, A.; An, J.; Suk, J. W.; Han, B.; Borysiak, M.; Cai, W.; Velamakanni, A.; Zhu, Y. Graphene Films with Large Domain Size by a Two-Step Chemical Vapor Deposition Process. *Nano Lett.* **2010,** *10*, 4328-4334.
(478) Vlassiouk, I.; Fulvio, P.; Meyer, H.; Lavrik, N.; Dai, S.; Datskos, P.; Smirnov, S. Large Scale Atmospheric Pressure Chemical Vapor Deposition of Graphene. *Carbon* **2013,** *54*, 58-67.
(479) Eizenberg, M.; Blakely, J. Carbon Monolayer Phase Condensation on Ni (111). *Surf. Sci.* **1979,** *82*, 228-236.
(480) Edwards, R. S.; Coleman, K. S. Graphene Film Growth on Polycrystalline Metals. *Acc. Chem. Res.* **2012,** *46*, 23-30.

(481) Starr, D. E.; Pazhetnov, E. M.; Stadnichenko, A. I.; Boronin, A. I.; Shaikhutdinov, S. K. Carbon Films Grown on Pt (1 1 1) as Supports for Model Gold Catalysts. *Surf. Sci.* **2006,** *600*, 2688-2695.
(482) Sutter, E.; Acharya, D.; Sadowski, J.; Sutter, P. Scanning Tunneling Microscopy on Epitaxial Bilayer Graphene on Ruthenium (0001). *Appl. Phys. Lett.* **2009,** *94*, 133101.
(483) Coraux, J.; N 'Diaye, A. T.; Busse, C.; Michely, T. Structural Coherency of Graphene on Ir (111). *Nano Lett.* **2008,** *8*, 565-570.
(484) Huang, H.; Chen, W.; Chen, S.; Wee, A. T. S. Bottom-up Growth of Epitaxial Graphene on 6H-SiC (0001). *ACS Nano* **2008,** *2*, 2513-2518.
(485) Wang, Y.; Chen, X.; Zhong, Y.; Zhu, F.; Loh, K. P. Large Area, Continuous, Few-Layered Graphene as Anodes in Organic Photovoltaic Devices. *Appl. Phys. Lett.* **2009,** *95*, 063302.
(486) Yin, Z.; Zhu, J.; He, Q.; Cao, X.; Tan, C.; Chen, H.; Yan, Q.; Zhang, H. Graphene-Based Materials for Solar Cell Applications. *Adv. Energy Mater.* **2014,** *4*, 1300574.
(487) Guo, C. X.; Guai, G. H.; Li, C. M. Graphene Based Materials: Enhancing Solar Energy Harvesting. *Adv. Energy Mater.* **2011,** *1*, 448-452.
(488) Yang, X.; Tang, S.; Ding, G.; Xie, X.; Jiang, M.; Huang, F. Layer-By-Layer Thinning of Graphene by Plasma Irradiation and Post-Annealing. *Nanotechnology* **2011,** *23*, 025704.
(489) Xie, L.; Jiao, L.; Dai, H. Selective Etching of Graphene Edges by Hydrogen Plasma. *J. Am. Chem. Soc.* **2010,** *132*, 14751-14753.
(490) Kim, H.; Miura, Y.; Macosko, C. W. Graphene/Polyurethane Nanocomposites for Improved Gas Barrier and Electrical Conductivity. *Chem. Mater.* **2010,** *22*, 3441-3450.
(491) Liu, J.; Tang, J.; Gooding, J. J. Strategies for Chemical Modification of Graphene and Applications of Chemically Modified Graphene. *J. Mater. Chem.* **2012,** *22*, 12435-12452.
(492) Han, T.-H.; Lee, Y.; Choi, M.-R.; Woo, S.-H.; Bae, S.-H.; Hong, B. H.; Ahn, J.-H.; Lee, T.-W. Extremely Efficient Flexible Organic Light-emitting Diodes with Modified Graphene Anode. *Nat. Photonics* **2012,** *6*, 105.
(493) Sung, H.; Ahn, N.; Jang, M. S.; Lee, J.-K.; Yoon, H.; Park, N.-G.; Choi, M. Transparent Conductive Oxide-Free Graphene-Based Perovskite Solar Cells with over 17% Efficiency. *Advanced Energy Materials* **2016,** *6*, 1501873.
(494) Iijima, S. Helical Microtubules of Graphitic Carbon. *Nature* **1991,** *354*, 56-58.
(495) Iijima, S.; Ichihashi, T. Single-shell Carbon Nanotubes of 1-nm Diameter. *Nature* **1993,** *363*, 603-605.
(496) Lee, C. J.; Park, J.; Jeong, A. Y. Catalyst Effect on Carbon Nanotubes Synthesized by Thermal Chemical Vapor Deposition. *Chem. Phys. Lett.* **2002,** *360*, 250-255.
(497) Terrones, M.; Grobert, N.; Olivares, J.; Zhang, J. P.; Terrones, H.; Kordatos, K.; Hsu, W. K.; Hare, J. P.; Townsend, P. D.; Prassides, K.et al. Controlled Production of Aligned-Nanotube Bundles. *Nature* **1997,** *388*, 52-55.
(498) Sugai, T.; Yoshida, H.; Shimada, T.; Okazaki, T.; Shinohara, H. New Synthesis of High-Quality Double-Walled Carbon Nanotubes by High-Temperature Pulsed Arc Discharge. *Nano Lett.* **2003,** *3*, 769-773.
(499) Hutchison, J. L.; Kiselev, N. A.; Krinichnaya, E. P.; Krestinin, A. V.; Loutfy, R. O.; Morawsky, A. P.; Muradyan, V. E.; Obraztsova, E. D.; Sloan, J.; Terekhov, S. V.et al. Double-walled Carbon Nanotubes Fabricated by a Hydrogen Arc Discharge Method. *Carbon* **2001,** *39*, 761-770.

(500) Nasibulin, A. G.; Pikhitsa, P. V.; Jiang, H.; Kauppinen, E. I. Correlation Between Catalyst Particle and Single-Walled Carbon Nanotube Diameters. *Carbon* **2005,** *43*, 2251-2257.
(501) Hayashi, T.; Kim, Y. A.; Matoba, T.; Esaka, M.; Nishimura, K.; Tsukada, T.; Endo, M.; Dresselhaus, M. S. Smallest Freestanding Single-Walled Carbon Nanotube. *Nano Lett.* **2003,** *3*, 887-889.
(502) Yang, G.-W.; Gao, G.-Y.; Wang, C.; Xu, C.-L.; Li, H.-L. Controllable Deposition of Ag Nanoparticles on Carbon Nanotubes as a Catalyst for Hydrazine Oxidation. *Carbon* **2008,** *46*, 747-752.
(503) Bhaviripudi, S.; Mile, E.; Steiner, S. A.; Zare, A. T.; Dresselhaus, M. S.; Belcher, A. M.; Kong, J. CVD Synthesis of Single-Walled Carbon Nanotubes from Gold Nanoparticle Catalysts. *J. Am. Chem. Soc.* **2007,** *129*, 1516-1517.
(504) Lee, C. J.; Park, J.; Kim, J. M.; Huh, Y.; Lee, J. Y.; No, K. S. Low-Temperature Growth of Carbon Nanotubes by Thermal Chemical Vapor Deposition Using Pd, Cr, and Pt as Co-Catalyst. *Chem. Phys. Lett.* **2000,** *327*, 277-283.
(505) Hofmann, S.; Blume, R.; Wirth, C. T.; Cantoro, M.; Sharma, R.; Ducati, C.; Hävecker, M.; Zafeiratos, S.; Schnoerch, P.; Oestereich, A. State of transition metal catalysts during carbon nanotube growth. *J. Phys. Chem. C* **2009,** *113*, 1648-1656.
(506) Tang, S.; Zhong, Z.; Xiong, Z.; Sun, L.; Liu, L.; Lin, J.; Shen, Z. X.; Tan, K. L. Controlled Growth of Single-Walled Carbon Nanotubes by Catalytic Decomposition of CH4 over Mo/Co/MgO Catalysts. *Chem. Phys. Lett.* **2001,** *350*, 19-26.
(507) Gamaly, E. G.; Ebbesen, T. W. Mechanism of carbon nanotube formation in the arc discharge. *Phys. Rev. B* **1995,** *52*, 2083-2089.
(508) Journet, C.; Bernier, P. Production of Carbon Nanotubes. *Appl. Phys. A* **1998,** *67*, 1-9.
(509) Shi, Z.; Lian, Y.; Zhou, X.; Gu, Z.; Zhang, Y.; Iijima, S.; Zhou, L.; Yue, K. T.; Zhang, S. Mass-Production of Single-Wall Carbon Nanotubes by Arc Discharge Method. *Carbon* **1999,** *37*, 1449-1453.
(510) Scott, C. D.; Arepalli, S.; Nikolaev, P.; Smalley, R. E. Growth Mechanisms for Single-Wall Carbon Nanotubes in a Laser-Ablation Process. *Appl. Phys. A* **2001,** *72*, 573-580.
(511) Zhang, Y.; Gu, H.; Iijima, S. Single-Wall Carbon Nanotubes Synthesized by Laser Ablation in a Nitrogen Atmosphere. *Appl. Phys. Lett.* **1998,** *73*, 3827-3829.
(512) Kazeimzadeh, F.; Malekfar, R.; Houshiar, M. The Effect of Graphitic Target Density on Carbon Nanotube Synthesis by Pulsed Laser Ablation Method. *AIP Conf. Proc.* **2018,** *1920*, 020018.
(513) Yudasaka, M.; Komatsu, T.; Ichihashi, T.; Iijima, S. Single-Wall Carbon Nanotube Formation by Laser Ablation Using Double-Targets of Carbon and Metal. *Chem. Phys. Lett.* **1997,** *278*, 102-106.
(514) Kataura, H.; Kumazawa, Y.; Maniwa, Y.; Ohtsuka, Y.; Sen, R.; Suzuki, S.; Achiba, Y. Diameter Control of Single-walled Carbon Nanotubes. *Carbon* **2000,** *38*, 1691-1697.
(515) Maser, W. K.; Muñoz, E.; Benito, A. M.; Martínez, M. T.; de la Fuente, G. F.; Maniette, Y.; Anglaret, E.; Sauvajol, J. L. Production of High-Density Single-Walled Nanotube Material by a Simple Laser-Ablation Method. *Chem. Phys. Lett.* **1998,** *292*, 587-593.
(516) Rinzler, A.; Liu, J.; Dai, H.; Nikolaev, P.; Huffman, C.; Rodriguez-Macias, F.; Boul, P.; Lu, A. H.; Heymann, D.; Colbert, D. Large-Scale Purification of Single-Wall Carbon Nanotubes: Process, Product, and Characterization. *Appl. Phys. A: Mater. Sci. Process.* **1998,** *67*, 29-37.

(517) Puretzky, A. A.; Geohegan, D. B.; Fan, X.; Pennycook, S. J. Dynamics of Single-Wall Carbon Nanotube Synthesis by Laser Vaporization. *Appl. Phys. A* **2000,** *70*, 153-160.
(518) Guo, T.; Nikolaev, P.; Thess, A.; Colbert, D. T.; Smalley, R. E. Catalytic Growth of Single-walled Nanotubes by Laser Vaporization. *Chem. Phys. Lett.* **1995,** *243*, 49-54.
(519) Thess, A.; Lee, R.; Nikolaev, P.; Dai, H.; Petit, P.; Robert, J.; Xu, C.; Lee, Y. H.; Kim, S. G.; Rinzler, A. G. Crystalline Ropes of Metallic Carbon Nanotubes. *Science* **1996,** *273*, 483-487.
(520) De Volder, M. F. L.; Tawfick, S. H.; Baughman, R. H.; Hart, A. J. Carbon Nanotubes: Present and Future Commercial Applications. *Science* **2013,** *339*, 535-539.
(521) Hongo, H.; Yudasaka, M.; Ichihashi, T.; Nihey, F.; Iijima, S. Chemical Vapor Deposition of Single-wall Carbon Nanotubes on Iron-film-coated Sapphire Substrates. *Chem. Phys. Lett.* **2002,** *361*, 349-354.
(522) Qingwen, L.; Hao, Y.; Yan, C.; Jin, Z.; Zhongfan, L. A Scalable CVD Synthesis of High-Purity Sngle-Wlled Carbon Nanotubes with Porous MgO as Support Material. *J. Mater. Chem.* **2002,** *12*, 1179-1183.
(523) Zaytseva, O.; Neumann, G. Carbon Nanomaterials: Production, Impact on Plant Development, Agricultural and Environmental Applications. *Chem. Biol. Technol. Agric.* **2016,** *3*, 17.
(524) Kong, J.; Cassell, A. M.; Dai, H. Chemical Vapor Deposition of Methane for Single-walled Carbon Nanotubes. *Chem. Phys. Lett.* **1998,** *292*, 567-574.
(525) Flahaut, E.; Bacsa, R.; Peigney, A.; Laurent, C. Gram-scale CCVD Synthesis of Double-walled Carbon Nanotubes. *Chem. Commun. (Camb.)* **2003,** 1442-1443.
(526) Flahaut, E.; Peigney, A.; Bacsa, W. S.; Bacsa, R. R.; Laurent, C. CCVD Synthesis of Carbon Nanotubes from (Mg, Co, Mo) O Catalysts: Influence of the Proportions of Cobalt and Molybdenum. *J. Mater. Chem.* **2004,** *14*, 646-653.
(527) Wang, Y.; Wei, F.; Luo, G. H.; Yu, H.; Gu, G. S. The Large-Scale Production of Carbon Nanotubes in a Nano-Agglomerate Fluidized-Bed Reactor. *Chem. Phys. Lett.* **2002,** *364*, 568-572.
(528) Wang, Y.; Kim, M. J.; Shan, H.; Kittrell, C.; Fan, H.; Ericson, L. M.; Hwang, W.-F.; Arepalli, S.; Hauge, R. H.; Smalley, R. E. Continued Growth of Single-Walled Carbon Nanotubes. *Nano Lett.* **2005,** *5*, 997-1002.
(529) Nerushev, O. A.; Sveningsson, M.; Falk, L. K.; Rohmund, F. Carbon Nanotube Films Obtained by Thermal Chemical Vapour Deposition. *J. Mater. Chem.* **2001,** *11*, 1122-1132.
(530) Choi, G.; Cho, Y.; Hong, S.; Park, J.; Son, K.; Kim, D. Carbon Nanotubes Synthesized by Ni-assisted Atmospheric Pressure Thermal Chemical Vapor Deposition. *J. Appl. Phys.* **2002,** *91*, 3847-3854.
(531) Zhu, S.; Su, C.-H.; Cochrane, J. C.; Lehoczky, S.; Cui, Y.; Burger, A. Growth Orientation of Carbon Nanotubes by Thermal Chemical Vapor Deposition. *J. Cryst. Growth* **2002,** *234*, 584-588.
(532) Griffiths, H.; Xu, C.; Barrass, T.; Cooke, M.; Iacopi, F.; Vereecken, P.; Esconjauregui, S. Plasma Assisted Growth of Nanotubes and Nanowires. *Surf. Coat. Technol.* **2007,** *201*, 9215-9220.
(533) Rohmund, F.; Morjan, R.-E.; Ledoux, G.; Huisken, F.; Alexandrescu, R. Carbon Nanotube Films Grown by Laser-Assisted Chemical Vapor Deposition. *J. Vac. Sci.*

Technol. B Microelectron. Nanometer. Struct. Process Meas. Phenom. **2002,** *20*, 802-811.

(534) Okamoto, A.; Gunjishima, I.; Inoue, T.; Akoshima, M.; Miyagawa, H.; Nakano, T.; Baba, T.; Tanemura, M.; Oomi, G. Thermal and Electrical Conduction Properties of Vertically Aligned Carbon Nanotubes Produced by Water-Assisted Chemical Vapor Deposition. *Carbon* **2011,** *49*, 294-298.

(535) Kuo, T.-F.; Juang, Z.-Y.; Tsai, C.-H.; Tsau, Y.-M.; Cheng, H.-F.; Lin, I.-N. Microwave-assisted Chemical Vapor Deposition Process for Synthesizing Carbon Nanotubes. *J. Vac. Sci. Technol. B Microelectron. Nanometer. Struct. Process Meas. Phenom.* **2001,** *19*, 1030-1033.

(536) Miao, H.; Lue, J.; Chen, S.; Chen, S.; Ouyang, M. Growth of Carbon Nanotubes on Transition Metal Alloys by Microwave-Enhanced Hot-Filament Deposition. *Thin Solid Films* **2005,** *484*, 58-63.

(537) Pasquier, A. D.; Unalan, H. E.; Kanwal, A.; Miller, S.; Chhowalla, M. Conducting and transparent single-wall carbon nanotube electrodes for polymer-fullerene solar cells. *Appl. Phys. Lett.* **2005,** *87*, 203511.

(538) Li, Z.; Kulkarni, S. A.; Boix, P. P.; Shi, E.; Cao, A.; Fu, K.; Batabyal, S. K.; Zhang, J.; Xiong, Q.; Wong, L. H.et al. Laminated Carbon Nanotube Networks for Metal Electrode-Free Efficient Perovskite Solar Cells. *ACS Nano* **2014,** *8*, 6797-6804.

(539) Luo, Q.; Ma, H.; Hao, F.; Hou, Q.; Ren, J.; Wu, L.; Yao, Z.; Zhou, Y.; Wang, N.; Jiang, K.et al. Carbon Nanotube Based Inverted Flexible Perovskite Solar Cells with All-Inorganic Charge Contacts. *Adv. Funct. Mater.* **2017,** *27*, 1703068.

(540) Suriyasena Liyanage, L.; Xu, X.; Pitner, G.; Bao, Z.; Wong, H. S. P. VLSI-Compatible Carbon Nanotube Doping Technique with Low Work-Function Metal Oxides. *Nano Lett.* **2014,** *14*, 1884-1890.

(541) Cao, Y.; Yu, H.; Tan, J.; Peng, F.; Wang, H.; Li, J.; Zheng, W.; Wong, N.-B. Nitrogen-, Phosphorous- and Boron-doped Carbon Nanotubes as Catalysts for the Aerobic Oxidation of Cyclohexane. *Carbon* **2013,** *57*, 433-442.

(542) Hellstrom, S. L.; Vosgueritchian, M.; Stoltenberg, R. M.; Irfan, I.; Hammock, M.; Wang, Y. B.; Jia, C.; Guo, X.; Gao, Y.; Bao, Z. Strong and Stable Doping of Carbon Nanotubes and Graphene by MoOx for Transparent Electrodes. *Nano Lett.* **2012,** *12*, 3574-3580.

(543) Zhou, Y.; Yin, X.; Luo, Q.; Zhao, X.; Zhou, D.; Han, J.; Hao, F.; Tai, M.; Li, J.; Liu, P.et al. Efficiently Improving the Stability of Inverted Perovskite Solar Cells by Employing Polyethylenimine-Modified Carbon Nanotubes as Electrodes. *ACS Appl. Mater. Interfaces* **2018,** *10*, 31384-31393.

(544) Tung, V. C.; Allen, M. J.; Yang, Y.; Kaner, R. B. High-Throughput Solution Processing of Large-Scale Graphene. *Nat. Nanotechnol.* **2008,** *4*, 25.

(545) Chen, C.-Y.; Chang, H.-W.; Chang, Y.-F.; Chang, B.-J.; Lin, Y.-S.; Jian, P.-S.; Yeh, H.-C.; Chien, H.-T.; Chen, E.-C.; Chao, Y.-C.et al. Continuous Blade Coating for Multi-layer Large-area Organic Lght-Emitting Diode and Solar Cell. *J. Appl. Phys.* **2011,** *110*, 094501.

(546) Zhao, Y.; Burda, C. Development of Plasmonic Semiconductor Nanomaterials with Copper Chalcogenides for a Future with Sustainable Energy Materials. *Energy Environ. Sci.* **2012,** *5*, 5564-5576.

(547) Li, W.; Dong, H.; Guo, X.; Li, N.; Li, J.; Niu, G.; Wang, L. Graphene Oxide as Dual Functional Interface Modifier for Improving Wettability and Retarding Recombination in Hybrid Perovskite Solar Cells. *J. Mater. Chem. A* **2014,** *2*, 20105-20111.
(548) Hall, D. B.; Underhill, P.; Torkelson, J. M. Spin Coating of Thin and Ultrathin Polymer Films. *Polym. Eng. Sci.* **1998,** *38*, 2039-2045.
(549) Sridhar, A.; van Dijk, D. J.; Akkerman, R. Inkjet Printing and Adhesion Characterisation of Conductive Tracks on a Commercial Printed Circuit Board Material. *Thin Solid Films* **2009,** *517*, 4633-4637.
(550) Kang, M.-G.; Joon Park, H.; Hyun Ahn, S.; Jay Guo, L. Transparent Cu Nanowire Mesh Electrode on Flexible Substrates Fabricated by Transfer Printing and Its Application in Organic Solar Cells. *Sol. Energy Mater. Sol. Cells* **2010,** *94*, 1179-1184.
(551) Bornside, D.; Macosko, C.; Scriven, L. Modeling OF Spin Coating. *J. Imaging Technol.* **1987,** *13*, 122-130.
(552) Chen, B. Investigation of the Solvent‐evaporation Effect on Spin Coating of Thin Films. *Polym. Eng. Sci.* **1983,** *23*, 399-403.
(553) Zhang, F.; Di, C.-a.; Berdunov, N.; Hu, Y.; Hu, Y.; Gao, X.; Meng, Q.; Sirringhaus, H.; Zhu, D. Ultrathin Film Organic Transistors: Precise Control of Semiconductor Thickness via Spin-Coating. *Adv. Mater.* **2013,** *25*, 1401-1407.
(554) Washo, B. Rheology and Modeling of the Spin Coating Process. *IBM J. Res. Dev.* **1977,** *21*, 190-198.
(555) Søndergaard, R.; Hösel, M.; Angmo, D.; Larsen-Olsen, T. T.; Krebs, F. C. Roll-to-Roll Fabrication of Polymer Solar Cells. *Mater. Today* **2012,** *15*, 36-49.
(556) Aktaruzzaman, A.; Sharma, G.; Malhotra, L. Electrical, Optical and Annealing Characteristics of ZnO: Al Films Prepared by Spray Pyrolysis. *Thin Solid Films* **1991,** *198*, 67-74.
(557) Zimmermann, B.; Schleiermacher, H.-F.; Niggemann, M.; Würfel, U. ITO-Free Flexible Inverted Organic Solar Cell Modules with High Fill Factor Prepared by Slot Die Coating. *Sol. Energy Mater. Sol. Cells* **2011,** *95*, 1587-1589.
(558) Kim, D.-J.; Shin, H.-I.; Ko, E.-H.; Kim, K.-H.; Kim, T.-W.; Kim, H.-K. Roll-to-roll Slot-die Coating of 400 mm Wide, Flexible, Transparent Ag Nanowire Films for Flexible Touch Screen Panels. *Sci. Rep.* **2016,** *6*, 34322.
(559) Larsen-Olsen, T. T.; Andreasen, B.; Andersen, T. R.; Böttiger, A. P. L.; Bundgaard, E.; Norrman, K.; Andreasen, J. W.; Jørgensen, M.; Krebs, F. C. Simultaneous Multilayer Formation of the Polymer Solar Cell Stack Using Roll-to-roll Double Slot-die Coating From Water. *Sol. Energy Mater. Sol. Cells* **2012,** *97*, 22-27.
(560) Stüwe, D.; Mager, D.; Biro, D.; Korvink, J. G. Inkjet Technology for Crystalline Silicon Photovoltaics. *Adv. Mater.* **2015,** *27*, 599-626.
(561) Mathies, F.; Eggers, H.; Richards, B. S.; Hernandez-Sosa, G.; Lemmer, U.; Paetzold, U. W. Inkjet-Printed Triple Cation Perovskite Solar Cells. *ACS Appl. Energy Mater.* **2018,** *1*, 1834-1839.
(562) Yu, Y.; Xiao, X.; Zhang, Y.; Li, K.; Yan, C.; Wei, X.; Chen, L.; Zhen, H.; Zhou, H.; Zhang, S.et al. Photoreactive and Metal-Platable Copolymer Inks for High-Throughput, Room-Temperature Printing of Flexible Metal Electrodes for Thin-Film Electronics. *Adv. Mater.* **2016,** *28*, 4926-4934.
(563) Soltman, D.; Smith, B.; Kang, H.; Morris, S. J. S.; Subramanian, V. Methodology for Inkjet Printing of Partially Wetting Films. *Langmuir* **2010,** *26*, 15686-15693.

(564) van Osch, T. H. J.; Perelaer, J.; de Laat, A. W. M.; Schubert, U. S. Inkjet Printing of Narrow Conductive Tracks on Untreated Polymeric Substrates. *Adv. Mater.* **2008,** *20*, 343-345.
(565) Matavž, A.; Frunză, R. C.; Drnovšek, A.; Bobnar, V.; Malič, B. Inkjet Printing of Uniform Dielectric Oxide Structures from Sol–Gel Inks by Adjusting the Solvent Composition. *J. Mater. Chem. C* **2016,** *4*, 5634-5641.
(566) Shin, P.; Sung, J.; Lee, M. H. Control of Droplet Formation for Low Viscosity Fluid by Double Waveforms Applied to a Piezoelectric Inkjet Nozzle. *Microelectron. Reliab.* **2011,** *51*, 797-804.
(567) Worthington, I.; Patton, D. Strategic Intent in the Management of the Green Environment within SMEs: An Analysis of the UK Screen-Printing Sector. *Long Range Plann.* **2005,** *38*, 197-212.
(568) Locher, I.; Tröster, G. Screen-Printed Textile Transmission Lines. *Text. Res. J.* **2007,** *77*, 837-842.
(569) El-Molla, M. M.; Schneider, R. Development of Ecofriendly Binders for Pigment Printing of All Types of Textile Fabrics. *Dyes Pigm.* **2006,** *71*, 130-137.
(570) Hyun, W. J.; Secor, E. B.; Hersam, M. C.; Frisbie, C. D.; Francis, L. F. High-Resolution Patterning of Graphene by Screen Printing with a Silicon Stencil for Highly Flexible Printed Electronics. *Adv. Mater.* **2015,** *27*, 109-115.
(571) Antoniadis, H.; Jiang, F.; Shan, W.; Liu, Y. 2010 35th IEEE Photovoltaic Specialists Conference, 2010; p 001193-001196.
(572) Aberle, A. G. Surface passivation of crystalline silicon solar cells: a review. *Prog. Photovoltaics Res. Appl.* **2000,** *8*, 473-487.
(573) Nakayama, N.; Matsumoto, H.; Nakano, A.; Ikegami, S.; Uda, H.; Yamashita, T. Screen Printed Thin Film CdS/CdTe Solar Cell. *Jpn. J. Appl. Phys.* **1980,** *19*, 703-712.
(574) Krebs, F. C.; Espinosa, N.; Hösel, M.; Søndergaard, R. R.; Jørgensen, M. 25th Anniversary Article: Rise to Power – OPV-Based Solar Parks. *Adv. Mater.* **2014,** *26*, 29-39.
(575) Organic solar cells. https://infinitypv.com/products/opv (accessed Jul. 29, 2019).
(576) A new type of solar cell is coming to market. https://www.economist.com/science-and-technology/2018/02/03/a-new-type-of-solar-cell-is-coming-to-market (accessed Jul. 29, 2019).
(577) Wu, H.; Hu, L.; Rowell, M. W.; Kong, D.; Cha, J. J.; McDonough, J. R.; Zhu, J.; Yang, Y.; McGehee, M. D.; Cui, Y. Electrospun Metal Nanofiber Webs as High-Performance Transparent Electrode. *Nano Lett.* **2010,** *10*, 4242-4248.
(578) Layani, M.; Magdassi, S. Flexible Transparent Conductive Coatings by Combining Self-assembly with Sintering of Silver Nanoparticles Performed at Room Temperature. *J. Mater. Chem.* **2011,** *21*, 15378-15382.
(579) Stubhan, T.; Krantz, J.; Li, N.; Guo, F.; Litzov, I.; Steidl, M.; Richter, M.; Matt, G. J.; Brabec, C. J. High Fill Factor Polymer Solar Cells Comprising a Transparent, Low Temperature Solution Processed Doped Metal Oxide/Metal Nanowire Composite Electrode. *Sol. Energy Mater. Sol. Cells* **2012,** *107*, 248-251.
(580) Mo, L.; Ran, J.; Yang, L.; Fang, Y.; Zhai, Q.; Li, L. Flexible Transparent Conductive Films Combining Flexographic Printed Silver Grids with CNT Coating. *Nanotechnology* **2016,** *27*, 065202.

(581) Kou, P.; Yang, L.; Chi, K.; He, S. Large-Area and Uniform Transparent Electrodes Fabricated by Polymethylmethacrylate-assisted Spin-coating of Silver Nanowires on Rigid and Flexible Substrates. *Opt. Mater. Express* **2015,** *5*, 2347-2358.
(582) Sahu, N.; Parija, B.; Panigrahi, S. Fundamental Understanding and Modeling of Spin Coating Process: A Review. *Indian J. Phys.* **2009,** *83*, 493-502.
(583) Liu, Z.; Parvez, K.; Li, R.; Dong, R.; Feng, X.; Müllen, K. Transparent Conductive Electrodes from Graphene/PEDOT:PSS Hybrid Inks for Ultrathin Organic Photodetectors. *Adv. Mater.* **2015,** *27*, 669-675.
(584) Reale, A.; La Notte, L.; Salamandra, L.; Polino, G.; Susanna, G.; Brown, T. M.; Brunetti, F.; Di Carlo, A. Spray Coating for Polymer Solar Cells: An Up-to-Date Overview. *Energy Technol.* **2015,** *3*, 385-406.
(585) Burgués-Ceballos, I.; Stella, M.; Lacharmoise, P.; Martínez-Ferrero, E. Towards Industrialization of Polymer Solar Cells: Material Processing for Upscaling. *J. Mater. Chem. A* **2014,** *2*, 17711-17722.
(586) Singh, M.; Haverinen, H. M.; Dhagat, P.; Jabbour, G. E. Inkjet Printing—Process and Its Applications. *Adv. Mater.* **2010,** *22*, 673-685.
(587) Zabihi, F.; Xie, Y.; Gao, S.; Eslamian, M. Morphology, Conductivity, and Wetting Characteristics of PEDOT:PSS Thin Films Deposited by Spin and Spray Coating. *Appl. Surf. Sci.* **2015,** *338*, 163-177.
(588) Leem, D.-S.; Edwards, A.; Faist, M.; Nelson, J.; Bradley, D. D. C.; de Mello, J. C. Efficient Organic Solar Cells with Solution-Processed Silver Nanowire Electrodes. *Adv. Mater.* **2011,** *23*, 4371-4375.
(589) Nair, R. R.; Blake, P.; Grigorenko, A. N.; Novoselov, K. S.; Booth, T. J.; Stauber, T.; Peres, N. M. R.; Geim, A. K. Fine Structure Constant Defines Visual Transparency of Graphene. *Science* **2008,** *320*, 1308-1308.
(590) Chang, N. L.; Yi Ho-Baillie, A. W.; Basore, P. A.; Young, T. L.; Evans, R.; Egan, R. J. A Manufacturing Cost Estimation Method with Uncertainty Analysis and Its Application to Perovskite on Glass Photovoltaic Modules. *Prog. Photovoltaics Res. Appl.* **2017,** *25*, 390-405.
(591) Jaczewska, J.; Budkowski, A.; Bernasik, A.; Raptis, I.; Raczkowska, J.; Goustouridis, D.; Rysz, J.; Sanopoulou, M. Humidity and Solvent Effects in Spin-coated Polythiophene–polystyrene Blends. *J. Appl. Polym. Sci.* **2007,** *105*, 67-79.
(592) Schwartz, L. W.; Roy, R. V. Theoretical and Numerical Results for Spin Coating of Viscous Liquids. *Phys. Fluids* **2004,** *16*, 569-584.
(593) Binda, M.; Natali, D.; Iacchetti, A.; Sampietro, M. Integration of an Organic Photodetector onto a Plastic Optical Fiber by Means of Spray Coating Technique. *Adv. Mater.* **2013,** *25*, 4335-4339.
(594) Choi, D. Y.; Kang, H. W.; Sung, H. J.; Kim, S. S. Annealing-free, Flexible Silver Nanowire–polymer Composite Electrodes via a Continuous Two-step Spray-coating Method. *Nanoscale* **2013,** *5*, 977-983.
(595) Lotya, M.; Hernandez, Y.; King, P. J.; Smith, R. J.; Nicolosi, V.; Karlsson, L. S.; Blighe, F. M.; De, S.; Wang, Z.; McGovern, I. T.et al. Liquid Phase Production of Graphene by Exfoliation of Graphite in Surfactant/Water Solutions. *J. Am. Chem. Soc.* **2009,** *131*, 3611-3620.
(596) Casaluci, S.; Gemmi, M.; Pellegrini, V.; Di Carlo, A.; Bonaccorso, F. Graphene-based Large Area Dye-sensitized Solar Cell Modules. *Nanoscale* **2016,** *8*, 5368-5378.

(597) Cameron, P. J.; Peter, L. M. Characterization of Titanium Dioxide Blocking Layers in Dye-sensitized Nanocrystalline Solar Cells. *J. Phys. Chem. B* **2003,** *107*, 14394-14400.
(598) Smestad, G. P.; Spiekermann, S.; Kowalik, J.; Grant, C. D.; Schwartzberg, A. M.; Zhang, J.; Tolbert, L. M.; Moons, E. A Technique to Compare Polythiophene Solid-State Dye Sensitized TiO2 Solar Cells to Liquid Junction Devices. *Sol. Energy Mater. Sol. Cells* **2003,** *76*, 85-105.
(599) Mahmood, K.; Swain, B. S.; Jung, H. S. Controlling the Surface Nanostructure of ZnO and Al-Doped ZnO Thin Films Using Electrostatic Spraying for Their Application in 12% Efficient Perovskite Solar Cells. *Nanoscale* **2014,** *6*, 9127-9138.
(600) Nomura, M.; Meester, B.; Schoonman, J.; Kapteijn, F.; Moulijn, J. A. Improvement of Thermal Stability of Porous Titania Films Prepared by Electrostatic Sol-Spray Deposition (ESSD). *Chem. Mater.* **2003,** *15*, 1283-1288.
(601) Park, S.-Y.; Kang, Y.-J.; Lee, S.; Kim, D.-G.; Kim, J.-K.; Kim, J. H.; Kang, J.-W. Spray-coated organic solar cells with large-area of 12.25cm2. *Sol. Energy Mater. Sol. Cells* **2011,** *95*, 852-855.
(602) Song, L.; Wang, W.; Körstgens, V.; Moseguí González, D.; Löhrer, F. C.; Schaffer, C. J.; Schlipf, J.; Peters, K.; Bein, T.; Fattakhova-Rohlfing, D.et al. In Situ Study of Spray Deposited Titania Photoanodes for Scalable Fabrication of Solid-State Dye-Sensitized Solar Cells. *Nano Energy* **2017,** *40*, 317-326.
(603) Sandström, A.; Dam, H. F.; Krebs, F. C.; Edman, L. Ambient Fabrication of Flexible and Large-Area Organic Light-Emitting Devices Using Slot-Die Coating. *Nat. Commun.* **2012,** *3*, 1002.
(604) Cheng, P.; Bai, H.; Zawacka, N. K.; Andersen, T. R.; Liu, W.; Bundgaard, E.; Jørgensen, M.; Chen, H.; Krebs, F. C.; Zhan, X. Roll-Coated Fabrication of Fullerene-Free Organic Solar Cells with Improved Stability. *Adv. Sci.* **2015,** *2*, 1500096.
(605) Flack, W. W.; Soong, D. S.; Bell, A. T.; Hess, D. W. A Mathematical Model for Spin Coating of Polymer Resists. *J. Appl. Phys.* **1984,** *56*, 1199-1206.
(606) Lucera, L.; Machui, F.; Kubis, P.; Schmidt, H. D.; Adams, J.; Strohm, S.; Ahmad, T.; Forberich, K.; Egelhaaf, H. J.; Brabec, C. J. Highly Efficient, Large Area, Roll Coated Flexible and Rigid OPV Modules with Geometric Fill Factors Up to 98.5% Processed with Commercially Available Materials. *Energy Environ. Sci.* **2016,** *9*, 89-94.
(607) Palumbiny, C. M.; Liu, F.; Russell, T. P.; Hexemer, A.; Wang, C.; Müller-Buschbaum, P. The Crystallization of PEDOT:PSS Polymeric Electrodes Probed In Situ during Printing. *Adv. Mater.* **2015,** *27*, 3391-3397.
(608) Hu, X.; Meng, X.; Xiong, J.; Huang, Z.; Yang, X.; Tan, L.; Chen, Y. Roll-to-Roll Fabrication of Flexible Orientated Graphene Transparent Electrodes by Shear Force and One-Step Reducing Post-Treatment. *Adv. Mater. Technol.* **2017,** *2*, 1700138.
(609) Shin, K.; Park, J.; Lee, C. A 250-mm-Width, Flexible, and Continuous Roll-To-Roll Slot-Die Coated Carbon Nanotube/Silver Nanowire Film Fabrication and a Study on the Effect of Anti-Reflective Overcoat. *Thin Solid Films* **2016,** *598*, 95-102.
(610) Angmo, D.; Andersen, T. R.; Bentzen, J. J.; Helgesen, M.; Søndergaard, R. R.; Jørgensen, M.; Carlé, J. E.; Bundgaard, E.; Krebs, F. C. Roll-to-Roll Printed Silver Nanowire Semitransparent Electrodes for Fully Ambient Solution-Processed Tandem Polymer Solar Cells. *Adv. Funct. Mater.* **2015,** *25*, 4539-4547.
(611) Jeong, H.; Park, S.; Lee, J.; Won, P.; Ko, S.-H.; Lee, D. Fabrication of Transparent Conductive Film with Flexible Silver Nanowires Using Roll-to-Roll Slot-Die Coating

and Calendering and Its Application to Resistive Touch Panel. *Adv. Electron. Mater.* **2018,** *4*, 1800243.
(612) Jakubka, F.; Heyder, M.; Machui, F.; Kaschta, J.; Eggerath, D.; Lövenich, W.; Krebs, F. C.; Brabec, C. J. Determining the Coating Speed Limitations for Organic Photovoltaic Inks. *Sol. Energy Mater. Sol. Cells* **2013,** *109*, 120-125.
(613) Carvalho, M. S.; Kheshgi, H. S. Low-flow Limit in Slot Coating: Theory and Experiments. *AIChE J.* **2000,** *46*, 1907-1917.
(614) Nam, J.; Carvalho, M. S. Flow Visualization and Operating Limits of Tensioned-Web-Over Slot Die Coating Process. *Chem. Eng. Process.* **2011,** *50*, 471-477.
(615) Eggenhuisen, T. M.; Galagan, Y.; Coenen, E. W. C.; Voorthuijzen, W. P.; Slaats, M. W. L.; Kommeren, S. A.; Shanmuganam, S.; Coenen, M. J. J.; Andriessen, R.; Groen, W. A. Digital Fabrication of Organic Solar Cells by Inkjet Printing Using Non-halogenated Solvents. *Sol. Energy Mater. Sol. Cells* **2015,** *134*, 364-372.
(616) Yunker, P. J.; Still, T.; Lohr, M. A.; Yodh, A. G. Suppression of the Coffee-Ring Effect by Shape-Dependent Capillary Interactions. *Nature* **2011,** *476*, 308.
(617) Soltman, D.; Subramanian, V. Inkjet-Printed Line Morphologies and Temperature Control of the Coffee Ring Effect. *Langmuir* **2008,** *24*, 2224-2231.
(618) Layani, M.; Gruchko, M.; Milo, O.; Balberg, I.; Azulay, D.; Magdassi, S. Transparent Conductive Coatings by Printing Coffee Ring Arrays Obtained at Room Temperature. *ACS Nano* **2009,** *3*, 3537-3542.
(619) Shimoni, A.; Azoubel, S.; Magdassi, S. Inkjet Printing of Flexible High-Performance Carbon Nanotube Transparent Conductive Films by "Coffee Ring Effect". *Nanoscale* **2014,** *6*, 11084-11089.
(620) Huang, L.; Huang, Y.; Liang, J.; Wan, X.; Chen, Y. Graphene-based Conducting Inks for Direct Inkjet Printing of Flexible Conductive Patterns and Their Applications in Electric Circuits and Chemical Sensors. *Nano Res.* **2011,** *4*, 675-684.
(621) Kim, S.-S.; Choi, S.-Y.; Park, C.-G.; Jin, H.-W. Transparent Conductive ITO Thin Films through the Sol-gel Process Using Metal Salts. *Thin Solid Films* **1999,** *347*, 155-160.
(622) Larsen-Olsen, T. T.; Søndergaard, R. R.; Norrman, K.; Jørgensen, M.; Krebs, F. C. All Printed Transparent Electrodes Through an Electrical Switching Mechanism: A Convincing Alternative to Indium-Tin-Oxide, Silver and Vacuum. *Energy Environ. Sci.* **2012,** *5*, 9467-9471.
(623) Fukuda, K.; Someya, T. Recent Progress in the Development of Printed Thin-Film Transistors and Circuits with High-Resolution Printing Technology. *Adv. Mater.* **2017,** *29*, 1602736.
(624) Overgaard, M. H.; Kühnel, M.; Hvidsten, R.; Petersen, S. V.; Vosch, T.; Nørgaard, K.; Laursen, B. W. Highly Conductive Semitransparent Graphene Circuits Screen-Printed from Water-Based Graphene Oxide Ink. *Adv. Mater. Technol.* **2017,** *2*, 1700011.
(625) Ito, S.; Zakeeruddin, S. M.; Humphry-Baker, R.; Liska, P.; Charvet, R.; Comte, P.; Nazeeruddin, M. K.; Péchy, P.; Takata, M.; Miura, H.et al. High-Efficiency Organic-Dye- Sensitized Solar Cells Controlled by Nanocrystalline-TiO2 Electrode Thickness. *Adv. Mater.* **2006,** *18*, 1202-1205.
(626) Ramasamy, E.; Lee, W. J.; Lee, D. Y.; Song, J. S. Portable, Parallel Grid Dye-Sensitized Solar Cell Module Prepared by Screen Printing. *J. Power Sources* **2007,** *165*, 446-449.

(627) Edwards, A. M. J.; Ledesma-Aguilar, R.; Newton, M. I.; Brown, C. V.; McHale, G. Not Spreading in Reverse: The Dewetting of a Liquid Film into a Single Drop. *Sci. Adv.* **2016,** *2*, e1600183.
(628) Liang, T.; Sun, W. Z.; Wang, L.; Wang, Y. H.; Li, H. Effect of surface energies on screen printing resolution. *IEEE Trans. Compon., Packag., Manuf.Technol. B* **1996,** *19*, 423-426.
(629) Hösel, M.; Søndergaard, R. R.; Angmo, D.; Krebs, F. C. Comparison of Fast Roll-to-Roll Flexographic, Inkjet, Flatbed, and Rotary Screen Printing of Metal Back Electrodes for Polymer Solar Cells. *Adv. Eng. Mater.* **2013,** *15*, 995-1001.
(630) Novoselov, K. S.; Fal, V.; Colombo, L.; Gellert, P.; Schwab, M.; Kim, K. A Roadmap for Graphene. *Nature* **2012,** *490*, 192.
(631) Suk, J. W.; Kitt, A.; Magnuson, C. W.; Hao, Y.; Ahmed, S.; An, J.; Swan, A. K.; Goldberg, B. B.; Ruoff, R. S. Transfer of CVD-Grown Monolayer Graphene onto Arbitrary Substrates. *ACS Nano* **2011,** *5*, 6916-6924.
(632) Yoon, J.; Sung, H.; Lee, G.; Cho, W.; Ahn, N.; Jung, H. S.; Choi, M. Superflexible, High-Efficiency Perovskite Solar Cells Utilizing Graphene Electrodes: Towards Future Foldable Power Sources. *Energy Environ. Sci.* **2017,** *10*, 337-345.
(633) Smith, I. C.; Hoke, E. T.; Solis-Ibarra, D.; McGehee, M. D.; Karunadasa, H. I. A Layered Hybrid Perovskite Solar-Cell Absorber with Enhanced Moisture Stability. *Angew. Chem. Int. Ed.* **2014,** *53*, 11232-11235.
(634) High-Performance Metal-Free Solar Cells Using Stamp Transfer Printed Vapor Phase Polymerized Poly(3,4-Ethylenedioxythiophene) Top Anodes. *Adv. Funct. Mater.* **2012,** *22*, 1454-1460.
(635) Gupta, D.; Wienk, M. M.; Janssen, R. A. J. Efficient Polymer Solar Cells on Opaque Substrates with a Laminated PEDOT:PSS Top Electrode. *Adv. Energy Mater.* **2013,** *3*, 782-787.
(636) Zhang, Y.; Wu, Z.; Li, P.; Ono, L. K.; Qi, Y.; Zhou, J.; Shen, H.; Surya, C.; Zheng, Z. Fully Solution-Processed TCO-Free Semitransparent Perovskite Solar Cells for Tandem and Flexible Applications. *Adv. Energy Mater.* **2018,** *8*, 1701569.
(637) Madaria, A. R.; Kumar, A.; Ishikawa, F. N.; Zhou, C. Uniform, Highly Conductive, and Patterned Transparent Films of a Percolating Silver Nanowire Network on Rigid and Flexible Substrates Using a Dry Transfer Technique. *Nano Res.* **2010,** *3*, 564-573.
(638) Yu, Z.; Zhang, Q.; Li, L.; Chen, Q.; Niu, X.; Liu, J.; Pei, Q. Highly Flexible Silver Nanowire Electrodes for Shape-Memory Polymer Light-Emitting Diodes. *Adv. Mater.* **2011,** *23*, 664-668.
(639) Gaynor, W.; Lee, J.-Y.; Peumans, P. Fully Solution-Processed Inverted Polymer Solar Cells with Laminated Nanowire Electrodes. *ACS Nano* **2010,** *4*, 30-34.
(640) Spyropoulos, G. D.; Ramirez Quiroz, C. O.; Salvador, M.; Hou, Y.; Gasparini, N.; Schweizer, P.; Adams, J.; Kubis, P.; Li, N.; Spiecker, E.et al. Organic and Perovskite Solar Modules Innovated by Adhesive Top Electrode and Depth-Resolved Laser Patterning. *Energy Environ. Sci.* **2016,** *9*, 2302-2313.
(641) Hoppe, H.; Sariciftci, N. S. Organic Solar Cells: An Overview. *J. Mater. Res.* **2011,** *19*, 1924-1945.
(642) Cui, Y.; Yao, H.; Zhang, J.; Zhang, T.; Wang, Y.; Hong, L.; Xian, K.; Xu, B.; Zhang, S.; Peng, J.et al. Over 16% Efficiency Organic Photovoltaic Cells Enabled By a Chlorinated Acceptor with Increased Open-circuit Voltages. *Nat. Commun.* **2019,** *10*, 2515.

(643) Park, S. H.; Roy, A.; Beaupré, S.; Cho, S.; Coates, N.; Moon, J. S.; Moses, D.; Leclerc, M.; Lee, K.; Heeger, A. J. Bulk heterojunction solar cells with internal quantum efficiency approaching 100%. *Nat. Photonics* **2009,** *3*, 297.
(644) Scharber, M. C.; Mühlbacher, D.; Koppe, M.; Denk, P.; Waldauf, C.; Heeger, A. J.; Brabec, C. J. Design Rules for Donors in Bulk-Heterojunction Solar Cells—Towards 10 % Energy-Conversion Efficiency. *Adv. Mater.* **2006,** *18*, 789-794.
(645) Zhao, W.; Li, S.; Yao, H.; Zhang, S.; Zhang, Y.; Yang, B.; Hou, J. Molecular Optimization Enables over 13% Efficiency in Organic Solar Cells. *J. Am. Chem. Soc.* **2017,** *139*, 7148-7151.
(646) Erb, T.; Zhokhavets, U.; Gobsch, G.; Raleva, S.; Stühn, B.; Schilinsky, P.; Waldauf, C.; Brabec, C. J. Correlation Between Structural and Optical Properties of Composite Polymer/Fullerene Films for Organic Solar Cells. *Adv. Funct. Mater.* **2005,** *15*, 1193-1196.
(647) Zhou, H.; Yang, L.; You, W. Rational Design of High Performance Conjugated Polymers for Organic Solar Cells. *Macromolecules* **2012,** *45*, 607-632.
(648) Günes, S.; Neugebauer, H.; Sariciftci, N. S. Conjugated Polymer-Based Organic Solar Cells. *Chem. Rev.* **2007,** *107*, 1324-1338.
(649) Li, G.; Zhu, R.; Yang, Y. Polymer Solar Cells. *Nat. Photonics* **2012,** *6*, 153-161.
(650) Peng, R.; Song, W.; Yan, T.; Fanady, B.; Li, Y.; Zhan, Q.; Ge, Z. Interface bonding engineering of a transparent conductive electrode towards highly efficient and mechanically flexible ITO-free organic solar cells. *J. Mater. Chem. A* **2019**, DOI:10.1039/C9TA02900A 10.1039/C9TA02900A
(651) Xiong, S.; Hu, L.; Hu, L.; Sun, L.; Qin, F.; Liu, X.; Fahlman, M.; Zhou, Y. 12.5% Flexible Nonfullerene Solar Cells by Passivating the Chemical Interaction Between the Active Layer and Polymer Interfacial Layer. *Adv. Mater. 0*, 1806616.
(652) Lungenschmied, C.; Dennler, G.; Neugebauer, H.; Sariciftci, S. N.; Glatthaar, M.; Meyer, T.; Meyer, A. Flexible, Long-Lived, Large-Area, Organic Solar Cells. *Sol. Energy Mater. Sol. Cells* **2007,** *91*, 379-384.
(653) Zeng, W. J.; Wu, H. B.; Zhang, C.; Huang, F.; Peng, J. B.; Yang, W.; Cao, Y. Polymer Light-Emitting Diodes with Cathodes Printed from Conducting Ag Paste. *Adv. Mater.* **2007,** *19*, 810-814.
(654) Sommer-Larsen, P.; Jørgensen, M.; Søndergaard, R. R.; Hösel, M.; Krebs, F. C. It is all in the Pattern—High-Efficiency Power Extraction from Polymer Solar Cells through High-Voltage Serial Connection. *Energy Technol.* **2013,** *1*, 15-19.
(655) Choi, H.; Kim, B.; Ko, M. J.; Lee, D.-K.; Kim, H.; Kim, S. H.; Kim, K. Solution processed WO3 Layer for the Replacement of PEDOT:PSS Layer in Organic Photovoltaic Cells. *Org. Electron.* **2012,** *13*, 959-968.
(656) Jørgensen, M.; Norrman, K.; Krebs, F. C. Stability/degradation of Polymer Solar Cells. *Sol. Energy Mater. Sol. Cells* **2008,** *92*, 686-714.
(657) Cho, A.; Kim, S.; Kim, S.; Cho, W.; Park, C.; Kim, F. S.; Kim, J. H. Influence of Imidazole-based Acidity Control of PEDOT:PSS on Its Electrical Properties and Environmental Stability. *J. Polym. Sci., Part B: Polym. Phys.* **2016,** *54*, 1530-1536.
(658) Thomas, J. P.; Rahman, M. A.; Srivastava, S.; Kang, J.-S.; McGillivray, D.; Abd-Ellah, M.; Heinig, N. F.; Leung, K. T. Highly Conducting Hybrid Silver-Nanowire-Embedded Poly(3,4-ethylenedioxythiophene):Poly(styrenesulfonate) for High-Efficiency Planar Silicon/Organic Heterojunction Solar Cells. *ACS Nano* **2018,** *12*, 9495-9503.

(659) Kim, A.; Won, Y.; Woo, K.; Kim, C.-H.; Moon, J. Highly Transparent Low Resistance ZnO/Ag Nanowire/ZnO Composite Electrode for Thin Film Solar Cells. *ACS Nano* **2013,** *7*, 1081-1091.
(660) Lei, T.; Peng, R.; Song, W.; Hong, L.; Huang, J.; Fei, N.; Ge, Z. Bendable and foldable flexible organic solar cells based on Ag nanowire films with 10.30% efficiency. *J. Mater. Chem. A* **2019,** *7*, 3737-3744.
(661) Chung, C.-H.; Song, T.-B.; Bob, B.; Zhu, R.; Duan, H.-S.; Yang, Y. Silver Nanowire Composite Window Layers for Fully Solution-Deposited Thin-Film Photovoltaic Devices. *Adv. Mater.* **2012,** *24*, 5499-5504.
(662) Choi, D. Y.; Oh, Y. S.; Han, D.; Yoo, S.; Sung, H. J.; Kim, S. S. Highly Conductive, Bendable, Embedded Ag Nanoparticle Wire Arrays Via Convective Self-Assembly: Hybridization into Ag Nanowire Transparent Conductors. *Adv. Funct. Mater.* **2015,** *25*, 3888-3898.
(663) Wu, J.; Que, X.; Hu, Q.; Luo, D.; Liu, T.; Liu, F.; Russell, T. P.; Zhu, R.; Gong, Q. Multi-Length Scaled Silver Nanowire Grid for Application in Efficient Organic Solar Cells. *Adv. Funct. Mater.* **2016,** *26*, 4822-4828.
(664) Krantz, J.; Stubhan, T.; Richter, M.; Spallek, S.; Litzov, I.; Matt, G. J.; Spiecker, E.; Brabec, C. J. Spray-Coated Silver Nanowires as Top Electrode Layer in Semitransparent P3HT:PCBM-Based Organic Solar Cell Devices. *Adv. Funct. Mater.* **2013,** *23*, 1711-1717.
(665) Selzer, F.; Weiß, N.; Kneppe, D.; Bormann, L.; Sachse, C.; Gaponik, N.; Eychmüller, A.; Leo, K.; Müller-Meskamp, L. A Spray-Coating Process for Highly Conductive Silver Nanowire Networks as the Transparent Top-Electrode for Small Molecule Organic Photovoltaics. *Nanoscale* **2015,** *7*, 2777-2783.
(666) Ji, G.; Wang, Y.; Luo, Q.; Han, K.; Xie, M.; Zhang, L.; Wu, N.; Lin, J.; Xiao, S.; Li, Y.-Q.et al. Fully Coated Semitransparent Organic Solar Cells with a Doctor-Blade-Coated Composite Anode Buffer Layer of Phosphomolybdic Acid and PEDOT:PSS and a Spray-Coated Silver Nanowire Top Electrode. *ACS Appl. Mater. Interfaces* **2018,** *10*, 943-954.
(667) Wang, Y.; Tong, S. W.; Xu, X. F.; Özyilmaz, B.; Loh, K. P. Interface Engineering of Layer-by-Layer Stacked Graphene Anodes for High-Performance Organic Solar Cells. *Adv. Mater.* **2011,** *23*, 1514-1518.
(668) Hsu, C.-L.; Lin, C.-T.; Huang, J.-H.; Chu, C.-W.; Wei, K.-H.; Li, L.-J. Layer-by-Layer Graphene/TCNQ Stacked Films as Conducting Anodes for Organic Solar Cells. *ACS Nano* **2012,** *6*, 5031-5039.
(669) Liu, Z.; Li, J.; Yan, F. Package-Free Flexible Organic Solar Cells with Graphene top Electrodes. *Adv. Mater.* **2013,** *25*, 4296-4301.
(670) Kim, H.; Byun, J.; Bae, S.-H.; Ahmed, T.; Zhu, J.-X.; Kwon, S.-J.; Lee, Y.; Min, S.-Y.; Wolf, C.; Seo, H.-K.et al. On-Fabrication Solid-State N-Doping of Graphene by an Electron-Transporting Metal Oxide Layer for Efficient Inverted Organic Solar Cells. *Adv. Energy Mater.* **2016,** *6*, 1600172.
(671) Kim, H. P.; Mohd Yusoff, A. R. b.; Jang, J. Organic Solar Cells Using a Reduced Graphene Oxide Anode Buffer Layer. *Sol. Energy Mater. Sol. Cells* **2013,** *110*, 87-93.
(672) Liu, J.; Xue, Y.; Gao, Y.; Yu, D.; Durstock, M.; Dai, L. Hole and Electron Extraction Layers Based on Graphene Oxide Derivatives for High-Performance Bulk Heterojunction Solar Cells. *Adv. Mater.* **2012,** *24*, 2228-2233.

(673) Konios, D.; Petridis, C.; Kakavelakis, G.; Sygletou, M.; Savva, K.; Stratakis, E.; Kymakis, E. Reduced Graphene Oxide Micromesh Electrodes for Large Area, Flexible, Organic Photovoltaic Devices. *Adv. Funct. Mater.* **2015,** *25*, 2213-2221.
(674) Ricciardulli, A. G.; Yang, S.; Feng, X.; Blom, P. W. M. Solution-Processable High-Quality Graphene for Organic Solar Cells. *ACS Appl. Mater. Interfaces* **2017,** *9*, 25412-25417.
(675) Liu, Z.; You, P.; Liu, S.; Yan, F. Neutral-Color Semitransparent Organic Solar Cells with All-Graphene Electrodes. *ACS Nano* **2015,** *9*, 12026-12034.
(676) Song, Y.; Chang, S.; Gradecak, S.; Kong, J. Visibly-Transparent Organic Solar Cells on Flexible Substrates with All-Graphene Electrodes. *Adv. Energy Mater.* **2016,** *6*, 1600847.
(677) Jeon, I.; Cui, K.; Chiba, T.; Anisimov, A.; Nasibulin, A. G.; Kauppinen, E. I.; Maruyama, S.; Matsuo, Y. Direct and Dry Deposited Single-Walled Carbon Nanotube Films Doped with MoOx as Electron-Blocking Transparent Electrodes for Flexible Organic Solar Cells. *J. Am. Chem. Soc.* **2015,** *137*, 7982-7985.
(678) Zhang, J.; Xu, G.; Tao, F.; Zeng, G.; Zhang, M.; Yang, Y.; Li, Y.; Li, Y. Highly Efficient Semitransparent Organic Solar Cells with Color Rendering Index Approaching 100. *Adv. Mater.* **2019,** *31*, 1807159.
(679) Mohd Yusoff, A. R. b.; Kim, D.; Schneider, F. K.; da Silva, W. J.; Jang, J. Au-Doped Single Layer Graphene Nanoribbons for a Record-High Efficiency ITO-Free Tandem Polymer Solar Cell. *Energy Environ. Sci.* **2015,** *8*, 1523-1537.
(680) Park, H.; Chang, S.; Zhou, X.; Kong, J.; Palacios, T.; Gradečak, S. Flexible Graphene Electrode-Based Organic Photovoltaics with Record-High Efficiency. *Nano Lett.* **2014,** *14*, 5148-5154.
(681) Yusoff, A. R. b. M.; Lee, S. J.; Shneider, F. K.; da Silva, W. J.; Jang, J. High-Performance Semitransparent Tandem Solar Cell of 8.02% Conversion Efficiency with Solution-Processed Graphene Mesh and Laminated Ag Nanowire Top Electrodes. *Adv. Energy Mater.* **2014,** *4*, 1301989.
(682) Seo, K.-W.; Noh, Y.-J.; Na, S.-I.; Kim, H.-K. Random Mesh-Like Ag Networks Prepared via Self-Assembled Ag Nanoparticles for ITO-Free Flexible Organic Solar Cells. *Sol. Energy Mater. Sol. Cells* **2016,** *155*, 51-59.
(683) Zhang, X.; Wu, J.; Wang, J.; Yang, Q.; Zhang, B.; Xie, Z. Low-Temperature All-Solution-Processed Transparent Silver Nanowire-Polymer/AZO Nanoparticles Composite Electrodes for Efficient ITO-Free Polymer Solar Cells. *ACS Appl. Mater. Interfaces* **2016,** *8*, 34630-34637.
(684) Zhang, Y.-X.; Fang, J.; Li, W.; Shen, Y.; Chen, J.-D.; Li, Y.; Gu, H.; Pelivani, S.; Zhang, M.; Li, Y.et al. Synergetic Transparent Electrode Architecture for Efficient Non-Fullerene Flexible Organic Solar Cells with >12% Efficiency. *ACS Nano* **2019,** *13*, 4686-4694.
(685) Song, M.; Kim, H.-J.; Kim, C. S.; Jeong, J.-H.; Cho, C.; Lee, J.-Y.; Jin, S.-H.; Choi, D.-G.; Kim, D.-H. ITO-Free Highly Bendable and Efficient Organic Solar Cells with Ag Nanomesh/ZnO Hybrid Electrodes. *J. Mater. Chem. A* **2015,** *3*, 65-70.
(686) O'Regan, B.; Grätzel, M. A Low-Cost, High-Efficiency Solar Cell Based on Dye-Sensitized Colloidal TiO2 Films. *Nature* **1991,** *353*, 737-740.
(687) Zhang, S.; Yang, X.; Numata, Y.; Han, L. Highly Efficient Dye-Sensitized Solar Cells: Progress and Future Challenges. *Energy Environ. Sci.* **2013,** *6*, 1443-1464.

(688) Calogero, G.; Calandra, P.; Irrera, A.; Sinopoli, A.; Citro, I.; Di Marco, G. A New Type of Transparent and Low Cost Counter-electrode Based on Platinum Nanoparticles for Dye-sensitized Solar Cells. *Energy Environ. Sci.* **2011,** *4*, 1838-1844.
(689) Yi, L.; Liu, Y.; Yang, N.; Tang, Z.; Zhao, H.; Ma, G.; Su, Z.; Wang, D. One Dimensional CuInS2–ZnS Heterostructured Nanomaterials as Low-Cost and High-Performance Counter Electrodes of Dye-Sensitized Solar Cells. *Energy Environ. Sci.* **2013,** *6*, 835-840.
(690) Kwon, J.; Ganapathy, V.; Kim, Y. H.; Song, K.-D.; Park, H.-G.; Jun, Y.; Yoo, P. J.; Park, J. H. Nanopatterned Conductive Polymer Films as a Pt, TCO-Free Counter Electrode for Low-cost Dye-sensitized Solar Cells. *Nanoscale* **2013,** *5*, 7838-7843.
(691) Cha, S. I.; Kim, Y.; Hwang, K. H.; Shin, Y.-J.; Seo, S. H.; Lee, D. Y. Dye-sensitized Solar Cells on Glass Paper: TCO-free Highly Bendable Dye-sensitized Solar Cells Inspired by the Traditional Korean Door Structure. *Energy Environ. Sci.* **2012,** *5*, 6071-6075.
(692) Ke, W.; Fang, G.; Tao, H.; Qin, P.; Wang, J.; Lei, H.; Liu, Q.; Zhao, X. In Situ Synthesis of NiS Nanowall Networks on Ni Foam as a TCO-Free Counter Electrode for Dye-Sensitized Solar Cells. *ACS Appl. Mater. Interfaces* **2014,** *6*, 5525-5530.
(693) Lee, K. S.; Lee, H. K.; Wang, D. H.; Park, N.-G.; Lee, J. Y.; Park, O. O.; Park, J. H. Dye-Sensitized Solar Cells with Pt- and TCO-Free Counter Electrodes. *Chem. Commun. (Camb.)* **2010,** *46*, 4505-4507.
(694) Yeon, C.; Yun, S. J.; Kim, J.; Lim, J. W. PEDOT:PSS Films with Greatly Enhanced Conductivity via Nitric Acid Treatment at Room Temperature and Their Application as Pt/TCO-Free Counter Electrodes in Dye-Sensitized Solar Cells. *Adv. Electron. Mater.* **2015,** *1*, 1500121.
(695) Ahmad, S.; Yum, J.-H.; Butt, H.-J.; Nazeeruddin, M. K.; Grätzel, M. Efficient Platinum-Free Counter Electrodes for Dye-Sensitized Solar Cell Applications. *ChemPhysChem* **2010,** *11*, 2814-2819.
(696) Yum, J.-H.; Baranoff, E.; Kessler, F.; Moehl, T.; Ahmad, S.; Bessho, T.; Marchioro, A.; Ghadiri, E.; Moser, J.-E.; Yi, C.et al. A Cobalt Complex Redox Shuttle for Dye-Sensitized Solar Cells with High Open-Circuit Potentials. *Nat. Commun.* **2012,** *3*, 631.
(697) Wu, J.; Li, Y.; Tang, Q.; Yue, G.; Lin, J.; Huang, M.; Meng, L. Bifacial Dye-Sensitized Solar Cells: A Strategy to Enhance Overall Efficiency Based on Transparent Polyaniline Electrode. *Sci. Rep.* **2014,** *4*, 4028.
(698) Xia, J.; Chen, L.; Yanagida, S. Application of Polypyrrole as a Counter Electrode for a Dye-Sensitized Solar Cell. *J. Mater. Chem.* **2011,** *21*, 4644-4649.
(699) Wu, J.; Li, Q.; Fan, L.; Lan, Z.; Li, P.; Lin, J.; Hao, S. High-Performance Polypyrrole Nanoparticles Counter Electrode for Dye-Sensitized Solar Cells. *J. Power Sources* **2008,** *181*, 172-176.
(700) Martinson, A. B.; Elam, J. W.; Hupp, J. T.; Pellin, M. J. ZnO Nanotube Based Dye-Sensitized Solar Cells. *Nano Lett.* **2007,** *7*, 2183-2187.
(701) Song, M. Y.; Kim, D. K.; Ihn, K. J.; Jo, S. M.; Kim, D. Y. Electrospun TiO2 Electrodes for Dye-Sensitized Solar Cells. *Nanotechnology* **2004,** *15*, 1861-1865.
(702) Yoo, K.; Kim, J.-Y.; Lee, J. A.; Kim, J. S.; Lee, D.-K.; Kim, K.; Kim, J. Y.; Kim, B.; Kim, H.; Kim, W. M.et al. Completely Transparent Conducting Oxide-Free and Flexible Dye-Sensitized Solar Cells Fabricated on Plastic Substrates. *ACS Nano* **2015,** *9*, 3760-3771.

(703) Fan, K.; Peng, T.; Chen, J.; Zhang, X.; Li, R. Low-cost, Quasi-solid-state and TCO-free Highly Bendable Dye-sensitized Cells on Paper Substrate. *J. Mater. Chem.* **2012,** *22*, 16121-16126.
(704) Sonigara, K. K.; Machhi, H. K.; Vaghasiya, J. V.; Gibaud, A.; Tan, S. C.; Soni, S. S. A Smart Flexible Solid State Photovoltaic Device with Interfacial Cooling Recovery Feature through Thermoreversible Polymer Gel Electrolyte. *Small* **2018,** *14*, 1800842.
(705) Chen, X.; Tang, Q.; He, B.; Lin, L.; Yu, L. Platinum-Free Binary Co-Ni Alloy Counter Electrodes for Efficient Dye-Sensitized Solar Cells. *Angew. Chem. Int. Ed.* **2014,** *53*, 10799-10803.
(706) Xiao, Y.; Wu, J.; Lin, J.-Y.; Tai, S.-Y.; Yue, G. Pulse Electrodeposition of CoS on MWCNT/Ti as a High Performance Counter Electrode for a Pt-Free Dye-Sensitized Solar Cell. *J. Mater. Chem. A* **2013,** *1*, 1289-1295.
(707) Xiao, Y.; Wu, J.; Lin, J.; Yue, G.; Lin, J.; Huang, M.; Huang, Y.; Lan, Z.; Fan, L. A High Performance Pt-Free Counter Electrode of Nickel Sulfide/Multi-Wall Carbon Nanotube/Titanium Used in Dye-Sensitized Solar Cells. *J. Mater. Chem. A* **2013,** *1*, 13885-13889.
(708) Gong, F.; Xu, X.; Li, Z.; Zhou, G.; Wang, Z.-S. NiSe2 as an Efficient Electrocatalyst for a Pt-free Counter Electrode of Dye-sensitized Solar Cells. *Chem. Commun. (Camb.)* **2013,** *49*, 1437-1439.
(709) Lin, J.-Y.; Wang, W.-Y.; Lin, Y.-T.; Chou, S.-W. Ni3S2/Ni–P Bilayer Coated on Polyimide as a Pt- and TCO-Free Flexible Counter Electrode for Dye-Sensitized Solar Cells. *ACS Appl. Mater. Interfaces* **2014,** *6*, 3357-3364.
(710) Zhang, X.; Guo, W.; Pan, C. Transparent Conducting Oxide-Free and Pt-Free Flexible Dye-Sensitized Solar Cells Employing CuS-Nanosheet Networks as Counter Electrodes. *J. Mater. Chem. A* **2016,** *4*, 6569-6576.
(711) Kavan, L.; Liska, P.; Zakeeruddin, S. M.; Grätzel, M. Optically Transparent FTO-Free Cathode for Dye-Sensitized Solar Cells. *ACS Appl. Mater. Interfaces* **2014,** *6*, 22343-22350.
(712) Kay, A.; Grätzel, M. Low Cost Photovoltaic Modules Based on Dye Sensitized Nanocrystalline Titanium Dioxide and Carbon Powder. *Sol. Energy Mater. Sol. Cells* **1996,** *44*, 99-117.
(713) Huang, Z.; Liu, X.; Li, K.; Li, D.; Luo, Y.; Li, H.; Song, W.; Chen, L.; Meng, Q. Application of Carbon Materials as Counter Electrodes of Dye-sensitized Solar Cells. *Electrochem. Commun.* **2007,** *9*, 596-598.
(714) Roy-Mayhew, J. D.; Bozym, D. J.; Punckt, C.; Aksay, I. A. Functionalized Graphene as a Catalytic Counter Electrode in Dye-Sensitized Solar Cells. *ACS Nano* **2010,** *4*, 6203-6211.
(715) Kavan, L.; Yum, J.-H.; Nazeeruddin, M. K.; Grätzel, M. Graphene Nanoplatelet Cathode for Co(III)/(II) Mediated Dye-Sensitized Solar Cells. *ACS Nano* **2011,** *5*, 9171-9178.
(716) Balamurugan, J.; Thanh, T. D.; Kim, N. H.; Lee, J. H. Nitrogen-Doped Graphene Nanosheets with FeN Core–Shell Nanoparticles as High-Performance Counter Electrode Materials for Dye-Sensitized Solar Cells. *Adv. Mater. Interfaces* **2016,** *3*, 1500348.
(717) Wang, H.; Hu, Y. H. Graphene as a Counter Electrode Material for Dye-Sensitized Solar Cells. *Energy Environ. Sci.* **2012,** *5*, 8182-8188.

(718) Lee, K. S.; Lee, Y.; Lee, J. Y.; Ahn, J.-H.; Park, J. H. Flexible and Platinum-Free Dye-Sensitized Solar Cells with Conducting-Polymer-Coated Graphene Counter Electrodes. *ChemSusChem* **2012,** *5*, 379-382.
(719) Lee, J.-S.; Ahn, H.-J.; Yoon, J.-C.; Jang, J.-H. Three-Dimensional Nano-Foam of Few-Layer Graphene Grown by CVD for DSSC. *Phys. Chem. Chem. Phys.* **2012,** *14*, 7938-7943.
(720) Wang, H.; Sun, K.; Tao, F.; Stacchiola, D. J.; Hu, Y. H. 3D Honeycomb-Like Structured Graphene and Its High Efficiency as a Counter-Electrode Catalyst for Dye-Sensitized Solar Cells. *Angew. Chem. Int. Ed.* **2013,** *52*, 9210-9214.
(721) Gagliardi, S.; Giorgi, L.; Giorgi, R.; Lisi, N.; Dikonimos Makris, T.; Salernitano, E.; Rufoloni, A. Impedance Analysis of Nanocarbon DSSC Electrodes. *Superlattices Microstruct.* **2009,** *46*, 205-208.
(722) Memon, A. A.; Arbab, A. A.; Sahito, I. A.; Sun, K. C.; Mengal, N.; Jeong, S. H. Synthesis of Highly Photo-Catalytic and Electro-Catalytic Active Textile Structured Carbon Electrode and Its Application in DSSCs. *Sol. Energy* **2017,** *150*, 521-531.
(723) Liu, C.-T.; Wang, Y.-C.; Dong, R.-X.; Wang, C.-C.; Huang, K.-C.; Vittal, R.; Ho, K.-C.; Lin, J.-J. A Dual-Functional Pt/CNT TCO-Free Counter Electrode for Dye-Sensitized Solar Cell. *J. Mater. Chem.* **2012,** *22*, 25311-25315.
(724) Zhang, J.; Yu, M.; Li, S.; Meng, Y.; Wu, X.; Liu, J. Transparent Conducting Oxide-Free Nitrogen-Doped Graphene/Reduced Hydroxylated Carbon Nanotube Composite Paper as Flexible Counter Electrodes for Dye-Sensitized Solar Cells. *J. Power Sources* **2016,** *334*, 44-51.
(725) Shin, H.-J.; Jeon, S. S.; Im, S. S. CNT/PEDOT Core/Shell Nanostructures as A Counter Electrode for Dye-Sensitized Solar Cells. *Synth. Met.* **2011,** *161*, 1284-1288.
(726) Arbab, A. A.; Sun, K. C.; Sahito, I. A.; Qadir, M. B.; Choi, Y. S.; Jeong, S. H. A Novel Activated-Charcoal-Doped Multiwalled Carbon Nanotube Hybrid for Quasi-Solid-State Dye-Sensitized Solar Cell Outperforming Pt Electrode. *ACS Appl. Mater. Interfaces* **2016,** *8*, 7471-7482.
(727) Kim, S. Y.; Kim, Y.; Lee, K. M.; Yoon, W. S.; Lee, H. S.; Lee, J. T.; Kim, S.-J.; Ahn, Y. H.; Park, J.-Y.; Lee, T. K.et al. Fully Solution-Processed Transparent Conducting Oxide-Free Counter Electrodes for Dye-Sensitized Solar Cells: Spray-Coated Single-Wall Carbon Nanotube Thin Films Loaded with Chemically-Reduced Platinum Nanoparticles. *ACS Appl. Mater. Interfaces* **2014,** *6*, 13430-13437.
(728) Low, F. W.; Lai, C. W. Recent Developments of Graphene-TiO2 Composite Nanomaterials as Efficient Photoelectrodes in Dye-Sensitized Solar Cells: A Review. *Renewable Sustainable Energy Rev.* **2018,** *82*, 103-125.
(729) Wang, J.; Lin, Y.; Pinault, M.; Filoramo, A.; Fabert, M.; Ratier, B.; Bouclé, J.; Herlin-Boime, N. Single-Step Preparation of TiO2/MWCNT Nanohybrid Materials by Laser Pyrolysis and Application to Efficient Photovoltaic Energy Conversion. *ACS Appl. Mater. Interfaces* **2015,** *7*, 51-56.
(730) Liu, J.; Fu, X.; Cao, D.-P.; Mao, L.; Wang, J.; Mu, D.-H.; Mi, B.-X.; Zhao, B.-M.; Gao, Z.-Q. Stacked Graphene–TiO2 Photoanode via Electrospray Deposition for Highly Efficient Dye-Sensitized Solar Cells. *Org. Electron.* **2015,** *23*, 158-163.
(731) Yu, M.; Qu, Y.; Pan, K.; Wang, G.; Li, Y. Enhanced Photoelectric Conversion Efficiency of Dye-Sensitized Solar Cells by the Synergetic Effect of NaYF4:Er3+/Yb3+ and g-C3N4. *Sci.China Mater.* **2017,** *60*, 228-238.

(732) Mathew, S.; Yella, A.; Gao, P.; Humphry-Baker, R.; Curchod, B. F. E.; Ashari-Astani, N.; Tavernelli, I.; Rothlisberger, U.; Nazeeruddin, M. K.; Grätzel, M. Dye-Sensitized Solar Cells with 13% Efficiency Achieved Through the Molecular Engineering of Porphyrin Sensitizers. *Nat. Chem.* **2014,** *6*, 242.
(733) Cho, S.; Hwang, S. H.; Kim, C.; Jang, J. Polyaniline Porous Counter-electrodes for High Performance Dye-sensitized Solar Cells. *J. Mater. Chem.* **2012,** *22*, 12164-12171.
(734) Khan, A.; Huang, Y.-T.; Miyasaka, T.; Ikegami, M.; Feng, S.-P.; Li, W.-D. Solution-Processed Transparent Nickel-Mesh Counter Electrode with in-Situ Electrodeposited Platinum Nanoparticles for Full-Plastic Bifacial Dye-Sensitized Solar Cells. *ACS Appl. Mater. Interfaces* **2017,** *9*, 8083-8091.
(735) Snaith, H. J. Present Status and Future Prospects of Perovskite Photovoltaics. *Nat. Mater.* **2018,** *17*, 372-376.
(736) Rong, Y.; Hu, Y.; Mei, A.; Tan, H.; Saidaminov, M. I.; Seok, S. I.; McGehee, M. D.; Sargent, E. H.; Han, H. Challenges for Commercializing Perovskite Solar Cells. *Science* **2018,** *361*, eaat8235.
(737) Kojima, A.; Teshima, K.; Shirai, Y.; Miyasaka, T. Organometal Halide Perovskites as Visible-Light Sensitizers for Photovoltaic Cells. *J. Am. Chem. Soc.* **2009,** *131*, 6050-6051.
(738) Kim, H.-S.; Lee, C.-R.; Im, J.-H.; Lee, K.-B.; Moehl, T.; Marchioro, A.; Moon, S.-J.; Humphry-Baker, R.; Yum, J.-H.; Moser, J. E.et al. Lead Iodide Perovskite Sensitized All-Solid-State Submicron Thin Film Mesoscopic Solar Cell with Efficiency Exceeding 9%. *Sci. Rep.* **2012,** *2*, 591.
(739) Liu, M.; Johnston, M. B.; Snaith, H. J. Efficient Planar Heterojunction Perovskite Solar Cells by Vapour Deposition. *Nature* **2013,** *501*, 395.
(740) Stranks, S. D.; Eperon, G. E.; Grancini, G.; Menelaou, C.; Alcocer, M. J. P.; Leijtens, T.; Herz, L. M.; Petrozza, A.; Snaith, H. J. Electron-Hole Diffusion Lengths Exceeding 1 Micrometer in an Organometal Trihalide Perovskite Absorber. *Science* **2013,** *342*, 341-344.
(741) Best Research-Cell Efficiencies https://www.nrel.gov/pv/assets/pdfs/best-research-cell-efficiencies.20191104.pdf (accessed Nov 06, 2019).
(742) McMeekin, D. P.; Sadoughi, G.; Rehman, W.; Eperon, G. E.; Saliba, M.; Hörantner, M. T.; Haghighirad, A.; Sakai, N.; Korte, L.; Rech, B.et al. A Mixed-Cation Lead Mixed-Halide Perovskite Absorber for Tandem Solar Cells. *Science* **2016,** *351*, 151-155.
(743) Zhao, D.; Yu, Y.; Wang, C.; Liao, W.; Shrestha, N.; Grice, C. R.; Cimaroli, A. J.; Guan, L.; Ellingson, R. J.; Zhu, K.et al. Low-Bandgap Mixed Tin–Lead Iodide Perovskite Absorbers with Long Carrier Lifetimes for All-Perovskite Tandem Solar Cells. *Nat. Energy* **2017,** *2*, 17018.
(744) Todorov, T.; Gershon, T.; Gunawan, O.; Lee, Y. S.; Sturdevant, C.; Chang, L.-Y.; Guha, S. Monolithic Perovskite-CIGS Tandem Solar Cells via In Situ Band Gap Engineering. *Adv. Energy Mater.* **2015,** *5*, 1500799.
(745) Eperon, G. E.; Leijtens, T.; Bush, K. A.; Prasanna, R.; Green, T.; Wang, J. T.-W.; McMeekin, D. P.; Volonakis, G.; Milot, R. L.; May, R.et al. Perovskite-perovskite Tandem Photovoltaics with Optimized Band Gaps. *Science* **2016,** *354*, 861-865.
(746) Oxford PV perovskite solar cell achieves 28% efficiency. https://www.oxfordpv.com/news/oxford-pv-perovskite-solar-cell-achieves-28-efficiency (accessed Jul. 29, 2019).

(747) Tong, J.; Song, Z.; Kim, D. H.; Chen, X.; Chen, C.; Palmstrom, A. F.; Ndione, P. F.; Reese, M. O.; Dunfield, S. P.; Reid, O. G.et al. Carrier Lifetimes of > 1 μs in Sn-Pb Perovskites Enable Efficient All-Perovskite Tandem Solar Cells. *Science* **2019**, DOI:10.1126/science.aav7911 10.1126/science.aav7911eaav7911.
(748) Hwang, K.; Jung, Y.-S.; Heo, Y.-J.; Scholes, F. H.; Watkins, S. E.; Subbiah, J.; Jones, D. J.; Kim, D.-Y.; Vak, D. Toward Large Scale Roll-to-Roll Production of Fully Printed Perovskite Solar Cells. *Adv. Mater.* **2015,** *27*, 1241-1247.
(749) Roldán-Carmona, C.; Malinkiewicz, O.; Soriano, A.; Mínguez Espallargas, G.; Garcia, A.; Reinecke, P.; Kroyer, T.; Dar, M. I.; Nazeeruddin, M. K.; Bolink, H. J. Flexible High Efficiency Perovskite Solar Cells. *Energy Environ. Sci.* **2014,** *7*, 994-997.
(750) Jeon, I.; Chiba, T.; Delacou, C.; Guo, Y.; Kaskela, A.; Reynaud, O.; Kauppinen, E. I.; Maruyama, S.; Matsuo, Y. Single-Walled Carbon Nanotube Film as Electrode in Indium-Free Planar Heterojunction Perovskite Solar Cells: Investigation of Electron-Blocking Layers and Dopants. *Nano Lett.* **2015,** *15*, 6665-6671.
(751) Jiang, F.; Liu, T.; Zeng, S.; Zhao, Q.; Min, X.; Li, Z.; Tong, J.; Meng, W.; Xiong, S.; Zhou, Y. Metal Electrode–free Perovskite Solar Cells with Transfer-laminated Conducting Polymer Electrode. *Opt. Express* **2015,** *23*, A83-A91.
(752) Troughton, J.; Bryant, D.; Wojciechowski, K.; Carnie, M. J.; Snaith, H.; Worsley, D. A.; Watson, T. M. Highly Efficient, Flexible, Indium-Free Perovskite Solar Cells Employing Metallic Substrates. *J. Mater. Chem. A* **2015,** *3*, 9141-9145.
(753) Chen, L.; Xie, X.; Liu, Z.; Lee, E.-C. A Transparent Poly(3,4-ethylenedioxylenethiophene):poly(styrene sulfonate) Cathode for Low Temperature Processed, Metal-oxide Free Perovskite Solar Cells. *J. Mater. Chem. A* **2017,** *5*, 6974-6980.
(754) Ramírez Quiroz, C. O.; Shen, Y.; Salvador, M.; Forberich, K.; Schrenker, N.; Spyropoulos, G. D.; Heumüller, T.; Wilkinson, B.; Kirchartz, T.; Spiecker, E.et al. Balancing Electrical and Optical Losses for Efficient 4-Terminal Si–Perovskite Solar Cells with Solution Processed Percolation Electrodes. *J. Mater. Chem. A* **2018,** *6*, 3583-3592.
(755) Wu, S.; Chen, R.; Zhang, S.; Babu, B. H.; Yue, Y.; Zhu, H.; Yang, Z.; Chen, C.; Chen, W.; Huang, Y.et al. A Chemically Inert Bismuth Interlayer Enhances Long-Term Stability of Inverted Perovskite Solar Cells. *Nat. Commun.* **2019,** *10*, 1161.
(756) Moreno-Moreno, M.; Troyano, J.; Ares, P.; Castillo, O.; Nijhuis, C. A.; Yuan, L.; Amo-Ochoa, P.; Delgado, S.; Gómez-Herrero, J.; Zamora, F.et al. One-Pot Preparation of Mechanically Robust, Transparent, Highly Conductive, and Memristive Metal–Organic Ultrathin Film. *ACS Nano* **2018,** *12*, 10171-10177.
(757) Jin, Z.; Yan, J.; Huang, X.; Xu, W.; Yang, S.; Zhu, D.; Wang, J. Solution-processed Transparent Coordination Polymer Electrode for Photovoltaic Solar Cells. *Nano Energy* **2017,** *40*, 376-381.
(758) Zhang, F.; Yang, X.; Cheng, M.; Wang, W.; Sun, L. Boosting the Efficiency and the Stability of Low Cost Perovskite Solar Cells by Using CuPc Nanorods as Hole Transport Material and Carbon as Counter Electrode. *Nano Energy* **2016,** *20*, 108-116.
(759) Aitola, K.; Domanski, K.; Correa-Baena, J.-P.; Sveinbjörnsson, K.; Saliba, M.; Abate, A.; Grätzel, M.; Kauppinen, E.; Johansson, E. M. J.; Tress, W.et al. High Temperature-Stable Perovskite Solar Cell Based on Low-Cost Carbon Nanotube Hole Contact. *Adv. Mater.* **2017,** *29*, 1606398.

(760) Chen, H.; Wei, Z.; He, H.; Zheng, X.; Wong, K. S.; Yang, S. Solvent Engineering Boosts the Efficiency of Paintable Carbon-Based Perovskite Solar Cells to Beyond 14%. *Adv. Energy Mater.* **2016,** *6*, 1502087.
(761) Jeon, I.; Yoon, J.; Ahn, N.; Atwa, M.; Delacou, C.; Anisimov, A.; Kauppinen, E. I.; Choi, M.; Maruyama, S.; Matsuo, Y. Carbon Nanotubes versus Graphene as Flexible Transparent Electrodes in Inverted Perovskite Solar Cells. *J. Phys. Chem. Lett.* **2017,** *8*, 5395-5401.
(762) Lang, F.; Gluba, M. A.; Albrecht, S.; Rappich, J.; Korte, L.; Rech, B.; Nickel, N. H. Perovskite Solar Cells with Large-Area CVD-Graphene for Tandem Solar Cells. *J. Phys. Chem. Lett.* **2015,** *6*, 2745-2750.
(763) Zhou, J.; Ren, Z.; Li, S.; Liang, Z.; Surya, C.; Shen, H. Semi-Transparent Cl-Doped Perovskite Solar Cells with Graphene Electrodes for Tandem Application. *Mater. Lett.* **2018,** *220*, 82-85.
(764) Heo, J. H.; Shin, D. H.; Kim, S.; Jang, M. H.; Lee, M. H.; Seo, S. W.; Choi, S.-H.; Im, S. H. Highly Efficient CH3NH3PbI3 Perovskite Solar Cells Prepared by AuCl3-doped Graphene Transparent Conducting Electrodes. *Chem. Eng. J.* **2017,** *323*, 153-159.
(765) Fang, Y.; Wu, Z.; Li, J.; Jiang, F.; Zhang, K.; Zhang, Y.; Zhou, Y.; Zhou, J.; Hu, B. High-Performance Hazy Silver Nanowire Transparent Electrodes through Diameter Tailoring for Semitransparent Photovoltaics. *Adv. Funct. Mater.* **2018,** *28*, 1705409.
(766) Schubert, M. B.; Werner, J. H. Flexible Solar Cells for Clothing. *Mater. Today* **2006,** *9*, 42-50.
(767) Giannouli, M.; Yianoulis, P. Study on the Incorporation of Photovoltaic Systems as an Auxiliary Power Source for Hybrid and Electric Vehicles. *Sol. Energy* **2012,** *86*, 441-451.
(768) Lemey, S.; Declercq, F.; Rogier, H. Dual-Band Substrate Integrated Waveguide Textile Antenna With Integrated Solar Harvester. *IEEE Antennas Wirel. Propag. Lett.* **2014,** *13*, 269-272.
(769) Mohr, N. J.; Meijer, A.; Huijbregts, M. A. J.; Reijnders, L. Environmental Life Cycle Assessment of Roof-Integrated Flexible Amorphous Silicon/Nanocrystalline Silicon Solar Cell Laminate. *Prog. Photovoltaics Res. Appl.* **2013,** *21*, 802-815.
(770) Wang, K.; Wu, H.; Meng, Y.; Zhang, Y.; Wei, Z. Integrated Energy Storage and Electrochromic Function in One Flexible Device: An Energy Storage Smart Window. *Energy Environ. Sci.* **2012,** *5*, 8384-8389.
(771) Rogers, J. A.; Someya, T.; Huang, Y. Materials and Mechanics for Stretchable Electronics. *Science* **2010,** *327*, 1603-1607.
(772) Liu, Y.; Pharr, M.; Salvatore, G. A. Lab-on-Skin: A Review of Flexible and Stretchable Electronics for Wearable Health Monitoring. *ACS Nano* **2017,** *11*, 9614-9635.
(773) Zeng, W.; Shu, L.; Li, Q.; Chen, S.; Wang, F.; Tao, X.-M. Fiber-Based Wearable Electronics: A Review of Materials, Fabrication, Devices, and Applications. *Adv. Mater.* **2014,** *26*, 5310-5336.
(774) Aernouts, T.; Vanlaeke, P.; Geens, W.; Poortmans, J.; Heremans, P.; Borghs, S.; Mertens, R.; Andriessen, R.; Leenders, L. Printable Anodes for Flexible Organic Solar Cell Modules. *Thin Solid Films* **2004,** *451-452*, 22-25.
(775) Kim, B. J.; Kim, D. H.; Lee, Y.-Y.; Shin, H.-W.; Han, G. S.; Hong, J. S.; Mahmood, K.; Ahn, T. K.; Joo, Y.-C.; Hong, K. S.et al. Highly Efficient and Bending Durable Perovskite Solar Cells: Toward a Wearable Power Source. *Energy Environ. Sci.* **2015,** *8*, 916-921.

(776) Fan, Z.; Razavi, H.; Do, J.-w.; Moriwaki, A.; Ergen, O.; Chueh, Y.-L.; Leu, P. W.; Ho, J. C.; Takahashi, T.; Reichertz, L. A.et al. Three-dimensional Nanopillar-array Photovoltaics on Low-cost and Flexible Substrates. *Nat. Mater.* **2009,** *8*, 648.
(777) Liao, J.-Y.; Lei, B.-X.; Chen, H.-Y.; Kuang, D.-B.; Su, C.-Y. Oriented Hierarchical Single Crystalline Anatase TiO2 Nanowire Arrays on Ti-Foil Substrate for Efficient Flexible Dye-Sensitized Solar Cells. *Energy Environ. Sci.* **2012,** *5*, 5750-5757.
(778) Jiang, Q. W.; Li, G. R.; Liu, S.; Gao, X. P. Surface-Nitrided Nickel with Bifunctional Structure As Low-Cost Counter Electrode for Dye-Sensitized Solar Cells. *J. Phys. Chem. C* **2010,** *114*, 13397-13401.
(779) Pan, S.; Yang, Z.; Chen, P.; Deng, J.; Li, H.; Peng, H. Wearable Solar Cells by Stacking Textile Electrodes. *Angew. Chem. Int. Ed.* **2014,** *53*, 6110-6114.
(780) Gao, Z.; Bumgardner, C.; Song, N.; Zhang, Y.; Li, J.; Li, X. Cotton-textile-enabled Flexible Self-sustaining Power Packs via Roll-to-roll Fabrication. *Nat. Commun.* **2016,** *7*, 11586.
(781) Chen, J.; Huang, Y.; Zhang, N.; Zou, H.; Liu, R.; Tao, C.; Fan, X.; Wang, Z. L. Micro-cable Structured Textile for Simultaneously Harvesting Solar and Mechanical Energy. *Nat. Energy* **2016,** *1*, 16138.
(782) Zhang, Z.; Li, X.; Guan, G.; Pan, S.; Zhu, Z.; Ren, D.; Peng, H. A Lightweight Polymer Solar Cell Textile that Functions when Illuminated from Either Side. *Angew. Chem. Int. Ed.* **2014,** *53*, 11571-11574.
(783) Wen, Z.; Yeh, M.-H.; Guo, H.; Wang, J.; Zi, Y.; Xu, W.; Deng, J.; Zhu, L.; Wang, X.; Hu, C.et al. Self-Powered Textile for Wearable Electronics by Hybridizing Fiber-Shaped Nanogenerators, Solar Cells, and Supercapacitors. *Sci. Adv.* **2016,** *2*, e1600097.
(784) Townsend, P. H.; Barnett, D. M.; Brunner, T. A. Elastic Relationships in Layered Composite Media with Approximation for the Case of Thin Films on a Thick Substrate. *J. Appl. Phys.* **1987,** *62*, 4438-4444.
(785) Hsueh, C.-H. Modeling of Elastic Deformation of Multilayers Due to Residual Stresses and External Bending. *J. Appl. Phys.* **2002,** *91*, 9652-9656.
(786) Li, L.; Lin, H.; Qiao, S.; Zou, Y.; Danto, S.; Richardson, K.; Musgraves, J. D.; Lu, N.; Hu, J. Integrated Flexible Chalcogenide Glass Photonic Devices. *Nat. Photonics* **2014,** *8*, 643.
(787) Li, S.; Su, Y.; Li, R. Splitting of the Neutral Mechanical Plane Depends on the Length of the Multi-Layer Structure of Flexible Electronics. *Proc. Royal Soc. A* **2016,** *472*, 20160087.
(788) Kim, W.; Lee, I.; Yoon Kim, D.; Yu, Y.-Y.; Jung, H.-Y.; Kwon, S.; Seo Park, W.; Kim, T.-S. Controlled Multiple Neutral Planes by Low Elastic Modulus Adhesive for Flexible Organic Photovoltaics. *Nanotechnology* **2017,** *28*, 194002.
(789) Laskarakis, A.; Logothetidis, S.; Kassavetis, S.; Papaioannou, E. Surface Modification of Poly(ethylene terephthalate) Polymeric Films for Flexible Electronics Applications. *Thin Solid Films* **2008,** *516*, 1443-1448.
(790) Xu, H.; Luo, D.; Li, M.; Xu, M.; Zou, J.; Tao, H.; Lan, L.; Wang, L.; Peng, J.; Cao, Y. A Flexible AMOLED Display on the PEN Substrate Driven by Oxide Thin-Film Transistors Using Anodized Aluminium Oxide as Dielectric. *J. Mater. Chem. C* **2014,** *2*, 1255-1259.
(791) Poorkazem, K.; Liu, D.; Kelly, T. L. Fatigue Resistance of a Flexible, Efficient, and Metal Oxide-Free Perovskite Solar Cell. *J. Mater. Chem. A* **2015,** *3*, 9241-9248.

(792) Khang, D.-Y.; Rogers, J. A.; Lee, H. H. Mechanical Buckling: Mechanics, Metrology, and Stretchable Electronics. *Adv. Funct. Mater.* **2009,** *19*, 1526-1536.
(793) Miyamoto, A.; Lee, S.; Cooray, N. F.; Lee, S.; Mori, M.; Matsuhisa, N.; Jin, H.; Yoda, L.; Yokota, T.; Itoh, A.et al. Inflammation-Free, Gas-Permeable, Lightweight, Stretchable On-Skin Electronics with Nanomeshes. *Nat. Nanotechnol.* **2017,** *12*, 907.
(794) Lomov, S. V.; Boisse, P.; Deluycker, E.; Morestin, F.; Vanclooster, K.; Vandepitte, D.; Verpoest, I.; Willems, A. Full-Field Strain Measurements in Textile Deformability Studies. *Compos. Pt. A Appl. Sci. Manuf.* **2008,** *39*, 1232-1244.
(795) Lee, J.; Kwon, H.; Seo, J.; Shin, S.; Koo, J. H.; Pang, C.; Son, S.; Kim, J. H.; Jang, Y. H.; Kim, D. E.et al. Conductive Fiber-Based Ultrasensitive Textile Pressure Sensor for Wearable Electronics. *Adv. Mater.* **2015,** *27*, 2433-2439.
(796) Pu, X.; Li, L.; Song, H.; Du, C.; Zhao, Z.; Jiang, C.; Cao, G.; Hu, W.; Wang, Z. L. A Self-Charging Power Unit by Integration of a Textile Triboelectric Nanogenerator and a Flexible Lithium-Ion Battery for Wearable Electronics. *Adv. Mater.* **2015,** *27*, 2472-2478.
(797) Liu, J.; Namboothiry, M. A. G.; Carroll, D. L. Fiber-Based Architectures for Organic Photovoltaics. *Appl. Phys. Lett.* **2007,** *90*, 063501.
(798) O'Connor, B.; Pipe, K. P.; Shtein, M. Fiber Based Organic Photovoltaic Devices. *Appl. Phys. Lett.* **2008,** *92*, 193306.
(799) Lee, M. R.; Eckert, R. D.; Forberich, K.; Dennler, G.; Brabec, C. J.; Gaudiana, R. A. Solar Power Wires Based on Organic Photovoltaic Materials. *Science* **2009,** *324*, 232-235.
(800) Yang, Z.; Sun, H.; Chen, T.; Qiu, L.; Luo, Y.; Peng, H. Photovoltaic Wire Derived from a Graphene Composite Fiber Achieving an 8.45 % Energy Conversion Efficiency. *Angewandte Chemie International Edition* **2013,** *52*, 7545-7548.
(801) Zhang, M.; Fang, S.; Zakhidov, A. A.; Lee, S. B.; Aliev, A. E.; Williams, C. D.; Atkinson, K. R.; Baughman, R. H. Strong, Transparent, Multifunctional, Carbon Nanotube Sheets. *Science* **2005,** *309*, 1215-1219.
(802) Veedu, V. P.; Cao, A.; Li, X.; Ma, K.; Soldano, C.; Kar, S.; Ajayan, P. M.; Ghasemi-Nejhad, M. N. Multifunctional Composites Using Reinforced Laminae with Carbon-Nanotube Forests. *Nat. Mater.* **2006,** *5*, 457-462.
(803) Qiu, L.; He, S.; Yang, J.; Deng, J.; Peng, H. Fiber-Shaped Perovskite Solar Cells with High Power Conversion Efficiency. *Small* **2016,** *12*, 2419-2424.
(804) Zhao, Z.; Yan, C.; Liu, Z.; Fu, X.; Peng, L.-M.; Hu, Y.; Zheng, Z. Machine-Washable Textile Triboelectric Nanogenerators for Effective Human Respiratory Monitoring through Loom Weaving of Metallic Yarns. *Adv. Mater.* **2016,** *28*, 10267-10274.
(805) Jost, K.; Stenger, D.; Perez, C. R.; McDonough, J. K.; Lian, K.; Gogotsi, Y.; Dion, G. Knitted and Screen Printed Carbon-fiber Supercapacitors for Applications in Wearable Electronics. *Energy Environ. Sci.* **2013,** *6*, 2698-2705.
(806) Wang, Z.; Zhang, L.; Bayram, Y.; Volakis, J. L. Embroidered Conductive Fibers on Polymer Composite for Conformal Antennas. *IEEE Trans. Antennas Propag.* **2012,** *60*, 4141-4147.
(807) Chai, Z.; Zhang, N.; Sun, P.; Huang, Y.; Zhao, C.; Fan, H. J.; Fan, X.; Mai, W. Tailorable and Wearable Textile Devices for Solar Energy Harvesting and Simultaneous Storage. *ACS Nano* **2016,** *10*, 9201-9207.
(808) Bi, C.; Chen, B.; Wei, H.; DeLuca, S.; Huang, J. Efficient Flexible Solar Cell based on Composition-Tailored Hybrid Perovskite. *Adv. Mater.* **2017,** *29*, 1605900.

(809) Chirilă, A.; Reinhard, P.; Pianezzi, F.; Bloesch, P.; Uhl, A. R.; Fella, C.; Kranz, L.; Keller, D.; Gretener, C.; Hagendorfer, H.et al. Potassium-induced Surface Modification of Cu(In,Ga)Se2 Thin Films for High-efficiency Solar Cells. *Nat. Mater.* **2013,** *12*, 1107.
(810) Kang, S.-B.; Kim, H.-J.; Noh, Y.-J.; Na, S.-I.; Kim, H.-K. Face-to-face Transferred Multicrystalline ITO Films on Colorless Polyimide Substrates for Flexible Organic Solar Cells. *Nano Energy* **2015,** *11*, 179-188.
(811) Wang, X.; Jin, H.; Nagiri, R. C. R.; Poliquit, B. Z. L.; Subbiah, J.; Jones, D. J.; Kopidakis, N.; Burn, P. L.; Yu, J. Flexible ITO-Free Organic Photovoltaics on Ultra-Thin Flexible Glass Substrates with High Efficiency and Improved Stability. *Sol. RRL* **2019,** *3*, 1800286.
(812) Liu, D.; Li, Y.; Zhao, S.; Cao, A.; Zhang, C.; Liu, Z.; Bian, Z.; Liu, Z.; Huang, C. Single-Layer Graphene Sheets as Counter Electrodes for Fiber-Shaped Polymer Solar Cells. *RSC Adv.* **2013,** *3*, 13720-13727.
(813) Liang, J.; Zhang, G.; Sun, W.; Dong, P. High Efficiency Flexible Fiber-Type Dye-Sensitized Solar Cells with Multi-Working Electrodes. *Nano Energy* **2015,** *12*, 501-509.
(814) Yun, M. J.; Cha, S. I.; Seo, S. H.; Lee, D. Y. Highly Flexible Dye-sensitized Solar Cells Produced by Sewing Textile Electrodes on Cloth. *Sci. Rep.* **2014,** *4*, 5322.
(815) Rong, Y.; Ming, Y.; Ji, W.; Li, D.; Mei, A.; Hu, Y.; Han, H. Toward Industrial-Scale Production of Perovskite Solar Cells: Screen Printing, Slot-Die Coating, and Emerging Techniques. *J. Phys. Chem. Lett.* **2018,** *9*, 2707-2713.
(816) Schneider, R.; Losio, P. A.; Nüesch, F. A.; Heier, J. Gravure Printed Ag/Conductive Polymer Electrodes and Simulation of Their Electrical Properties. *Int. J. Adv. Manuf. Technol* **2019**, DOI:10.1007/s00170-019-03835-7 10.1007/s00170-019-03835-7
(817) Kim, J.; Kumar, R.; Bandodkar, A. J.; Wang, J. Advanced Materials for Printed Wearable Electrochemical Devices: A Review. *Adv. Electron. Mater.* **2017,** *3*, 1600260.
(818) News Release: Perovskite Technology is Scalable, But Questions Remain about the Best Methods. https://www.nrel.gov/news/press/2018/perovskite-technology-is-scalable-but-questions-remain-about-the-best-methods.html (accessed Jul. 29, 2019).
(819) Meng, L.; You, J.; Yang, Y. Addressing the Stability Issue of Perovskite Solar Cells for Commercial Applications. *Nat. Commun.* **2018,** *9*, 5265.
(820) Grancini, G.; Roldán-Carmona, C.; Zimmermann, I.; Mosconi, E.; Lee, X.; Martineau, D.; Narbey, S.; Oswald, F.; De Angelis, F.; Graetzel, M.et al. One-Year Stable Perovskite Solar Cells by 2D/3D Interface Engineering. *Nat. Commun.* **2017,** *8*, 15684.
(821) Song, Z.; McElvany, C. L.; Phillips, A. B.; Celik, I.; Krantz, P. W.; Watthage, S. C.; Liyanage, G. K.; Apul, D.; Heben, M. J. A Technoeconomic Analysis of Perovskite Solar Module Manufacturing with Low-Cost Materials and Techniques. *Energy Environ. Sci.* **2017,** *10*, 1297-1305.
(822) Dupont, S. R.; Novoa, F.; Voroshazi, E.; Dauskardt, R. H. Decohesion Kinetics of PEDOT:PSS Conducting Polymer Films. *Adv. Funct. Mater.* **2014,** *24*, 1325-1332.
(823) Kim, S.; Kim, S. Y.; Chung, M. H.; Kim, J.; Kim, J. H. A one-step roll-to-roll process of stable AgNW/PEDOT:PSS solution using imidazole as a mild base for highly conductive and transparent films: optimizations and mechanisms. *J. Mater. Chem. C* **2015,** *3*, 5859-5868.
(824) Rider, D. A.; Worfolk, B. J.; Harris, K. D.; Lalany, A.; Shahbazi, K.; Fleischauer, M. D.; Brett, M. J.; Buriak, J. M. Stable Inverted Polymer/Fullerene Solar Cells Using a Cationic

Polythiophene Modified PEDOT:PSS Cathodic Interface. *Adv. Funct. Mater.* **2010,** *20*, 2404-2415.
(825) McCarthy, J. E.; Hanley, C. A.; Brennan, L. J.; Lambertini, V. G.; Gun'ko, Y. K. Fabrication of Highly Transparent and Conducting PEDOT:PSS Films Using a Formic Acid Treatment. *J. Mater. Chem. C* **2014,** *2*, 764-770.
(826) Zimmermann, B.; Würfel, U.; Niggemann, M. Longterm Stability of Efficient Inverted P3HT:PCBM Solar Cells. *Sol. Energy Mater. Sol. Cells* **2009,** *93*, 491-496.
(827) Khaligh, H. H.; Goldthorpe, I. A. Failure of Silver Nanowire Transparent Electrodes under Current Flow. *Nanoscale Res. Lett.* **2013,** *8*, 235.
(828) Jiu, J.; Wang, J.; Sugahara, T.; Nagao, S.; Nogi, M.; Koga, H.; Suganuma, K.; Hara, M.; Nakazawa, E.; Uchida, H. The Effect of Light and Humidity on the Stability of Silver Nanowire Transparent Electrodes. *RSC Adv.* **2015,** *5*, 27657-27664.
(829) Ahn, Y.; Jeong, Y.; Lee, Y. Improved Thermal Oxidation Stability of Solution-Processable Silver Nanowire Transparent Electrode by Reduced Graphene Oxide. *ACS Appl. Mater. Interfaces* **2012,** *4*, 6410-6414.
(830) Lee, D.; Lee, H.; Ahn, Y.; Jeong, Y.; Lee, D.-Y.; Lee, Y. Highly Stable and Flexible Silver Nanowire–Graphene Hybrid Transparent Conducting Electrodes For Emerging Optoelectronic Devices. *Nanoscale* **2013,** *5*, 7750-7755.
(831) Galagan, Y.; de Vries, I. G.; Langen, A. P.; Andriessen, R.; Verhees, W. J. H.; Veenstra, S. C.; Kroon, J. M. Technology Development for Roll-to-roll Production of Organic Photovoltaics. *Chem. Eng. Process.* **2011,** *50*, 454-461.
(832) Vak, D.; Weerasinghe, H.; Ramamurthy, J.; Subbiah, J.; Brown, M.; Jones, D. J. Reverse Gravure Coating for Roll-To-Roll Production of Organic Photovoltaics. *Sol. Energy Mater. Sol. Cells* **2016,** *149*, 154-161.
(833) Ye, S.; Rathmell, A. R.; Chen, Z.; Stewart, I. E.; Wiley, B. J. Metal Nanowire Networks: The Next Generation of Transparent Conductors. *Adv. Mater.* **2014,** *26*, 6670-6687.
(834) Das, R. OLED Display Market to Reach $25.5Bn in 2018. https://www.idtechex.com/en/research-article/oled-display-market-to-reach-25-5bn-in-2018/15287?donotredirect=true (accessed Nov 06, 2019).
(835) Ghaffarzadeh, K. Transparent Conductive Films and Materials: Past, Present and Future. https://www.idtechex.com/en/research-article/transparent-conductive-films-and-materials-past-present-and-future/14052?donotredirect=true (accessed Nov 06, 2019).

BIOGRAPHY

Yaokang Zhang received his B.Sc. in chemistry from Renmin University of China in 2013 and his Ph.D. degree in 2018 under the supervision of Prof. Zijian Zheng in the Institute of Textiles and Clothing at The Hong Kong Polytechnic University. His research interest focuses on the fabrication of solution-processed flexible electronic devices.

BIOGRAPHY

Sze-Wing Ng received her B.A in fashion technology and B.Sc. in chemical technology from The Hong Kong Polytechnic University in 2013. She received her Ph.D. degree in 2019 under the supervision of Prof. Zijian Zheng. Her research interest focuses on graphene and carbon-based materials and their applications on flexible electronics.

BIOGRAPHY

Xi Lu received his B.Eng (2010) from material science and engineering from Tsinghua University (China) and M.Eng (2013) from Institute of Metal Research, Chinese Academy of Sciences (China). He is currently a PhD candidate under the supervision of Prof. Zijian Zheng at Institute of Textiles & Clothing, The Hong Kong Polytechnic University. His research interests include fabrication approaches and applications of flexible and stretchable electronic materials.

BIOGRAPHY

Zijian Zheng is currently Full Professor at The Hong Kong Polytechnic University. His research interest includes surface and polymer science, nanolithography, flexible and wearable materials

and devices. He received his BEng. in Chemical Engineering at Tsinghua University in 2003 and PhD in Chemistry at the University of Cambridge in 2007. He worked as postdoctoral researcher at Northwestern University before moving to The Hong Kong Polytechnic University as Assistant Professor in 2009. He is Founding Member of The Young Academy of Sciences of Hong Kong.

TOC Graphic


Material
Design
Solution-processed
Transparent Electrodes
for Solar Cells
Processing
Application